Title

Laboratory and field-based instrumentation developments and noble gas-stable isotope systematics of Rungwe Volcanic Province, Iceland and the Central Indian Ridge

Permalink

https://escholarship.org/uc/item/1mt7t4pv

Authors

Barry, Peter Hagan
Barry, Peter Hagan

Publication Date

2012

Peer reviewed|Thesis/dissertation

UNIVERSITY OF CALIFORNIA, SAN DIEGO

Laboratory and field-based instrumentation developments and noble gas-stable

isotope systematics of Rungwe Volcanic Province, Iceland and the Central Indian Ridge

A dissertation submitted in partial satisfaction of the
requirements for the degree Doctor of Philosophy

in

Earth Sciences

by

Peter Hagan Barry

Committee in Charge:

David Hilton, Chair
Paterno Castillo
James Day
Devendra Lal
Mark Thiemens
Michael Tryon

2012

The Dissertation of Peter Hagan Barry is approved, and it is acceptable

in quality and in form for publication on microfilm and electronically:

_____

_____

_____

_____

_____
Chair

University of California, San Diego

2012

DEDICATION

This dissertation is dedicated to my parents, Valentina and Robert Barry.

TABLE OF CONTENTS

LIST OF FIGURES

LIST OF TABLES

ACKNOWLEDGMENTS

I would like to thank several people for their guidance and inspiration during the course of my PhD. First and foremost, I would like to thank my advisor, Dave Hilton, who opened his laboratory to me and shared with me his vast knowledge of geochemistry. He served as my mentor and taught me the skills required to be a good scientist. In addition, he provided me the funding necessary to complete all of the various projects and the unique opportunity to travel to many exciting places to conduct fieldwork and attend scientific conferences. And finally, he was always reliable and supportive – both in life and in science.

In addition, I would like to thank my committee members James Day, Pat Castillo, Devendra Lal, Mark Thiemens and Mike Tryon for their constructive comments on my thesis and their helpful insights during our various meetings during the last few years. I would like to acknowledge all my co-authors for their contributions to the work presented in this dissertation; thanks to Justin Kulongoski, Mike Tryon, Kevin Brown, Evelyn Füri, Saemi Halldórsson, Doshik Hahm, Kurt Marti, Toby Fischer, Maarten de Moor, Fredrick Mangasini, Carlos Rameriez, Karl Grönvold, Bramley Murton, Jérome Dyment, Christophe Hémond for their valuable comments and suggestions. I am also very grateful to Bruce Deck and Martin Wahlen for their assistance in carbon isotope analyses.

I was fortunate to participate in several fieldtrips and research cruises to collect samples for the work presented in this dissertation. I would like to thank Carlos Ramirez, Karl Gronvold, Fredrick Mangasini, Evelyn Füri, Matt Forrest, James Day, Maarten de Moor and Toby Fischer for their assistance in the field. Thanks to the captain and crew of the R/V

Revelle as well as all the scientists who participated in the 2007 cruise from the Seychelles to Mauritius.

Chapter II, in full, is a reprint of the material as it appeared in Geochemistry Geophysics Geosystems 2009, as Barry, P. H., D. R. Hilton, M. D. Tryon, K. M. Brown, and J. T. Kulongoski (2009), A new syringe pump apparatus for the retrieval and temporal analysis of helium in groundwaters and geothermal fluids, *Geochemistry Geophysics Geosystems*, 10, Q05004, doi:10.1029/2009GC002422. The dissertation author was the primary investigator and lead author of this paper and conducted all the analyses presented herein.

Chapter III in full, is a reprint of the material as it appeared in Geochemistry Geophysics Geosystems 2012, as Barry, P. H., D. R. Hilton, S. A. Halldórsson, D. Hahm, and K. Marti (2012), High precision nitrogen isotope measurements in oceanic basalts using a static triple collection noble gas mass spectrometer, *Geochemistry Geophysics Geosystems*, 13, Q01019, doi:10.1029/2011GC003878. The dissertation author was the primary investigator and lead author of this paper and conducted all the analyses presented herein.

Chapter IV in full, is a reprint of the material as it appeared in Chemical Geology 2012, as Barry, P. H., D. R. Hilton, T.P. Fischer, J.M. de Moor, F. Mangasini, and C. Ramirez (2012), Helium and carbon isotope systematics of cold "mazuku" CO_2 vents and hydrothermal gases and fluids from Rungwe Volcanic Province, southern Tanzania, *Chemical Geology*, doi: 10.1016/j.chemgeo.2012.07.003. The dissertation author was the primary investigator and lead author of this paper and conducted all the analyses presented herein.

VITA

2000-2004	The State University of New York (SUNY) at Geneseo, USA – B.A. Geological Sciences
2002	The University of Melbourne, Australia – visiting scholar
2004	The University of Utah, USA – visiting undergraduate researcher
2006-2012	Research Assistant Scripps Institution of Oceanography, UCSD, USA
2007-2011	Teaching Assistant Scripps Institution of Oceanography, UCSD, USA
2008	NSF EAPSI Fellow
2008	The University of Tokyo – Ocean Research Institute – visiting researcher
2011	Scripps Institution of Oceanography, UCSD, USA – M.S. Oceanography
2011-2012	UC President's Dissertation Fellow
2012	Scripps Institution of Oceanography, UCSD, USA – Ph.D. Earth Sciences

PUBLICATIONS

Barry, P.H., Hilton, D.R., Fischer, T.P., de Moor, J.M., Mangasini, F, Ramirez, C.J., (2012) Helium and carbon isotope systematics of cold "mazuku" CO_2 vents and hydrothermal gases and fluids from Rungwe Volcanic Province, southern Tanzania, In Press – *Chemical Geology*, doi:10.1016/j.chemgeo.2012.07.003.

Barry, P.H., Hilton, D.R., Halldórsson S. A., Hahm, D. and Marti, K. (2012) High precision nitrogen isotope measurements in oceanic basalts using a static triple collection noble gas

mass spectrometry. *Geology, Geophysics, and Geosystems (G-Cubed), (Technical Briefs), Volume 13, Number 1*, doi: 10.1029/2011GC003878, 2012.

Kulongoski J.T., Hilton, D.R., Barry, P.H., Esser, B., Hillegonds, D., and Belitz, K. (2012) Mantle-volatile weakening of the Big Bend Section of the San Andreas Fault, California: helium and carbon-dioxide systematics, In Press - *Chemical Geology.*

de Moor J.M., Fischer, T.P., Sharp, Z.D., Hilton, D.R., Barry, P.H., Mangasini, F., and Ramirez, C. (2012) Gas chemistry and nitrogen isotope compositions of cold mantle gases from Rungwe Volcanic Province, southern Tanzania, In Press - *Chemical Geology.*

Barry, P.H., Hilton, D.R., Füri, E, Murton, B.J., Hemond, C. and Dyment, J. (2011) Stable Isotope (C-N) and Noble Gas (Ne-Ar) Evidence for Recycled Plume Components at the CIR *Geochim. Cosmochim. Acta* 75(15) Supplement 1.

Hilton, D.R., Halldórsson, S.A., Barry, P.H., Fischer, T.P., de Moor, J.M., Ramirez, C.J., Mangasini, F. and Scarsi, P. Deep mantle plume contribution to the Rungwe volcanic province revealed by helium isotopes. *GRL.*

Füri, E., Hilton, D.R., Halldórsson, S.A., Barry, P.H., Hahm, D., Fischer, T.P. and Grönvold, K. (2010) Apparent decoupling of the He and Ne isotope systematics of the Icelandic mantle: the role of He depletion, melt mixing, degassing fractionation and air interaction. *Geochim. Cosmochim. Acta* 74, pp 3307-3332.

Hilton, D.R., Ramirez, C., Amador, R.A., Fischer, T.P., Füri, E, Barry, P.H. and Shaw, A.M. (2010) Monitoring of temporal and spatial variations in fumarole helium and carbon dioxide characteristics at Poas and Turrialba volcanoes, Costa Rica (2001-2009). *Geochemical Journal* 44 pp 431-440.

Barry, P.H., Hilton, D.R., Füri, E., Halldórsson, S.A., Fischer T.P. and Grönvold K. (2010) Abundance and isotope systematics of carbon in Icelandic subglacial basalts, geothermal gases and fluids. *Eos Trans*. AGU, 90 (52), Fall Meet. Suppl., Abstract U21A-0006.

Barry, P.H. Hilton, D.R., Tryon, M.D., Brown, K.M., and Kulongoski, J.T. (2009) A New Syringe Pump Apparatus for the Retrieval and Temporal Analysis of Helium (SPARTAH) in groundwaters and geothermal fluids, *Geology, Geophysics, and Geosystems (G-Cubed), (Technical Briefs), Volume 10, Number 5,* doi:10.1029/2009GC002422, 2009.

Barry, P.H., Hilton, D.R., Fischer, T.P., de Moor, J.M., Mangasini F., and Ramirez., C. (2009) Helium and carbon isotope systematics of Rungwe geothermal gases and fluids; southern Tanzania. *Eos Trans.* AGU, 90 (52), Fall Meet. Suppl., Abstract V11G-02.

Barry, P.H., Hilton, D.R., Sano, Y., Takahata, N., Murton, B.J., Füri, E., Hemond, C., and Dyment, J. (2009) Nitrogen isotopes and plume-ridge interaction: the Central Indian Ridge and the Reykjanes Ridge. *Geochim. Cosmochim. Acta* 73(13) Supplement 1, A93.

ABSTRACT OF THE DISSERTATION

Laboratory and field-based instrumentation developments and noble gas-stable

isotope systematics of Rungwe Volcanic Province, Iceland and the Central Indian Ridge

by

Peter Hagan Barry

Doctor of Philosophy in Earth Sciences

University of California, San Diego, 2012

Professor David R. Hilton, Chair

Volatile studies in various tectonic settings have revealed important information about interactions between different mantle reservoirs and the Earth's surface. By employing a combined noble gas and stable isotope approach, we are able to discern surficial processes from intrinsic mantle characteristics. This dissertation discusses laboratory and field based instrumentation developments, which enable high precision measurements of volatile species in the laboratory and improved sampling techniques of volatiles in the field. In addition, the origin(s), transport and behavior of volatiles are discussed in three plume-rift related geological settings: a) Rungwe Volcanic Province (RVP), b) Iceland, and c) the Central Indian Ridge (CIR).

Following a short introduction to the utility of noble gas and stable isotopes as geochemical tracers in plume-rift systems in Chapter I, we discuss the main objectives of the various studies that comprise this dissertation.

Chapter II is a description of syringe pump apparatus for the retrieval and temporal analysis of helium (SPARTAH), a recently developed, semi-autonomous instrument, which enables continuous collection of fluid samples in the field. Fluids can subsequently be sectioned, time-stamped and targeted for volatile characteristics (e.g., He-isotopes), thus creating a time-series record of chemical perturbations in the groundwater system.

Chapter III describes a N_2 extraction and purification system recently constructed in the Fluids and Volatiles Laboratory at SIO. We describe the configuration of the system as well as initial test results that demonstrate the utility of our technique.

Chapter IV examines He-CO_2 and abundance systematics of RVP geothermal fluids and gases. We evaluate the origin of cold CO_2 mazuku-like features, estimate CO_2 fluxes, and address the apparent He-isotope disparity observed between gas, fluid, rock and mineral phases in the region.

Chapter V focuses on the CO_2 isotope and abundance systematics of Iceland geothermal fluids, gases and basalts. We consider various processes such as hydrothermal phase separation, calcite precipitation and degassing which may act to alter intrinsic mantle-source features and attempt to reconstruct source characteristics of the Icelandic mantle prior to modification. In addition, CO_2 fluxes are estimated for Iceland and compared with previous estimates from Iceland and analogous geological settings.

Chapter VI investigates the combined Ne-N-Ar-CO_2 systematics of the CIR as well as Ne-Ar systematics of Réunion xenoliths. We demonstrate that a Réunion-like plume

component is evident in the coupled Ne-N-Ar systematics and that both solar and recycled crustal components are detectable in the Réunion-plume source. Finally, we adopt a coupled assimilation and fractional equilibrium degassing model to explain and reconstruct initial volatile ratios and CO_2 source characteristics.

CHAPTER I: Introduction

The combined study of noble gas (e.g., He, Ne, Ar) and major volatile (e.g., CO_2, N_2) isotopes as well as various elemental ratios, in subaerial and submarine settings enables assessment of the chemical evolution of Earth's mantle and its subsequent degassing history. Mantle-derived volatiles are transferred to the Earth's surface in volcanically- and seismically-active regions through gas manifestations (e.g., fumaroles, bubbling gas springs) and in gases dissolved in groundwater systems. In addition, volatiles are transferred directly to the surface through magmatic eruptions, and can subsequently be sampled in basaltic glasses, phenocrysts and xenoliths at Earth's surface. By using a combined volatile isotope and relative abundance approach, we are able to identify intrinsic mantle characteristics and understand processes occurring during volatile transfer, including interactions between the mantle-crust-atmosphere system.

Noble gases are valuable geochemical tools for determining magma sources and understanding interactions between Earth's mantle and the surface, particularly in seismogenic and/or volcanically active regions (e.g., Tedesco et al., 1998; Italiano and Martinelli, 2001; Hilton et al., 2002). They have been used to place constraints on the structure and evolution of the Earth, including the degassing history of the mantle (Allègre et al., 1983; Marty et al., 1989). Their utility is based on their (a) chemical inertness, (b) highly mobile and incompatible nature in melts, (c) relatively low abundances in the solid Earth, and (d) large isotopic contrasts between different terrestrial reservoirs (e.g., mantle, crust, and atmosphere; Hilton and Porcelli, 2003). Helium and neon are particularly useful due to their unique ability to differentiate between mantle source features and crustal processes.

Helium has two stable isotopes: ^{3}He (primordial in origin) and ^{4}He (produced from radioactive decay of U and Th). The ^{3}He/^{4}He ratio of well-mixed upper mantle, as sampled by mid-ocean ridge basalts (MORB) is uniform at 7-9 R_A (where R_A = the air ^{3}He/^{4}He ratio of 1.4

x 10^{-6}). In contrast, some plume-related and ocean island basalts (OIB) samples show a marked relative enrichment in ^{3}He, with ^{3}He/^{4}He values extending as high as 50 R_A (Stuart et al., 2003), indicating a (plume) mantle reservoir with a high time-integrated ^{3}He/(U+Th) has remained largely undegassed since Earth's accretion. In stark contrast, the continents are characterized by low ^{3}He/^{4}He ratios - in the range of 0.01 to 0.1 R_A – indicating that crustal helium is dominated by the radiogenic ^{4}He component. Large variations between mantle and crustal reservoirs (> three orders of magnitude) form the basis for the utility of helium isotopes as a tracer of mantle-derived volatiles.

Neon has three stable isotopes: nucleogenic ^{21}Ne and ^{22}Ne and primordial ^{20}Ne. Nucleogenic ^{21}Ne is generated by the so-called Wetherill reactions: ^{18}O $(\alpha,n)^{21}$Ne and ^{24}Mg(n, $\alpha)^{21}$Ne (Wetherill, 1954), with the former reaction being dominant for Earth's mantle (Yatsevich and Honda, 1997). Nucleogenic ^{22}Ne production is relatively minor compared to ^{21}Ne, resulting in an increase of the ^{21}Ne/^{22}Ne ratio over time. In contrast, primordial ^{20}Ne is produced in stellar nucleosynthesis (Burbidge et al., 1957; Dickin, 2005). Like He, the utility of Ne is based on the contrast between mantle-derived (e.g., MORB, plume) reservoirs. The best estimate of neon in the mantle source can be achieved by considering that all Ne-isotope signals from volcanic sources likely represent a binary mixture between air and mantle (Moreira et al., 1995) and that Earth's mantle is characterized by elevated ratios of ^{20}Ne /^{22}Ne and ^{21}Ne /^{22}Ne compared to air. However, distinct Ne reservoirs are apparent within the mantle. For example, plume-derived samples define a markedly steeper Ne-isotope trajectory compared with MORB (Sarda et al., 1988), due to larger solar contributions (e.g., solar wind; Ne-B) in the plume-mantle (Graham, 2002).

Argon isotopes also provide important constraints on the isotopic evolution of various mantle reservoirs and the early degassing history of Earth (Matsuda and Marty, 1995; Graham,

2002). Argon has three stable isotopes: ^{40}Ar, ^{38}Ar and ^{36}Ar, and like He and Ne, Argon's utility is centered on the different isotopic compositions in various terrestrial reservoirs. For example, the $^{40}Ar/^{36}Ar$ ratio in the depleted mantle, as sampled by MORB, is as high as 28,000-32,000 (Matsuda and Marty, 1995; Burnard et al., 1997; Trieloff et al, 2003). In contrast, the $^{40}Ar/^{36}Ar$ ratio in plume-related systems is much lower (~6,000-8,000; Valbracht et al., 1997; Marty et al., 1998; Trieloff et al., 2003), however this finding has been strongly debated (Graham, 2002).

Characterizing CO_2 source features is important because CO_2 is the second most abundant major volatile species in the mantle, after H_2O. Unlike the noble gases, there is no clear isotopic distinction between the various mantle reservoirs, suggesting that the mantle may be homogenized with respect to CO_2. The apparent homogenization of mantle carbon can be attributed, in part, to the fact that CO_2 is chemically reactive and thus ($\delta^{13}C$) source characteristics are highly susceptible to external fractionation processes (e.g., degassing) during magma emplacement. In order to circumvent these issues, CO_2 is often used in conjunction with noble gases to determine elemental ratios (e.g., $CO_2/^3He$), which also help constrain physiochemical processes in the crust.

CO_2 is highly incompatible in basaltic melts and during melting is strongly partitioned into the melt phase (Jambon et al., 1986). Due to the low solubility of CO_2 versus H_2O in basaltic melts a CO_2-rich vapor phase exsolves upon decompression, and serves as the primary carrier gas for all other volatiles – including the noble gases. The magmatic concentration of CO_2 is controlled by style of eruption and physical properties of the magma. The process of degassing results in rapid loss of volatiles from the melt and leads to C-isotopic fractionation, so that residual CO_2 in magma becomes progressively depleted in ^{13}C as degassing progresses (Javoy et al. 1978; Mattey, 1991). The extent and mode of degassing can be determined by

considering residual $\delta^{13}C$ and CO_2 concentrations together. In this way, estimates of pre-eruptive source characteristics can be determined.

Characterization of CO_2 source features together with knowledge of magma effusion rates, allow an estimate of mantle CO_2 fluxes at different volcanic settings (arcs, ridges and plumes). This provides important contrasts between tectonic settings, thereby facilitating a better understanding of the carbon cycle between surface and mantle reservoirs. However, CO_2 fluxes from plume-related volcanic provinces are relatively poorly constrained, and thus a primary goal of this dissertation is to derive estimates of CO_2 release rates via both geothermal and magmatic systems in various plume-related systems (e.g., Iceland, Rungwe Volcanic Province), for comparison with better constrained spreading ridge fluxes (Marty and Tolstikhin, 1998).

Volatiles are efficiently transferred from the solid Earth to the surface during magma ascension. For the noble gases, this is mostly a unidirectional process (i.e., they are not recycled back into the mantle through the process of subduction; Moreira et al., 2003; Ballentine et al., 2005; Mukhopadhyay, 2012). In contrast, chemically reactive species (e.g., N_2 and CO_2) are bound in rocks and sediments at the Earth's surface and thus can be recycled into the (deep) mantle at subduction zones (Javoy et al., 1984; Boyd et al., 1987; Marty and Humbert, 1997; Hilton et al., 2002; Marty and Dauphas, 2003; Shaw et al., 2003; de Leeuw, 2007). For example, estimates suggest that up to ~85% of potentially available CO_2 may be recycled into the deep mantle at subduction zones (Hilton et al., 2002; Shaw et al., 2003) and that nearly all mantle nitrogen may be recycled (Marty and Humbert, 1997; Marty and Dauphas, 2003).

Nitrogen is the primary gas in Earth's atmosphere (78%), but is found in trace concentrations (ppm) only in mantle-derived materials. However, nitrogen in the mantle is

considered predominantly recycled on the basis of N/K and $N/^{36}Ar$ ratios (Marty and Dauphas, 2003). Unlike CO_2, distinct nitrogen isotope reservoirs are apparent in the Earth's mantle; the MORB mantle is estimated to be ~ -4 to -5‰ (Javoy et al., 1986; Marty and Zimmerman, 1999) (air is the standard at 0‰), although this range could extend to values as low as −12‰ (Mohapatra and Murty, 2004). In contrast, the deep (plume) mantle, as sampled in the Kola magmatic province, Iceland, Loihi Seamount, Hawaii and the Society Islands is enriched in ^{15}N by up to +8‰, with a mean value of +3 ± 2‰ (Marty and Dauphas, 2003). Various types of diamonds display $\delta^{15}N$ values ranging from -25 up to +15 ‰, with a mode of approximately -5 ‰ (Cartigny et al., 1997, 1998, 1998b, 2001b; Marty and Dauphas, 2003). Modern ocean floor sediments are enriched in ^{15}N with $\delta^{15}N$ values from +5 to +7 ‰ (Peters et al., 1978; Kienast, 2000). As a result, isotopically high $\delta^{15}N$ may be preferentially recycled into the mantle by modern subduction processes. Due to large concentration and isotopic contrasts between surface and mantle reservoirs, N_2 is considered a highly sensitive tracer of interactions between the exosphere and solid Earth.

In this dissertation, we describe field and laboratory based instrumentation developments, which enable us to improve sampling and measurement techniques. In addition, we set out to further constrain the origin, transport and behavior of volatiles (He-Ne-Ar, N_2 and CO_2) at three different geologic settings: a) the Rungwe Volcanic Province (RVP), southern Tanzania, an area of active continental rifting, b) Iceland, a ridge-centered hotspot, and c) the Central Indian Ridge, a mid-ocean ridge segment near an off-axis hotspot.

Chapter II describes newly developed field-based instrumentation that enables water (and dissolved gas) samples to be collected over extended periods. Previous studies (e.g., Sano et al., 1998; Areshidze et al., 1992) have shown that helium and other dissolved gases in groundwater can be monitored to trace physical changes or perturbations induced by seismic

activity in the Earth's crust. In these studies, the general aim of a monitoring program (i.e., repeated sampling at a given location over an extended period of time) was to discover changes in a geochemical parameter, such as He-isotopes, which can either forewarn the impending occurrence of an earthquake or result from, and hence provide information and insight about, a past seismic event. However, geochemical signals are often transient in nature and variable in duration. Therefore, unless sampling frequency is extraordinarily high, there is a strong likelihood that perturbations to the geochemical record will be missed. To this end, we developed a syringe pump apparatus for the retrieval and temporal analysis of helium (SPARTAH), a sampling device designed for collecting geothermal fluid and groundwater samples (containing helium and other dissolved gases and chemical species). SPARTAH is a sampling apparatus that can produce a quasi-continuous temporal record of any selected geochemical parameter as water samples are collected and stored in small diameter Cu-tubing during deployments of up to 6 months. The parameters (e.g., duration) of the deployment are set by the user, and thus all geochemical anomalies, irrespective of duration, can be captured, and later matched against the timing of external transients (i.e. earthquake events). In this way, we show that SPARTAH has the potential to revolutionize the approach to time-series geochemical monitoring.

Chapter III describes laboratory-based instrumentation developments and the construction of new nitrogen extraction and purification system at SIO. Historically, nitrogen isotope ratios ($^{15}N/^{14}N$) were measured using an isotope ratio mass spectrometer (IRMS) operated in dynamic pumping mode (Chang et al., 1974; Thiemens and Clayton, 1983; Javoy and Pineau, 1991), with improvements to the precision of $\delta^{15}N$ measurements achieved only by utilization of ion beam multi-collection (Cartigny et al., 1997; Boyd and Philippot, 1998; Cartigny et al., 2001a; Busigny et al., 2005a). However, low nitrogen abundance samples are not conducive to this technique, leading to the use of noble gas mass spectrometers in nitrogen

isotope studies as they are operated under static vacuum condition during measurement (i.e., not dynamically pumping) (Frick and Pepin, 1981; Wright et al., 1988; Boyd et al., 1988; Hashizume and Sugiura, 1990; Boyd et al., 1993; Murty and Marti, 1994; Craig et al., 1993; Marty et al., 1995; Takahata et al., 1998; Hashizume and Marty, 2004). In this chapter, we describe a newly designed extraction system interfaced to a noble gas mass spectrometer (VG 5440) set up with multiple fixed detectors (two Faraday collectors and one Daly multiplier) for the simultaneous triple-collection of nitrogen isotopes (at masses 28, 29) and interfering species (at mass 30). In addition, we report new $\delta^{15}N$ data on standards and ocean basalts in order to assess internal precision and external reproducibility of the new system as well as accuracy of sample results. These results demonstrate the ability of the new system to make high precision nitrogen isotope measurements on low-N abundance samples (e.g., oceanic basalts), while highlighting the advantages provided by simultaneous triple collection.

Chapter IV discusses He and CO_2 isotope systematics and relative abundance features of geothermal fluids and gases at Rungwe Volcanic Province (RVP) – and from two locations in northern Tanzania. The main objective of this study is to add to the He isotope database already established for the RVP and explore the apparent He-isotope disparity between hydrothermal fluids and gases, e.g., $^3He/^4He$ ratios in fluids are equal to or less than MORB (Pik et al., 2006) whereas higher $^3He/^4He$ values characterize mafic phenocrysts (Hilton et al., 2011). This chapter also reports new carbon isotope (CO_2) values, which provide valuable insight into the mantle characteristics of this major volatile phase. Furthermore, by combining He and CO_2 measurements of the same gas/fluid samples, we are able to identify a number of natural processes (e.g., phase separation, fluid mixing), which occur in the hydrothermal systems. A key finding of this study is that cold CO_2 (mazuku) vents have He-CO_2 characteristics distinct from hydrothermal samples, and we suggest that they may represent storage and release sites located within the volcanic stratigraphy, which are, for the most part,

independent of any regional or local hydrothermal system. In addition, we estimate CO_2 fluxes from the RVP and compare to other areas of active rifting. Finally, using the combined He-CO_2 approach, we are able to offer an explanation for the apparent He-isotope discrepancy observed at RVP when hydrothermal fluids and mafic phenocrysts are used independently to infer He isotope characteristics of the mantle source region.

Chapter V examines the CO_2 systematics (isotope and relative abundance characteristics) of geothermal fluids and subglacial glasses from Iceland. These new CO_2 data are combined with previously published noble gas (He-Ne-Ar) constraints on the same sample suite (Füri et al., 2010) to discern the underlying processes controlling CO_2 abundance, isotope variations, and CO_2-noble gas relationships. Previous geothermal CO_2 studies from Iceland are limited, but suggest a mantle source characterized by higher than MORB-like $\delta^{13}C$ values and $CO_2/^3He$ ratios in axial rift zone samples (Poreda et al., 1992). Due to extremely low CO_2 concentration in basalts, the CO_2 systematics of Icelandic subglacial basalts are very poorly constrained (Höskuldsson et al., 2006; Tuffen et al., 2010), however adjacent ridge segments have both been characterized to contain ~400 ppm CO_2 in their mantle sources. In this study, we estimate initial carbon source characteristics for the various segments of the Icelandic mantle and calculate an average mantle source composition of ~531 ± 64 ppm. Furthermore, by investigating carbon characteristics of both geothermal fluids/gases and subglacially emplaced basalts we are able to effectively identify processes that may act to modify initial CO_2 compositions. Finally, using both new basalt and geothermal data we are able to provide the most comprehensive CO_2 flux estimates for Iceland to date.

Chapter VI investigates the proposed plume-ridge interaction between the Central Indian Ridge (CIR) and the Réunion hotspot, currently located ~1100 km west of the CIR rift axis. We measured stable isotope (C-N) and noble gas (Ne-Ar) characteristics in basalts

collected on the CIR spreading axis between 17 ºS and 21 ºS, and along the adjacent Gasitao, Three Magi, and Rodrigues ridges to the west of the CIR. In addition, Ne and Ar isotope and abundance characteristics were determined in Réunion Island xenoliths. All samples were previously characterized for He isotopes (Füri et al., 2011). Previous volatile studies of CIR basalts are rare, with a single study (Cartigny et al., 2001a) reporting $\delta^{15}N$ values (n=3) and $\delta^{13}C$ values (n=2) for the region. CIR samples have distinct Ne-isotope anomalies and plot intermediate between MORB and Réunion on a Ne three-isotope, suggesting a solar-derived Ne component in the CIR mantle source. N-isotopes of CIR basalts suggest that ^{15}N enriched oceanic sediments are recycled into the CIR mantle source. Combined Ne-N mixing relationships indicate CIR basalts can be explained by mixing of a mantle component with variable (20-50 %) recycled sedimentary contributions and a relatively small (< 0.2 %) proportion of a solar component. Finally, by using an equilibrium degassing model, we reconstruct primary CO_2 contents prior to degassing by combining constraints imposed by CO_2–$\delta^{13}C$ variations. Primary CO_2 concentrations for the CIR mantle source are estimated at (CO_2 = ~1300 ppm; $\delta^{13}C$ = -4.2 ± 0.2 ‰). We conclude that CIR volatiles are derived from a heterogeneous mantle source with both recycled and solar contributions – likely derived from the Réunion hotspot.

Chapter VII is the final chapter of the dissertation. It summarizes the main findings and conclusions of each study and addresses some of the possible directions of future research in the field of volatile and noble gas studies.

CHAPTER II: A New Syringe Pump Apparatus for the Retrieval and Temporal Analysis of Helium (SPARTAH) in groundwaters and geothermal fluids

A new syringe pump apparatus for the retrieval and temporal analysis of helium in groundwaters and geothermal fluids

P. H. Barry, D. R. Hilton, M. D. Tryon, and K. M. Brown
*Geosciences Research Division, Scripps Institution of Oceanography, UCSD, La Jolla, California 92093-0244, USA
(pbarry@ucsd.edu; kmbrown@ucsd.edu; drhilton@ucsd.edu; mtryon@ucsd.edu)*

J. T. Kulongoski
*California Water Science Center, U.S. Geological Survey, 4165 Spruance Road, Suite 200, San Diego,
California 92101, USA (kulongos@usgs.gov)*

[1] We present details of a newly designed syringe pump apparatus for the retrieval and temporal analysis of helium (SPARTAH). The device is composed of a commercially available syringe pump connected to coils of Cu tubing, which interface the syringe and the groundwater or geothermal wellhead. Through test deployments at geothermal wells in Iceland and California, we show that well fluids are drawn smoothly, accurately, and continuously into the Cu tubing and can be time-stamped through user-determined operating parameters. In the laboratory, the tubing is sectioned to reveal helium (He) characteristics of the fluids at times and for durations of interest. The device is capable of prolonged deployments, up to 6 months or more, with minimal maintenance. It can be used to produce detailed time series records of He, or any other geochemical parameter, in groundwaters and geothermal fluids. SPARTAH has application in monitoring projects assessing the relationship between external transient events (e.g., earthquakes) and geochemical signals in aqueous fluids.

1. Introduction

[2] Numerous studies of the helium characteristics of crustal aqueous fluids (groundwater and geothermal fluids) have been carried out in regions prone to seismic activity. As He is chemically inert, variations in its concentration or isotopic composition can be related to physical changes or perturbations occurring within the crust. Studies at Kobe, Japan [*Sano et al.*, 1998], and the Georgian Caucasus [*Areshidze et al.*, 1992] are examples where monitoring of helium trends in aqueous fluids has identified stress readjustments in aquifers, resulting in changes in fluid provenance, mixing and/or flow histories related to specific seismic events. In these studies, the general aim of the monitoring program (i.e., repeated sampling at a given location over an extended period of time) is to reveal changes in a

geochemical parameter, such as He, which can either forewarn the impending occurrence of a seismic event or result from, and hence provide information and insight on, a past event.

[3] The relationship between a transient event, such as an earthquake, and a time-monitored geochemical parameter, such as He isotopes or concentration, is undoubtedly complex and likely site-specific. It should be no surprise, therefore, that monitoring programs in some seismically active areas (e.g., Long Valley Caldera [*Hilton*, 1996]; the North Anatolian Fault, Turkey [*De Leeuw et al.*, 2009]) showed little or no changes in $^3He/^4He$ values, even over extended periods. Clearly, the magnitude of particular events and proximity to monitoring sites are key factors in generating anomalous geochemical signals: however, the frequency of monitoring used to produce a time series can be just as critical. Indeed, in the above-cited Caucasus case, the duration of the seismically induced He anomaly lasted 5–10 days, a signal thus identified only because of the daily sampling regimen. At Long Valley and in Turkey, sampling frequency was every 3–4 months, so an anomaly of the duration seen in the Georgian Caucasus would have been caught only fortuitously.

[4] In this contribution, we describe the syringe pump apparatus for the retrieval and temporal analysis of helium (SPARTAH), a new sampling device for helium (and other chemical species) which can produce a quasi-continuous record in groundwaters and geothermal fluids. Samples are captured and stored in Cu tubing, for periods of 6 months or more in a single deployment, and are time-stamped by user-defined, setup parameters. Thus, all geochemical anomalies, irrespective of duration, can be captured, and later matched against the timing of external transients. Sampling frequency is selected following instrument retrieval, i.e., prior to analysis. This is a key advantage in that it promotes efficient targeting of specific sections of the time series. In this way, we argue that SPARTAH has the potential to revolutionize the approach to time series geochemical monitoring.

2. Description of SPARTAH

[5] The SPARTAH device consists of a programmable syringe pump (model PHD 4400 Hpsi manufactured by Harvard Apparatus; see Figure 1). The pump is an off-the-shelf single syringe pump unit equipped with a high-power stepper motor capable of withdrawal rates between 0.0001 ml/h and 220 ml/min at an accuracy of 0.35%. The stepper motor can provide an average linear pumping force of 91 kg (200 lbs), and so is ideally suited for high-pressure applications. We have equipped the unit with a 100 ml stainless steel syringe, which can withstand fluid pressures of 5.17×10^6 Pa (750 psi). We operate the pump in withdrawal mode whereby fluid is accurately and smoothly drawn into the syringe at a user-defined rate.

[6] In order to use the device to collect groundwaters and/or geothermal fluids, the syringe pump needs a conduit to connect to the wellhead and a storage device for the fluids of interest. These requirements are met using standard 15.2 m (50′) coils of Cu tubing (OD = 3.18 mm = 1/8″). Additionally, the coils can be connected in series to provide the desired storage capacity. Copper is the preferred material for our application because of its low permeability to helium [*Weiss*, 1968]. The copper tubing is first interfaced to commercially available brass Swagelok shutoff valves (B-41S2) and then directly to the syringe and wellhead (Figure 1).

[7] Prior to connection, the Cu tubing is filled with deionized (DI) water using the refill mode of the syringe pump. During operation, the DI water is drawn into the stainless steel syringe, and is replaced by water from the wellhead. Water is drawn into the coils at a constant rate set by the syringe pump, and is independent of the pumping rate of the well. The only stipulation is that the well operates continuously so that the water pressure remains constant throughout the deployment thereby avoiding exsolution of dissolved gases or, in the case of well shutdown, air entrainment into the tubing. At any time during a deployment, the tubing can be isolated by closing the Swagelok shutoff valves, and disengaged (for transfer to the laboratory) or replaced to extend the duration of sampling.

[8] The SPARTAH device is housed in a protective Pelican case (model 1610), which not only shields it from the elements (if installed outside) but also enables the entire apparatus to be secured at the deployment site to help prevent theft or tampering. Small inlet ports, drilled into the outer casing, allow inlet of power cables and the Cu tubing (Figure 1). In addition, the instrument has been equipped with an uninterrupted power supply designed to provide several hours of backup power in the event of power outage. Cooling fans have also been installed to ventilate SPARTAH during extended deployments where temperature extremes are a factor. The weight of the entire instrument, including three 15.2 m (50′)

Figure 1. (top) The Harvard syringe pump apparatus with stainless steel syringe along with sectioned Cu tubing of 12.7 cm (5″) length. Note the sectioned Cu coil with two refrigeration clamps and ultratorr fitting attached to one end. (bottom) Deployment of SPARTAH at the San Bernardino wellhead. The Pelican case houses the syringe pump apparatus and one Cu coil. One end of the coil is attached to the syringe, and the other leads through a hole in the case to the wellhead.

Cu tubes, is ∼30 kg, making transportation manageable. In 2008 prices, the cost of SPARTAH is approximately USD 7,000 (net).

3. Operation of SPARTAH

[9] The volume of the syringe presently configured on SPARTAH (100 ml) is the limiting factor governing the number of Cu coils that can be usefully connected for a deployment. Given a nominal internal diameter (ID) of 1.65 mm (0.065″) for 3.18 mm (1/8″) Cu tubing, 100 ml of fluid can be accommodated in a coil length of approximately 46.7 m (153′3″): therefore, it is useful to connect a maximum of three 15.2 m (50′) tubes in series for any deployment as a fourth tube, nearest the syringe, would mostly contain DI water at the end of the deployment. The question that then arises is how to
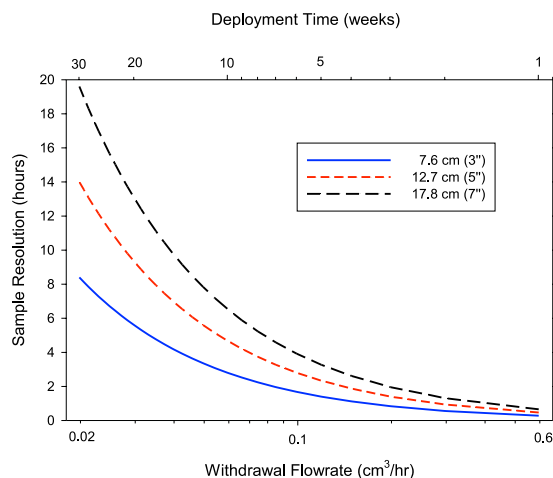
Figure 2. Relationship between user-set withdrawal flow rate (cm^3/h) and total deployment time (weeks) for three 15.2 m (50′) copper coils (OD = 3.18 mm = 1/8″) placed in series. The three curves give the sample resolution (in hours) as a function of flow rate resulting from sectioning the Cu coils into 7.62 cm (3″), 12.7 cm (5″), and 17.8 cm (7″) lengths (excluding 2.5 cm (1″) on either side, see text).

determine the pump withdrawal rate to obtain the optimum temporal resolution, taking into account the required volume of fluid necessary for a precise helium isotope analysis.

[10] To illustrate our approach to this issue, we note that air-saturated water (ASW) at 10°C contains 4.0×10^{-8} cm^3 STPHe/gH_2O [*Ozima and Podosek*, 1983]. This concentration most probably represents a minimum value: groundwaters and geothermal fluids are likely to be characterized by He concentrations orders of magnitude higher (as shown by our test deployments; section 4). Our laboratory extraction line, interfaced directly to our 215E noble gas mass spectrometer, can easily process 1 cm^3 of water for a He isotope analysis at a precision <2%. Indeed, our procedural blanks for such an extraction are <10^{-10} cm^3 STPHe. We note that 1 cm^3 of water occupies a length of 46.7 cm (18.39″) of Cu coil. Therefore we could section 97 individual aliquots of length 46.7 cm (18.39″), using only three 15.2 m (50′) Cu tubes in series, with each aliquot (containing only ASW He) containing more than sufficient He for a precise analysis.

[11] Upon return to the laboratory, the Cu tubes are straightened and then sectioned using refrigeration clamps (Figure 1). Practically speaking, the minimum length of Cu tube that can accommodate two

clamps, while leaving ∼2.5 cm (1″) for inlet into the UHV extraction system using a Cajon ultratorr fitting is 12.7 cm (5″) (7.6 cm (3″) containing ∼0.16 cm^3 of trapped fluid and 2.5 cm (1″) protruding on either side of the clamps). Thus, in theory, three 15.2 m (50′) Cu coils connected in series could be sectioned to yield 360 individual aliquots of fluid for He isotopic analysis.

[12] In Figure 2, we show the temporal resolution that can be achieved for each of those 360 aliquots as a function of withdrawal flow rate. Clearly, at extremely low withdrawal rates, SPARTAH could be deployed for long time periods with the trade-off that a single 12.7 cm (5″) section of coil (i.e., 7.6 cm (3″) of sample plus 2.5 cm (1″) of coil protruding at each end) would represent a relatively large time interval. For example, at a flow rate of 0.02 cm^3/h, SPARTAH could be deployed for ∼30 weeks (∼7 months) with each 7.6 cm (3″) section representing ∼8.3 h of fluid sampling. By increasing the withdrawal rate, the time resolution would be improved (i.e., the time required for water to travel 7.6 cm (3″) in the coil would be decreased) but the total deployment time would be correspondingly reduced. A withdrawal rate of 0.1 cm^3/h would yield a time resolution of ∼1.7 h per 7.6 cm (3″) length of Cu tube but SPARTAH could

Table 1. Test Deployments of SPARTAH at Selfoss, Iceland, and San Bernardino, California: He Isotope and Concentration Results

Sample Location and ID	Distance to First Clamp[a] (cm)	Sample Date and Time (Local Time)	^{3}He/^{4}He (R/R$_A$)	X	R$_c$/R$_A$[b] ($\pm2\sigma$)	[He]$_c$[c] (μcm^3 STP/g H$_2$O)
Selfoss, Iceland[d]						
Selfoss-28	1288	30 Jul, 2300–0200	19.5	19.0	20.3 ± 0.72	1.99 ± 0.20
Selfoss-27	1239	31 Jul, 0200–0500	16.8	4.72	20.1 ± 0.46	3.17 ± 0.32
Selfoss-26	1196	31 Jul, 0500–0800	19.9	20.3	20.7 ± 0.73	2.04 ± 0.20
Selfoss-21	955	31 Jul, 2000–2300	19.8	21.0	20.6 ± 0.76	3.15 ± 0.32
Selfoss-5	196	2 Aug, 2000–2300	19.6	19.5	20.4 ± 0.63	2.26 ± 0.23
Selfoss-4	145	2 Aug, 2300–0200	19.8	20.2	20.6 ± 0.32	3.04 ± 0.30
Selfoss-2	53.0	3 Aug, 0500–0800	19.7	20.2	20.5 ± 0.68	2.15 ± 0.22
Selfoss-1	2.00	3 Aug, 0800–1100	19.5	17.9	20.3 ± 0.37	2.56 ± 0.26
San Bernardino, CA[e]						
SB-Coil-9	1806	16 Apr, 0100–0300	0.72	4.87	0.66 ± 0.02	1.87 ± 0.09
SB-Coil-8	1745	17 Apr, 0100–0300	0.68	42.2	0.67 ± 0.02	2.05 ± 0.10
SB-Coil-7	1394	22 Apr, 0800–1000	0.66	57.3	0.65 ± 0.02	4.93 ± 0.25
SB-Coil-5	1334	23 Apr, 0800–1000	0.66	45.2	0.65 ± 0.01	3.49 ± 0.17
SB-Coil-4	1273	24 Apr, 0800–1000	0.65	48.7	0.64 ± 0.02	3.96 ± 0.19
SB-Coil-11	856	1 May, 0400–0600	0.67	40.2	0.66 ± 0.02	2.83 ± 0.14
SB-Coil-12	429	8 May, 0400–0600	0.66	44.6	0.66 ± 0.01	4.25 ± 0.21
SB-Coil-2	66.0	14 May, 0400–0600	0.65	47.1	0.64 ± 0.02	3.72 ± 0.19

[a]Distance to first clamp refers to the length of Cu tube from the shutoff value situated at the well head to the first refrigeration clamp used for sectioning. This is the primary measurement needed to infer the date/time of the fluid (column 3). The second clamp was always placed downstream (i.e., toward the syringe pump). The distance between the two clamps was 46 cm (Selfoss) and 5 cm (San Bernardino). The uncertainty associated with measuring the distance between the shutoff valve and first clamp is approximately 1% at the center of each 50′ coil (i.e., 25′ from either shutoff value). This corresponds to approximately 7.6 cm (3 inches), maximum: it will be less for samples sectioned closer to the valves. The corresponding uncertainty on the date/time stamp will vary with the duration of the deployment; that is, it will be greater for longer deployments. We estimate uncertainty of ≤7 hours for a 26-week deployment.

[b]The ^{3}He/^{4}He ratios (R) are normalized to the atmospheric value (R$_A$), and corrected for air-derived He (R$_c$/R$_A$) using the correction factor X = [{(He/Ne)$_{sample}$/(He/Ne)$_{air}$} × (β_{Ne}/β_{He})], where β = Bunsen solubility coefficient. For pure water at 13°C (β_{Ne}/β_{He}) = 1.23. See *Hilton* [1996] for details of the correction protocol.

[c]The quoted errors on the He concentrations largely reflects the uncertainty on estimating the weight of water processed. Selfoss samples (46 cm Cu tube length and ∼1g H$_2$O) were weighted before and after processing using a digital readout balance to 1 decimal place: therefore, uncertainties are estimated at ±10%. San Bernardino sample weights (5 cm Cu tube length and ∼0.1g H$_2$O) were calculated from the length of Cu tube processed and knowledge of the total weight of water (approximately 42 g H$_2$O) taken to fill the entire Cu tube assuming a length of 50′. In this case, we estimate an uncertainty of ±5%.

[d]Selfoss well located at N63°56′49″, W20°57′21″. Deployment was initiated at 1100 local time on 29 July 2007 and terminated at 1100 local time on 3 August 2007. The syringe pump withdrawal rate was set at 0.3333 cm^3/h.

[e]San Bernardino Well 66 located at N34°05′10″, W117°17′23″. Deployment was initiated at 0800 local time on 14 April 2008 and terminated at 1200 local time on 16 May 2008. The syringe pump withdrawal rate was set at 0.0416 cm^3/h.

only be deployed at this rate for a total of ∼6 weeks before the coils would have to be replaced. Sectioning longer lengths of Cu coil would diminish the sample resolution for a given withdrawal flow rate (and deployment duration). For example, sectioning 12.7 cm (5″) and 17.8 cm (7″) lengths of tubing would diminish the sample resolution to ∼2.8 and ∼3.9 h, respectively, for a withdrawal rate of 0.1 cm^3/h. An additional but key factor in determining the withdrawal rate for a given deployment is the user-anticipated frequency of coil changes: lower withdrawal rates would be necessary in the case of infrequent access to the sampling site.

4. Test Deployments

[13] In order to develop and test the SPARTAH system, we took advantage of access to two con-tinuously pumping geothermal wells used to supply water for space heating purposes. In the first case (Selfoss, Iceland), a prototype device utilizing an older model syringe pump employing two 50 ml plastic syringes was deployed for 1 week as an initial test of the feasibility of the system. Success in this deployment (section 4.1) led to the SPARTAH device described herein, which was test deployed for 1 month at a well in San Bernardino, California. The additional refine-ments of protective case (and backup power supply) resulted from the fact that the San Bernardino well is situated outdoors whereas the Selfoss well is located within a secure hut. In both cases, we processed sections of the Cu coils for dissolved helium (iso-topes and concentrations) with results reported in Table 1.
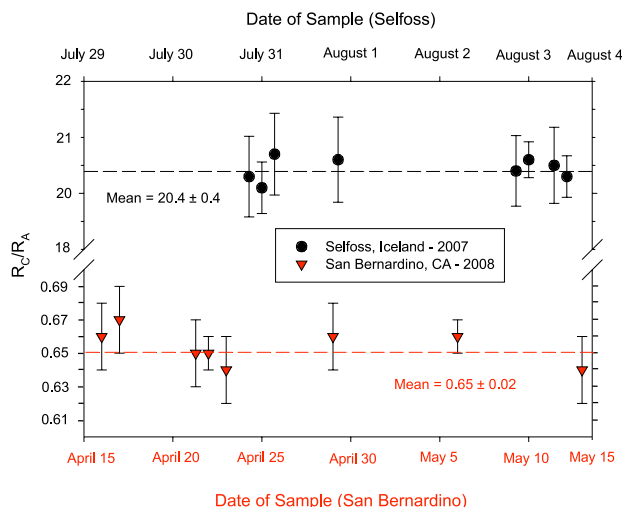
Figure 3. Helium isotope variations captured in the Cu coils at Selfoss, Iceland (1-week deployment), and San Bernardino, California (1-month deployment). Note that helium is mainly mantle-derived in Selfoss but is predominantly crustal in origin at San Bernardino [see *Hilton and Porcelli*, 2003]. Individual error bars are given at the 2σ level. The mean $^3He/^4He$ values for Selfoss (black) and San Bernardino (red) are illustrated by dashed lines. The standard deviation on the mean values is also at the 2σ level.

4.1. Selfoss, Iceland: South Iceland Seismic Zone

[14] The first deployment of SPARTAH took place at Selfoss, Iceland in July 2007. The withdrawal rate on the pump was set at 0.3333 cm^3/h, so it would take ~98 h (4 days, 2 h) to completely displace the DI water from a single 15.2 m (50′) Cu coil. We terminated the experiment after 5 days anticipating that the Cu tubing would be completely filled with well water. Upon return to the laboratory, the coil was sectioned into eight 45.7 cm (18″) segments using refrigeration clamps at distances starting at 2.0 cm (~0.8″) and extending to 1288 cm (507″) from the shutoff valve closest to the wellhead. The actual time and duration of sampling of each segment (column 3 in Table 1) was calculated using the withdrawal rate, assumed tubing diameter and measured length of tubing from the shutoff valve. We calculated that the sample furthest from the valve (at a distance = 1288 cm) entered the Cu tubing on 30 July at 2300 local time whereas our last sample (2.0 cm from the valve) entered on 3 August at 0800 local time, fully 3 days, 9 h later. At the set withdrawal rate, each 46 cm

segment of tubing contained ~0.98 cm^3H_2O which corresponded to ~3 h of sampling.

[15] We report the He results of the Selfoss deployment in Table 1 with the isotope systematics and concentrations presented in Figures 3 and 4, respectively. The principal point to note is that all 8 segments of Cu tubing are enriched in mantle-derived He. The $^3He/^4He$ ratios consistently fall between 20 and 21 R_A (R_A = atmospheric $^3He/^4He$ value), remarkably similar to values reported previously for this area [*Poreda et al.*, 1992]. Additionally, the He/Ne values are high (4.7 < X < 21; Table 1), consistent with addition of extraneous He, as are the He concentrations (2.0–3.2 $\mu cm^3STP/gH_2O$) relative to anticipated starting values of ~0.04 μcm^3 STP/gH_2O) for air-equilibrated DI water. Taken together, this evidence shows that the SPARTAH device successfully sampled well fluids for the duration of the experiment. We note, also, that He isotope values remained constant within 2σ uncertainty over the 3 1/2-day deployment. Although there were more significant variations in He concentrations, values did not vary beyond 2σ from the mean. This observation suggests that
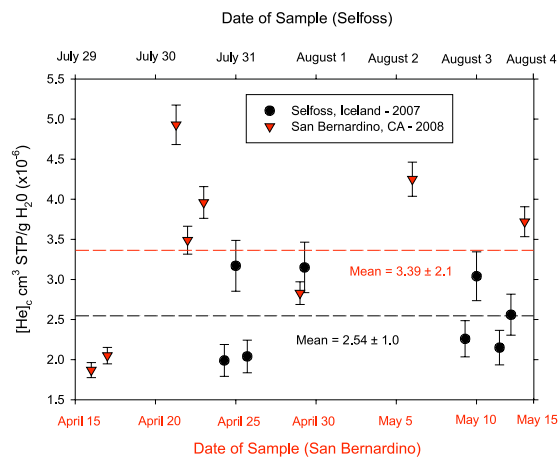
Figure 4. Helium concentration variations captured in the Cu coils for Selfoss, Iceland (1-week deployment), and San Bernardino, California (1-month deployment). Individual errors on He concentration values are estimated at ±10% for Selfoss and ±5% for San Bernardino (see Table 1 footnote). The mean values (dashed lines) for Selfoss (black) and San Bernardino (red) are given with 2σ uncertainties.

helium concentrations may also respond to external factors, particularly if the He inventory is overwhelmed by one end-member only (mantle-derived He in the case of the South Iceland Seismic Zone).

4.2. San Bernardino, California (San Jacinto Fault)

[16] We continued our development of SPARTAH by introducing a protective housing equipped with cooling fans and backup power in response to a test deployment opportunity at a geothermal well situated approximately 3 km from the San Jacinto Fault in San Bernardino, California. We employed a significantly lower withdrawal rate ($0.0416\,\mathrm{cm}^3$/h) to run the experiment for ~1 month. Additionally, we weighed the Cu tubing before and after filling with DI water. This procedure has three advantages. First, it allows us to more accurately gauge the internal volume of the tube, thus enabling selection of a withdrawal rate that would guarantee complete displacement of the DI water. Second, assuming that the internal diameter is constant (although not necessarily at values specified by the manufacturer), we can produce more accurate date and time stamping for aliquots selected for analysis. Finally, we can reduce the uncertainty on He concentrations,

introduced by weighing, by measuring the length of tubing sectioned and estimating the amount of water processed for an analysis based on this measurement. This is important for the San Bernardino deployment as we sectioned short (5 cm) lengths for processing which contained ~0.14 cm^3 water.

[17] In Table 1, we report 8 He isotope and concentration results obtained from a single Cu coil deployed at San Bernardino in April 2008. The coil was sectioned to produce aliquots throughout the deployment with the first and last segments approximately 30 days apart. Again, we can confirm that the DI water has been displaced from the entire length of the Cu tube by geothermal well water characterized by a ^{3}He/^{4}He ratio of ~0.65R$_A$ (Figure 3). In this case, the ^{3}He/^{4}He ratio is heavily weighted toward a crustal He input, in agreement with other studies in the region [*Kennedy et al.*, 1997; *Kulongoski et al.*, 2003]. Notably, the ^{3}He/^{4}He ratio is constant within 2σ of the mean over the entire deployment period in spite of a M = 4.1 earthquake which occurred on 23 April 2008 at 0155 local time approximately 90 km to the northeast of the well (N 34°51′57″, W 116°20′24″). As in the case of Selfoss, helium concentrations did vary somewhat

over the deployment period, by approximately a factor of two.

5. Discussion

[18] The two test deployments of SPARTAH demonstrate its ability to produce time series records of He isotopic and concentration data from groundwater and/or geothermal wells. In each case, a single deployment and retrieval visit produced a weeklong (Selfoss) and monthlong (San Bernardino) He time series which would have involved a total of 8 visits to each locality if we had adopted conventional means of sampling the wells periodically. Cost saving considerations aside, the question that then arises is whether SPARTAH can retain anomalous signals, defined as a concentration spike or step in ^{3}He and/or ^{4}He (manifested as an isotopic or concentration difference), for the duration of a deployment? Both diffusion of helium in water and dispersion of the fluid will act to attenuate helium anomalies in the Cu tubing.

[19] The characteristic diffusion length (x) for He in fresh water at 25°C is ~33 cm (13″) for a typical 6-month deployment ($x = \sqrt{Dt}$ where $D = 7 \times 10^{-5}$ cm^2/s [*Jahne et al.*, 1987] and t = time). Thus, aliquots collected early during a deployment will experience greater diffusive smearing of a He pulse compared to later samples. This will impact the intensity of a He signal: however, the He anomaly should still be readily discernible against background values, i.e., defined by aliquots > x away from the pulse. Processing of the coil in a timely fashion following retrieval will prevent further loss of an anomalous He signal. Dispersion of the signal is a potentially greater problem, however, with differential flow between water close to the tubing wall versus that in the center of the tube acting to smear out sharp concentration gradients. This effect is exacerbated by high flow rates and large diameter tubing; however, diffusion tends to counter this effect in small diameter tubes at slow flow rates [*Cussler*, 1984]. In this respect, we note that *Tryon et al.* [2001] found no evidence for dispersion during a submarine tracer test of 70 days duration using 2.4 mm ID tubing and a flow rate of ~1 m/d. The San Bernardino deployment (this work) was set at a flow rate of ~0.5 m/d, which is likely a factor of 2 greater than envisaged flow rates for future deployments (e.g., using 3 coils for 6 months). Moreover, the tube ID on SPARTAH is smaller (1.6 mm) and the tracer (He) has a higher diffusivity than that employed for the submarine test. All three factors

act together to mitigate the possibility of signal loss by dispersion in the coils.

6. Concluding Remarks

[20] The use of SPARTAH has the potential to revolutionize studies relying on time series records of dissolved He variations and has the following advantages over conventional sampling strategies:

[21] 1. The monitoring period can be long: in the present SPARTAH configuration (1–3 Cu coils and low withdrawal rate), up to 6 months of sampling can be accomplished with a single deployment and retrieval visit. The instrument requires no maintenance. Changing coils can prolong the monitoring period indefinitely.

[22] 2. Sampling is continuous so no hiatus exists in the time record. Irrespective of the duration of a geochemical anomaly, SPARAH will capture any event, transient or long-term.

[23] 3. The sample resolution can be selected by two independent factors: these are (1) the withdrawal rate and/or (2) the length of tubing sectioned. For example, in the case of short monitoring periods (days to weeks), the sample withdrawal rate can be increased so that the entire Cu coil is filled with well water, hence improving sample resolution. The sample resolution can be further improved by shortening the length of Cu tubing selected for analysis. Conversely, withdrawal rates can be set extremely low, extending the duration of the deployment (up to 6 months) at a loss of sample resolution. This (relatively low) resolution can be improved by sectioning at shorter intervals of coil.

[24] 4. The constant withdrawal rate of the syringe pump allows any sectioned sample aliquot to be related directly to time. Therefore, certain lengths of the Cu coil can be targeted for sectioning (and follow-up analytical work) based on knowledge obtained at the end of a deployment. For example, in the case of a seismic event occurring sometime during a deployment, the tubing can be sectioned to reveal He isotope variations prior to, during and/or after the event.

[25] 5. SPARTAH reduces analytical effort considerably in that samples representing times of interest can be targeted for sectioning and analysis. Samples collected in portions of the coil corresponding to any other periods can be either archived or disregarded.

[26] Finally, we emphasize that use of SPARTAH is not restricted to He or any other dissolved gas. The Cu tubing can be sectioned and processed for certain trace elements, stable isotopes or any other intrinsic water property of interest. Indeed, through innovative analytical processing, it should be possible to produce contemporary records of a variety of different tracers, enabling assessments of their relative sensitivities to external perturbations. In this respect, we argue that deployment of SPARTAH at strategically placed locations will lead to more detailed and accurate assessments of the geochemical responses to external forcing factors such as earthquakes.

Acknowledgments

References

Areshidze, G., et al. (1992), Anomalies in geophysical and geochemical parameters revealed on the occasion of the Paravani (M = 5.6) and Spitak (M = 6.9) earthquakes (Caucasus), *Tectonophysics*, *202*, 23–41, doi:10.1016/0040-1951(92)90453-D.

Cussler, E. L. (1984), *Diffusion: Mass Transfer in Fluid Systems*, 525 pp., Cambridge Univ. Press, Cambridge, U. K.

De Leeuw, G. A., D. R. Hilton, N. Güleç, and H. Mutlu (2009), Regional and temporal variations in $CO_2/^3He$, $^3He/^4He$ and $\delta^{13}C$ along the North Anatolian Fault Zone, Turkey, *Appl. Geochem.*, in press.

Hilton, D. R. (1996), The helium and carbon isotope systematics of a continental geothermal system: Results from monitoring studies at Long Valley caldera (California U.S.A.), *Chem. Geol.*, *127*, 269–295, doi:10.1016/0009-2541(95)00134-4.

Hilton, D. R., and D. Porcelli (2003), Noble gases as mantle tracers, in *Treatise on Geochemistry*, vol. 2, *The Mantle and Core*, edited by R. W. Carlson, pp. 277–318, Elsevier, Oxford, U. K.

Jahne, B., G. Heinz, and W. Dietrich (1987), Measurement of diffusion-coefficients of sparingly soluble gases in water, *J. Geophys. Res.*, *92*, 10,767–10,776, doi:10.1029/JC092iC10p10767.

Kennedy, B. M., Y. K. Kharaka, W. C. Evans, A. Ellwood, D. J. Depaolo, J. Thordsen, G. Ambats, and R. H. Marineret (1997), Mantle fluids in the San Andreas fault system, California, *Science*, *278*, 1278–1281, doi:10.1126/science.278.5341.1278.

Kulongoski, J. T., D. R. Hilton, and J. A. Izbicki (2003), Helium isotope studies in the Mojave Desert, California: Implications for groundwater chronology and regional seismicity, *Chem. Geol.*, *202*, 95–113, doi:10.1016/j.chemgeo.2003.07.002.

Ozima, M., and F. A. Podosek (1983), *Noble Gas Geochemistry*, 367 pp., Cambridge Univ. Press, Cambridge, U. K.

Poreda, R. J., H. Craig, S. Arnórsson, and J. Welhan (1992), Helium isotopes in Icelandic geothermal systems: I. ^3He, gas chemistry, and ^{13}C relations, *Geochim. Cosmochim. Acta*, *56*, 4221–4228, doi:10.1016/0016-7037(92)90262-H.

Sano, Y., N. Takahata, G. Igarishi, N. Koizumi, and N. C. Sturchio (1998), Helium degassing related to the Kobe earthquake, *Chem. Geol.*, *150*, 171–179, doi:10.1016/S0009-2541(98)00055-2.

Tryon, M., K. Brown, L. R. Dorman, and A. Sauter (2001), A new benthic aqueous flux meter for very low to moderate discharge rates, *Deep Sea Res., Part I*, *48*, 2121–2146, doi:10.1016/S0967-0637(01)00002-4.

Weiss, R. F. (1968), Piggyback sampler for dissolved gas studies on sealed water samples, *Deep Sea Res.*, *15*, 721–735.

II. Acknowledgements

In addition to those mentioned within the acknowledgements section of the published work, we also thank AGU for allowing us use a reprint of the material as it appeared in Geochemistry Geophysics Geosystems 2009, as Barry, P. H., D. R. Hilton, M. D. Tryon, K. M. Brown, and J. T. Kulongoski (2009), A new syringe pump apparatus for the retrieval and temporal analysis of helium in groundwaters and geothermal fluids, *Geochemistry Geophysics Geosystems*, 10, Q05004, doi:10.1029/2009GC002422. The dissertation author was the primary investigator and lead author of this paper and conducted all the analyses presented herein.

CHAPTER III: High precision nitrogen isotope measurements in oceanic basalts using a static triple collection noble gas mass spectrometer

High precision nitrogen isotope measurements in oceanic basalts using a static triple collection noble gas mass spectrometer

P. H. Barry, D. R. Hilton, and S. A. Halldórsson
Fluids and Volatiles Laboratory, Scripps Institution of Oceanography, University of California, San Diego, La Jolla, California 92093-0244, USA (pbarry@ucsd.edu)

D. Hahm
Fluids and Volatiles Laboratory, Scripps Institution of Oceanography, University of California, San Diego, La Jolla, California 92093-0244, USA

Now at Korea Polar Research Institute, 12 Gaetbeol-ro Yeonsu-gu, Incheon 406-840, South Korea

K. Marti
Department of Chemistry and Biochemistry, University of California, San Diego, La Jolla, California 92093-0244, USA

[1] We describe a new system for the simultaneous static triple-collection of nitrogen isotopes at the <10 μcm^3 STP [N$_2$] (<1 $\times$ 10^{-5} cm^3 STP; <0.5 nmol) level using a modified VG-5440 noble gas mass spectrometer. The system consists of an internal N$_2$-STD with a δ^{15}N value of -0.11 ± 0.22 ‰ (1σ) calibrated against an air-standard (Air-STD). The N$_2$-STD was measured repeatedly with an average uncertainty on an individual δ^{15}N measurement being 0.03 ‰ (1σ) versus an average single day reproducibility of 0.38 ‰ (1σ). Additional refinements include (1) monitoring of interfering CO contributions at mass 30, allowing a comprehensive CO correction to be applied to all samples, (2) quantification of procedural N$_2$ blanks (n = 22) in both size (4.2 $\pm$ 0.5 μcm^3 STP) and isotopic composition (δ^{15}N = 12.64 $\pm$ 2.04 ‰), allowing consistent blank corrections to all samples, and (3) independent measurement of N$_2$/Ar ratios using a quadrupole mass spectrometer (QMS). The new system was tested by measuring nitrogen isotopes (δ^{15}N), concentrations and N$_2$/Ar ratios on 11 submarine basalt glasses. Results show that the uncertainty on the δ^{15}N data is improved as a consequence of multiple standards being run per day. Reduced analytical times, afforded by triple collection, also minimize sample depletion and memory effects, thus improving measurement statistics. Additionally, we show that CO corrections can be accomplished using mass 30 to monitor CO interferences, leading to substantial improvements in reproducibility and the overall accuracy of results when the contribution of CO is significant.

1. Introduction

[2] Although nitrogen is the principal gas of Earth's atmosphere (78%), it is found in trace concentrations (ppm) only in materials derived from the mantle. This large concentration contrast makes N_2 a highly sensitive tracer of interactions between surficial reservoirs and the solid Earth, and has led to numerous studies characterizing the N_2 composition – isotopic and abundance – in different terrestrial samples such as mid-ocean ridge basalts [*Sakai et al.*, 1984; *Javoy et al.*, 1986; *Exley et al.*, 1987; *Javoy and Pineau*, 1991; *Marty and Zimmerman*, 1999], ocean island basalts and seamounts [*Marty and Humbert*, 1997; *Marty and Dauphas*, 2003], carbonatites [*Dauphas and Marty*, 1999; *Fischer et al.*, 2009], diamonds [*Javoy et al.*, 1984; *Boyd et al.*, 1987, 1994a; *Cartigny et al.*, 2001a], mafic phenocrysts and xenoliths [*Fischer et al.*, 2005; *Yokochi et al.*, 2009] and ocean floor sediments and metasediments [*Peters et al.*, 1978; *Kienast*, 2000; *Pinti et al.*, 2001; *Thomazo et al.*, 2009]. These studies have been accompanied by others exploiting nitrogen in subduction zones [*Sano et al.*, 1998, 2001; *Fischer et al.*, 2002; *Hilton et al.*, 2002; *Busigny et al.*, 2011] where information on volatile recycling can be gained. Additionally, the large $\delta^{15}N$ difference (where $\delta^{15}N = [(^{15}N^{14}N/^{14}N^{14}N)_{sample}/(^{15}N^{14}N/^{14}N^{14}N)_{air} - 1] \times 1000$) between terrestrial and solar abundances makes nitrogen an important tracer for planetary evolution [e.g., *Marty et al.*, 2011].

[3] Historically, nitrogen isotope ratios ($^{15}N/^{14}N$) were measured using an isotope ratio mass spectrometer (IRMS) operated in dynamic pumping mode [*Chang et al.*, 1974; *Thiemens and Clayton*, 1983; *Javoy and Pineau*, 1991], with improvements to the precision of nitrogen isotope measurements accomplished by utilization of multiple collection of ion beams [*Cartigny et al.*, 1997; *Boyd and Philippot*, 1998; *Cartigny et al.*, 2001b, *Busigny et al.*, 2005]. However, low nitrogen abundance samples are not amenable to this technique, leading to the exploitation of noble gas mass spectrometers in nitrogen isotope studies as they are operated under static vacuum condition during measurement (i.e., not dynamically pumping) [*Frick and Pepin*, 1981; *Wright et al.*, 1988; *Boyd et al.*, 1988;

Hashizume and Sugiura, 1990; *Boyd et al.*, 1993; *Murty and Marti*, 1994; *Craig et al.*, 1993; *Marty et al.*, 1995; *Takahata et al.*, 1998; *Hashizume and Marty*, 2004]. Here, we describe a newly designed extraction system interfaced to a noble gas mass spectrometer (VG 5440) set up with multiple fixed detectors (two Faraday collectors and one Daly multiplier) for the simultaneous triple-collection of nitrogen isotopes (at masses 28, 29) and interfering species (at mass 30). We report new $\delta^{15}N$ data on standard gases (air and an in-house N_2 standard) and select oceanic basalts to assess internal precision and external reproducibility of the new system as well as accuracy of sample results. These results demonstrate the ability of the new system to make high precision nitrogen isotope measurements while highlighting the advantages provided by simultaneous triple collection. We show that this new approach greatly reduces analytical times, which (1) minimizes sample depletion and memory effects in the flight tube, improving both measurement statistics and accuracy, and (2) allows for more standards to be processed per day, thus improving accuracy on individual sample measurements. In addition, by quantifying interfering ($^{12}C^{18}O$) species at mass 30, we are able to apply a comprehensive CO correction ($^{12}C^{16}O$, $^{13}C^{16}O$, and $^{12}C^{17}O$) to all nitrogen data, again improving sample accuracy. Taken together, our experimental approach and triple collection instrumentation lead to high quality nitrogen isotope data on low-N abundance samples such as oceanic basalts.

2. Analytical Methods

2.1. Mass Spectrometer − Modified VG-5440

[4] The VG-5440 is a modified sector-type noble gas mass spectrometer equipped with a wide-angle 2.17-L flight-tube, five fixed Faraday collectors, one Daly collector and an electron bombardment source [*Craig et al.*, 1993]. The system is designed to perform static triple-collection for nitrogen isotopes using off-axis Faraday collectors (L3 and L1) for masses 28 and 29 and a single axial Daly collector positioned in front of a Faraday cage (Ax Faraday) for mass 30 (Figure 1). The system can also be used for triple neon isotope collection - utilizing collectors
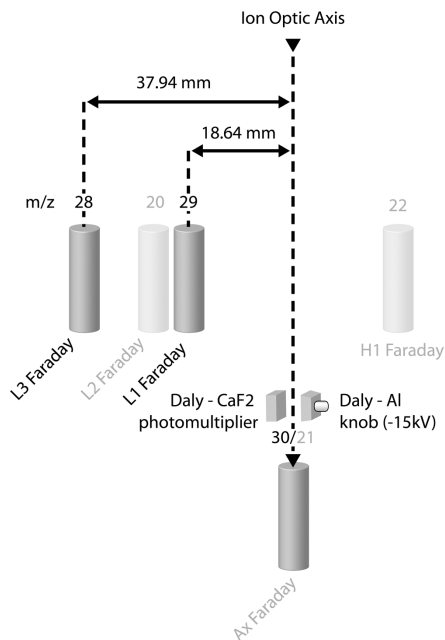
Figure 1. Schematic of triple collection configuration designed for simultaneous collection of nitrogen isotopes [after *Craig et al.*, 1993]. In addition to nitrogen, the system can also be configured for simultaneous neon isotope collection (lightly shaded collectors). The axial collector slit is ~0.7 mm yielding a mass resolution of approximately 620 on the Daly multiplier and axial Faraday cup. Off-axis slits are spaced at ~2 mm, giving a resolving power of 200.

L2, Ax and H1. The Faraday-cup sensitivity is 2.5×10^{-4} amps/Torr for m/z = 28 ($^{14}N^{14}N$). All Faraday-cups are equipped with resistors of 10^{11} Ω with the exception of L3 which has a resistor of 1.19×10^{10} Ω due to the larger signal at m/z = 28 ($^{14}N^{14}N$). The flight-tube magnet is shimmed such that the focal plane is rotated to lie in a plane normal to the optic axis for all collector defining slits. The Daly multiplier system consists of a polished Al knob (−15 kV) which collects nitrogen ions and ejects secondary electrons which are measured on a CaF_2 scintillator and photo-multiplier. In contrast to other multicollection configurations [e.g., *Cartigny et al.*, 2001b], this novel setup enables precise measurement of the mass 30 beam, allowing a comprehensive CO correction to be applied to masses 28 and 29 (see section 3.3 for details). The Daly deflects the (m/z = 30) beam in the ion optical axis whereas Faraday

collectors L3 (m/z = 28) and L1 (m/z = 29) are offset by fixed amounts (37.94 mm and 18.54 mm, respectively) for simultaneous collection (Figure 1). At a multiplier voltage of 850 V, the gain on the Daly multiplier system is ~1180. Operating conditions of the source use a trap current of 220 μA and an electron voltage of 78 eV. The mass resolving power for the axial (Daly) collector is ~620, which is adequate to resolve $^{15}N^{15}N + {}^{12}C^{18}O + {}^{13}C^{17}O$ from C_2H_6.

2.2. Purification Line

[5] The nitrogen extraction and purification vacuum line (Figure 2) is constructed of stainless steel, with the exception of three Pyrex glass cold fingers (CF) which are used to prevent any potential nitrogen gas adsorption at liquid nitrogen temperature (−196°C). The line is divided into five distinct
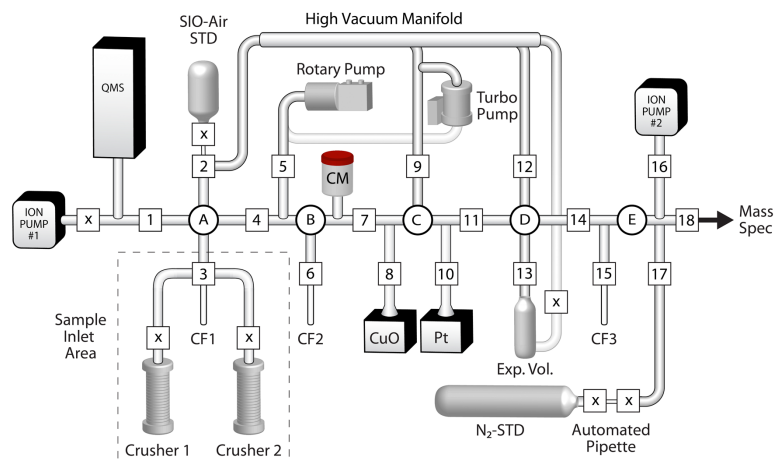
Figure 2. Schematic diagram of the nitrogen extraction and purification vacuum line. The line is constructed of stainless steel with the exception of Pyrex glass tubes, used for cold fingers (CF). Double walled quartz glass tubes (held at vacuum by a rotary pump) are used for both the copper-oxide furnace (CuO) and platinum-foil catalyst (Pt) fingers. The line is separated into five distinct volumes (A–E): volume A is the dedicated inlet section of the line where gas is first introduced after crushing and prior to cleanup. Additionally, gas in this section is characterized for N_2/Ar using the quadrupole mass spectrometer (QMS). The QMS is continuously pumped when not in use by Ion Pump #1. Volume B is where the pressure of gas released during crushing is measured using a capacitance manometer (CM). Volume C is where the oxidation-cleanup procedure occurs. Oxygen is generated using a CuO furnace in the presence of a Pt-catalyst. Volume D is equipped with an expansion volume which enables sample pressure reduction prior to inlet into the mass spectrometer. Volumes A+B+C+D are held at vacuum by a rotary pump backed turbo molecular pump. Volume E is the clean part of the line where the N_2-STD is housed and inlet via a pneumatically actuated volume. Volume E is pumped using Ion Pump #2.

sections (Volumes A-E): Volume A is the dedicated inlet section of the line where the sample inlet apparatus (e.g., hydraulic crusher) is interfaced. A Stanford Research Systems RGA 200 Quadrupole Mass Spectrometer (QMS), held at high vacuum by a dedicated ion pump, and a standard 1-L reservoir of Air-Standard (Air-STD) connected via a calibrated pipette volume, are also interfaced to Volume A. Volume B contains a 0.05 Torr (full-scale) capacitance gauge manometer (CM), enabling a manometric measurement of gas pressure and first-order evaluation of gas load. Volume C is the dedicated clean-up (oxidation) section of the line where oxygen is generated using a copper-oxide furnace (CuO) in the presence of a platinum-foil catalyst (Pt). Double-walled quartz glass tubes are used to house both the CuO and Pt fingers to accommodate operating temperatures of nearly 1000°C. The vacuum between the outer and the inner walls of the quartz glass tubes is continuously pumped using a rotary

pump. Volume D serves as an expansion volume which enables sample gases to be split to an appropriate size via valve 13 prior to inlet into the mass spectrometer. Volume E is the dedicated clean section of the line where the ultra-pure nitrogen standard reservoir (N_2-STD) is housed: aliquots of this standard are inlet via a pneumatically actuated pipette. Volume E is held at high vacuum by a dedicated ion pump.

2.3. Sample Preparation

[6] Visually fresh oceanic basalt glasses are hand-picked and ultrasonically cleaned in a methanol bath for one hour, then dried and loaded into one of two crushers (Figure 2), which are baked at 100°C overnight in an attempt to remove any adsorbed atmospheric nitrogen. Simultaneously, the whole extraction and purification line is baked at 120°C.

2.4. Sample Crushing

[7] Before crushing commences, the crusher and vacuum lines are cooled to room temperature. In order to isolate the sample from the vacuum line, valve 3 (Figure 2) is closed and the sample is crushed using a hydraulically operated crushing press at 5000 psi, effectively releasing trapped vesicle-sited gas. We typically crush between 1 and 3 g of fresh basaltic glass, free of visible alteration. Crushing is the favored bulk nitrogen extraction method over conventional online stepped heating [*Exley et al.*, 1987; *Murty and Marti*, 1994; *Marty and Zimmerman*, 1999] as well as sealed tube extraction methods [*Boyd et al.*, 1994b; *Busigny et al.*, 2005] in order to minimize blanks and, in the former case, avoid any potential nitrogen losses or fractionation effects associated with hot molybdenum furnaces [*Yokochi and Marty*, 2006].

2.5. Gas Purification Protocol

[8] As crushing commences, released CO_2, H_2O and other condensable gases are separated from nitrogen gas by use of a cold finger (CF1) held at liquid-nitrogen temperature. After 5 min of freezing, all remaining non-condensable gases are expanded into volumes A+B+C+D by opening valve 3, with valves 4, 7 and 11 already open and 8 and 10 closed (i.e., the furnaces are isolated) (Figure 2). Five min are allowed for gas expansion and equilibration before gas in Volume A is again isolated by closing valve 4. The fraction of gas remaining in Volume A is then inlet into the QMS section where the N_2/Ar ratio is measured. Importantly, gas inlet into the QMS section of the line is not utilized for N_2-isotope measurement as it may be affected by ionization in the QMS source [*Takahata et al.*, 1998]. Calibration of the QMS for the N_2/Ar ratio was achieved by repeatedly running air standards (Air-STD) and subsequently normalizing to an assumed air ratio of 83.6.

[9] The pressure of the remaining gas fraction in volumes B+C+D (~50% of total gas) is then measured manometrically using the CM. The gas is then reacted for 10 min with pure O_2, produced by heating a copper oxide (CuO) finger to 850°C. This procedure is carried out in the presence of a platinum foil (Pt) catalyst, held at 1000°C, to promote the oxidation of carbonaceous (CO, C_2H_4) and nitrogenous (NO) species to CO_2 and NO_2, respectively. Additionally, any residual hydrogen and sulfur are oxidized to H_2O and SO_2. After 10 min, excess oxygen is reabsorbed back onto the CuO finger, first at 600°C for 15 min and then at 450°C for 15 min. During this period, the condensable gases (CO_2, SO_2 and H_2O) are adsorbed onto cold finger (CF2) held at liquid nitrogen temperature.

[10] The oxidized gas can then be split using the expansion volume via valve 13 in order to reduce the pressure prior to mass spectrometer inlet. In this respect, the CM is used semiquantitatively to determine if reducing the gas load is necessary. While the expansion volume is rarely used for relatively gas-poor rock and mineral samples, it provides the option and capability to effectively split larger N_2 gas loads (e.g., N_2 in geothermal samples). Any remaining gas is then further expanded into volume E, where it is exposed to yet another cold finger (CF3) for 5 min prior to inlet into the mass spectrometer.

2.6. Analytical Protocol

[11] We simultaneously measure m/z = 28, 29 and 30 (CO correction) using fixed triple collection mass spectrometry. IonVantage software is used to interface and communicate with the mass spectrometer. Immediately after inlet, we manually scan over mass 30 to ensure that all peaks are positioned correctly prior to running the data acquisition protocol. In total, twenty-four data collection cycles are run per sample, using an integration time of 10 s per cycle. Background levels are monitored between sample measurements at mass 29.5 in order to apply a background subtraction to all data. The nitrogen isotope ratio is calculated using the mean value of the 24 cycles. Mean values are in good agreement with values determined by extrapolating data to time zero (i.e., time of inlet) using a liner regression method: however, average values are preferred due to smaller statistical errors (Table 1).

3. Standards, Blanks and Corrections

[12] Precise characterization of standards, blanks and correction factors are critical when making high precision N-isotope measurements. Here, we describe the analytical methods adopted and show results for standards, blanks and corrections. Triple-collection takes less than 5 min to complete allowing a significant number of standards to be measured (8–10 per day on average), thus enabling precise characterization of the N_2-STD (see Table B1). Furthermore, reduced analytical times help minimize any potential sample depletion (<2%) and/or memory effects in the flight tube.
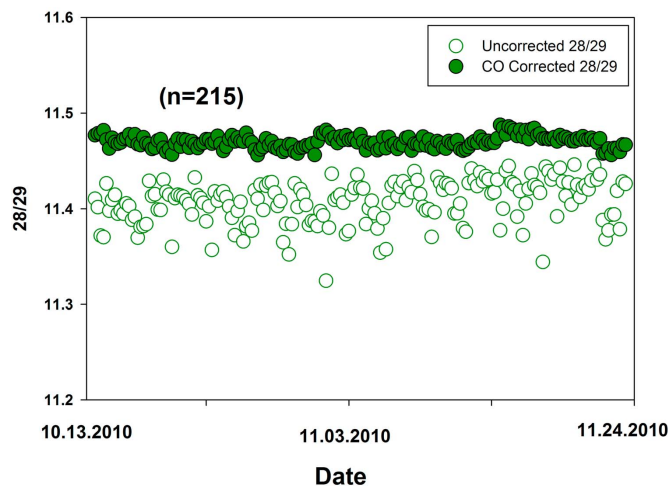
Figure 3. Overall reproducibility of the internal N_2-STD between 13 October 2010 and 24 November 2010. Open green circles indicate uncorrected (raw-measured) mass 28/29 ratios and green filled circles indicate CO-corrected 28/29 ratios. The average analytical uncertainty on an individual 28/29 measurement is 0.03 ‰ and is thus encompassed by the size of the symbol. The mean uncorrected 28/29 ratio is 11.407 ± 0.022 (1σ). The uncorrected N_2-STD reproducibility during a single day, expressed as the standard deviation from the mean, was 1.75 ‰ (1σ) compared to an overall reproducibility, over the 43-day run-period, of 2.06 ‰ (1σ). The mean CO-corrected 28/29 ratio is 11.470 ± 0.006 (1σ). The CO-corrected N_2-STD reproducibility during a single day was 0.38 ‰ (1σ) compared to an overall reproducibility, over the same 43-day run-period, of 0.56 ‰ (1σ).

3.1. N_2 Standards

[13] The N_2-STD is an ultra high purity (>99.99%) N_2-gas housed in a 3.8-L internally electro-polished stainless steel cylinder. N_2-STD gas is introduced into volume E (Figure 2) using a pneumatically actuated pipette valve, with an internal volume of 0.100 ± 0.002 cm^3. The N_2-STD gas is held at a reduced pressure such that an aliquot delivers 7.29 ± 0.15 [N_2] μcm^3 STP. The automated pipette helps insure peak height reproducibility for all monitored masses by inletting a consistent amount of N_2-STD gas per aliquot, thus removing any potential operator-induced inconsistency or bias. Before inlet into the mass spectrometer, the N_2-STD gas is purified for 2 min using cold finger (CF3) held at liquid nitrogen temperature. The $^{15}N/^{14}N$ ratio is determined by the CO-corrected 28/29 ratio. The N_2-STD is typically measured 8–10 times per day—several times before and after each sample analysis, with the daily mean value used to normalize unknowns. The rapidity of the analysis

allows each (unknown) sample to be bracketed by several standards, which in turn contributes to improving overall accuracy.

[14] As part of the initial testing of the system, we measured the isotopic ratio of the N_2-STD repeatedly (n = 215) and determined its uncorrected 28/29 ratio to be 11.407 ± 0.022 (1σ) (Figure 3). Importantly, this uncorrected ratio varies systematically from the canonical $^{28}N/^{29}N$ ratio of air (136.5) by the ratio of resistors L1 to L3 (11.9). Notably, the CO-corrected (section 3.3) N_2-STDs are considerably more reproducible at 11.470 ± 0.006 (1σ). The improved reproducibility of CO-corrected N_2-STDs demonstrates the necessity of CO interference corrections when making high precision nitrogen isotope measurements. To test for mass discrimination effects, several different sized aliquots of the N_2-STD were inlet and measured. The mean 28/29 values of the different sized aliquots show good agreement (Figure 4, top), indicating any pressure-induced discrimination effects in the mass spectrometer were
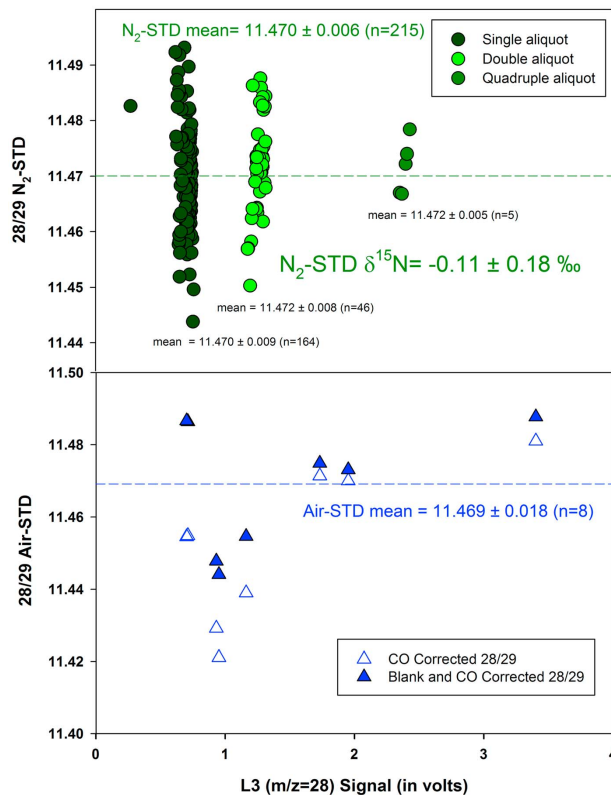
Figure 4. (top) N_2-STD 28/29 ratio as a function of L3 (m/z = 28) signal (in volts). One aliquot of N_2-STD is $\sim$7.29 $\pm$ 0.15 [N_2] μcm^3 STP. Note: we measure 28/29 for single, double and quadruple aliquots, thereby spanning the concentration range for samples in this study. Overall reproducibility of the N_2-STD is 11.470 $\pm$ 0.006 (1σ). The mean of each group of STDs is also listed. Overall, there is no evidence for mass discrimination or any pressure effects within the size range of samples. The blank correction on an N_2-STD is less than 1%. (bottom) Air-STD mass 28/29 as a function of of L3 (m/z = 28) signal (in volts). Overall reproducibility of the SIO Air-STD is 11.469 $\pm$ 0.018 (n = 8). Open blue triangles are CO-corrected whereas filled blue triangles are blank and CO-corrected. The dotted blue line represents the mean blank and CO-corrected value. We calculate a δ^{15}N value of -0.11 ‰ $\pm$ 0.22 (1σ) for the N_2-STD by normalizing to Air-STDs (0 ‰ by definition).

negligible over the range of N_2 pressures under consideration.

[15] The reproducibility of standards before and after a sample run (e.g., during a single day) is the most important factor controlling the uncertainty of sample nitrogen isotope measurements. The average

measurement uncertainty associated with a single N_2-STD δ^{15}N measurement was 0.03 ‰ (1σ). However, the average reproducibility of the N_2-STD, taken as the standard deviation from the mean of all N_2-STDs run during a single day, was 0.38 ‰ (1σ) (see Table B1) which compares well with quoted

precisions of 0.5 ‰ from the Atmosphere and Ocean Research Institute (AORI) at the University of Tokyo [*Sano et al.*, 2001] and the Institut de Physique du Globe at the University of Paris (IPGP) [*Busigny et al.*, 2005]. Notably, over longer time intervals the reproducibility of the N_2-STD was slightly worse: for example, the reproducibility was 0.56 ‰ (1σ) over a period of 43 days. Quantification of these highly precise and reproducible daily variations in standard $\delta^{15}N$ values demonstrates one of the principal advantages provided by short analytical times associated with static triple collection methods.

3.2. Air Standards

[16] Throughout the 43-day calibration period, we ran a total of 8 Air-STDs (Figure 4, bottom) at approximately one-week intervals. The mean $\delta^{15}N$ value of the running N_2-STD was -0.11 ± 0.22 ‰ (1σ) versus the Air-STD (by definition = 0 ‰). As a consequent of the ease of preparation and measurement, sample (i.e., unknown) $\delta^{15}N$ values were calculated versus the running N_2-STD and subsequently corrected for the difference between the N_2-STD and the Air-STD (taken as the mean of the 8 Air-STDs throughout the run period). Notably, the reproducibility of the Air-STD (0.22 ‰) compares favorably to literature reports (0.3 ‰ and 2.6 ‰, *Takahata et al.* [1998] and *Mohapatra et al.* [2009], respectively). Our ability to produce a reproducible external standard $\delta^{15}N$ value again derives from our use of simultaneous triple collection protocols.

3.3. CO Interference and Correction

[17] Carbon monoxide (CO) and hydrocarbons (e.g., C_2H_6) are released during sample crushing and subsequently oxidized and removed prior to inlet into the mass spectrometer. During the oxidation process, sample gas is reacted with hot (1000°C) platinum catalyst [*Boyd et al.*, 1988] in order to dissociate NO ($^{14}N^{16}O$) molecules, which interfere at mass 30. Any residual CO ($^{12}C^{18}O + ^{13}C^{17}O$) and C_2H_6 species remaining after cleanup are combined with small amounts of background CO produced in the ion source and measured at m/z 30. The mass resolution of ~620 on the axial detector is adequate to effectively resolve $^{15}N^{15}N + ^{12}C^{18}O + ^{13}C^{17}O$ from C_2H_6, leaving only the $^{15}N^{15}N$ and CO species ($^{12}C^{18}O + ^{13}C^{17}O$) where the mass 30 peak is measured. The $^{15}N^{15}N$ contribution (typically <2% of peak height) at mass 30 is calculated based upon the measured $^{14}N^{14}N$ ratio, assuming

terrestrial air-like proportions of $^{15}N^{15}N:^{14}N^{14}N$. This value is subtracted from the intensity at mass 30, leaving only CO ($^{12}C^{18}O + ^{13}C^{17}O$). This CO value at mass 30 is then used to apply a correction to account for corresponding CO contributions at masses 28 ($^{12}C^{16}O$) and 29 ($^{12}C^{17}O + ^{13}C^{16}O$), again based on the assumption that interfering species are present in air-like proportions (Appendix A). In addition, $^{12}C_2H_6$ is closely monitored due to potential hydrocarbon ($^{12}C_2H_4$, $^{12}C_2H_5$) interferences at masses 28 and 29, respectively. If the $^{12}C_2H_6$ peak increases by ~30% over typical baseline values then we consider the measurement precision to be compromised and the preparation line is extensively baked and pumped in order to remove the interfering hydrocarbon species.

[18] Applying a comprehensive CO correction and monitoring C_2H_6 greatly improves precision and therefore provides better overall standard and sample reproducibility (Figure 3), which improves the accuracy of the measurements. For example, the reproducibility, given as the standard deviation from the mean, of all N_2-STDs over a 43-day run period (n = 215) improved from a raw (non-CO-corrected) value of 2.06 ‰ to 0.56 ‰ when a CO correction was applied to the data (Figure 3). Similarly, the reproducibility of Air-STDs (n = 8) improved from 0.86 ‰ to 0.22 ‰, thus significantly improving the overall accuracy of the measurement. It is important to note that due to variable contributions of CO for individual sample and standard runs, the CO correction factor was non-systematic necessitating an individualized correction for every analysis. These new results illustrate that the CO correction is critical when making high precision nitrogen isotope measurements.

3.4. Blank Contribution and Correction

[19] Due to the anticipated range of N_2 concentrations in oceanic basalts (e.g., ~1 to 500 μcm^3 STP/g [e.g., *Marty and Dauphas*, 2003]), procedural blanks can potentially represent a significant contribution to nitrogen-poor samples: thus, it is critical to characterize blanks as accurately as possible. To this end, our analytical protocol includes a procedural crushing blank run prior to each individual sample run. To gain an appreciation of the likely characteristics of the blank, a total of 22 procedural crusher blanks were run during the 43-day test period following the identical procedure adopted for samples (Figure 5). Procedural crusher N_2 blanks averaged 4.2 ± 0.5 μcm^3 STP (1σ). This blank
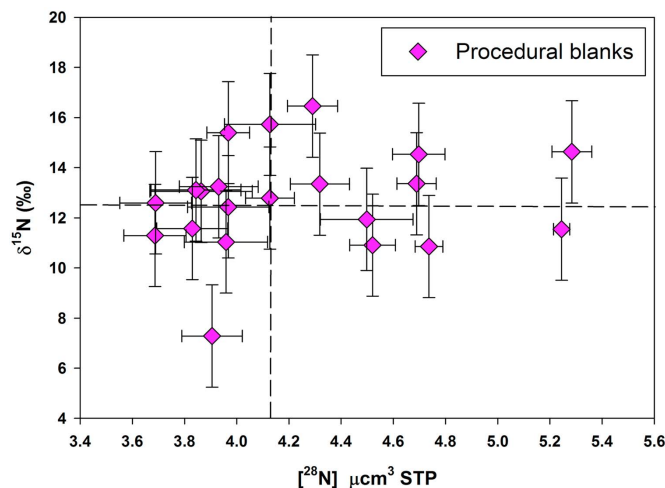
Figure 5. δ^{15}N (‰) versus Blank contribution [N$_2$] μcm^3 STP. The average (n = 22) procedural blank concentration of 4.2 ± 0.5 [N$_2$] μcm^3 STP (1σ) is shown with a vertical dashed line whereas the average δ^{15}N value for the procedural blank (12.64 ‰ ± 2.04 ‰) (1σ) is shown as a horizontal dashed line.

compares favorably with values reported from other groups performing triple collection (e.g., 7.2–14.6 μcm^3 STP [*Boyd et al.*, 1995; *Busigny et al.*, 2005]). In addition, the isotopic composition of each blank was measured and used for blank-correction purposes. The blank was reproducible in δ^{15}N (12.64 ± 2.04 ‰) (1σ) (Figure 5). A simple isotopic mass balance in the form

$$\delta^{15}N_C = \frac{\delta^{15}N_S - \left[\delta^{15}N_B \times \left(\frac{[N_2]_B}{[N_2]_S}\right)\right]}{\left[1 - \left(\frac{[N_2]_B}{[N_2]_S}\right)\right]}$$

is used to determine the corrected isotopic composition of a given sample, where C = corrected, B = blank and S = sample.

4. Ocean Basalt Results

[20] To assess potential advantages of triple collection and gauge the accuracy of results obtained with our new system, we report data obtained on a suite of oceanic glasses from the Reykjanes Ridge (RR) and a gas-rich sample (D22–1) from the Central Indian Ridge (CIR). Specifically, we analyzed 11 samples for nitrogen isotopes (δ^{15}N),

N$_2$ concentrations and N$_2$/Ar ratios (Table 1); samples were processed using vacuum crushing following protocols described in section 2.4.

4.1. Sample Classification

[21] In order to test the capabilities of the new system, we targeted ocean basalt samples that display a wide range in gas (e.g., helium) concentrations. To facilitate discussion, we subdivide samples into three distinct groups using previously published helium concentrations [*Hilton et al.*, 2000; *Füri et al.*, 2011] as a metric for N$_2$ gas concentration. We refer to RR samples with more than 0.2 [He] μcm^3 STP/g as Group A and RR samples with less than 0.2 [He] μcm^3 STP/g as Group B (Figure 6). In addition to being helium poor, Group B samples exhibit additional characteristics of highly degassed samples – in that they display, low CO$_2$ concentrations (23.3–102.6 ppm), air-like ^{40}Ar/^{36}Ar (285–390), and high N$_2$/Ar ratios (142–218). Furthermore, Group B sample 121D3G has the highest ^{4}He/^{40}Ar* (where ^{40}Ar* = ^{40}Ar, corrected for air) of 50.4 – indicating extensive degassing [*de Leeuw*, 2007]. The 3rd category is a gas-rich basalt sample (D22–1) from the CIR that was targeted because of its high helium

Table 1. Nitrogen and Helium Systematics of Reykjanes Ridge (RR) and D22–1 Replicate Samples[a]

Sample ID	[He] μcm³ STP/g ($\pm$5%)	[N₂] μcm³ STP/g ($\pm$2.5%)	Blank Contribution (%)	δ^{15}N (‰)	N₂/Ar ($\pm$10%)
		Group A			
40D3G	4.90	61.0	4	-0.44 ± 0.60	78.9
66D3G	3.89	41.9	7	-1.87 ± 0.32	53.0
46D5G	2.70	31.5	7	-0.39 ± 0.32	66.1
75D10G	2.77	17.0	13	-1.57 ± 0.40	49.4
96D1G	1.92	7.54	16	0.87 ± 0.45	56.6
131D3G	0.61	11.8	19	-1.69 ± 0.58	70.0
		Group B			
157D3G	0.15	41.6	6	-0.39 ± 0.52	42.2
13D2G	0.16	1.85	56	5.35 ± 1.29	145.6
121D3G	0.021	0.45	82	9.70 ± 1.74	58.8
173D1G	0.022	1.37	61	4.26 ± 1.46	225
		Replicate Sample			
D22–1	7.13	74.2	3	1.71 ± 0.45	82.8
D22–1	-	78.7	3	1.80 ± 0.52	127
D22–1	-	92.6	10	1.74 ± 0.48	104

[a]All uncertainties on δ^{15}N are 1-sigma. Blank subtractions have been applied to all δ^{15}N and N₂/Ar results and a CO correction has been applied to δ^{15}N results. Helium values from *Hilton et al.* [2000] (Groups A and B; Reykjanes Ridge) and *Füri et al.* [2011] (D22–1; Central Indian Ridge). N₂ concentration measurements are accurate within 3% based on the reproducibility STDs. All N₂/Ar uncertainties are less than 10%.

concentration [*Füri et al.*, 2011]. Sample D22–1 was analyzed a total of three times (Figure 7), thus providing a useful test of the reproducibility of its δ^{15}N and N₂ concentration characteristics.

4.2. N₂ Concentration Comparisons

[22] We adopted two independent approaches to quantify the concentration of N₂ released from each sample: both employed peak height measurement
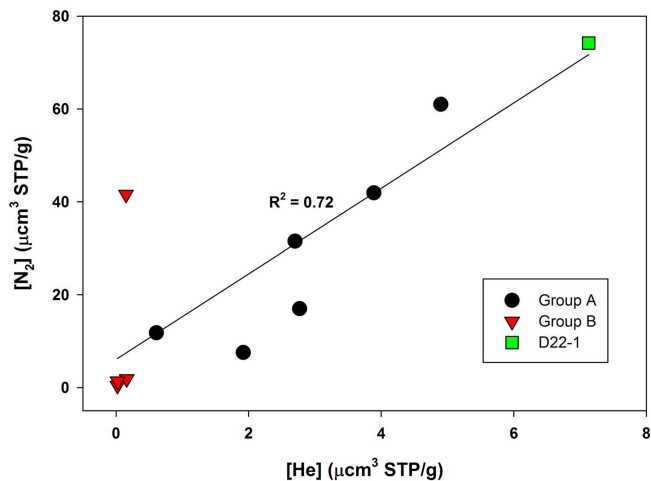
Figure 6. [N₂] μcm³ STP/g versus [He] μcm³ STP/g concentrations, helium results are from *Hilton et al.* [2000]. We targeted ocean basalt samples that display a wide range in gas (e.g., helium) concentrations. Note: the R^2 correlation between gas concentrations is 0.72.
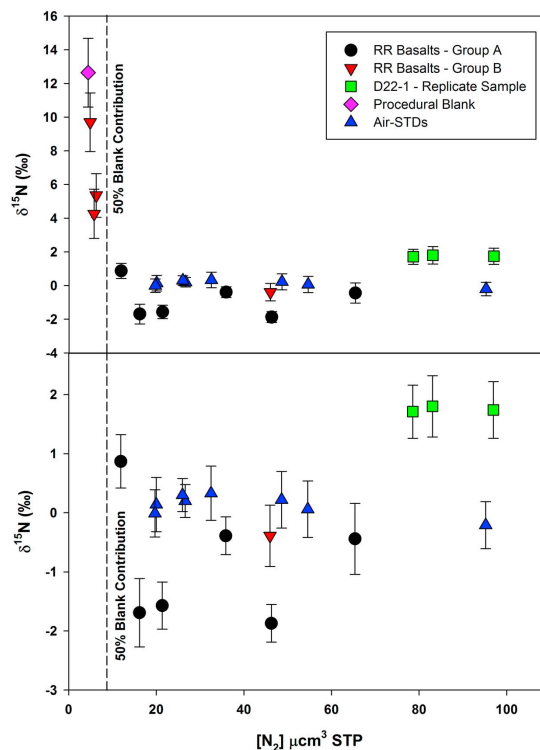
Figure 7. (top) $\delta^{15}N$ (‰) versus $[N_2]$ μcm^3 STP for all samples, Air-STDs and blanks. The mean procedural blank ($\delta^{15}N = 12.64 \pm 2.04$ ‰) (1σ) is plotted as a purple diamond. RR basalts are broken into two sub-groups based on helium concentration: Group A (>0.2 [He] μcm^3 STP/g) denoted by black circles and Group B (<0.2 [He] μcm^3 STP/g) denoted by red triangles. Replicate sample D22–1 (green squares) was run repeatedly (three times in total) because of its relatively high N_2 concentration as well as its isotopically high $\delta^{15}N$ signature. A total of 8 Air-STDs were run (blue triangles). Note: concentration data are not blank corrected in order to show the relative blank contribution (dashed line = 50% blank contribution). (bottom) $\delta^{15}N$ (‰) versus $[N_2]$ μcm^3 STP for samples with less than 50% blank contribution. All samples and STDs fall between +2 and −2 ‰ and, as a result, the y axis has been contracted. At this scale, the natural variation of samples versus Air-STDs is evident.

relative to calibrated air aliquots. After dividing the gas into two aliquots following inlet (section 2.5), we measured N_2 independently on the VG-5440 mass spectrometer and the QMS. The positive correlation ($R^2 = 0.98$) in N_2 concentration between these two techniques gives us confidence in the reliability of these data (Figure 8). The uncertainty on the N_2 concentration measured on the VG-5440 mass spectrometer is less than 2.5%, estimated

by combining repeat measurements of mass 28 intensity of the N_2-STD with the uncertainty on the pipette volume.

[23] Nitrogen gas loads are consistent with helium gas loads, as shown by the positive correlation ($R^2 = 0.72$) between helium and nitrogen concentrations (Figure 6). Group A samples yielded blank corrected N_2 concentrations between 7.54 and
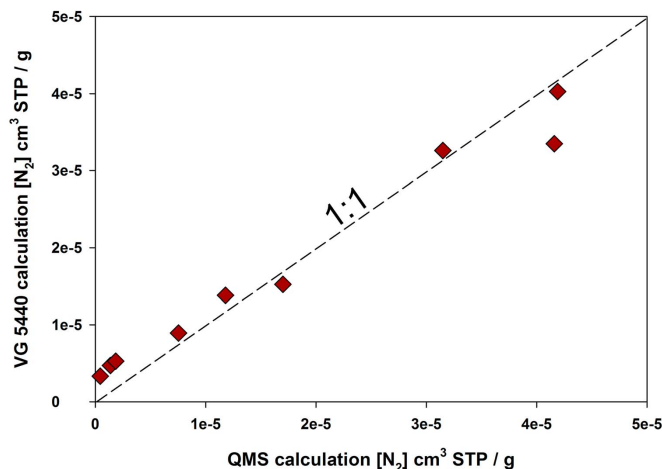
Figure 8. N_2 concentration of samples measured by peak height comparison using the VG5440 and the QMS (in $[N_2]$ cm³ STP/g). The estimated uncertainties on individual measurements are encompassed by the symbol size. The two independent measurements show excellent agreement ($R^2 = 0.98$) for the RR samples. Concentration measurements reported in this contribution use the estimate from mass spectrometer voltage.

61.0 μcm³ STP/g – within the range reported for other oceanic basalts [*Marty and Dauphas*, 2003]. Group B samples range from 0.45 to 41.6 $[N_2]$ μcm³ STP/g: however, three of the four samples displayed extremely low (<2 $[N_2]$ μcm³ STP/g) nitrogen concentrations and, as a result, blank contributions were relatively large (56–82%).

4.3. Nitrogen Isotope (δ^{15}N) Results

[24] Gas-rich (Group A and D22–1) δ^{15}N values varied from −1.87 ‰ to +1.80 ‰, within the range of previously reported mantle values (−5 to +8 ‰) [*Marty and Dauphas*, 2003]. Sample D22–1, run a total of three times on different days, displayed highly reproducible results - yielding an average δ^{15}N value of 1.75 ± 0.28‰ (1σ). On the whole, gas-rich oceanic basalt samples varied by nearly 4 ‰ whereas Air-STDs (which underwent identical purification procedures) varied by just 0.6 ‰ with a standard deviation of 0.22 ‰. The highly reproducible nature of the replicate sample and Air-STDs indicates that the quoted precision of 0.38 ‰ (determined by the reproducibility of N_2-STDs) may be a conservative estimate. Note that all δ^{15}N uncertainties are calculated combining measurement uncertainty as well as the uncertainties

associated with the reproducibility of both N_2- and Air-STDs.

[25] In contrast, the low (<2 μcm³ STP/g) nitrogen concentrations Group B (RR) samples had consistently higher δ^{15}N values, relative to Group A samples, extending from −0.39 ‰ to 9.70 ‰. We attribute the isotopically high values to either (1) an inappropriate blank correction when the blank exceeds ~50%, or (2) degassing induced fractionation only evident in extremely low concentration samples. We note that the large blank/high δ^{15}N samples plot close to the average procedural blank value (12.64 ± 2.04 ‰) (Figure 7), suggesting that the former explanation may have merit. Further experiments targeting highly degassed (low N_2) samples are needed to confirm this possibility.

4.4. Elemental (N_2/Ar) Ratio Comparisons

[26] The N_2/Ar ratios of samples, Air-STDs and procedural blanks were determined using the QMS. Air-STD N_2/Ar ratios were reproducible within 10%. The mean N_2/Ar ratio of 11 procedural blanks was determined to be 200 ± 80 (1σ). Using this value, a comprehensive blank correction was applied
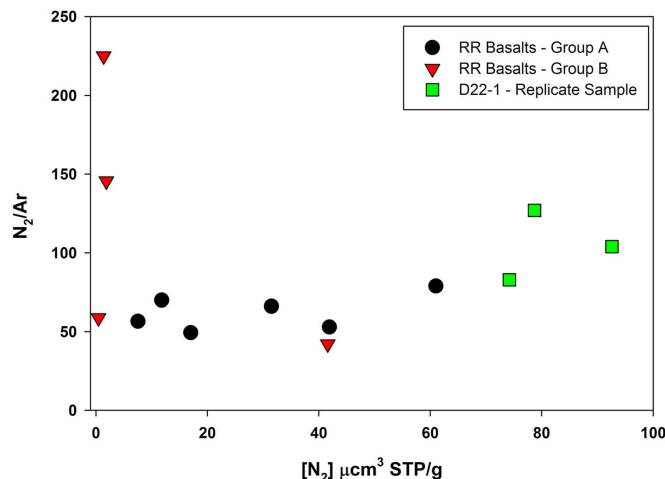
Figure 9. N_2/Ar versus $[N_2]$ concentration for RR and CIR basalts. Uncertainties on N_2/Ar ratios are less than 10% and concentration uncertainties are less than 2.5%. Notably, the gas-poor Group B samples display a wide range in N_2/Ar – high ratios are likely influenced by inappropriate blank corrections.

to all QMS data by applying a similar mass balance correction as detailed in section 3.4. Gas-rich (Group A and D22–1) N_2/Ar ratios varied from ~49.4 to ~127, within the expected mantle range [*Marty and Dauphas*, 2003]. By contrast, low (<2 $[N_2]$ μcm^3 STP/g) nitrogen concentration Group B samples displayed higher N_2/Ar ratios in two of the four samples, relative to Group A, extending the range from 42.2 to 225 (Figure 9). We note that the same gas-poor Group B samples that display high $\delta^{15}N$ values also have high N_2/Ar ratios (close to blank levels), which we attributed to an inappropriate blank correction when the blank exceeds ~50%.

5. Concluding Remarks

[27] A newly constructed nitrogen extraction and purification system has been interfaced to a noble gas VG-5440 mass spectrometer designed for simultaneous triple collection of nitrogen isotopes. Here, we demonstrate the advantages afforded by our new system coupled to static triple collection. In particular, triple collection improves overall precision by enabling shorter analytical times, thus allowing standards and samples to be better characterized.

Moreover, shorter analytical times help minimize sample depletion and memory effects in the mass spectrometer. We also carried out an individual CO and blank correction to all runs thus improving both precision on individual measurements and accuracy of results. We tested the new system with a series of oceanic basalts analyzed for $\delta^{15}N$, N_2 concentration and N_2/Ar ratios. Based on these results, we conclude that static triple collection, utilizing simultaneous collection on two Faraday and one Daly collector, provides clear advantages over peak jumping methods as is demonstrated by the highly reproducible nature of both internal and external standards and unknowns.

Appendix A

[28] The nitrogen isotope ratio is determined by comparing peak heights at masses 28 and 29. However, the contribution of interfering species (CO, C_2H_X) at masses 28 and 29 can potentially alter this ratio - particularly at extremely low N concentrations. Therefore, we simultaneously measure output voltages at masses = 28, 29 and 30 using three separate collectors (two Faradays and one Daly). At mass 30, the C_2H_6 peak is resolved from

Table B1. Reproducibility of the N_2-STD on Individual Days That Samples Were Processed

Date	Number of N_2-STD run	Mean 28/29	28/29 S.D. ($\pm$)	$\delta^{15}N$ S.D. (‰)
20 October 2010	11	11.471	0.005	0.45
09 November 2010	9	11.468	0.004	0.36
10 November 2010	10	11.466	0.004	0.34
17 November 2010	8	11.467	0.008	0.67
18 November 2010	9	11.481	0.004	0.34
19 November 2010	6	11.478	0.005	0.43
22 November 2010	10	11.473	0.002	0.17
23 November 2010	7	11.473	0.002	0.14
24 November 2010	9	11.464	0.006	0.54

the N_2 + CO peak and thus we only quantify the CO contribution. The amount of CO interfering at masses 28 and 29 can then be determined by solving these simple mass balance equations [after *Beaumont et al.*, 1994; *Hashizume and Marty*, 2004]:

$$\text{Mass } 28 = {}^{14}N^{14}N + {}^{12}C^{16}O$$
$$\text{Mass } 29 = {}^{14}N^{15}N + {}^{13}C^{16}O \left(+ {}^{12}C^{17}O\right)$$
$$\text{Mass } 30 = {}^{15}N^{15}N + {}^{12}C^{18}O \left(+ {}^{13}C^{17}O\right)$$

[29] CO species in parenthesis are statistically negligible compared to the primary interfering CO species and are therefore ignored here in order to simplify the equations; however, all contributing species are fully accounted for in our CO correction. Assuming isotopic equilibrium between N_2 molecules, the abundance ratios between isotopes are ${}^{14}N^{14}N$: ${}^{14}N^{15}N$: ${}^{15}N^{15}N = 1: 2r: r^2$ where $r = {}^{15}N/{}^{14}N$. Therefore, the mass balance equations are

$$\text{Mass } 28 = {}^{14}N^{14}N + {}^{12}C^{16}O = {}^{14}N^{14}N + {}^{16}O/{}^{18}O \times {}^{12}C^{18}O$$
$$\text{Mass } 29 = {}^{14}N^{14}N \times 2r + {}^{13}C/{}^{12}C \times {}^{12}C^{16}O$$
$$= {}^{14}N^{14}N \times 2r + {}^{13}C/{}^{12}C \times {}^{16}O/{}^{18}O \times {}^{12}C^{18}O$$
$$\text{Mass } 30 = {}^{14}N^{14}N \times r^2 + {}^{12}C^{18}O$$

If we assume that the ${}^{13}C/{}^{12}C$ and ${}^{18}O/{}^{16}O$ ratios of the interfering CO are equal to terrestrial air values, then the only remaining unknowns are (1) $r = {}^{15}N/{}^{14}N$, (2) the amount of ${}^{14}N^{14}N$, and (3) the amount of ${}^{12}C^{18}O$. Therefore, we obtain a unique solution by solving the three above equations.

[30] These calculations are applied by processing raw data using a Python correction code written specifically for this correction.

Appendix B

[31] Table B1 reports the daily reproducibility of the N_2-STD on individual days that samples were processed. The standard deviation (s.d.) is given

as an absolute ($\pm$) and (‰) variation from the mean N_2-STD value on an individual day.

References

Beaumont, V., P. Agrinier, M. Javoy, and F. Robert (1994), Determination of the CO contribution to the ${}^{15}N/{}^{14}N$ ratio measured by mass spectrometry, *Anal. Chem.*, *66*, 2187–2189, doi:10.1021/ac00085a039.

Boyd, S. R., and P. Philippot (1998), Precambrian ammonium biogeochemistry: A study of the Moine metasediments, Scotland, *Chem. Geol.*, *144*, 257–268, doi:10.1016/S0009-2541(97)00135-6.

Boyd, S. R., D. R. Mattey, C. T. Pillinger, H. J. Milledge, M. Mendelssohn, and M. Seal (1987), Multiple growth events during diamond genesis: An integrated study of carbon and nitrogen isotopes and nitrogen aggregation state in coated stones, *Earth Planet. Sci. Lett.*, *86*, 341–353, doi:10.1016/0012-821X(87)90231-7.

Boyd, S. R., I. P. Wright, I. A. Franchi, and C. T. Pillinger (1988), Preparation of sub-nanomole quantities of nitrogen gas for stable isotopic analysis, *J. Phys. E Sci. Instrum.*, *21*, 876–885, doi:10.1088/0022-3735/21/9/012.

Boyd, S. R., I. P. Wright, and C. T. Pillinger (1993), Accurate determination of nitrogen concentrations by static vacuum mass spectrometry, *Meas. Sci. Technol.*, *4*, 1000–1005, doi:10.1088/0957-0233/4/9/014.

Boyd, S. R., F. Pineau, and M. Javoy (1994a), Modeling the growth of natural diamonds, *Chem. Geol.*, *116*, 29–42, doi:10.1016/0009-2541(94)90156-2.

Boyd, S. R., A. Réjou-Michel, and M. Javoy (1994b), Non-cryogenic purification of nanomole quantities of nitrogen gas for isotopic analysis, *Anal. Chem.*, *66*, 1396–1402, doi:10.1021/ac00081a006.

Boyd, S. R., A. Réjou-Michel, and M. Javoy (1995), Improved techniques for the extraction, purification and quantification of nanomole quantities of nitrogen gas: The nitrogen content of diamond, *Meas. Sci. Technol.*, *6*, 297–305, doi:10.1088/0957-0233/6/3/007.

Busigny, V., M. Ader, and P. Cartigny (2005), Quantification and isotopic analysis of nitrogen in rocks at the ppm level using tube combustion technique: A prelude to the study of altered oceanic crust, *Chem. Geol.*, *223*, 249–258, doi:10.1016/j.chemgeo.2005.08.002.

Busigny, V., P. Cartigny, and P. Philippot (2011), Nitrogen isotopes in ophiolitic metagabbros: A re-evaluation of modern nitrogen fluxes in subduction zones and implication for the early Earth atmosphere, *Geochim. Cosmochim. Acta*, *75*, 7502–7521, doi:10.1016/j.gca.2011.09.049.

Cartigny, P., S. R. Boyd, J. W. Harris, and M. Javoy (1997), Nitrogen isotopes in peridotitic diamonds from Fuxian, China: The mantle signature, *Terra Nova*, *9*, 175–179, doi:10.1046/j.1365-3121.1997.d01-26.x.

Cartigny, P., J. W. Harris, and M. Javoy (2001a), Diamond genesis, mantle fractionations and mantle nitrogen content: A study of δ^{13}C-N concentrations in diamonds, *Earth Planet. Sci. Lett.*, *185*, 85–98, doi:10.1016/S0012-821X(00)00357-5.

Cartigny, P., N. Jendrzejewski, F. Pineau, E. Petit, and M. Javoy (2001b), Volatile (C, N, Ar) variability in MORB and the respective roles of mantle source heterogeneity and degassing: The case of the Southwest Indian Ridge, *Earth Planet. Sci. Lett.*, *194*, 241–257, doi:10.1016/S0012-821X(01)00540-4.

Chang, S., J. Lawless, M. Romiez, I. R. Kaplan, C. Petrowski, H. Sakai, and J. W. Smith (1974), Carbon, nitrogen and sulfur in lunar fines 15012 and 15013: Abundances, distributions and isotopic composition, *Geochim. Cosmochim. Acta*, *38*, 853–872, doi:10.1016/0016-7037(74)90060-X.

Craig, H., K. Marti, and R. Wiens (1993), *A Static Mass Spectrometer With Triple Collection for Nitrogen and Neon Isotopes*, *SIO Reference Ser.*, vol. 93-11, pp. 1–20A, Scripps Inst. of Oceanogr., La Jolla, Calif.

Dauphas, N., and B. Marty (1999), Heavy nitrogen in carbonatites of the Kola Peninsula: A possible signature of the deep mantle, *Science*, *286*, 2488–2490, doi:10.1126/science.286.5449.2488.

de Leeuw, G. A. M. (2007), The noble gas and carbon systematics of divergent convergent and strike-slip plate boundaries: Examples from the Reykjanes Ridge, Central American Arc and North Anatolian Fault Zone, PhD thesis, Scripps Inst. of Oceanogr., Univ. of Calif., San Diego, La Jolla.

Exley, R. A., S. R. Boyd, D. P. Mattey, and C. T. Pillinger (1987), Nitrogen isotope geochemistry of basaltic glasses: Implications for mantle degassing and structure?, *Earth Planet. Sci. Lett.*, *81*, 163–174, doi:10.1016/0012-821X(87)90153-1.

Fischer, T. P., D. R. Hilton, M. M. Zimmer, A. M. Shaw, Z. D. Sharp, and J. A. Walker (2002), Subduction and recycling of nitrogen along the Central American margin, *Science*, *297*, 1154–1157, doi:10.1126/science.1073995.

Fischer, T. P., N. Takahata, Y. Sano, H. Sumino, and D. R. Hilton (2005), Nitrogen isotopes of the mantle: Insights from mineral separates, *Geophys. Res. Lett.*, *32*, L11305, doi:10.1029/2005GL022792.

Fischer, T. P., P. Burnard, B. Marty, D. R. Hilton, E. Füri, F. Palhol, Z. D. Sharp, and F. Mangasini (2009), Upper-mantle volatile chemistry at Oldonyo Lengai volcano and the origin of carbonatites, *Nature*, *459*, 77–80, doi:10.1038/nature07977.

Frick, U., and R. O. Pepin (1981), Microanalysis of nitrogen isotope abundances: Association of nitrogen with noble gas carriers in Allende, *Earth Planet. Sci. Lett.*, *56*, 64–81, doi:10.1016/0012-821X(81)90117-5.

Füri, E., D. R. Hilton, B. J. Murton, C. Hémond, J. Dyment, and J. M. D. Day (2011), Helium isotope variations between Réunion Island and the Central Indian Ridge (17°–21°S): New evidence for ridge–hot spot interaction, *J. Geophys. Res.*, *116*, B02207, doi:10.1029/2010JB007609.

Hashizume, K., and B. Marty (2004), Nitrogen isotopic analyses at the sub-picomole level using an ultra-low blank laser extraction technique, in *Handbook of Stable Isotope Analytical Techniques*, edited by P. D. Groot, pp. 361–375, Elsevier, Amsterdam.

Hashizume, K., and N. Sugiura (1990), Precise measurement of nitrogen isotopic composition using a quadrupole mass spectrometer, *Mass Spectrosc.*, *38*, 269–286.

Hilton, D. R., M. F. Thirlwall, R. N. Taylor, B. J. Murton, and A. Nichols (2000), Controls on magmatic degassing along the Reykjanes Ridge with implications for the helium paradox, *Earth Planet. Sci. Lett.*, *183*, 43–50, doi:10.1016/S0012-821X(00)00253-3.

Hilton, D. R., T. P. Fischer, and B. Marty (2002), Noble gases and volatile recycling at subduction zones, *Rev. Mineral. Geochem.*, *47*, 319–370, doi:10.2138/rmg.2002.47.9.

Javoy, M., and F. Pineau (1991), The volatile record of a popping rock from the Mid-Atlantic Ridge at 14°N: Chemical and isotopic composition of gases trapped in the vesicles, *Earth Planet. Sci. Lett.*, *107*, 598–611, doi:10.1016/0012-821X(91)90104-P.

Javoy, M., F. Pineau, and D. Demaiffe (1984), Nitrogen and carbon isotopic composition in the diamonds of Mbuji Mayi (Zaire), *Earth Planet. Sci. Lett.*, *68*, 399–412, doi:10.1016/0012-821X(84)90125-0.

Javoy, M., F. Pineau, and H. Delorme (1986), Carbon and nitrogen isotopes in the mantle, *Chem. Geol.*, *57*, 41–62, doi:10.1016/0009-2541(86)90093-8.

Kienast, M. (2000), Unchanged nitrogen isotopic composition of organic matter in the South China Sea during the last climatic cycle: Global implications, *Paleoceanography*, *15*(2), 244–253, doi:10.1029/1999PA000407.

Marty, B., and N. Dauphas (2003), The nitrogen record of crust-mantle interaction and mantle convection from Archean to present, *Earth Planet. Sci. Lett.*, *206*, 397–410, doi:10.1016/S0012-821X(02)01108-1.

Marty, B., and F. Humbert (1997), Nitrogen and argon isotopes in oceanic basalts, *Earth Planet. Sci. Lett.*, *152*, 101–112, doi:10.1016/S0012-821X(97)00153-2.

Marty, B., and L. Zimmerman (1999), Volatiles (He, C, N, Ar) in mid-ocean basalts: Assessment of shallow-level fractionation and characterization of source composition, *Geochim. Cosmochim. Acta*, *63*, 3619–3633, doi:10.1016/S0016-7037(99)00169-6.

Marty, B., M. Lenoble, and N. Vassard (1995), Nitrogen, helium and argon in basalt: A static mass spectrometer study, *Chem. Geol.*, *120*, 183–195, doi:10.1016/0009-2541(94)00120-W.

Marty, B., M. Chaussidon, R. C. Wiens, A. J. G. Jurewicz, and D. S. Burnett (2011), A ^{15}N-poor isotopic composition for the solar system as shown by Genesis solar wind samples, *Science*, *332*, 1533–1536, doi:10.1126/science.1204656.

Mohapatra, R. K., D. Harrison, U. Ott, J. D. Gilmour, and M. Trieloff (2009), Noble gas and nitrogen isotope components in Ocean Island Basalts, *Chem. Geol.*, *266*, 29–37, doi:10.1016/j.chemgeo.2009.03.022.

Murty, S. V. S., and K. Marti (1994), Nitrogen isotopic signatures in Cape York: Implications for formation of Group III A irons, *Geochim. Cosmochim. Acta*, *58*, 1841–1848, doi:10.1016/0016-7037(94)90540-1.

Peters, K. E., R. E. Sweeny, and I. R. Kaplan (1978), Correlation of carbon and nitrogen stable isotope ratios in sedimentary organic matter, *Limnol. Oceanogr.*, *23*, 598–604.

Pinti, D. L., K. Hashizume, and J. Matsuda (2001), Nitrogen and argon signatures in 3.8 to 2.8 Ga metasediments: Clues on the chemical state of the archean ocean and the deep biosphere, *Geochim. Cosmochim. Acta*, *65*, 2301–2315, doi:10.1016/S0016-7037(01)00590-7.

Sakai, H., D. J. des Marais, A. Ueda, and J. G. Moore (1984), Concentrations and isotope ratios of carbon, nitrogen and sulfur in ocean-floor basalts, *Geochim. Cosmochim. Acta*, *48*, 2433–2441, doi:10.1016/0016-7037(84)90295-3.

Sano, Y., N. Takahata, Y. Nishio, and B. Marty (1998), Nitrogen recycling in subduction zones, *Geophys. Res. Lett.*, *25*, 2289–2292, doi:10.1029/98GL01687.

Sano, Y., N. Takahata, Y. Nishio, T. P. Fischer, and S. N. Williams (2001), Volcanic flux of nitrogen from the Earth, *Chem. Geol.*, *171*, 263–271, doi:10.1016/S0009-2541(00)00252-7.

Takahata, N., Y. Nishio, N. Yoshida, and Y. Sano (1998), Precise isotopic measurements of nitrogen at the sub-nanomole level, *Anal. Sci.*, *14*, 485–491, doi:10.2116/analsci.14.485.

Thiemens, M. H., and R. N. Clayton (1983), Nitrogen contents and isotopic ratios of clasts from enstatite chondrite Abee, *Earth Planet. Sci. Lett.*, *62*(1), 165–168, doi:10.1016/0012-821X(83)90080-8.

Thomazo, C., D. L. Pinti, V. Busigny, M. Ader, K. Hashizume, and P. Philippot (2009), Biological activity and the Earth's surface evolution: Insights from carbon, sulfur, nitrogen and iron stable isotopes in the rock record, *C. R. Palevol*, *8*, 665–678, doi:10.1016/j.crpv.2009.02.003.

Wright, I. P., S. R. Boyd, I. A. Franchi, and C. T. Pillinger (1988), Determination of high precision nitrogen stable isotope ratios at the sub-nanomole level, *J. Phys. E Sci. Instrum.*, *21*, 865–875, doi:10.1088/0022-3735/21/9/011.

Yokochi, R., and B. Marty (2006), Fast chemical and isotopic exchange of nitrogen during reaction with hot molybdenum, *Geochem. Geophys. Geosyst.*, *7*, Q07004, doi:10.1029/2006GC001253.

Yokochi, R., B. Marty, G. Chazot, and P. Burnard (2009), Nitrogen in peridotite xenoliths: Lithophile behavior and magmatic isotope fractionation, *Geochim. Cosmochim. Acta*, *73*, 4843–4861, doi:10.1016/j.gca.2009.05.054.

III. Acknowledgements

In addition to those mentioned within the acknowledgements section of the published work, we also thank AGU for allowing us use a reprint of the material as it appeared in Geochemistry Geophysics Geosystems 2012, as Barry, P. H., D. R. Hilton, S. A. Halldórsson, D. Hahm, and K. Marti (2012), High precision nitrogen isotope measurements in oceanic basalts using a static triple collection noble gas mass spectrometer, *Geochemistry Geophysics Geosystems*, 13, Q01019, doi:10.1029/2011GC003878. The dissertation author was the primary investigator and lead author of this paper and conducted all the analyses presented herein.

CHAPTER IV: Helium and carbon isotope systematics of cold "mazuku" CO_2 vents and hydrothermal gases and fluids from Rungwe Volcanic Province, southern Tanzania

Helium and carbon isotope systematics of cold "mazuku" CO_2 vents and hydrothermal gases and fluids from Rungwe Volcanic Province, southern Tanzania

P.H. Barry [a,*], D.R. Hilton [a], T.P. Fischer [b], J.M. de Moor [b], F. Mangasini [c], C. Ramirez [d]

[a] Fluids and Volatiles Laboaoratory, Scripps Institution of Oceanography, UCSD, La Jolla, California 92093-0244, USA
[b] Department of Earth and Planetary Sciences, MSC 03 2040, 1 University of New Mexico, Albuquerque, New Mexico 87131-0001, USA
[c] Department of Mining and Mineral Processing Engineering, University of Dar Es Salaam, PO Box 35131, Dar Es Salaam, Tanzania
[d] Centro de Investigaciones en Ciencias Geologicas, Escuela Centroamericana de Geologia, Universidad de Costa Rica, Costa Rica

ARTICLE INFO

ABSTRACT

We report new helium and carbon isotope ($^3He/^4He$ and $\delta^{13}C$) and relative abundance ($CO_2/^3He$) characteristics of a suite of 20 gases and fluids (cold mazuku-like CO_2 vents, bubbling mud-pots, hot and cold springs) from 11 different localities in Rungwe Volcanic Province (RVP), southern Tanzania and from 3 additional localities in northern Tanzania (Oldoinyo Lengai Volcano and Lake Natron). At RVP, fluids and gases are characterized by a large range in He-isotope compositions ($^3He/^4He$) from 0.97 R_A to 7.18 R_A (where R_A = air $^3He/^4He$), a narrow range in $\delta^{13}C$ ratios from -2.8 to -6.5‰ (versus VPDB), and a large range in $CO_2/^3He$ values spanning nearly four orders of magnitude (4×10^9 to 3.2×10^{13}). Oldoinyo Lengai possesses upper-mantle-like He–CO_2 characteristics, as reported previously (Fischer et al., 2009), whereas hot springs at Lake Natron have low $^3He/^4He$ (~0.6 R_A), $CO_2/^3He$ (~5–15×10^8) and intermediate $\delta^{13}C$ (~−3.7 to −4.9 ‰). At RVP, fluid phase samples have been modified by the complicating effects of hydrothermal phase-separation, producing $CO_2/^3He$ and $\delta^{13}C$ values higher than postulated starting compositions. In contrast, gas-phase samples have not been similarly affected and thus retain more mantle-like $CO_2/^3He$ and $\delta^{13}C$ values. However, the addition of crustal volatiles, particularly radiogenic helium from ^4He-rich reservoir rocks, has modified $^3He/^4He$ values at all but the three cold CO_2 gas vent (i.e., mazuku) localities (Ikama Village, Kibila Cold Vent and Kiejo Cold Vent) which retain pristine upper-mantle He-isotope (~7 R_A) and He–CO_2 characteristics. The extent of crustal contamination is controlled by the degree of interaction within the hydrothermal system, which increases with distance from each major volcanic center. In contrast, we propose that pristine cold CO_2 mazuku gases collected at stratigraphic contacts on the flanks of RVP volcanoes may potentially tap isolated gas pockets, which formed during previous eruptive events and have remained decoupled from the local hydrothermal system. Furthermore, by identifying and utilizing unmodified gas samples, we determine mantle versus crustal provenance of the CO_2, which we use to estimate mantle-derived CO_2 fluxes at both Rungwe and Lake Natron. Finally, we investigate the origin of the apparent discrepancy in He isotopes between fluids/gases and mafic phenocrysts at RVP (from Hilton et al., 2011), and discuss the tectonic (i.e., rift zone dynamics) and petrogenic conditions that distinguish RVP from other plume-related subaerial rift zones.

1. Introduction

There is continuing debate on the source of intra-plate volcanism along the East African Rift System (EARS). Geochemical (Ebinger et al., 1989a; Furman, 1995; Marty et al., 1996; Scarsi and Craig, 1996; Furman et al., 2004; Furman, 2007; Hilton et al., 2011) and geophysical (Burke, 1996; Ebinger et al., 1997; Nyblade et al., 2000; Park and Nyblade, 2006; Adams et al., 2012) evidence suggests EARS volcanism is associated with contributions from a single mantle plume, and that the two broadly uplifted regions of the EARS (i.e., the Ethiopian and Kenyan domes; Fig. 1A) represent surface expressions of the African Superplume, which originates at the core–mantle boundary (e.g., Ebinger and Sleep, 1998; Ritsema et al., 1999). In contrast, multiple plumes could potentially be supplying magma and volatiles to various segments of the EARS (e.g., George et al., 1998). Rogers et al. (2000) presented radiogenic isotope evidence which suggests that two distinct plumes are present under these two adjacent uplifted provinces. Another possibility is that volcanism along the EARS may be associated with several heterogeneous mantle sources, including significant upper-mantle (e.g., metasomatized subcontinental lithospheric mantle and/or depleted upper mantle) contributions. In this respect, major and trace element data (Furman, 1995) and radiogenic (Sr–Nd) isotope results from the Kenyan Dome region (e.g., Rogers, 2006; Chakrabarti et al., 2009) suggest that melts are derived from metasomatic provinces within the sub-continental lithospheric mantle (SCLM): consequently,

* Corresponding author.
E-mail address: pbarry@ucsd.edu (P.H. Barry).
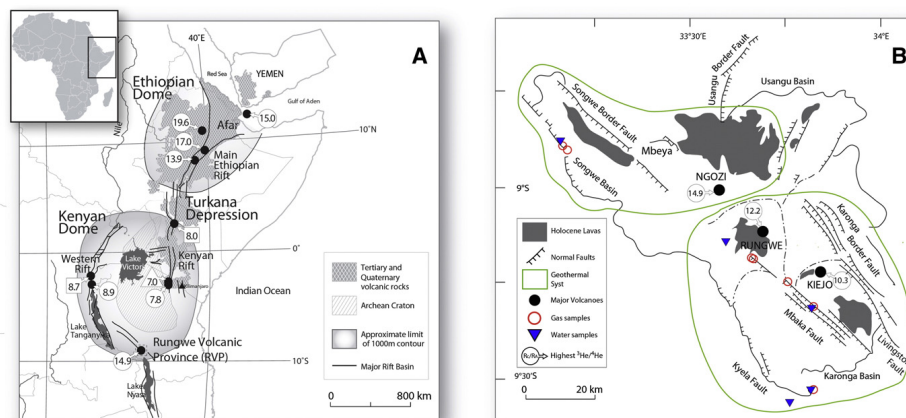
Fig. 1. A — Left: the location of the EARS (after Hilton et al., 2011). The highest reported ^{3}He/^{4}He ratios are plotted for various segments of the EARS, using circles (lavas), squares (hydrothermal fluids) and triangles (xenoliths). In the Western Rift of the Kenyan Dome region, ^{3}He/^{4}He ratios do not exceed canonical MORB values (8 ± 1 R$_A$) with the exception of high ^{3}He/^{4}He phenocryst values from RVP (Hilton et al., 2011). In addition, high He-isotopes (^{3}He/^{4}He > MORB) are observed in the Ethiopia Dome, nearly 2000 km north of RVP (Scarsi and Craig, 1996) and extend throughout the Afar region to the Gulf of Aden, Red Sea and Yemen (Marty et al., 1996). B — Right: enlarged map of RVP with sample locations, fault systems, lava outcrops, major volcanoes and the main hydrothermal systems (e.g., Ngozi-Songwe in the north, Kiejo-Mbaka in the south). Open red circles denote gas samples and blue inverted triangles represent fluids samples. For reference, the highest measured ^{3}He/^{4}He values (Hilton et al., 2011) at RVP are shown inside circles for each of the three main volcanic centers.

volcanism in this region has been largely attributed to melting in the uppermost mantle.

Helium isotopes (^{3}He/^{4}He) serve as sensitive tracers of volatile provenance and are used to differentiate between various mantle and crustal sources. The ^{3}He/^{4}He ratio of well-mixed asthenospheric upper mantle, as sampled by mid ocean ridge basalts (MORB), is uniform at 7 to 9 R$_A$ (where R$_A$ = the atmospheric ^{3}He/^{4}He ratio of 1.4×10^{-6}). Typical SCLM values are slightly lower and range from 5.2 to 7.0 R$_A$ (Gautheron and Moreira, 2002). Similarly, continental intraplate alkaline volcanics (CIAV) range from 5.3 to 6.7 R$_A$ (Day et al., 2005). In contrast, many mantle plume regions (e.g., Iceland, Hawaii, Samoa — see review by Graham, 2002) show a marked relative enrichment in ^{3}He, with values extending as high as ~50 R$_A$ (e.g., Stuart et al., 2003). Such high values are consistent with a mantle reservoir with a high time-integrated ^{3}He/(U + Th) ratio, which has remained largely undegassed since Earth's accretion. In stark contrast, continental crust is characterized by low ^{3}He/^{4}He ratios of ~0.05 R$_A$ (Morrison and Pine, 1955) due to production of radiogenic He. Large variations in ^{3}He/^{4}He ratios between mantle and continental reservoirs (>three orders of magnitude) form the basis for the utility of helium isotopes as a tracer of mantle-derived volatiles.

Helium isotopes have been extensively studied throughout the EARS: the Ethiopian Dome is marked by a large range in He-isotopes with the highest ^{3}He/^{4}He values in the EARS (up to 19.6 R$_A$) suggesting significant plume-like contributions (Marty et al., 1996; Scarsi and Craig, 1996), whereas ^{3}He/^{4}He ratios throughout the Kenyan Dome were, until recently, consistently MORB-like (8 ± 1 R$_A$) or lower, indicating an asthenospheric upper mantle or SCLM source, with crustal assimilation resulting in ^{3}He/^{4}He values well below 8 R$_A$ (Darling et al., 1995; Pik et al., 2006; Hopp et al., 2007; Fischer et al., 2009; Tedesco et al., 2010). However, Hilton et al. (2011) reported high He-isotope ratios (up to ~15 R$_A$) at RVP at the southernmost extent of the EARS. These new He-isotope data imply that mantle source(s) of volatiles at RVP, and by inference the Kenyan Dome region as a whole, are no longer constrained to the upper mantle alone.

In this contribution, we target fluids and gases at RVP – and from two locations in northern Tanzania – to characterize the regional He isotope systematics as well as C-isotope (CO$_2$) and relative abundance features. In part, our motivation is to add to the He isotope database already established for the region (Pik et al., 2006) whereby the hydrothermal fluids and gases appeared to only sample ^{3}He/^{4}He ratios equal to or less than MORB — in contrast to higher values recently measured in mafic phenocrysts at RVP (Hilton et al., 2011). In addition, we report new C-isotope (CO$_2$) values in order to ascertain the characteristics and provenance of this major volatile phase. Furthermore, by combining He and CO$_2$ measurements of the same gas/fluid samples, we are able to identify potentially complicating factors (e.g., phase separation, fluid mixing) related to utilizing hydrothermal systems versus cold CO$_2$ (mazuku-like) vents which are also found at RVP. As these cold CO$_2$ vents have He–CO$_2$ characteristics distinct from hydrothermal samples, we suggest that they may represent storage and release sites located within the volcanic stratigraphy, which are, for the most part, independent of any regional or local hydrothermal system. Finally, using the combined He–CO$_2$ approach, we are able to offer an explanation for the apparent He-isotope discrepancy observed at RVP when hydrothermal fluids and mafic phenocrysts are used independently to infer He isotope characteristics of the mantle source region.

2. Geological background

The EARS is the classic example of modern continental rifting, with extension accommodated by faulting, crustal thinning, and volcanism (e.g., Dawson, 2008). The rift stretches from the Afar Depression in northern Ethiopia/Eritrea to RVP in southern Tanzania (Fig. 1A). It crosses the Ethiopian Dome before splitting into two main branches (Western and Kenyan rifts), encircling the Tanzanian craton located on the Kenyan Dome and forming a triple junction at RVP (Delvaux and Hanon, 1993; Mnjokava, 2007). Rift initiation began in southern Ethiopia at approximately 45 Ma (George et al, 1998) and was followed by volcanism in northern Ethiopia and Yemen at approximately 30 Ma

(Schilling et al, 1992; Pik et al, 1999). Present-day magmatic occurs intermittently along the ~2000 km rift, which spans pre-rift, syn-rift, and post-rift periods. Volcanic activity at RVP dates from 8.6 Ma to the present (Ebinger et al., 1989b, 1993; Ebinger and Furman, 2003).

The geology of Tanzania is dominated by the Precambrian Tanzania Craton (>2 Ga) bounded by Proterozoic metamorphic and intrusive rocks marking the intersection of three distinct Proterozoic mobile belts: the Ubendian, Irumide, and Mozambique belts (Harkin, 1960). Inland Tanzanian basins are filled with Cenozoic sediments and volcanic rocks associated with rifting of the EARS. RVP is located directly south of the Tanzanian Craton (Fig. 1B) and covers an area of ~1500 km^2. It is located at the intersection of the Karonga, Songwe, and Usangu basins (Fig. 1) (Harkin, 1960; Delvaux and Hanon, 1993). The Karonga basin is the northernmost sub-basin of the Malawi rift (Ebinger et al., 1987), and is comprised of Precambrian basement rocks overlain by basalt, trachyte, and phonolite from the northern volcanic highlands, and by both Permian–Triassic and younger (Neogene) sediments of the Kyela lowlands. RVP consists of asymmetric half grabens which accommodate the overall WSW–ENE extension (Ebinger et al., 1989b; Iranga, 1992; Delalande et al., 2011) and NW–SE trending normal faults which are manifested in three main rift-bounding fault segments: Kyela, Mbaka and Livingstone faults (Hochstein et al., 2000) (Fig. 1B).

Late Miocene to Quaternary volcanism and associated hydrothermal activity characterize recent magmatism at RVP (Ebinger et al., 1989b). RVP is comprised of three main volcanic centers: Ngozi, which last erupted <1 ka before present (trachytic tuff); Rungwe volcano, which last erupted <1.2 ka before present (trachytic tephra); and Kiejo, which last erupted a tephrite lava flow <0.2 ka before present (tephrite lava flow) (Harkin, 1955; Ebinger et al., 1989b; Fontijn et al., 2010a, 2010b, 2011). In addition, the region hosts abundant smaller monogenic volcanoes and cinder cones located along the Mbaka fault, which were constructed during the last 0.5 Ma (Ebinger et al., 1989b; Williams et al., 1993; Fontijn et al., 2010b).

Hydrothermal activity occurs throughout RVP and is marked by abundant bubbling springs, located along streambeds and riverbanks believed to be connected to groundwater aquifers by an extensive fault network (Delalande et al., 2011). Fluids are characterized as Na–HCO$_3$ waters, with variable Ca–Mg and Cl contributions (Harkin, 1960; Hochstein et al., 2000; Branchu et al., 2005; Kraml et al., 2010; Delalande et al., 2011), and all show evidence for the degassing of CO$_2$ (Ebinger et al., 1993). Based on sample location and field observations (i.e., temperature, salinity and pH), RVP hydrothermal activity is divided into two main groups (Delalande et al., 2011):

(1) A group of cold gas-rich bubbling springs which is located at high elevations (1500–1700 m). These freshwater, Na (Ca–Mg)–HCO$_3$ type, springs display low temperatures (15 to 23 °C), are slightly acidic (pH between 5.2 and 6.7) and show intense gas bubbling. In addition, vigorously degassing cold CO$_2$ vents have also been reported on the flanks of Ngozi, Rungwe and Kiejo volcanoes (Delalande et al., 2011).

(2) A group of hot gaseous springs is located at lower elevations (500–800 m) in the Kyela plain and lies on or close to major active NW–SE faults. Spring temperatures range from 32 to 63 °C suggesting connection to low enthalpy thermal activity (Arnórsson, 2000). Waters are saline, Na–HCO$_3$(Cl) type, and display neutral to slightly basic pH (7.0–7.9) (Delalande et al., 2011). Significantly, hot springs show weaker gas activity (generally fewer/smaller bubbles, higher water flows) than the higher elevation cold springs and gas vents.

This second group of hot springs has been further sub-divided into two distinct hydrothermal systems on the basis of fluid chemistry and geographic extent (Kraml et al., 2010): (a) Ngozi-Songwe hydrothermal system, located in the NW, and (b) Kiejo-Mbaka hydrothermal system, in the south (Fig. 1B). Each hydrothermal is described in turn:

The Ngozi-Songwe hydrothermal area is located to the NW of Ngozi volcanic center and 30 km west of Mbeya (Fig. 1A). The Songwe hot spring area is located ~43 km NW of the Ngozi volcanic center and is the most thermally-active and best-studied hydrothermal area in Tanzania: its thermal output is approximately 10 MW (Hochstein et al., 2000; Kraml et al., 2010). Volcanological investigations suggest that a trachytic magma chamber of Ngozi volcano provides an ideal heat source for the region (Kraml et al., 2010). In addition, Songwe is marked by hot Na-bicarbonate springs, CO$_2$ vents and extensive travertine deposits (~150 million tons) (Kraml et al., 2010). Together, the chemical composition of the thermal waters, the CO$_2$ discharge of the springs, and the presence of travertine, indicate that Songwe hot springs mark the terminus of a concealed outflow of hot water, channeled by a confined aquifer (Hochstein et al., 2000). Tectonic investigations show that fluid flow is fault controlled. Furthermore, hydrological investigations have determined that recharge for the Songwe hydrothermal fluids occurs at elevations between 1800 and 2200 m, likely near the Ngozi volcanic summit (James, 1967; Delvaux et al., 2010; Kraml et al., 2010).

The Kiejo-Mbaka hydrothermal system encompasses both the Kiejo and Rungwe volcanic centers. Kiejo is located ~36 km NW of Lake Malawi at an elevation of approximately 2200 m (Fig. 1B). The Rungwe volcanic center is located approximately 20 km to the northwest of Kiejo and is comprised of mostly alkali-basaltic and trachytic/phonolitic rocks of Miocene to Quaternary age (Hochstein et al., 2000). The most prominent structure within the Kiejo-Mbaka hydrothermal system is the Mbaka fault, which crosscuts the volcanoes and serves as a permeable conduit for gas and hydrothermal fluid activity (Hochstein et al., 2000). Springs and gases principally emanate from sites where disconnected or recently reactivated conjugate faults cross the Mbaka fault system (Kraml et al., 2010). Fluid chemistry (i.e., Na and HCO$_3$ contents and Na/K ratios) indicates a homogenous fluid at depth (Mnjokava, 2007), with both the relatively high heat-flow and chemistry of hot springs consistent with the presence of a significant magmatic intrusion driving the system (Branchu et al., 2005).

3. Samples and analytical techniques

We sampled a total of 7 localities from the two high temperature hydrothermal systems (i.e., Ngozi-Songwe and Kiejo-Mbaka) and 4 sites of cold CO$_2$ vents/springs. In total, 20 samples (7 fluid-phase and 13 gas-phase) were collected, with duplicate (or triplicate) samples taken at 8 of the 11 localities. In addition, we sampled 3 localities (4 fluid-phase and 2 gas-phase samples) in the Oldoinyo Lengai/Lake Natron region of northern Tanzania (Table 1). All samples (n=26) were collected in evacuated 1720-glass bottles using standard sampling techniques (e.g., inverted funnel) in order to minimize possible air contamination (see Hilton et al., 2002 for details).

Within the Ngozi-Songwe hydrothermal system, 4 samples were collected from 3 distinct bubbling hot (54–71 °C) spring sites — both in and immediately adjacent to a travertine quarry located ~40 km NW of the Ngozi volcanic center (Songwe Overlook, Mesa and Quarry). A total of 4 hot (36–70 °C) spring sites were targeted in the Kiejo-Mbaka hydrothermal system: Kilambo Springs, located ~16 km S of the Kiejo volcanic center, and three springs in the Mampulo and Kasimulo springs region located ~50 km SSE of the Rungwe volcanic center.

Additionally, we collected gases from three vigorously degassing dry CO$_2$ cold (12–23 °C) vents on the flanks of Kiejo and Rungwe volcanoes, at the contact between basaltic flows and phonolitic tuff units, and one cold (20 °C) spring (Kafwira Njuni) from the flank (~9 km W) of Rungwe volcano (Harkin, 1960). The Kiejo Cold Vent sample was collected <5 km from the summit of Kiejo, close to the factory where CO$_2$ gas is commercially extracted from three shallow boreholes (Hochstein et al., 2000). Two cold CO$_2$ vents near Ikama Village (Kibila and Ikama Village

Table 1
Helium and carbon isotope and relative abundance characteristics of hydrothermal fluids and gases from RVP and northern Tanzania.

Sample location	Phase[a]	Latitude (°S)	Longitude (°E)	Elevation (m)	Distance to volcano[b] (km)	Temp (°C)	R/R_A[c]	X[d]	R_C/R_A[e]	$CO_2/^3He$ ($\times10^9$)[f]	$\delta^{13}C$ (‰)[g]	$[CO_2]$ (mmol/kg)	$[He]$ ($\mu cm^3/gH_2O$)
Rungwe Volcanic Province (RVP)													
Ngozi-Songwe hydrothermal system													
Songwe Overlook	F	08° 52′ 16.3″	33° 10′ 52.7″	1137	43 (N)	71	1.19	2.63	1.28 ± 0.05	2300	−4.37	35.0	0.222
Songwe Mesa	G	08° 52′ 23.9″	33° 10′ 52.6″	1,137	43 (N)	64	3.61	18.7	3.73 ± 0.12	35.5	−5.36	–	–
(Dup)							3.75	527	3.75 ± 0.09	22.7	−6.10	–	–
Songwe Quarry	G	08° 53′ 21.6″	33° 12′ 37.9″	1177	40 (N)	54	1.21	1.88	1.38 ± 0.07	2350	−5.92	–	–
Kiejo-Mbaka hydrothermal system													
Kilambo Springs	F	09° 21′ 43.7″	33° 49′ 01.3″	637	16 (K)	57	0.97	3.19	0.97 ± 0.09	32,200	−3.77	48.7	0.032
Kilambo Springs	G	09° 21′ 44.0″	33° 49′ 01.5″	637	16 (K)	36	3.65	85.6	3.67 ± 0.11	57.9	−5.43	–	–
Mampulo Spring #1	F	09° 33′ 01.9″	33° 47′ 49.6″	515	50 (R)	60	2.00	19.4	2.05 ± 0.10	2420	−4.81	56.4	0.341
(Dup)							2.05	28.3	2.08 ± 0.09	1680	−5.34	53.8	0.703
Mampulo Spring #2	G	09° 33′ 01.9″	33° 47′ 43.8″	523	50 (R)	55	2.20	9480	2.20 ± 0.07	3.05	−6.45	–	–
(Dup)							2.13	10,400	2.13 ± 0.07	2.94	−6.01	–	–
(Dup)							2.10	4220	2.01 ± 0.06	3.21	−6.41	–	–
Kasimulo Spring	F	09° 34′ 52.7″	33° 45′ 42.2″	520	53 (R)	52	1.04	2.48	1.06 ± 0.05	6660	−2.79	47.5	0.100
(Dup)							1.02	1.96	1.03 ± 0.06	12,200	−3.14	48.8	0.058
Cold CO_2 mazuku vents and bubbling springs													
Kafwira Njuni	F	09° 08′ 12.5″	33° 35′ 17.5″	1552	9 (R)	20	4.49	3.63	5.49 ± 0.23	320	−4.12	19.6	0.178
Ikama Village	G	09° 12′ 41.6″	33° 39′ 14.2″	1505	10 (R)	23	6.31	15.9	6.60 ± 0.12	4.53	−4.56	–	–
(Dup)							7.16	269	7.18 ± 0.13	4.46	−5.17	–	–
Kibila Cold Vent	G	09° 12′ 54.3″	33° 39′ 28.8″	1490	11 (R)	12	7.09	4950	7.09 ± 0.20	4.00	−4.24	–	–
(Dup)							7.08	298	7.09 ± 0.20	4.53	−3.89	–	–
Kiejo Cold Vent	G	09° 15′ 03.8″	33° 45′ 43.2″	1504	4 (K)	15	6.12	870	6.12 ± 0.17	3.85	−4.43	–	–
(Dup)							6.61	2570	6.61 ± 0.11	5.34	−4.96	–	–
Northern Tanzania (Lengai/Lake Natron)													
Lake Natron #2	F	02° 23′ 23.2″	35° 53′ 50.9″	620	–	50	0.64	5890	0.64 ± 0.02	1.53	−4.02	15.1	300
(Dup)							0.67	12, 800	0.67 ± 0.02	0.48	−4.42	16.2	724
Lake Natron #1	F	02° 22′ 14.2″	35° 54′ 17.7″	608	–	51	0.63	7170	0.63 ± 0.02	1.12	−4.92	15.1	209
(Dup)							0.61	5510	0.61 ± 0.02	1.21	−3.70	17.4	331
Lengai North Crater	G	02° 45′ 22.6″	35° 54′ 41.2″	2827	–	70	6.76	6530	6.77 ± 0.16	2.60	−2.43	–	–
(Dup)							70	6.87	1210	6.88 ± 0.20	2.91	−2.77	–	–

All reported errors are at the 1sigma level.
[a] Fluid (F), Gas (G).
[b] Volcanic center: (N) = Ngozi, (K) = Kiejo, (R) = Rungwe.
[c] R/R_A is measured $^3He/^4He$ ratio divided by the $^3He/^4He$ in air = 1.4×10^{-6}.
[d] X-value (gas) = $(^4He/^{20}Ne)_{measured}/(^4He/^{20}Ne)_{air}$. X-value (fluid) = $(^4He/^{20}Ne)_{measured}/(^4He/^{20}Ne)_{air}\times(\beta_{Ne}/\beta_{He})]$, where β = Bunsen solubility coefficient. For pure water at 15 °C (β_{Ne}/β_{He}) = 1.22 (Weiss, 1971). See Hilton (1996) for further details of the correction protocol.
[e] R_C/R_A is the air corrected He isotope ratio = $[(R/R_A\times X)-1]/(X-1)$.
[f] Accuracy is estimated to be better than 5%.
[g] Accuracy is ±0.5‰.

samples), located <9 km from the summit of Rungwe volcanic center, were also sampled. All three cold CO_2 vent features show remarkable similarities to "mazuku", previously described along parts of the western branch of the EARS, in the Goma region of the Democratic Republic of Congo (Smets et al., 2010). Mazuku means "evil-wind" in Swahili and is used to describe lowland (depressions) where CO_2 is released to the atmosphere. Being heavier than air, CO_2 can accumulate in depressions at high and often lethal levels (Tuttle et al., 1990; Smets et al., 2010). Notably, mazuku from the Lake Kivu region (western branch of EARS) display mantle helium isotope values and have thus been unambiguously linked to an upper-mantle source (Tedesco et al., 2010). These cold CO_2 mazuku-like vents are grouped with Kafwira Njuni cold spring in Table 1 as they share low temperatures (<23 °C); however, it is not obvious that they are related to localized hydrothermal systems (see Section 5.3).

Finally, three northern Tanzania sites were sampled (Table 1). The hyper-saline Lake Natron is located towards the southern end of the Kenyan Rift, about 45 km north of Oldoinyo Lengai volcano, and discharges numerous warm springs (32–52 °C) along the shoreline (Hochstein et al., 2000). Two warm springs located along a shoreline scree slope were sampled. Additionally, we collected moderate temperature gases (~70 °C) from a fumarole on the outer summit crater wall of Oldoinyo Lengai volcano at an elevation ~2800 m. Details on sampling locations – latitude, longitude, elevation and distance to nearest volcanic edifice – are included in Table 1.

Helium, Ne and CO_2 were extracted from all samples at the Fluids and Volatiles Laboratory, Scripps Institution of Oceanography (SIO), using a dedicated UHV purification line (see Kulongoski and Hilton, 2002 for description). Following sample inlet into the vacuum system, waters were acidified with phosphorus pentoxide to ensure complete release of CO_2; consequently, CO_2 amounts represent the total dissolved inorganic carbon (TDIC) content. Water vapor was isolated on a water-trap held at −78 °C (cooled using a slurry of acetone and dry-ice). Subsequently, CO_2 was frozen onto a liquid nitrogen cooled U-tube. The remaining light noble gases (He and Ne) were then isolated using a hot (700 °C) Ti-getter and charcoal finger held at liquid nitrogen temperature, which acted to remove active gases (N_2, CO, and CH_4) and heavy noble gases (Ar, Kr and Xe), respectively. A calibrated fraction of the He and Ne gas was captured in an AR-glass breakseal for transfer to a MAP-215 noble gas mass spectrometer. Finally, the CO_2 fraction was transferred to a Pyrex breakseal for transfer to a dedicated CO_2 cleanup line.

The He and Ne gas fraction was released from the breakseal and prepared for inlet into the MAP-215 mass spectrometer using a combination of charcoal traps held at liquid nitrogen temperature and active-gas getters. Following this initial clean-up, a helium-cooled cryogenic trap was used to separate He from Ne, which were inlet sequentially into the mass spectrometer. The measured $^3He/^4He$ ratio of the sample was normalized to standard aliquots of air run before and after each sample analysis.

The carbon dioxide (CO_2) sample fraction was transferred to a secondary clean-up and quantification line, constructed from Pyrex glass, where CO_2 and any sulfur-bearing species (if present) were separated using a variable temperature trap. Following clean-up, the total amount of CO_2 was measured using a capacitance manometer in a calibrated volume. The manometrically-derived CO_2 abundance was then combined with the mass spectrometer-derived $^3He/^4He$ value and helium abundance to calculate the $CO_2/^3He$ ratio. Following manometric measurement, CO_2 was again frozen into a Pyrex tube for transfer to a Thermo Finnigan Delta XP$_{plus}$ isotope ratio mass spectrometer for carbon isotopic ($\delta^{13}C$) analysis. δ^{13} (CO_2) values are reported relative to the international reference standard Vienna Pee Dee Belemnite (VPDB) and have a precision of less than 0.1‰. We estimate the accuracy of our $\delta^{13}C$ determinations (± 0.5‰) by repeat analyses of a working laboratory standard, itself calibrated relative to VPDB.

4. Results

4.1. Helium isotopes ($^3He/^4He$ ratios)

Helium isotope results ($^3He/^4He$ ratios = R) are reported relative to air (R_A) (where R_A = atmospheric $^3He/^4He = 1.4 \times 10^{-6}$) and corrected for the presence of atmospheric He (to R_C/R_A). By monitoring sample $^4He/^{20}Ne$ ratios, and assuming all sample ^{20}Ne is derived from air or air saturated water, the atmospheric He contribution can be calculated and subsequently subtracted from the measured value. The air–He correction is based on known $^4He/^{20}Ne$ values of air or air saturated water (adjusted for He and Ne solubility variations in water – assuming a recharge temperature of 15 °C – for fluid samples only) (Ozima and Podosek, 1983; Hilton, 1996). Relative $^4He/^{20}Ne$ enrichments versus air are expressed as X-values (where $X = (He/Ne)_S/(He/Ne)_A$). X-values vary by over 4 orders of magnitude in RVP and northern Tanzania samples (Fig. 2) and are markedly higher in gas-phase versus fluid phase samples. We note the following two general features of the helium data: (a) duplicate samples (i.e., same phase and locality) are in excellent agreement and deviate by less than 0.2 R_A for all samples except Ikama Village, where duplicates vary by 0.58 R_A, and (b) fluid-phase samples display lower $^3He/^4He$ values than gas-phase samples from the same site.

At RVP, helium isotope ratios cover a wide range (0.97 R_A to 7.18 R_A), and are in good agreement with earlier reports of He isotopes (0.22 R_A to 7.76 R_A) from the region (Pik et al., 2006) (Fig. 3). For

example, we report a $^3He/^4He$ value of 7.2 R_A from Ikama Village, in good agreement with that reported by Pik et al. (2006). In detail, we point out the following salient features of the air-corrected He isotope results:

1. Cold CO_2 mazuku vents range from 6.1 to 7.2 R_A with the cold fluid-phase sample from Kafwira Njuni having a $^3He/^4He$ value of 5.5 R_A. These ratios are consistently the highest values in this study.
2. Localities in the Kiejo-Mbaka hydrothermal system range in $^3He/^4He$ from 0.97 (fluid phase at Kilambo Springs) to 3.67 R_A (corresponding gas phase at the same locality). Mampulo Spring samples (2 locations) range from 2.0 to 2.2 R_A whereas Kasimulo Spring fluids overlap with the atmospheric value (1 R_A) within analytical uncertainty.
3. In the Ngozi-Songwe hydrothermal system, $^3He/^4He$ ratios at Songwe range from 1.3 (fluid phase) to 3.75 R_A and display evidence for both mantle and radiogenic contributions to the total He inventory.
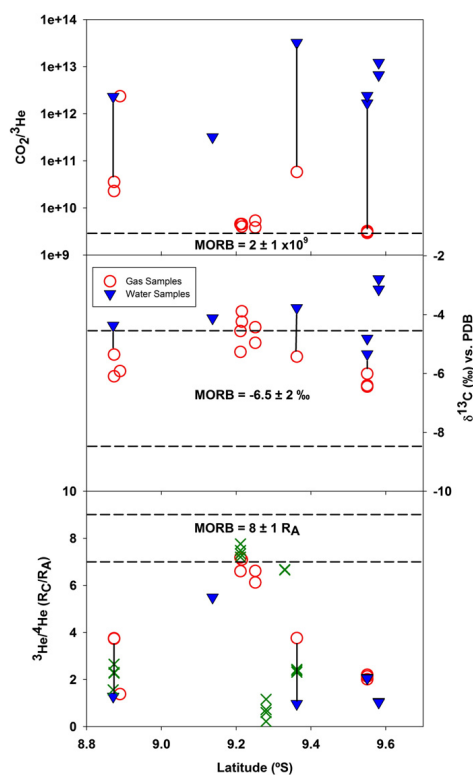
Fig. 3. Helium and carbon isotope ($^3He/^4He$ — corrected for air and given in R_C/R_A notation; $\delta^{13}C$) and relative abundances ($CO_2/^3He$) plotted versus latitude for all 11 RVP localities sampled. Open red circles represent gas-phase samples and solid blue triangles represent fluid-phase samples. In addition, hydrothermal fluid He-isotopes (from Pik et al., 2006) are shown (green X's). Vertical tie-lines connect gas and fluid phase samples from the same locality. Horizontal dashed lines delineate typical MORB ranges for carbon and helium isotopes. (For interpretation of the references to color in this figure legend, the reader is referred to the web of this article.)

Fig. 2. He-isotopes versus $^4He/^{20}Ne$ data for hydrothermal fluids (blue inverted triangles) and gases (red open circles) from RVP. Data are shown with previously reported hydrothermal fluid data (green X's) from Pik et al. (2006). Calculated binary mixing lines between air saturated water (ASW), crustal and mantle endmember compositions are shown. Endmembers are: ASW $^3He/^4He = 1$ R_A, $^4He/^{20}Ne = 0.250$–0.285; (Ozima and Podosek, 1983), High $^3He/^4He = 14.9$ R_A, (Hilton et al., 2011), MORB $^3He/^4He = 8$ R_A, (Graham, 2002), SCLM $^3He/^4He = 6.1$ R_A, (Gautheron and Moreira, 2002) Crustal $^3He/^4He = 0.05$ R_A (Morrison and Pine, 1955): in the latter 4 cases a $^4He/^{20}Ne$ ratio ~3500 is assumed. (For interpretation of the references to color in this figure legend, the reader is referred to the web of this article.)

We also note that there is a distinct peak in ^{3}He/^{4}He values at 9.2°S (Fig. 3), which is associated with the location of the cold CO_2 mazuku vents (Ikama Village, Kibila and Kiejo Cold Vent samples) near the termination of the Mbaka fault system in the central region of the Kiejo-Mbaka hydrothermal system. In summary, the most prominent characteristic of RVP helium isotope results is that all samples are characterized by a mantle-derived contribution (Section 5.4). The highest values fall at the lower end of the range normally associated with mid-ocean ridge basalt (MORB) helium (8 ± 1 R_A) whereas the lowest ratios, although having a large proportion of radiogenic helium, are still well above the radiogenic He production ratio (0.05 R_A) (Morrison and Pine, 1955).

In addition, we report ^{3}He/^{4}He values for northern Tanzania samples (Lake Natron and Oldoinyo Lengai). Lake Natron springs cluster tightly between 0.61 to 0.67 R_A, showing a strong radiogenic He signal. In contrast, the Oldoinyo Lengai fumarole has a ^{3}He/^{4}He ratio of 6.88 R_A, in good agreement with fumaroles sampled in 2005 (~6.86 R_A; Fischer et al., 2009) prior to the 2007 eruptive events.

4.2. Carbon isotopes ($\delta^{13}C$ (CO_2))

C-isotopes ($\delta^{13}C$) range from −2.8 to −6.5‰ (versus VPDB) at RVP and from −2.4 to −4.9‰ (versus VPDB) in northern Tanzania, with all values falling within or slightly higher than the range normally associated with MORB (-6.5 ± 2‰) (Sano and Marty, 1995). Agreement between duplicate samples is at the level of ~1.2‰ or less.

The Ngozi-Songwe hydrothermal system C-isotope compositions range from −4.4 to −6.1‰, with overlap (within uncertainty) between the Mesa and Quarry localities. The range of $\delta^{13}C$ values is much greater for the Kiejo-Mbaka hydrothermal system with the highest $\delta^{13}C$ value (−2.8‰) observed at Kasimulo springs, in a fluid sample with a ^{3}He/^{4}He value overlapping with air, and the lowest $\delta^{13}C$ value (−6.5‰) measured in a gas-phase sample from Mampulo Springs #2 with a higher ^{3}He/^{4}He ratio (2.2 R_A) and negligible air addition (X = 9475).

The cold gas vents range from −3.9 to −5.2‰ with the single fluid phase sample (Kafwira Njuni) having an intermediate value (−4.1‰). Three localities at RVP have both fluid and gas-phase samples with $\delta^{13}C$ data (see samples connected by tie-lines in Fig. 3). In each case, carbon isotope values were significantly higher in the fluid phase. Unlike He-isotopes, there is no clear latitudinal control on the range of ($\delta^{13}C$) values (Fig. 2).

At Lake Natron, $\delta^{13}C$ values fall between −4.9 and −3.7‰ with duplicate values in good agreement and overlapping within uncertainty at location #2. The Oldoinyo Lengai fumarole $\delta^{13}C$ values are higher than at Natron (−2.3 to −2.8‰) and again overlap within analytical uncertainty (0.5‰). They fall within the range of values reported for summit fumaroles collected in 2005 (Fischer et al., 2009).

4.3. CO_2/^{3}He ratios

The elemental CO_2/^{3}He ratio varies over 4 orders of magnitude in RVP samples, from ~3×10^9 (MORB-like) to higher values (~3×10^{13}) normally associated with crustal lithologies (O'Nions and Oxburgh, 1988). By comparison, northern Tanzania samples span a more limited range, extending from 5×10^8 to 3×10^9, at the MORB range or lower.

The Ngozi-Songwe hydrothermal system CO_2/^{3}He values range from 22.7 to 2350 ($\times 10^9$), with good agreement of low values, 23 and 36 ($\times 10^9$), at the Mesa locality and between the Overlook and Quarry sites (2300 and 2350) ($\times 10^9$). Kiejo-Mbaka hydrothermal system CO_2/^{3}He values span a greater range, with values falling between 2.94 and 32,200 ($\times 10^9$). Several gas samples at Mampulo Springs have CO_2/^{3}He values that fall within the MORB-range ($2 \pm 1 \times 10^9$; Marty and Jambon, 1987) whereas all other samples (i.e., both fluid and gas phases) are significantly higher.

Cold CO_2 mazuku vent CO_2/^{3}He values are consistently low, between 3.85 and 5.34 ($\times 10^9$) whereas the cold fluid-phase sample (Kafwira Njuni) has a CO_2/^{3}He value of 320 ($\times 10^9$). In general, fluid samples at RVP have significantly higher CO_2/^{3}He values, ranging from 3.2×10^{11} to 3.2×10^{13}, compared with the range in corresponding gas samples (3×10^9 to 2×10^{12}). The three localities where both fluid and a gas samples were collected display much higher CO_2/^{3}He ratios in the fluid-phase samples (see samples with tie-lines in Fig. 3), indicating that the fluids may reflect modified CO_2/^{3}He characteristics (see Section 5.2 for discussion).

At Lake Natron, the CO_2/^{3}He values are consistently low, with values between 4.8×10^8 and 1.5×10^9. Whereas there is poor agreement for site #2 samples, this is not the case for site #1 where values are 1.1 and 1.2 ($\times 10^9$). Such low values are unusual given the low ^{3}He/^{4}He ratios at these localities indicative of a significant crustal (radiogenic) He input: this observation may reflect loss of CO_2 (Section 5.2.2). The CO_2/^{3}He values at Oldoinyo Lengai fall within the MORB range and are slightly lower than values published previously for summit fumaroles (Fischer et al., 2009).

5. Discussion

In the following discussion, we investigate processes that could affect regional hydrothermal ^{3}He/^{4}He values (and associated He–CO_2 characteristics) and thus lead to the discrepancy in helium isotopes between fluids and phenocrysts. Our approach is to identify samples that exhibit ^{3}He/^{4}He, CO_2/^{3}He and $\delta^{13}C$ values representative of the mantle source region versus those whose features have been modified by other processes (i.e., magmatic and/or hydrothermal-related). In this way, volatile signatures can be utilized to understand the nature of mantle sources. A corollary of this approach allows us to focus on the He–CO_2 systematics of the three cold CO_2 mazuku-like features in the region and assess their role in transferring mantle-derived volatiles to the surface. Finally, we address the factors behind the apparent He-isotope discrepancy observed between mafic crystals of RVP lavas and tephra (Hilton et al., 2011) and geothermal gases/fluids (this work) which is conspicuously absent at other plume-related localities such as Iceland (Hilton et al., 1990).

5.1. Observed CO_2–^{3}He–^{4}He characteristics

To evaluate sample integrity (gases versus fluids), particularly regarding possible elemental fractionation effects between He and CO_2, we plot all RVP samples (n = 20) and the northern Tanzanian samples (n = 6) on a CO_2–^{3}He–^{4}He ternary diagram (Fig. 4; after Giggenbach et al., 1993). For reference, we include mixing lines showing binary mixing between mantle ^{3}He/^{4}He endmembers (e.g., SCLM = 6.1 ± 0.9 R_A (Gautheron and Moreira, 2002); MORB = 8 ± 1 R_A (Graham, 2002); high ^{3}He/^{4}He (RVP) = 15 ± 1 R_A (Hilton et al., 2011), crustal values (~0.05 R_A) (Shaw et al., 2003) and/or pure radiogenic ^{4}He. In the case of CO_2/^{3}He endmembers, we adopt values of 2 ± 1 ($\times 10^9$) for MORB-mantle (Marty and Jambon, 1987), 4 ± 2 ($\times 10^9$) for SCLM (Hahm et al., 2008; Fischer et al., 2009), assuming that Oldoinyo Lengai volcano in northern Tanzania with ^{3}He/^{4}He ratios <7 R_A represents this component, and 10^{13} for the crustal endmember (O'Nions and Oxburgh, 1988).

In Fig. 4, we note the following features with respect to the gas phase samples from RVP:

(1) All six cold gas (mazuku) vents (e.g., duplicate samples from Kibila Cold Vent, Ikama Village and the Kiejo Cold Vent) plot within the range of MORB/SCLM ^{3}He/^{4}He values (8 ± 1 R_A and 6.9 ± 0.9, respectively; Graham, 2002; Gautheron and Moreira, 2002) and SCLM-like CO_2/^{3}He ($4 \pm 2 \times 10^9$) values (Hahm et al., 2008; Fischer et al., 2009).

(2) three additional gas samples (all from Mampulo Spring #2) fall
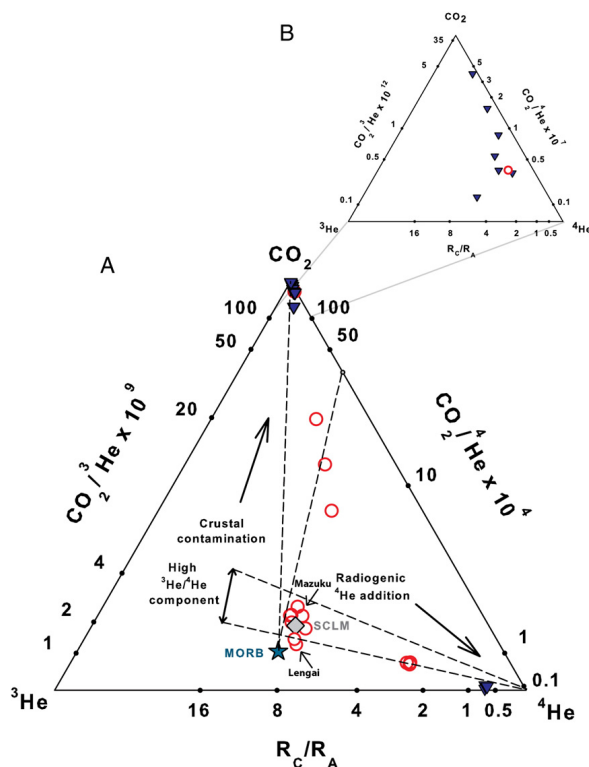
Fig. 4. A — Ternary plot of CO_2, ^3He, and ^4He for gas (open red circles) and fluid samples (blue triangles) from RVP and northern Tanzania, illustrating the effects of crustal and radiogenic contamination of mantle-like volatiles. For reference, we plot "mantle average" (MORB = 8 ± 1 R_A) with a turquoise star (Marty and Jambon, 1987), sub-continental lithospheric mantle (SCLM = 6.1 ± 0.9 R_A) with a grey diamond (Gautheron and Moreira, 2002) and "high $^3He/^4He$ component" ($CO_2/^3He = 3–6 \times 10^9$ after Poreda et al., 1992; Marty and Tolstikhin, 1998; $^3He/^4He = 14.9$ R_A after Hilton et al., 2011). All gas samples fall on or are close to a binary mixing trajectory between upper mantle-like (MORB; SCLM) helium and variable amounts of crustal contamination (calculated from $CO_2/^3He = 5–50 \times 10^{12}$; $^3He/^4He = 0.05$ R_A) (Shaw et al., 2003) and/or air. Fluid samples of RVP display much higher $CO_2/^3He$ (3.2×10^{11} to 3.2×10^{13}) and helium isotope values compared with northern Tanzania fluid samples (i.e. Lake Natron) which display both low $CO_2/^3He$ ($<2 \times 10^9$) and helium isotope values. As a result, RVP fluid samples plot close to the CO_2 apex whereas Lake Natron samples plot close to the ^4He apex. B — Ternary plot of CO_2, ^3He, and ^4He, with different scale axes focused on the CO_2 apex in order to show fluid-phase samples from RVP. Fluid samples of RVP display much higher $CO_2/^3He$ (3.2×10^{11} to 3.2×10^{13}) and lower helium isotope values compared RVP gas samples. (For interpretation of the references to color in this figure legend, the reader is referred to the web of this article.)

on the mixing line between mantle endmembers and radiogenic ^4He.

(3) the four remaining gas samples, three from the Ngozi-Songwe (Mesa and Quarry localities) and one from Kiejo-Mbaka (Kilambo Springs), plot on a trajectory extending from mantle values of ~6–8 R_A towards the CO_2 apex (i.e., high $CO_2/^3He$). This relationship is compatible with mixing between crustal and mantle endmembers.

Therefore, we conclude that there is significant mantle-derived helium, and by inference mantle CO_2, present in all RVP gas-phase samples. Notably, the six relatively unmodified (mantle-like) samples are all cold CO_2 mazuku-like vents, and thus plot close to the MORB/SCLM value in Fig. 4A. However, all additional gas samples can be explained by a mantle-like source composition, and subsequent mixing with crustal components. In Section 5.4 we use mixing models to calculate relative (%) mantle and crustal contributions.

Another feature of the RVP dataset (Fig. 4A) is the marked disparity in elemental ratios (e.g. $CO_2/^3He$) between fluid and gas-phase samples. Fluid and gas-phase $CO_2/^3He$ ratios range from ~10^9 to ~10^{13}; however, all fluid-phase samples display relatively high $CO_2/^3He$ ratios ($>10^{11}$) consistent with significant elemental fractionation between the two volatile species — most likely resulting from hydrothermal degassing and/or solubility controlled phase-separation (see Section 5.2). As a result, all RVP fluid samples plot in a cluster close to the CO_2 apex. In order to identify and interpret fluid variations, a second ternary diagram, with a contracted scale, is shown (Fig. 4B). Notably, the majority of fluid-phase samples displays significantly lower $^3He/^4He$ values compared to gas-phase samples, suggesting that fluid samples contain more radiogenic (crustal) helium. Thus, we conclude that fluids are

more susceptible to radiogenic ^{4}He additions, particularly following volatile depletion induced by phase-separation. These processes are discussed in detail in Section 5.2.

We also plot the northern Tanzania samples (n=6) in Fig. 4A and note that Oldoinyo Lengai samples (n=2) overlap, and help define, the SCLM endmember values, plotting close to the mazuku vents. In contrast, Lake Natron waters (n=4) display significantly lower $CO_2/^3$He values ($<2\times10^9$) compared with RVP fluids ($>10^{11}$), indicating that a process acting to decrease $CO_2/^3$He values has extensively modified them. In the next section, we investigate the effects of CO_2 loss due to calcite precipitation as a means to lower $CO_2/^3$He ratios for these Lake Natron samples.

5.2. Potential fractionation processes

Phase separation within a hydrothermal system can potentially fractionate both elemental (i.e., $CO_2/^3$He) and isotope (i.e., δ^{13}C) ratios. Phase-partitioning can be caused by either vapor/steam separation at high temperatures (>100 °C) and/or gas exsolution due to supersaturation of a particular gas species. In both cases, elemental fractionation can occur between CO_2 and He due to the greater solubility of CO_2 in aqueous solution relative to helium (Ellis and Golding, 1963; Weiss, 1971). Solubility experiments indicate that CO_2 is ~42 times more soluble than He in water at temperatures up to 100 °C (Ellis and Golding, 1963; Stephen and Stephen, 1963; Ozima and Podosek, 1983): therefore, helium partitions preferentially into the vapor phase relative to CO_2. As a result, gas-phase $CO_2/^3$He ratios will represent a minimum estimate of the original (starting) ratio and fluid samples containing residual volatiles would be expected to have higher $CO_2/^3$He values. Phase-separation can also cause isotopic fractionation as the partitioning of CO_2 between water vapor and liquid induces fractionation between $^{13}CO_2$ and $^{12}CO_2$ (Vogel et al., 1970; Mook et al., 1974; van Soest et al., 1998; Ray et al., 2009) with $^{13}CO_2$ being relatively depleted in the vapor phase at temperatures <110 °C.

Notably, the lowest $CO_2/^3$He values from RVP are observed in cold CO_2 mazuku vents on the flanks of the Rungwe and Kiejo volcanoes, falling within error of the typical MORB $CO_2/^3$He range (e.g., $2\pm1\times10^9$) (Marty and Jambon, 1987), whereas fluid samples extend upwards over several orders of magnitude. If we assume a mantle-like starting composition (~2×10^9) then the absence of lower values at RVP implies that processes such as magma degassing prior to eruption and/or calcite precipitation – processes that act to lower $CO_2/^3$He in residual volatiles (Ray et al., 2009) – cannot have a marked effect. However, we note that extensive travertine deposits are found at RVP (particularly the Songwe region) indicating that, at this locality at least, calcite precipitation may have an effect on $CO_2/^3$He values. To further assess the potential effects of phase-separation and/or calcite precipitation on RVP fluid samples, we consider the relationship between volatile (He and CO_2) content and $CO_2/^3$He ratios in order to identify possible links between extreme $CO_2/^3$He values and low concentration fluid samples (following Van Soest et al., 1998) .

5.2.1. Effects of hydrothermal phase-separation: $CO_2/^3$He

$CO_2/^3$He versus helium concentration $[He]_C$ (μcm^3 STP/g H$_2$O) for all fluid samples from RVP and northern Tanzania is plotted in Fig. 5A. Fluid samples with <0.1 $[He]_C$ μcm^3 STP/g H$_2$O clearly display the highest measured $CO_2/^3$He values. Furthermore, all fluid samples display significantly higher ($>10^{11}$) $CO_2/^3$He compared to corresponding gas-phase samples. For example, two of the four samples with >0.1 $[He]_C$ μcm^3 STP/g H$_2$O have corresponding gas-phase samples (collected from the same locality) with (significantly lower) $CO_2/^3$He ratios, which fall within the MORB range.

5.2.2. Effects of calcite precipitation: $CO_2/^3$He

In Fig. 5B we plot $CO_2/^3$He versus $[CO_2]$ content and note that the cold Kafwira Njuni (Rungwe) sample displays the lowest $[CO_2]$ content
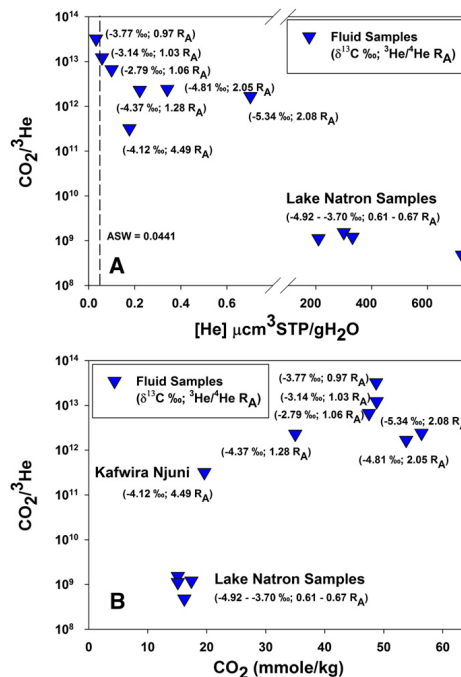
Fig. 5. A — $CO_2/^3$He versus $[He]_C$ μcm^3 STP/g H$_2$O for all RVP and Lake Natron fluid samples. The three lowest $[He]$ content samples display the highest $CO_2/^3$He ratios. Notably, the three samples with the highest $CO_2/^3$He values also display the three highest δ^{13}C values among RVP samples. As a result, we attribute both elemental and isotope fractionation processes at RVP to solubility controlled phase-separation within the hydrothermal system (see Section 5.2). B — $CO_2/^3$He versus CO_2 (mmol/kg) for all RVP and Lake Natron fluid samples. The lowest $[CO_2]$ content samples are from Lake Natron and display the lowest $CO_2/^3$He values, suggesting that CO_2 loss due to calcite precipitation may be responsible for the low $CO_2/^3$He values observed in this region. However, there is no clear correlation between $CO_2/^3$He and $[CO_2]$ content with the remaining RVP samples, indicating that CO_2 loss does not significantly affect RVP $CO_2/^3$He values.

as well as the lowest $CO_2/^3$He value at RVP. However, no clear correlation exists between these two parameters for the remaining RVP fluid samples suggesting that calcite precipitation, which should act to lower $CO_2/^3$He in the residual water phase, is not pervasive throughout RVP. Importantly, the observation that all fluid $CO_2/^3$He values at RVP are significantly higher than canonical mantle values indicates that phase partitioning is the likely primary process responsible for the observed $CO_2/^3$He variations. In contrast, northern Tanzania fluid samples from Lake Natron all display low $[CO_2]$ contents together with low $CO_2/^3$He values which lie within or below the canonical mantle range ($2\pm1\times10^9$). The only plausible mechanism to lower $CO_2/^3$He ratios is CO_2 loss due to calcite precipitation as any additions of crustal volatiles – consistent with the low ^{3}He/^{4}He ratios at Lake Natron – would act to increase values.

5.2.3. Fractionation effects on helium (^{3}He/^{4}He) and carbon isotopes (δ^{13}C)

Here, we consider the effects of phase partitioning and calcite precipitation on the carbon and helium isotope systematics. We note that all fluid samples display higher carbon isotope ratios (-2.79 to -3.77‰) relative to corresponding gas-phase samples

(-5.36 to -6.45‰) collected at the same locality (Fig. 3). Moreover, the three highest measured $\delta^{13}C$ values occur in the fluid-phase of the three most extremely fractionated and helium poor samples (i.e., those with the highest $CO_2/^3He$ and lowest $[He]_C$ μcm^3 STP/g H_2O) (Fig. 5A). These $\delta^{13}C$ variations are consistent with experimentally-determined isotopic ($^{13}C/^{12}C$) fractionation factors at low (<60 °C) temperatures, with ^{13}C being relatively depleted in the vapor phase (Vogel et al., 1970). At temperatures up to ~110 °C, the C isotope fractionation factor between vapor and liquid is greater than unity (i.e. ($\alpha^{13}C_{vapor-liquid} > 1$) (Mook et al., 1974; Zhang et al., 1995; Szaran, 1997): all RVP samples have discharge temperatures below this temperature-threshold and display $\delta^{13}C$ values consistent with phase separation within the hydrothermal system.

Finally, we note that fluid-phase samples generally display lower He-isotope ratios relative to gas-phase samples. For example, at the three localities where both fluid and gas-phases samples were collected, two of the three fluid-phase samples (e.g., Songwe and Kilambo Springs) displayed significantly lower $^3He/^4He$ ratios versus the corresponding gas-phase sample, with the third sample (i.e., Mampulo Spring) displaying overlapping $^3He/^4He$ values between the two phases. Furthermore, we note that Songwe and Kilambo Springs are among the most volatile depleted (i.e., He-poor) fluid samples whereas the Mampulo Spring samples are the most volatile enriched RVP fluid samples. Therefore, we suggest that lower $^3He/^4He$ ratios are observed in fluid-phase samples because they are more susceptible to record radiogenic (crustal) additions of helium due to lower volatile concentrations following phase-separation. If a significant portion of the intrinsic magmatic volatile signature is lost to the vapor phase, small additions of radiogenic ^4He can drastically reduce the $^3He/^4He$ ratio of any He residual in the water phase.

In summary, the effect of hydrothermal phase-separation has significantly altered the He–CO$_2$ characteristics of all fluid-phase samples, resulting in extremely high $CO_2/^3He$ values ($>3 \times 10^{11}$) due to preferential helium loss from the fluid-phase. Therefore, gas-phase samples are considered most representative of magmatic sources at RVP, and are thus able to provide greater insight into primary mantle source characteristics.

5.3. Crustal-mantle mixing

In this section, we use both gas and fluid phase results to illustrate the effects of crust–mantle mixing on the He isotope systematics and to further demonstrate that gas phase samples possess the most representative signature of the mantle source. We consider a variety of factors, such as proximity to volcanic center, elevation and temperature constraints, which may act individually or together to control the extent of crust–mantle interaction.

5.3.1. Crustal–mantle mixing: proximity to volcanic center

In Fig. 6 we plot sample temperature and sampling locality elevation as well as distance from the nearest volcanic edifice versus the helium isotope ($^3He/^4He$) composition. The highest proportions of magmatic volatiles (i.e., highest $^3He/^4He$ ratios) are found at the cold CO_2 mazuku vents (Fig. 6A), on the flanks of Kiejo and Rungwe volcanoes, with $^3He/^4He$ ratios systematically decreasing with increasing distance from the volcanic edifice ($R^2 = 0.68$) (Fig. 6C). Similar spatial patterns of $^3He/^4He$ versus distance from volcano summits have been reported previously for hydrothermal fluids at volcanoes worldwide (e.g., Sano et al., 1984; Marty et al., 1989; Hilton et al., 1993; Van Soest et al., 1998). These results suggest that high elevation cold mazuku vents (Fig. 6B), collected relatively close to the summits (<11 km), derive their volatiles from a MORB-like or SCLM source and that they have remained unmodified by extraneous volatile additions. In contrast, more distally-located hydrothermal samples from both Ngozi-Songwe and Kiejo-Mbaka hydrothermal systems have been affected by additions of radiogenic He (Fig. 4A), likely due to
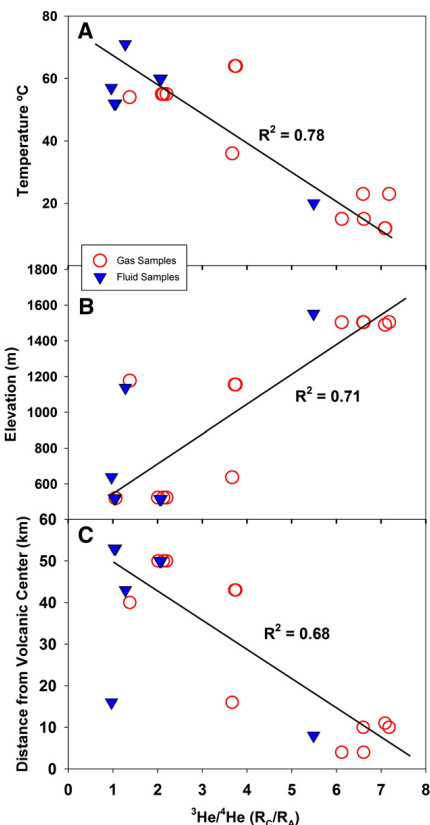
Fig. 6. He-isotopes versus distance from volcanic edifice (km) (6A), elevation (m) (6B), and temperature (°C) (6C) for fluid (blue triangles) and gas (red open circles) samples of RVP. Both fluid and gas phase samples are considered as He-isotopes are not affected by modification processes such as phase separation. Notably the highest measured (MORB-like) $^3He/^4He$ ratios are from the highest elevation and lowest temperature $CO2$ mazuku vent samples found in close proximity to volcanic centers. (For interpretation of the references to color in this figure legend, the reader is referred to the web of this article.)

more extensive interaction with ^4He-rich basement rock during deep circulation of fluids in the hydrothermal system.

5.3.2. Crustal–mantle mixing: temperature-helium isotope relationships

The most pristine, mantle-like, $^3He/^4He$ values at RVP occur in the low temperature CO_2 mazuku gas vents (Fig. 6A) found in close proximity to topographic highs on the flanks of Rungwe and Kiejo volcanoes (Fig. 6B). Indeed, the coldest gas sample of this study (Kibila Cold Vent; T = 12 °C) has the second highest $^3He/^4He$ value (7.09 R$_A$). This observation can be contrasted with the Songwe Overlook sample which is the hottest fluid sampled (T = 71 °C) yet possess one of the lowest $^3He/^4He$ values measured in this study. Surprisingly, therefore, the highest $^3He/^4He$ samples are associated with the lowest sample temperatures (12–23 °C) – in some cases, lower than ambient air temperatures.

In general, the occurrence of magmatic helium in high enthalpy hydrothermal samples implies a direct transfer of heat and helium between magmatic and hydrothermal systems (e.g., Torgersen and Jenkins, 1982). In the case of RVP, however, the temperature-helium relationships indicate that heat and (magmatic) volatile transfer are apparently inversely related and potentially decoupled. Indeed, the lowest temperature (mazuku) samples have the highest ^{3}He/^{4}He values. We suggest two hypotheses to explain this observation:

(1) Low temperatures in gas-phase samples result from a combination of geothermal gradient cooling at higher elevations (~18.3 °C/km) (Tiab and Donaldson, 2011), conductive cooling associated with colder meteoric-water recharge temperatures at higher elevations (Delalande et al., 2011; de Moor et al., this volume), and possibly adiabatic expansion and rapid cooling of gases during release to the surface. Adiabatic cooling is supported by our field observation that the coldest (~12 °C) mazuku gases (Kibila Cold Vent) display the most vigorous degassing rates. A combination of these three processes near volcanic centers could act to transfer relatively unmodified magmatic volatiles to surface manifestations while effectively dampening corresponding heat transfer.

(2) Alternatively, low temperature gas-phase (mazuku) vents are completely decoupled from the hydrothermal systems at RVP and thus are immune from modifications associated with volatiles derived from the hydrothermal system. Mazuku form as gases accumulate in cavities or partially-drained lava flow tunnels following eruptive events (Smets et al., 2010). As a result, pristine mantle-derived volatiles could accumulate in large cavities during prior eruptive events, only to be subsequently released at lava flow contacts or by recent faulting. All mazuku vents were collected at stratigraphic contacts between phonolitic tuff units and basalts (Harkin, 1960; see also Tedesco et al., 2010). This volatile storage and release mechanism could explain (a) low discharge temperatures (as isolated gases would have ample time to cool), (b) the rarity of mazuku, (c) their restricted occurrence — only along volcanic flanks and at lava flow contacts, and (d) the pristine nature of these gases.

In contrast, we propose that higher temperatures (50–70 °C) and associated low He-isotope ratios are related to conductive heat transfer associated with faulting and (deep) infiltration and circulation of hydrothermal fluids (de Moor et al., this volume) during transport through ^{4}He-rich country rocks (Section 5.3.1). The negative correlation between temperature and ^{3}He/^{4}He (Fig. 6A) indicates that high temperatures may promote leaching and facilitate release of radiogenic ^{4}He from water-bearing reservoir rocks (Porcelli and Ballentine, 2002). Mantle volatiles are ubiquitous throughout RVP, so increased travel times with increasing distance from volcanic centers would act to mask magmatic ^{3}He/^{4}He ratios with greater contributions of radiogenic He (Fig. 6C).

5.4. RVP volatile provenance (% mantle and crust)

In this section, we calculate relative mantle and crustal contributions to the volatile inventory using He and combined He–CO$_2$ systematics.

5.4.1. Helium isotope mixing model

Utilizing only representative non-fractionated gas-phase samples (see Section 5.2), we first calculate mantle He contributions by assuming He-isotope distributions at RVP are controlled by simple two-component mixing between radiogenic helium (derived from ^{4}He-rich country rocks) and mantle-derived helium. We consider three mixing scenarios, each with different mantle endmembers (e.g., High ^{3}He/^{4}He, MORB, SCLM). In the 'High ^{3}He/^{4}He endmember' case, samples are divided according to hydrothermal system (Fig. 1B), and assigned a He endmember value based on the highest measured phenocryst ^{3}He/^{4}He value from the nearest volcanic center (e.g., Ngozi-Songwe = 14.9 R$_A$, Rungwe = 12.2 R$_A$, Kiejo = 10.3 R$_A$; Hilton et al., 2011) associated with a particular hydrothermal system. In Table 2, we compare these results to endmember scenarios calculated with upper-mantle He endmembers: MORB = 8 R$_A$ and SCLM = 6.1 R$_A$ (Graham, 2002; Gautheron and Moreira, 2002). If a 'High ^{3}He/^{4}He' endmember is used then the He-isotope distributions of the most pristine gases (e.g., Kiejo Cold Vent, Kibila Cold Vent and Ikama Village samples) can be explained by 54–64% mantle contributions. In contrast, when a MORB-like He-isotope endmember is evoked, these same samples involve 76–90% mantle contributions versus 100% mantle contribution if a SCLM-like He-isotope endmember is selected. Importantly, if an upper-mantle (MORB, SCLM) He-isotope endmember is adopted, these data suggest that virtually pristine unmodified mantle gases are vigorously degassing

Table 2
Proportions of mantle versus crustal helium and mantle versus limestone versus sediment derived carbon contribution to each sample.

Sample location	Phase[a]	Proportion of High ^{3}He/^{4}He He (%) [b]	Proportion of MORB He (%) [c]	Proportion of SCLM He (%) [d]	(CO$_2$ %) [e] mantle	(CO$_2$ %) [e] limestone	(CO$_2$ %) [e] sediments
Rungwe Volcanic Province (RVP)							
Ngozi-Songwe hydrothermal system							
Songwe Mesa	G	24.8	46.3	60.8	5.6	77.7	16.7
(Dup)	G	24.9	46.5	61.2	8.8	72.8	18.4
Songwe Quarry	G	9.0	16.7	22.0	0.1	80.2	19.7
Kiejo-Mbaka hydrothermal system							
Kilambo Springs	G	35.3	45.5	59.8	3.4	79.2	17.4
Mampulo Spring #2	G	17.7	27.0	35.5	65.6	27.1	7.3
(Dup)	G	17.1	26.2	34.4	68.0	26.7	5.3
(Dup)	G	16.1	24.7	32.4	62.3	29.8	7.9
Cold CO$_2$ mazuku vents							
Ikama Village	G	53.9	82.4	100	44.1	50.2	5.6
(Dup)	G	58.7	89.7	100	44.8	47.7	7.5
Kibila Cold Vent	G	57.9	88.6	100	50.0	46.7	3.3
(Dup)	G	57.9	88.6	100	44.1	52.5	3.4
Kiejo Cold Vent	G	59.2	76.4	100	51.9	44.6	3.5
(Dup)	G	64.0	82.5	100	37.4	54.1	8.4

[a] Sample phase: G = gas.
[b] Considering a simple binary mixture between "High ^{3}He/^{4}He" (Ngozi-Songwe = 14.9 R$_A$, Rungwe = 12.2 R$_A$, Kiejo = 10.3 R$_A$) and crustal helium (0.05 R$_A$).
[c] Considering a simple binary mixture between MORB (8 R$_A$) and crustal helium (0.05 R$_A$).
[d] Considering a simple binary mixture between SCLM (6.1 R$_A$) and crustal helium (0.05 R$_A$).
[e] Assuming δ^{13}C values of −6.5‰, 0‰ and −30‰ (relative to VPDB) with corresponding CO$_2$/^{3}He ratios of 2×10^9, 1×10^{13} and 1×10^{13} for mantle, limestone and sediments.

from low temperature mazuku gas vents at the Kiejo Cold Vent, Kibila Cold Vent and Ikama Village.

5.4.2. $CO_2/^3He$–$\delta^{13}C$ mixing model

In order to determine relative CO_2 contributions from potential endmembers at RVP, we plot $CO_2/^3He$ ratios versus $\delta^{13}C$ for the gas phase samples (Fig. 7). Potential endmembers contributing to the CO_2 inventory are mantle (M), limestone (L) and sediment (S), and assumed endmember compositions are: $\delta^{13}C = -6.5$‰ for (M), 0‰ for (L), -30‰ for (S) (relative to VPDB), and $CO_2/^3He = 2\times10^9$ for (M), 10^{13} for (L) and (S) (Sano and Marty, 1995). Superimposed on the diagram are the trajectories for binary mixing between (1) M and L, (2) M and S, and (3) L and S. The most important feature of Fig. 7 is that all samples plot within the area bounded by the three mixing trajectories, indicating that gas samples require a contribution from all three endmembers to explain their combined $CO_2/^3He$–$\delta^{13}C$ characteristics.

In Table 2 we provide a quantitative estimation of the various contributions of the three endmembers to the total carbon inventory at RVP. In the Kiejo-Mbaka system, mantle and limestone-derived carbon are the principal contributors to the carbon budget in all cases, typically representing >90% of the total. The highest mantle CO_2 contributions (62–68%) were measured in Mampulo Spring in an area marked by relatively low $^3He/^4He$ values (2.01–2.20 R_A). Sedimentary organic carbon is a minor contributor to all but one sample (Kilambo Springs; 17%). The finding that limestone contributions are more significant than organic contributions is consistent with widespread travertine deposition throughout the region (Hochstein et al., 2000). In contrast, the Ngozi-Songwe system displays the highest limestone contributions, where samples were collected at or adjacent to a travertine quarry. Notably this area is also marked by the highest organic carbon contributions and the lowest (<10%) mantle contributions. The cold CO_2 mazuku vents are characterized by 37–51% mantle-derived CO_2, with mantle and limestone-derived carbon comprising >90% of the total for all samples. Note, however, if a SCLM $CO_2/^3He$ endmember value of 4×10^9 is adopted (see Section 5.1), the proportion of mantle-derived CO_2 of the mazuku increases to >90%. In effect, virtually the entire He and CO_2 inventory is derived from the mantle.

5.4.3. He–CO_2 crustal–mantle endmember contributions

In addition to quantifying the relative proportions of mantle and crustal contributions to the He–CO_2 volatile inventory, we can also ascertain the relative roles of the crustal and mantle endmembers in

Fig. 8. $CO_2/^3He$ versus He-isotopes with mixing trajectories between a MORB-like starting composition and various crustal $CO_2/^3He$ endmembers (1×10^9–1×10^{15}). Note: all data can be explained by mixing relationships between a mantle endmember and a crustal-$CO_2/^3He$ endmember between 1×10^{11} and 5×10^{13} with the exception of one (Ngozi-Songwe) sample that indicates a mixing trajectory between a mantle endmember and a $CO_2/^3He$ value of ~5×10^{15}.

supplying the CO_2. In Fig. 8, we plot $^3He/^4He$ versus $CO_2/^3He$ with binary mixing trajectories between a MORB like starting composition and various crustal $CO_2/^3He$ endmembers (1×10^9–1×10^{15}). We note that: (1) all but one gas-phase sample (Songwe Quarry) can be explained by binary mixing between a mantle (MORB-like) endmember and a crustal-$CO_2/^3He$ endmember in the range between ~1×10^{11} and 5×10^{13}, and (2) nine of thirteen gas-phase samples fall on a mixing trajectory between MORB and a crustal $CO_2/^3He$ endmember of ~10^{13}. By adopting these endmembers, all six mazuku samples plot in a cluster close to the mantle endmember, indicating a minimal (5–10%) contribution of the crustal endmember ($CO_2/^3He = 10^{13}$) in supplying the CO_2. The three remaining samples (e.g., Kilambo Springs and duplicate samples from Songwe Mesa) display higher $CO_2/^3He$ and are characterized by larger contributions (42–68%) of the crustal endmember ($CO_2/^3He = 10^{13}$). The observation that 9 of 13 gas phase $CO_2/^3He$ values can be explained by mixing between MORB ($CO_2/^3He = 2\times10^9$) and a crustal endmember with $CO_2/^3He = 10^{13}$ confirms that assumed (L) and (S) $CO_2/^3He$ values used to calculate CO_2 provenance (above) are justified (see Table 2; Fig. 7). However, four RVP samples (i.e., Mampulo #2 and duplicates and Songwe Quarry) require different crustal $CO_2/^3He$ endmember values to explain their combined $^3He/^4He$ and $CO_2/^3He$ characteristics. This indicates that the RVP crust is heterogeneous with respect to $CO_2/^3He$, likely resulting from variable crustal compositions. For example, if present, old basaltic lithologies would impart mantle-like $CO_2/^3He$ values (~2×10^9) whereas sediments (organic and/or limestone) would typically display much higher $CO_2/^3He$ values (~10^{13}) — see Fig. 8.

5.5. CO_2 flux calculations

By combining measured fluid CO_2 contents (TDIC) with estimated regional fluid discharge rates (Hochstein et al., 2000), a first order estimate of the CO_2 and ^3He fluxes from the two hydrothermal systems of RVP and the Lake Natron region of northern Tanzania can be estimated. Using these results, and previously published heat loss estimates from the respective regions (Hochstein et al., 2000), we also estimate the ^3He/enthalpy relationships for comparison with other hydrothermal systems worldwide (see Table 3).

The fluid discharge rate for the Ngozi-Songwe hydrothermal system is estimated to be between 50 and 70 l/s (Hochstein et al., 2000), with a median temperature of 60 °C, this leads to a total heat transfer of 10 MW (Hochstein et al., 2000). Assuming that our measured CO_2

Fig. 7. Plot of $CO_2/^3He$ versus $\delta^{13}C$ for RVP gas samples. The endmember compositions for sedimentary organic carbon (S), mantle carbon (M) and limestone (L) are $\delta^{13}C = -30$, -6.5 and 0 ‰; and $CO_2/^3He = 1\times10^{13}$, 2×10^9 and 1×10^{13}, respectively (Sano and Marty, 1995). In addition, mixing trajectories between the various components are shown with fractions of the mantle contribution. Note: all data can be explained by a 3-component mixing model between M–L–S.

Table 3
Helium and carbon fluxes of fluids from RVP and northern Tanzania.

Sample location	Discharge temp. (°C)	Heat Output (MW)[a]	$^3He/^4He$ (R_C/R_A)	$CO_2/^3He$ ($\times 10^9$)	$[CO_2]$ (mmol/kg)	Fluid discharge (l/s)[a]	Total CO_2 flux ($\times 10^7$ mol/yr)	Total ^3He flux ($\times 10^{-5}$ mol/yr)	$^3He/enthalpy$ ($\times 10^{-15}$ mol/J)
Rungwe Volcanic Province (RVP)									
Ngozi-Songwe hydrothermal system									
Songwe Overlook	71	10	1.28	2300	35.0	50–70	6–8	2–4	2–3
Kiejo-Mbaka hydrothermal system									
Kilambo Springs	57	3.5–7.0	0.97	32,200	48.7	20–40	3–6	0.1–0.2	0.2
Mampulo & Kasimulo Springs	56*	1.0	1.56*	5740*	51.6*	5–10	1–2	0.1–0.3	1–2
Northern Tanzania									
(Lengai/Lake Natron)									
Lake Natron	51*	50	0.64*	1.09*	15.9*	~1000	50	46,000	6600
Reference values									
Lower Mantle[b]	–	–	–	–	–	–	–	–	24,000
Upper Mantle[b]	–	–	–	–	–	–	–	–	500
Hydrothermal Vent (Mid Atlantic Ridge)[c]	–	–	–	–	–	–	–	–	130
Hydrothermal Vent (Galapagos Rift)[d]	–	–	–	–	–	–	–	–	120
Hydrothermal Vent (Juan de Fuca Ridge)[d]	–	–	–	–	–	–	–	–	120
Young Volcanoes (Krafla, Iceland)[e]	–	–	–	–	–	–	–	–	14,000
Cooling Lavas (Hveragaerdi, Iceland)[e]									15
Western Anatolia (Turkey)[f]	–	–	–	–	–	–	–	–	190

*Average value — calculated as mean of all samples at the locality.
[a] Values taken from Hochstein et al. (2000).
[b] Values taken from Elderfield and Schultz (1996).
[c] Values taken from Rudnicki and Elderfield (1992).
[d] Values taken from Lupton et al. (1989).
[e] Values taken from Poreda and Arnórsson (1992).
[f] Values taken from Mutlu et al. (2008).

concentration of 35 mmol/kg (Songwe Overlook) is representative of the system then the total CO_2 flux from Songwe is ~$6–8 \times 10^7$ mol/yr. In the Kiejo-Mbaka hydrothermal system, discharge rates (20–40 l/s; Hochstein et al., 2000) have been estimated for Kilambo Springs so that the CO_2 flux from this area is ~$3–6 \times 10^7$ mol/yr assuming a CO_2 concentration of 49 mmol/kg (Table 1). In the Mampulo and Kasimulo Springs area, near Lake Malawi in the south, the fluid discharge rate is estimated to be significantly lower (5–10 l/s; Hochstein et al., 2000) and as a result the CO_2 flux from this area is just ~$1–2 \times 10^7$ mol/yr for an assumed CO_2 concentration of ~50 mmol/kg. Given that these localities dominate the fluid flux at RVP (Hochstein et al., 2000) then our best estimate of the total flux of CO_2 transferred to the surface dissolved in hydrothermal fluids for RVP is 9–16 ($\times 10^7$ mol/yr). Using the estimated contributions of the mantle endmembers to the total CO_2 inventory allows an estimate of the mantle-derived flux of CO_2 to the surface. At Ngozi-Songwe, we estimate the mantle CO_2 contribution to be ~7% using the Songwe Mesa locality: at Kiejo-Mbaka, we estimate mantle contributions to be ~3% (Kilambo Springs locality) and ~65% at the Mampulo Spring locality. Combining these percentage contributions (Table 2) with the total CO_2 fluxes from each area (Table 3), we estimate a total mantle-derived CO_2 flux of 1.0–1.9 ($\times 10^7$ mol/yr) for RVP. Furthermore, we note that this estimate does not include gas phase emissions nor CO_2 released via mazuku vents (see de Moor et al., this volume) and consequently represents a minimum estimate only.

In contrast, the Lake Natron region in northern Tanzania has a much higher fluid discharge rate of ~1000 l/s (Hochstein et al., 2000) resulting in a higher total CO_2 flux of ~50×10^7 mol/yr. However, the mantle-derived CO_2 component most likely represents only a minor proportion of the total CO_2 given the low $^3He/^4He$ ratios at this locality. Furthermore, a substantial fraction of the total CO_2 has been sequestered (Section 5.2.2) resulting in low measured $CO_2/^3He$ ratios. Therefore, the mantle CO_2 flux is unknown at Natron but likely represents a small fraction of the estimated total CO_2 flux. Notably, taken together, the mantle CO_2 fluxes at Lake Natron and RVP represent a negligible fraction of the global ridge CO_2 flux (~2.2×10^{12} mol/yr) (Marty and Tolstikhin, 1998).

By combining CO_2 flux estimates with measured $CO_2/^3He$ values, ^3He fluxes of $2–4 \times 10^{-5}$ mol/yr, $0.1–0.2 \times 10^{-5}$ mol/yr, $0.1–0.3 \times 10^{-5}$

mol/yr and $46,000 \times 10^{-5}$ mol/yr are calculated for Songwe, Kilambo, Mampulo and Kasimulo and Lake Natron, respectively (Table 3). These fluxes are combined with heat loss estimates (Hochstein et al., 2000) to calculate $^3He/enthalpy$ ratios — which are believed to be controlled by the maturity of the magmatic system (Poreda and Arnórsson, 1992). $^3He/enthalpy$ estimates are orders of magnitude higher in the Lake Natron (6600) region compared to RVP (~5), suggesting a significantly more active system. For comparison, we provide $^3He/enthalpy$ estimates from other regions, including recently-active (Krafla) and cooli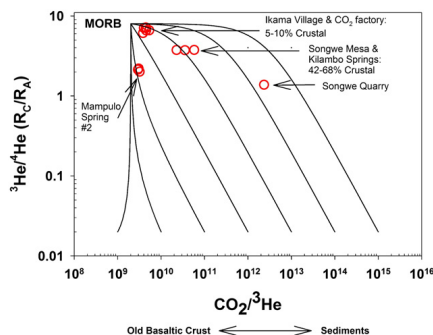ng magmatic systems (Hveragaerdi) of Iceland (Table 3). We note that RVP $^3He/enthalpy$ values are similar to cooling magma systems at Hveragaerdi whereas Lake Natron values are much closer to ratios expected at active volcanic centers. These results are not surprising considering the dormant nature of RVP volcanic centers and the highly active nature of Oldoinyo Lengai volcano, found in close proximity to Lake Natron.

5.6. Gas and fluid phase versus lava $^3He/^4He$: apparent He-isotope discrepancy

In subaerial plume-driven rift zones, such as Afar and Iceland, there is generally good correspondence between $^3He/^4He$ values in hydrothermal fluids and mafic mineral phases such as olivine and pyroxene suggesting that these various sample media are capturing He from the same mantle source(s) (Hilton et al., 1990; Scarsi and Craig, 1996; Marty et al., 1996; Füri et al., 2010). However, Hilton et al. (2011) made the observation that RVP hydrothermal fluid $^3He/^4He$ values (~1–7 R_A) (Pik et al., 2006) do not significantly overlap with $^3He/^4He$ values (~7–15 R_A) in mineral separate samples. The results of this study (Table 1) confirm this apparent He-isotope discrepancy with the most pristine gas-phase (mazuku) samples from RVP lying in the SCLM to MORB range, suggesting no involvement of (plume-like) mantle in supplying He to the region. This observation is illustrated in Fig. 9A which plots $^3He/^4He$ ratios in fluids/gases versus mafic crystals (olivine and clinopyroxene). In this section, we investigate factors that could potentially control this apparent He-isotope discrepancy by addressing the following queries: (1) Is this He-isotope discrepancy real, or simply the result of restricted/
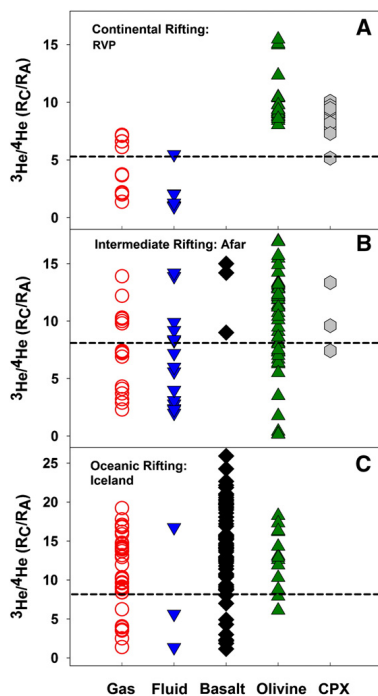
Fig. 9. Helium isotopes measured in different sample phases (gas, fluid, basalt, olivine and clinopyroxene) from three distinct plume-related subaerial rift systems. Fig. 9A illustrates the apparent He-isotope disparity between hydrothermal fluids and gases (this study) and phenocrysts (Hilton et al., 2011) values at RVP. In contrast, at intermediate rift zones (e.g., Afar; Main Ethiopian Rift — Fig. 9B) (Scarsi and Craig, 1996; Marty et al., 1996) and oceanic spreading centers (e.g., Iceland — Fig. 9C) (Füri et al., 2010) there is significant overlap between hydrothermal and rock derived samples.

that the absence of hydrothermal samples and/or mazuku in close proximity to high (plume-like) ^{3}He/^{4}He phenocryst localities could explain why plume-like ^{3}He/^{4}He ratios (> 10 R_A) are not found in fluid and gas samples. A more comprehensive sampling strategy would enable us to test this suggestion further.

Regarding the possibility that there is a temporal control on the presence of (plume-like) ^{3}He/^{4}He ratios at RVP, we note the observation that high ^{3}He/^{4}He values are found in both Younger and Older Extrusive rocks (Hilton et al., 2011) suggesting that the high ^{3}He/^{4}He component is a long-term, as opposed to transient or ephemeral, feature of the underlying mantle source. As a result, plume-like He should potentially be detectable in present-day hydrothermal activity. Its absence, therefore, points to another factor — in addition to the proximity issue discussed above, as the reason why high ^{3}He/^{4}He ratios are not found in fluids and gases.

We suggest that the likeliest scenario to explain lower ^{3}He/^{4}He values in hydrothermal fluids involves large-scale tectonic factors such as plume–craton interaction and the introduction of radiogenic He into the gas/fluid phases. This case is made based upon a comparison between three different subaerial plume-driven rift zones: RVP, Afar, and Iceland, all at various stages of development and characterized by different crustal thicknesses. In the first case, RVP is a nascent continental rift zone located at the southern terminus of the EARS, within Precambrian orogenic belts, on the margin of the Tanzanian Craton — itself comprised of Archean (3.0–2.6 Ga) amalgamated terrains (Maboko, 2000; Manya et al., 2006; Yirgu et al., 2006; Furman, 2007). Furthermore, geophysical and xenolith evidence suggest that the Tanzanian craton has a deep (200–350 km) lithospheric keel that has not been extensively disrupted by Cenozoic tectonic and/or magmatic activity (Chesley et al., 1999; Lee and Rudnick, 1999; Ritsema et al., 1999; Belluci et al., 2011). As a result, RVP marks the intersection of old/thick cratonic crust with contemporary plume-influenced volcanism and recent rifting. Second, the Afar region marks the northern terminus of EARS rifting and is characterized by intermediate crustal thicknesses — from ~45 km in the highlands to as thin as ~16 km in the incipient ocean spreading centers of northern Afar (Yirgu et al., 2006). Voluminous igneous crust is actively being generated and basaltic rocks are characterized by high ^{3}He/(U–Th) contents (Marty et al., 1996). Finally, Iceland is a plume-driven oceanic spreading center, marked by extremely young crust (0–17 Ma) (McDougall et al., 1984; Einarsson, 2008). Crustal thicknesses vary between 20 and 100 km, with an average rift zone age of (<2 Ma) and thickness of 20–40 km (Bjarnason et al., 1993; Bjarnason and Schmeling, 2009; Staples et al., 1997).

In Fig. 9 we plot ^{3}He/^{4}He values measured in hydrothermal gases and fluids, basalts, and mafic phenocryst phases (olivine and clinopyroxene) for the three different plume-driven rift zones: RVP, Afar and Iceland. We note the readily apparent He-isotope discrepancy between hydrothermal fluids and gases and mazuku versus mineral phases at RVP, compared with the considerable overlap between the various sample phases at both Afar and Iceland. Thus, we suggest that rift dynamics may control ^{3}He/^{4}He ratios in fluids/gases through increased interaction with ^{4}He derived from the crust. For example, volatiles emanating from the magmatic source at depth at RVP are exposed to old (Archean) bedrock and ^{4}He-rich sediments en route to the surface. Due to the relative thickness of the crust, magmatic volatiles likely undergo longer storage times, with increased potential to acquire a more radiogenic signature during ascent. In contrast, Afar crust is significantly thinner (e.g., no plume–craton interaction) so that residence times of He in various hydrothermal systems are likely reduced, along with the potential for extensive radiogenic-He additions. Similarly, radiogenic He contributions also occur in parts of the Icelandic crust (Condomines et al., 1983); however, they are generally less pervasive and typically have little effect on either hydrothermal and basalt phases (Hilton et al., 1990). Thus, it is the combination of old Archean/Proterozoic basement rocks and their derivatives that make up the fluid reservoir host rocks that imparts such a strong

limited hydrothermal sampling opportunities at RVP? (2) Could this discrepancy be the result of temporal He-isotope variations? (3) Are variations in rift dynamics, such as extent of lithospheric extension, crustal thickness and crustal age, influencing the degree of crustal modification and hence preferentially lowering ^{3}He/^{4}He in some sample types?

The primary finding of this study is that pristine SCLM to MORB-like mantle ^{3}He/^{4}He values (~7 R_A) are found in three distinct sites (Kiejo Cold Vent, Kibila Cold Vent and Ikama Village), and that these localities are characterized by vigorously degassing cold CO_2 (mazuku-like) vents in close proximity to volcanic edifices. In contrast, predominantly mantle-like ^{3}He/^{4}He ratios (i.e. ^{3}He/^{4}He > 7 R_A; n = 30) were measured in mafic phenocrysts throughout RVP (Hilton et al., 2011), with 14 values falling in the MORB range (8 ± 1 R_A), (b) 9 lying between 9 and 10 R_A and (c) 7 falling above 10 R_A. Notably, phenocryst samples closest to Ikama Village (i.e., within 1 km; samples RNG-8, 9, 11, 12) have an average ^{3}He/^{4}He value of 8.7 R_A, with the closest (~8 km) sample to Kiejo Cold Vent (TAZ09-12) also yielding a ^{3}He/^{4}He value of 8.7 R_A (Hilton et al., 2011). On a spatial basis, therefore, there is not a ^{3}He/^{4}He disparity between phenocrysts and geothermal fluids/gases as both capture MORB-like He. In this respect, we could argue

radiogenic ^{4}He signal at RVP which is difficult to by-pass by most hydrothermal samples except in relatively rare cases, such as when mazuku are present.

6. Concluding remarks

This study has shown that RVP fluids and gases are characterized by a wide range of ^{3}He/^{4}He and CO_2/^{3}He vales, and a narrow range in δ^{13}C (CO_2) values, reflecting variable mantle and crustal contributions. We show that phase-separation within the hydrothermal system has a clear influence on fluid-phase samples and is likely the principal controls on their CO_2/^{3}He ratios and δ^{13}C values. Additionally, fluid samples are especially susceptible to radiogenic helium additions following gas (helium) loss and subsequent ^{4}He addition due to prolonged interaction with the crust during fluid transport.

Several cold CO_2 mazuku gas vents display He–CO_2 characteristics typical of either MORB or SCLM. Additionally, their low temperatures, rarity, and occurrence at stratigraphic contacts, together suggest that they may be derived from an isolated source that is decoupled from the modern hydrothermal system. Using He-isotope compositions, we calculate the percentage of mantle contribution to each gas-phase RVP sample for three different endmember ^{3}He/^{4}He scenarios (SCLM, MORB and 'High-^{3}He/^{4}He'). In addition, we use a CO_2/^{3}He–δ^{13}C model to quantitatively assess mantle and crustal CO_2 budgets and calculate CO_2 fluxes for fluid samples. We suggest that the extent of crustal contamination in samples is regionally controlled by proximity to volcanic edifices and extent of hydrothermal interaction; however, rift zone evolution (e.g., stage of rifting) also heavily influences observed regional trends as it acts to control the extent of ^{4}He addition from old, He-rich reservoir rocks. We conclude that the apparent He-isotope disparity between mafic phenocrysts and hydrothermal fluids does not exist on small spatial scales and that the absence of hydrothermal manifestations and/or mazuku-like features in close proximity to high ^{3}He/^{4}He phenocryst localities can explain this apparent He-isotope disparity at RVP.

Acknowledgements

References

Adams, A., Nyblade, A., Weerarantne, D., 2012. Upper mantle shear wave velocity structure beneath the East African plateau: evidence for a deep, plateau wide low velocity anomaly. Geophysical Journal International 189, 123–142. http://dx.doi.org/10.1111/j.1365-246X.2012.05373.x.

Arnórsson, S., 2000. Isotopic and Chemical Techniques in Geothermal Exploration, Development and Use: Sampling Methods, Data Handling. Interpretation. IAEA, Vienna, p. 351.

Belluci, J.J., McDonough, W.F., Rudnick, R.L., 2011. Thermal history and origin of the Tanzanian Craton from Pb isotope thermochronology of feldspars from lower crustal xenoliths. Earth and Planetary Science Letters 301, 493–501. http://dx.doi.org/10.1016/j.epsl.2010.11.031.

Bjarnason, I.T., Schmeling, H., 2009. The lithosphere and asthenosphere of the Iceland hotspot from surface waves. Geophysical Journal International 178, 394–418. http://dx.doi.org/10.1111/j.1365-246X.2009.04155.x.

Bjarnason, I, Menke, W., Flovenz, O., Caress, D., 1993. Tomographic image of the spreading center in south Iceland. Journal of Geophysical Research 98, 6607–6622.

Branchu, P., Bergonzini, L., Delvaux, D., De Batist, M., Golubev, V., Benedetti, M., Klerkx, J., 2005. Tectonic, climatic and hydrothermal control on sedimentation and water chemistry of northern Lake Malawi (Nyasa), Tanzania. Journal of African Earth Sciences 43, 433–446. http://dx.doi.org/10.1016/j.jafrearsci.2005.09.004.

Burke, K., 1996. The African Plate. South Afr. Journal of Geology 99, 339–409.

Chakrabarti, R., Basu, A.R., Santo, A.P., Tedesco, D., Vaselli, O., 2009. Isotopic and geochemical evidence for a heterogeneous mantle plume origin of the Virunga volcanics, Western rift, East African Rift system. Chemical Geology 259, 273–289.

Chesley, J.T., Rudnick, R.L., Lee, C.T., 1999. Re–Os systematics of mantle xenoliths from the East African Rift: age, structure, and history of the Tanzanian Craton. Geochimica et Cosmochimica Acta 63 (7–8), 1203–1217. http://dx.doi.org/10.1016/S0016-7037(99)00004-6.

Condomines, M., Gronvold, K., Hooker, P.J., Muehlenbachs, K., O'Nions, R.K., Oskarsson, N., Oxburch, E.R., 1983. Helium. oxygen, strontium and neodymium isotopic relationships in Icelandic volcanics. Earth and Planetary Science Letters 66, 125–137.

Darling, W.G., Griesshaber, E., Andrews, J.N., Armannsson, H., O'Nions, R.K., 1995. The origin of hydrothermal and other gases in the Kenya Rift Valley. Geochimica et Cosmochimica Acta 59, 2501–2512. http://dx.doi.org/10.1016/0016-7037(95)00145-X (358).

Dawson, J.B., 2008. The Gregory Rift Valley and Neogene-Recent volcanoes of Northern Tanzania. Geological Society, London, Memoirs 33, 102.

Day, J.M.D., Hilton, D.R., Pearson, D.G., MacPherson, C.G., Kjarsgaard, B.A., Janney, P.E., 2005. Absence of a high time integrated ^{3}He/(U+Th) source in the mantle beneath continents. Geology 33, 733–736.

de Moor, J.M., Fischer, T.P., Sharp, Z.D., Hilton, D.R., Barry, P.H., Mangasini, F., Ramirez, C., (this volume). Gas chemistry and nitrogen isotope compositions of cold mantle gases from Rungwe Volcanic Province, southern Tanzania. Chemical Geology Special Issue - Frontiers in Gas Geochemistry.

Delalande, M., Bergonzini, L., Gherardi, F., Guidi, M., Andre, L., Abdallah, I., Williamson, D., 2011. Fluid geochemistry of natural manifestations from the Southern Poroto–Rungwe hydrothermal system (Tanzania): Preliminary conceptual model. Journal of Volcanology and Geothermal Research 199 (1–2), 127–141. http://dx.doi.org/10.1016/j.jvolgeores.2010.11.002.

Delvaux, D., Hanon, M., 1993. Neotectonics of the Mbeya area, SW Tanzania. Mus roy Afr centr, Tervuren. Dept. Geol. Min. Rapp. Ann, pp. 87–97.

Delvaux, D., Kraml, M., Sierralta, M., Wittenberg, A., Mayalla, J.W., Kabaka, K., Makene, C., GEOTHERM working group, 2010. Surface exploration of a viable geothermal resource in Mbeya area, SW Tanzania. Part I: Geology, Proceedings, World Geothermal Congress 2010, Bali, Indonesia 25– 29 April.

Ebinger, C.J., Furman, T., 2003. Geodynamical setting of the Virunga volcanic province, East Africa. Acta Vulcanologica 15 (1–2), 9–16.

Ebinger, C.J., Sleep, N.H., 1998. Cenozoinc magmatism through-out east Africa resulting from impact of a single plume. Nature 395, 788–791. http://dx.doi.org/10.1038/27417.

Ebinger, C.J., Rosendahl, B.R., Reynolds, D.J., 1987. Tectonic model of the Malawi rift, Africa. Tectonophysics 141, 215–235. http://dx.doi.org/10.1016/0040-1951(87)90187-9.

Ebinger, C.J., Bechtel, T.D., Forsyth, D.W., Bowin, C.O., 1989a. Effective elastic plate thickness beneath the East African and Afar Plateaus and dynamic compensation of the uplifts. Journal of Geophysical Research 94, 2883–2901. http://dx.doi.org/10.1029/JB094iB03p02883.

Ebinger, C.J., Deino, A.L., Drake, R.E., Tesha, A.L., 1989b. Chronology of volcanism and rift Basin propagation: Rungwe Volcanic Province, East Africa. Journal of Geophysical Research 94, 15,785–15,803. http://dx.doi.org/10.1029/B094iB11p15785.

Ebinger, C.J., Klerkx, J., Delvaux, D., Wuest, A., 1993. Evaluation of Natural Hazards in the Northern Part of the Malawi Rift (Tanzania). Mus. roy. Afr. centr., Tervuren (Belg.), Dept. Geol, Min., Rapp, ann. 1991–1992, pp. 83–86.

Ebinger, C., Djomani, Y., Mbede, Y., Foster, F., Dawson, J., 1997. Rifting Archean lithosphere: the Eyasi–Manyara–Natron rifts, East Africa. Journal of the Geological Society of London 154, 947–960.

Einarsson, P., 2008. Plate boundaries, rifts and transform zones in Iceland. Jökull 58, 35–58.

Elderfield, H., Schultz, A., 1996. Mid-ocean ridge hydrothermal fluxes and the chemical composition of the ocean. Annual Review of Earth and Planetary Sciences 24, 191–224.

Ellis, A.J., Golding, R.M., 1963. The solubility of carbon dioxide above 100 °C in water and sodium chloride solutions. American Journal of Science 261, 47–60.

Fischer, T.P., Burnard, P., Marty, B., Hilton, D.R., Füri, E., Palhol, F., Sharp, Z.D., Mangasini, F., 2009. Upper-mantle volatile chemistry at Oldoinyo Lengai volcano and the origin of carbonatites. Nature 459, 77–80. http://dx.doi.org/10.1038/nature07977.

Fontijn, K., Ernst, G.G.J., Elburg, M.A., Williamson, D., Abdallah, E., Kwelwa, S., Mbede, E., Jacobs, P., 2010a. Holocene explosive eruptions in the Rungwe Volcanic Province, Tanzania. Journal of Volcanology and Geothermal Research 196, 91–110.

Fontijn, K., Delvaux, D., Ernst, G.G.J., Kervyn, M., Mbede, E., Jacobs, P., 2010b. Tectonic control over active volcanism at a range of scales: case of the Rungwe Volcanic Province, SW Tanzania; and hazard implications. Journal of African Earth Sciences 58, 764–777.

Fontijn, K., Williamson, D., Mbede, E., Ernst, G., 2011. The Rungwe Volcanic Province, Tanzania – A volcanological review. Journal of African Earth Sciences 63 (2012), 12–31. http://dx.doi.org/10.1016/j.jafrearsci.2011.11.005.

Füri, E., Hilton, D.R., Halldorsson, S.A., Barry, P.H., Hahm, D., Fischer, T.P., Gronvold, K., 2010. Apparent decoupling of the He and Ne isotope systematics of the Icelandic mantle: the role of He depletion, melt mixing, degassing fractionation and air interaction. Geochimica et Cosmochimica Acta 74, 3307–3332. http://dx.doi.org/10.1016/j.gca.2010.03.023.

Furman, T., 1995. Melting of metasomatized subcontinental lithosphere: Undersaturated mafic lavas from Rungwe, Tanzania. Contributions to Mineralogy and Petrology 122, 97–115. http://dx.doi.org/10.1007/s004100050115.

Furman, T., 2007. Geochemistry of East African Rift basalts: an overview. Journal of African Earth Sciences 48 (2–3), 147–160. http://dx.doi.org/10.1016/j.jafrearsci.2006.06.00.

Furman, T., Bryce, J., Karson, J., Iotti, A., 2004. East African Rift System (EARS) plume structure: insights from Quaternary Mafic Lavas of Turkana, Kenya. Journal of Petrology 45, 1069–1088. http://dx.doi.org/10.1093/petrology/egh004.

Gautheron, C., Moreira, M., 2002. Helium signature of the subcontinental lithospheric mantle. Earth and Planetary Science Letters 199, 39–47. http://dx.doi.org/10.1016/S0012-821X(02)00563-0.

George, R., Rogers, N., Kelley, S., 1998. Earliest magmatism in Ethiopia: evidence for two mantle plumes in one flood basalt province. Geology 26, 923–926. http://dx.doi.org/10.1130/0091-7613(1998) 026<0923:EMIEEF>2.3.CO;2.

Giggenbach, W.F., Sano, Y., Wakita, H., 1993. Isotopes of He, and CO_2 and CH_4 contents in gases produced along the New Zealand part of a convergent plate boundary. Geochimica et Cosmochimica Acta 57, 3427–3455. http://dx.doi.org/10.1016/0016-7037(93)90549-C.

Graham, D.W., 2002. Noble gas isotope geochemistry of mid-ocean and ocean island basalts: characterization of mantle source reservoirs. Reviews in Mineralogy and Geochemistry 47, 247–317. http://dx.doi.org/10.2138/rmg.2002.47.8.

Hahn, D., Hilton, D.R., Cho, M., Wei, H., Kim, K.R., 2008. Geothermal He and CO_2 variations at Changbaishan intra-plate volcano (NE China) and the nature of the subcontinental lithospheric mantle. Geophysical Research Letters 33, L12304. http://dx.doi.org/10.1029/2008GL035955.

Harkin, D.A., 1955. The Sarabwe Lava Flow, Kiejo, Rungwe District. Tanganyika Notes 40, 20–23.

Harkin, D.A., 1960. The Rungwe Volcanics at the Northern End of Lake Nyasa, Geological Survey of Tanganyika, Dodoma. 172 pp.

Hilton, D.R., 1996. The helium and carbon isotope systematics of a continental geothermal system: results from monitoring studies at Long Valley caldera, California, U.S.A. Chemical Geology 127, 269–295. http://dx.doi.org/10.1016/0009-2541(95)00134-4.

Hilton, D.R., Gronvöld, K., O'Nions, R.K., Oxburgh, E.R., 1990. Regional distribution of ^{3}He anomalies in the Icelandic crust. Chemical Geology 88, 53–67.

Hilton, D.R., Hammerschmidt, K., Teufel, S., Friedrichsen, H., 1993. Helium isotope characteristics of Andean geothermal fluids and lavas. Earth and Planetary Science Letters 120, 265–282. http://dx.doi.org/10.1016/0012-821X(93)90244-4.

Hilton, D.R., Fischer, T.P., Marty, B., 2002. Noble gases and volatile recycling at subduction zones. Mineralogical Society Of America 47, 319–370. http://dx.doi.org/10.2138/rmg.2002.47.9.

Hilton, D.R., Halldórsson, S.A., Barry, P.H., Fischer, T.P., de Moor, J.M., Ramirez, C.J., Mangasini, F., Scarsi, P., 2011. Helium isotopes at Rungwe Volcanic Province, Tanzania, and the origin of East African Plateaux. Geophysical Research Letters 38, L21304. http://dx.doi.org/10.1029/2011GL049589.

Hochstein, M.P., Temu, E.P., Moshy, C.M.A., 2000. Geothermal resources of Tanzania Proceedings World Geothermal Congress. Kyushu–Tohoku, Japan, May 28 to June 10, 2000, pp. 1233–1238.

Hopp, J., Trieloff, M., Altherr, R., 2007. Noble gas compositions of the lithospheric mantle below the Chyulu Hills volcanic field, Kenya. Earth and Planetary Science Letters 261, 635–648. http://dx.doi.org/10.1016/j.epsl.2007.07.027.

Iranga, M.D., 1992. Seismicity of Tanzanian: distribution in time, space, magnitude, and strain release. Tectonophysics 209, 313–320.

James, T.C., 1967. Thermal springs in Tanzania. Transactions Applied Earth Science 76, B1–B18 (sect.B).

Kraml, M., Mnjokava, T.T., Mayalla, J.W., Kabaka, K., GEOTHERM working group, 2010. Surface exploration of a viable geothermal resource in Mbeya area, SW Tanzania - Part II: Geochemistry. Proceedings World Geothermal Congress 2010, Bali, Indonesia, pp. 25–29.

Kulongoski, J.T., Hilton, D.R., 2002. A quadrupole-based mass spectrometric system for the determination of noble gas abundances in fluids. Geochemistry, Geophysics, Geosystems 3, 1032–1042. http://dx.doi.org/10.1029/2001GC000267.

Lee, C.T., Rudnick, R.L., 1999. Compositionally stratified cratonic lithosphere: petrology and geochemistry of peridotite xenoliths from the Labait tuff cone, Tanzania. Proceedings of the Seventh International Kimberlite Conference, pp. 503–521.

Lupton, J.E., Baker, E.T., Massoth, G.J., 1989. Variable ^{3}He/heat ratios in submarine hydrothermal systems: evidence from two plumes over the Juan de Fuca Ridge. Nature 337, 161–164.

Maboko, M.A.H., 2000. Nd and Sr isotopic investigation of the Archean–Proterozoic boundary in north eastern Tanzania: constraints on the nature of Neoproterozoic tectonism in the Mozambique Belt. Precambrian Research 102 (1–2), 87–98. http://dx.doi.org/10.1016/S0301-9268(00)00060-7.

Manya, S., Kobayashi, K., Maboko, M.A.H., Nakamura, E., 2006. Ion microprobe zircon U–Pb dating of the late Archean metavolcanics and associated granites of the Musoma–Mara Greenstone Belt, Northeast Tanzania: implications for the geological evolution of the Tanzania Craton. Journal of African Earth Sciences 45 (3), 355–366. http://dx.doi.org/10.1016/j.jafearsci.2006.03.004.

Marty, B., Jambon, A., 1987. C/^{3}He in volatile fluxes from the solid Earth: implication for carbon geodynamics. Earth and Planetary Science Letters 83, 16–26. http://dx.doi.org/10.1016/0012-82X(87)90047-1.

Marty, B., Tolstikhin, I.N., 1998. CO_2 fluxes from mid-ocean ridges, arcs and plumes. Earth and Planetary Science Letters 145, 233–248. http://dx.doi.org/10.1016/S0009-2541(97)00145-9.

Marty, B., Jambon, A., Sano, Y., 1989. Helium isotopes and CO_2 in volcanic gases of Japan. Chemical Geology 76 (1989), 25–40. http://dx.doi.org/10.1016/0009-2541(89)90125-3.

Marty, B., Pik, R., Yirgu, G., 1996. Helium isotopic variations in Ethiopian plume lavas: nature of magmatic sources and limit on lower mantle contribution. Earth and Planetary Science Letters 144, 223–237. http://dx.doi.org/10.1016/0012-821X(96)00158-6.

McDougall, I., Kristjansson, L., Saemundsson, K., 1984. Magnetostratigraphy and geochronology of northwest Iceland. Journal of Geophysical Research 89, 7029–7060. http://dx.doi.org/10.1029/JB089iB08p07029.

Mnjokava, T.T., 2007. Interpretation of Exploration Geochemical Data for Geothermal Fluids from the Geothermal Field of the Rungwe Volcanic Area, SWTanzania. UNU-GTP Reykjavík, Iceland, Reports 2007, Number 14, pp. 303–332.

Mook, W.G., Bommerson, J.C., Stavermann, W.H., 1974. Carbon isotope fractionation between dissolved bicarbonate and gaseous carbon dioxide. Earth and Planetary Science Letters 22, 169. http://dx.doi.org/10.1016/0012-821X(74)90078-8.

Morrison, P., Pine, J., 1955. Radiogenic origin of the Helium isotopes in rock. Annals of the New York Academy of Sciences 62, 71–92. http://dx.doi.org/10.1111/j.1749-6632.1955.tb35366.x.

Mutlu, H., Güleç, N., Hilton, D.R., 2008. Helium–carbon relationships in geothermal fluids of western Anatolia, Turkey. Chemical Geology 247, 305–321. http://dx.doi.org/10.1016/j.chemgeo.2007.10.021.

Nyblade, A.A., et al., 2000. Seismic evidence for a deep upper mantle plume thermal anomaly beneath east Africa. Geology 28, 599–602. http://dx.doi.org/10.1130/0091-7613(2000) 28<599:SEFADU>2.0.CO;2.

O'Nions, R.K., Oxburgh, E.R., 1988. Helium, volatile fluxes and the development of continental crust. Earth and Planetary Science Letters 90 (1988), 331–347.

Ozima, M., Podosek, F.A., 1983. Noble Gas Geochemistry. Cambridge University Press, Cambridge, p. 367.

Park, Y., Nyblade, A., 2006. P-wave tomography reveals a westward dipping low velocity zone beneath the Kenya Rift. Geophysical Research Letters 33, 4. http://dx.doi.org/10.1029/2005GL025605.

Pik, R., Deniel, C., Coulon, C., Yirgu, G., Marty, B., 1999. Isotopic and trace element signatures of Ethiopian flood basalts: evidence for plume–lithosphere interactions. Geochimica et Cosmochimica Acta 63, 2263–2279. http://dx.doi.org/10.1016/S0016-7037(99)00141-6.

Pik, R., Marty, B., Hilton, D.R., 2006. How many mantle plumes in Africa? The geochemical point of view. Chemical Geology 226, 100–114. http://dx.doi.org/10.1016/j.chemgeo.2005.09.016.

Porcelli, D., Ballentine, C.J., 2002. An overview of noble gas geochemistry and cosmochemistry. In: Porcelli, D., Ballentine, C.J., Wieler, R. (Eds.), Noble Gases in Geochemistry and Cosmochemistry: Rev. Mineral. Geochem., vol. 47, pp. 1–19.

Poreda, R.J., Arnórsson, S., 1992. Helium isotopes in Icelandic geothermal systems: II. Helium–heat relationships. Geochimica et Cosmochimica Acta 56, 4229–4235.

Poreda, R.J., Craig, H., Arnórsson, S., Welhan, J.A., 1992. Helium isotopes in Icelandic geothermal systems: I, ^{3}He gas chemistry, and ^{13}C relations. Geochimica et Cosmochimica Acta 56, 4221–4228. http://dx.doi.org/10.1016/0016-7037(92)90263-I.

Ray, M.C., Hilton, D.R., Munoz, J., Fischer, T.P., Shaw, A.M., 2009. The effects of volatile recycling, degassing and crustal contamination on the helium and carbon geochemistry of hydrothermal fluids from the Southern Volcanic Zone of Chile. Chemical Geology 266 (1–2), 38–49. http://dx.doi.org/10.1016/j.chemgeo.2008.12.026.

Ritsema, J., Van Heijst, H., Woodhouse, J., 1999. Complex shear wave velocity structure imaged beneath Africa and Iceland. Science 286, 1925–1928. http://dx.doi.org/10.1126/science.286.5446.1925.

Rogers, N.W., 2006. Basaltic magmatism and the geodynamics of the East African Rift System. In: Yirgu, G., Ebinger, C.J., Maguire, P.K.H. (Eds.), The afar volcanic province within the East African Rift System: Geological Society Special Publication, 259, pp. 77–93. http://dx.doi.org/10.1144/GSL.SP.2006.259.01.08.

Rogers, N., McDonald, R., Fitton, J.G., George, R., Smith, M., Barreiro, B., 2000. Two mantle plumes beneath the East African rift system: Sr, Nd and Pb isotope evidence from Kenya Rift basalts. Earth and Planetary Science Letters 176, 387–400. http://dx.doi.org/10.1016/S0012-821X(00)00012-1.

Rudnicki, M.D., Elderfield, H., 1992. Theory applied to the Mid-Atlantic Ridge hydrothermal plumes: the finite difference approach. Journal of Volcanology and Geothermal Research 50, 163–174.

Sano, Y., Marty, B., 1995. Origin of carbon in fumarolic gas from island arcs. Chemical Geology 119, 265–274.

Sano, Y., Nakamura, Y., Wakita, H., Urabe, A., Tominaga, Y., 1984. ^{3}He emission related to volcanic activity. Science 224, 150–151. http://dx.doi.org/10.1126/science.224.4645.150.

Scarsi, P., Craig, H., 1996. Helium isotope ratios in Ethiopian Rift basalts. Earth and Planetary Science Letters 144, 505–516. http://dx.doi.org/10.1016/S0012-821X(96)00185-9.

Schilling, J.G., Kingsley, R.H., Hanan, B.B., McCully, B.L., 1992. Nd–Sr–Pb isotopic variations along the gulf of Aden: evidence for mantle plume–continental lithosphere interactions. Journal of Geophysical Research 97, 10927–10966. http://dx.doi.org/10.1029/92JB00415.

Shaw, A.M., Hilton, D.R., Fischer, T.P., Walker, J.A., Alvarado, G.E., 2003. Contrasting He-C relationships in Nicaragua and Costa Rica; insights into C cycling through subduction zones. Earth and Planetary Science Letters 214 (3–4), 499–513. http://dx.doi.org/10.1016/S0012-821X(03)00401-1.

Smets, B., Tedesco, D., Kervyn, F., Kies, A., Vaselli, O., Yalire, M.M., 2010. Dry gas vents ("mazuku") in Goma region (North-Kivu, Democratic Republic of Congo): Formation and risk assessment. Journal of African Earth Sciences 50, 787–798. http://dx.doi.org/10.1016/j.jafrearsci.2010.04.008.

Staples, R., White, R., Brandsdottir, B., Menke, W., Maguire, P., McBride, J., 1997. Faroes-Iceland experiment - 1: the crustal structure of northeastern Iceland. Journal of Geophysical Research 102, 7849–7866.

Stephen, H., Stephen, T., 1963. Solubilities of Inorganic and Organic Compounds, I. Binary Systems, Part I. Pergamon Press.

Stuart, F.M., Lass-Evand, S., Fitton, J.G., Ellam, R.M., 2003. High ^{3}He/^{4}He ratios in picritic basalts from Baffin Island and the role of a mixed reservoir in mantle plumes. Nature 424, 57–59. http://dx.doi.org/10.1038/nature01711.

Szaran, J., 1997. Achievement of carbon isotope equilibrium in the system HCO_3^- (solution)–CO_2 (gas). Chemical Geology 142, 79–86. http://dx.doi.org/10.1016/S0009-2541(97)00077-6.

Tedesco, D., Tassi, F., Vaselli, O., Poreda, R.J., Darrah, T., Cuoco, E., Yalire, M.M., 2010. Gas isotopic signatures (He, C, and Ar) in the Lake Kivu region (Western branch of the East Africa rift system): Geodynamic and volcanological implications. Journal of Geophysical Research 115 (B01205), 450. http://dx.doi.org/10.1029/2008JB006227.

Tiab, D., Donaldson, E.C., 2011. Petrophysics Theory and Practice of Measuring Reservoir Rock and Fluid Transport Properties. Gulf Publishing Company, Houston, TX. 53.

Torgersen, T., Jenkins, W.J., 1982. Helium isotopes in geothermal systems: Iceland, The Geysers, Raft River and Steamboat Springs. Geochimica et Cosmochimica Acta 46, 739–748. http://dx.doi.org/10.1016/0016-7037(82)90025-4.

Tuttle, M.L., Lockwood, J.P., Evans, W.C., 1990. Natural hazards associated with Lac Kivu and adjoining areas of the Virunga Volcanic Field, Rwanda and Zaïre, Central Africa: Final Report: USGS Open File Report, 90–691. 40pp.

Van Soest, M.C., Hilton, D.R., Kreulen, R., 1998. Tracing crustal and slab contributions to arc magmatism in the Lesser Antilles island arc using helium and carbon relationships in geothermal fluids. Geochimica et Cosmochimica Acta 62, 3323–3335. http://dx.doi.org/10.1016/S0016-7037(98)00241-5.

Vogel, J.C., Grootes, P.M., Mook, W.G., 1970. Isotope fractionation between gaseous and dissolved carbon dioxide. Zeitschrift für Physik 230, 255–258. http://dx.doi.org/10.1007/BF01394688.

Weiss, R.F., 1971. Solubility of Helium and Neon in Water and Seawater. Journal of Chemical and Engineering Data 16 (2), 235–241. http://dx.doi.org/10.1021/je60049a019.

Williams, T.M., Henney, P.J., Owen, R.B., 1993. Recent eruptive episodes of the Rungwe Volcanic Field (Tanzania) recorded in lacustrine sediments of the Northern Malawi Rift. Journal of African Earth Sciences 17, 33–39.

Yirgu, G., Ebinger, C.J., Maguire, P.K.H., 2006. The structure and evolution of the East African Rift System in the Afar Volcanic Province. Geological Society Special Publication 259, 1–327. http://dx.doi.org/10.1144/GSL.SP.2006.259.01.01.

Zhang, J., Quay, P.D., Wilbur, D.O., 1995. Carbon isotope fractionation during gas–water exchange and dissolution of CO_2. Geochimica et Cosmochimica Acta 59, 107–1146. http://dx.doi.org/10.1016/0016-7037(95)91550-D.

IV. Acknowledgements

In addition to those mentioned within the acknowledgements section of the published work, we also thank Elsevier for allowing us use a reprint of the material as it appeared in Chemical Geology 2012, as Barry, P. H., D. R. Hilton, T.P. Fischer, J.M. de Moor, F. Mangasini, and C. Ramirez (2012), Helium and carbon isotope systematics of cold "mazuku" CO_2 vents and hydrothermal gases and fluids from Rungwe Volcanic Province, southern Tanzania, *Chemical Geology*, doi: 10.1016/j.chemgeo.2012.07.003. The dissertation author was the primary investigator and lead author of this paper and conducted all the analyses presented herein.

CHAPTER V: Carbon isotope and abundance systematics, and CO₂ fluxes from Icelandic geothermal gases, fluids and subglacial basalts

V.1 ABSTRACT

New carbon dioxide (CO_2) data are presented for 71 geothermal gases and fluids from the high-temperature (HT > 200 ºC) Icelandic neovolcanic zones and older low-temperature (LT < 200 ºC) parts of the Icelandic crust as well as 47 subglacial basaltic glasses collected from the rift zones of Iceland. This suite of samples has previously been well characterized for He-Ne (geothermal) and He-Ne-Ar (basalt) systematics (Füri et al., 2010), allowing elemental ratios (e.g., $CO_2/^3He$) to be calculated for individual samples. Geothermal fluids are characterized by a wide range in carbon isotope ratios ($\delta^{13}C$) from -18.8 to +4.6 ‰ and $CO_2/^3He$ values that span eight orders of magnitude, from 1×10^4 to 2×10^{12}. Extreme geothermal values suggest that original source compositions have been extensively modified by hydrothermal processes such as calcite precipitation and/or hydrothermal degassing. The fractionation effects of calcite precipitation are most pronounced in LT off-axis portions of the Icelandic crust. In contrast, basaltic glasses are characterized by a wider range in $\delta^{13}C$ values, from -27.2 to -3.6 ‰ and $CO_2/^3He$ values which span a narrower range, from 1×10^8 to 1×10^{12}. The combination of both low $\delta^{13}C$ values and low CO_2 contents in basalts indicates that magmas are extensively and variably degassed. Using an equilibrium degassing model, we estimate that pre-eruptive melts in the Icelandic mantle source contained $\sim 531 \pm 64$ ppm CO_2 with $\delta^{13}C$ values of -2.5 ± 1.1 ‰, in good agreement with previous estimates of 519 ppm for E-MORB (Marty, 2012). In addition, CO_2 source compositions are estimated for the individual axial rift zones and show a marked decrease from north to south (Northern Rift Zone = 550 ± 66 ppm; Eastern Rift Zone = 371 ± 45 ppm; Western Rift Zone = 206 ± 24 ppm). Degassing can adequately explain low CO_2 contents in basalts, however degassing alone is unlikely to generate the entire range of observed $\delta^{13}C$ variations in dissolved basalt CO_2, and we suggest that melt-crust interaction, with an isotopically low $\delta^{13}C$ component, also

contributes to the observed signatures. To this end, the potential effects of coupled assimilation and degassing are investigated by modeling expected elemental ratio co-variations in vesicle-sited gases. Finally, we calculate the CO_2 flux from Iceland using three independent methods: 1) combining measured $CO_2/^3He$ values (in gases and basalts) with ^3He flux estimates (Hilton et al., 1998), 2) assuming 12% partial melting of a mantle source with ~531 ± 64 ppm CO_2, and 3) combining fluid CO_2 contents with estimated regional discharge rates. These methods yield CO_2 flux estimates from of 2-23 × 10^{10} mol a^{-1}, which represent ~1 to 10 % of the estimated global ridge flux (2.2 × 10^{12} mol a^{-1}).

V.2 INTRODUCTION

The study of carbon dioxide (CO_2) in volcanically-active regions provides insight into the sources of volatiles and the nature of the deep carbon cycle (Varekamp et al., 1992; Dasgupta and Hirschmann, 2010). Iceland is of particular interest due to its unique geological setting: it marks the intersection of plume-related volcanism with the subaerial expression of mid ocean ridge (MOR) spreading and allows direct and detailed sampling of both magmatic gases released by geothermal activity and Neogene volcanism. To date, however, there are relatively few studies which have focused on CO_2 characteristics in hydrothermal systems of Iceland. Poreda et al. (1992) conducted the most detailed investigation, characterizing He-CO_2 systematics in 17 high-temperature (HT) and 22 low-temperature (LT) geothermal sites throughout the various axial rift zones of Iceland, whereas other studies (e.g., Arnórsson and Barnes, 1983; Sano et al., 1985; Armannsson, 1998; Hilton et al., 1998b), are generally less extensive and/or more provincial in scope. The CO_2 systematics of Icelandic subglacial basalts are much more limited, as CO_2 contents of basalts typically fall below the detection limit (<30–40 ppm) for Fourier transform infrared (FTIR) spectroscopy analysis (Höskuldsson et

al., 2006; Tuffen et al., 2010). Some carbon data are available for drill core lavas collected in eastern Iceland as part of the Icelandic Research Drilling Project (IRDP) (Flowers et al., 1982). Drill core values range from 300-3000 ppm CO_2 with a median value of ~500 ppm; however, this value is expected to be skewed (to higher values) due to hydrothermal alteration of basalts (Sveinbjörnsdóttir et al., 1995).

The importance of CO_2 as the dominant non-aqueous volatile species lies in the fact that it is found in geothermal gases and serves as the principal carrier gas for other volatile species (e.g., helium), which are found in trace concentrations (O'Nions and Oxburgh, 1988). In basaltic magmas, a gas phase is typically present due to the relative insolubility of CO_2 and consequent transfer from melt to vapor during magma ascent. Upon subglacial eruption, Icelandic lavas are rapidly quenched forming pillow basalts and/or hyaloclastite formations. Over the past ~4 Ma, at least 20 distinct glacial periods have affected Iceland (Einarsson and Albertsson, 1988), and an ice sheet covered most of Iceland for the past ~2.5 Ma (Geirsdottir and Eiriksson, 1994). The most recent glacial period (i.e., Weichselian) lasted from ~100 - 10 ka BP (Einarsson and Albertsson, 1988; Norddahl, 1990; Ingolfsson, 1991; Tuffen et al., 2010). Sigvaldason (1968) showed that pillow basalts in Iceland form when glacial confining pressures are sufficient to inhibit significant exsolution of dissolved magmatic gases. By investigating CO_2 partitioning between vapor and dissolved components trapped in glassy rims of pillows, a number of intrinsic melt properties, including source volatile concentrations, storage depths and transport rates through the crust can be determined (Macpherson and Mattey 1994; Macpherson et al., 2005b).

An important caveat with carbon is that it is highly susceptible to alteration within the crust due to its reactive nature. As such, potential modification processes need to be taken into account prior to characterizing mantle source features. Recent efforts at sequestering and

permanently storing CO_2 in the basaltic Icelandic crust (Matter et. al., 2007; Oelkers et al., 2008) have identified basalt dissolution and reprecipitation of calcite in the Icelandic crust as a significant process. In addition, several studies (e.g., Macpherson and Mattey, 1994; Macpherson et al., 2005b) have highlighted the effects of pre-eruptive magma degassing. The superimposed effects of these various processes need to be determined in order to reveal and characterize the carbon abundance and isotopic features of the underlying mantle source.

By characterizing CO_2 source features, mantle CO_2 fluxes can be estimated. Flux estimates from different volcanic settings – arcs, ridges and plumes – provide important contrasts between tectonic settings and facilitate a better understanding of carbon cycling involving surface and mantle reservoirs. Total (global) volcanic CO_2 fluxes represent the aggregate of all subaerial (i.e., arcs and plumes) and submarine volcanic emissions (Marty and Tolstikhin, 1998). CO_2 fluxes from plume-related volcanic provinces such as Iceland are relatively poorly constrained, and thus a primary goal of this study is to derive estimates of CO_2 release via both geothermal and magmatic systems for comparison with better constrained ridge fluxes (Marty and Tolstikhin, 1998). Furthermore, accurate baseline volcanic CO_2 flux estimates are critical for placing anthropogenic outputs into a meaningful context (Gerlach, 2011).

We present new carbon (isotope and abundance) data for subglacial glasses and geothermal fluids of Icelandic neovolcanic and off-axis regions. These new CO_2 data are combined with previously published noble gas (He-Ne-Ar) constraints on the same sample suite (Füri et al., 2010) to discern the underlying processes controlling CO_2 abundance, isotope variations, and CO_2-noble gas relationships. We estimate initial carbon source characteristics for the various segments of the Icelandic mantle by investigating carbon characteristics of both geothermal fluids/gases and subglacially emplaced basalts. In addition,

we identify processes which may act to modify initial CO_2 compositions. Based on these data, we are able to provide the most comprehensive CO_2 flux estimates for Iceland to date.

V.3 GEOLOGICAL SETTING AND BACKGROUND

Iceland is a ~100,000 km^2 subaerial segment of the Mid-Atlantic Ridge, marked by enhanced crustal thickness, considered the result of anomalous melting associated with a mantle hotspot (White et al., 1995; Bjarnason et al., 1996; Darbyshire et al, 2000). Three-dimensional seismic tomography studies show a cylindrical-to-tabular shaped zone of low P- and S-wave velocities beneath central Iceland, suggesting that the underlying mantle is characterized by a hot, narrow conduit of upwelling asthenosphere (Wolfe et al., 1997). However, the depth of the conduit is widely debated; with some models indicating that the low velocity anomaly is confined to the upper mantle (Ritsema et al., 1999; Foulger et al., 2000; Foulger et al., 2001) while others suggest that the seismic velocity anomaly may extend as deep as the core-mantle boundary (Helmberger et al., 1998; Bijwaard and Spakman, 1999; Zhao, 2001). In this respect, several authors call for a mantle plume in order to explain the anomalous mantle. Regardless of the structure or depth of origin, geochemical evidence suggests that the hotspot is currently centered under central Iceland. For example, the highest ^{3}He/^{4}He ratios (up to ~34 R_A) within the neovolcanic rift zones are found in central Iceland and along the Eastern Rift Zone (ERZ) and in the South Iceland Volcanic Zone (SIVZ) (Condomines et al., 1983; Kurz et al., 1985; Hilton et al., 1990; Breddam et al., 2000; Macpherson et al., 2005a; Füri et al., 2010), consistent with the hypothesized center of the Icelandic hotspot from seismic investigations (Tryggvason et al., 1983). However, helium isotope studies both to the N and S of Iceland along the Kolbeinsey and Reykjanes ridges

(Macpherson et al., 2005b; de Leeuw, 2007) indicate that plume material is widely dispersed over lateral distances > 2000 km^2 (Hart et al., 1983; Poreda et al., 1986; Hilton et al., 2000).

Recent volcanic activity is widespread throughout much of Iceland and occurs in two types of neovolcanic zones: axial rift zones and off-rift volcanic flank zones (Sæmundsson, 1978; Jakobsson, 1979). Individual volcanic systems are typically comprised of a central volcano and/or surrounding fissure swarms (Sæmundsson, 1978; Jakobsson, 1979). Subglacial basalt compositions range from alkalic (off-axis) through transitional to tholeiitic along the axial rift zones. Axial rift zones represent the on-land equivalent of mid-ocean-ridge spreading and traverse Iceland connecting the Reykjanes and Kolbeinsey ridges. In southern Iceland, the axial rift zone is subdivided into the Western (WRZ) and Eastern (ERZ) Rift Zone segments which are separated by a transform fault system known as the South Iceland Seismic Zone (SISZ) (Figure V.1). The tholeiitic axial rift zone system extends to the north of the Vatnajökull glacier towards the Kolbeinsey Ridge along the Northern Rift Zone (NRZ). The off-axis volcanic flank zones consist of the South Iceland Volcanic Zone (SIVZ), the Snæfellsnes Volcanic Zone (SNVZ) and the Öræfajökull Volcanic Zone (OVZ) – all located on older basement and distinguished by slightly more alkalic volcanism (Oskarsson et al., 1982). The SIVZ is a direct continuation of the ERZ and represents an area characterized by rift
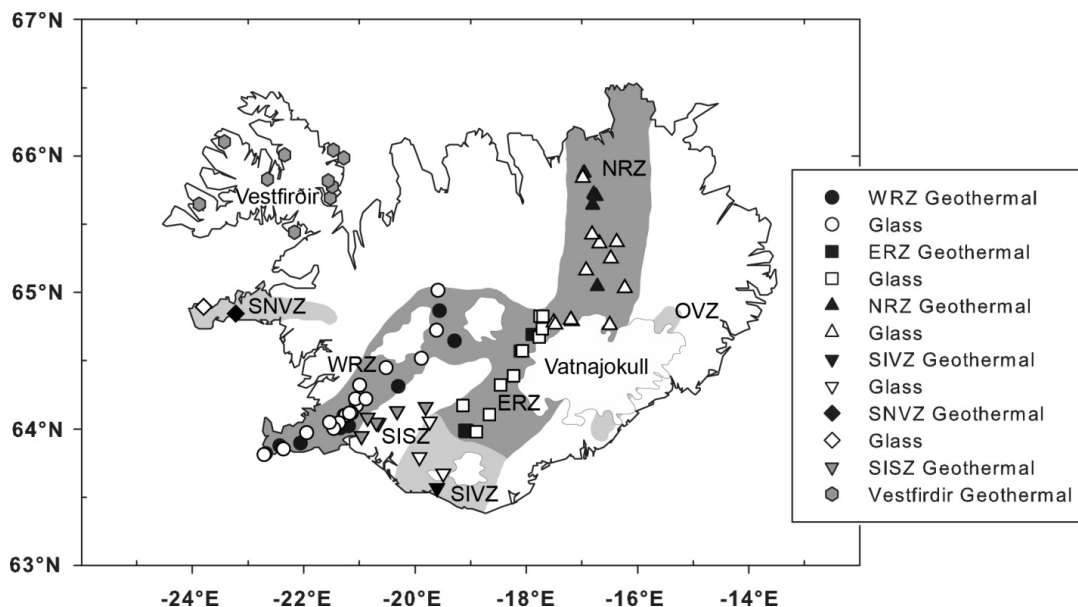
Figure V.1: Map of Iceland showing neovolcanic rift zones (light to dark grey), sample locations, and the location of current glacial cover. These include tholeiitic axial rift zones, i.e., the Western (WRZ), Eastern (ERZ), and Northern rift zones (NRZ), shaded with dark grey as well as transitional-alkalic to alkalic off-axis volcanic zones, i.e., the South Iceland Volcanic Zone (SIVZ), Snæfellsnes Volcanic Zone (SNVZ), and Öræfajökull Volcanic Zone (OVZ), shaded with light grey. Also shown are the South Iceland Seismic Zone (SISZ) and Vestfirðir located along the northwest peninsula. Sample locations for geothermal fluids are denoted with closed symbols and basalts with open symbols; black symbols refer to samples collected within the neovolcanic zones and grey symbols represent samples collected in older parts of the Icelandic crust. Subglacial basaltic glasses are shown with open symbols.

propagation to the south (Oskarsson et al., 1982; Einarsson, 2008). The SNVZ is distinct and classified as intraplate volcanism due to the fact that the area is not connected to any active rift zones and/or plate boundaries (Einarsson, 2008). It may, however, be a dying remnant of an earlier rift configuration, prior to the eastward migration of the current rift system (~6 Ma) (Oskarsson et al., 1982). In contrast, the OVZ in southeast Iceland likely represents the opening of old crust above or in close proximity to the mantle plume (Einarsson, 2008). Finally, the Vestfirðir region, located in northwest Iceland, is characterized by tholeiitic lavas which range in age from ~16 Myr furthest to the west to about 9 Myr in the southeast (McDougall et al., 1984; Hardarson et al., 1997).

The geochemical evolution of Iceland is complicated and likely involves mixing of a variety of mantle endmember compositions (e.g., plume vs. depleted upper-mantle). A variety of geochemical tracers have previously been employed in order to determine relative upper-mantle vs. plume contributions. For example, He and Ne isotopes – while apparently decoupled – are both consistent with contributions from depleted mid ocean ridge basalt (MORB)-mantle and a primordial, 'solar' mantle component (Trieloff et al., 2000; Dixon et al., 2000; Moreira et al., 2001; Dixon et al., 2003; Füri et al., 2010). Trace element and radiogenic isotope evidence suggests mantle source heterogeneities exist throughout the neovolcanic zones of Iceland (Thirlwall et al., 2004; Peate et al., 2010) with contributions from at least five distinct mantle components required to explain combined radiogenic (Pb-Sr-Nd) isotope ratios. Additional geochemical variations observed in submarine basalts from adjoining ridge segments (i.e., Reykjanes and Kolbeinsey ridges) suggest binary mixing between depleted asthenospheric mantle and relatively enriched Icelandic mantle plume material (Schilling, 1973; Hart et al., 1973; Sun et al., 1975; Hilton et al., 2000; Thirwall et al., 2004; Macpherson et al., 2005b). For example, $^{87}Sr/^{86}Sr$ and $^{3}He/^{4}He$ values increase northward along the Reykjanes Ridge as it shoals towards Iceland and reach a maximum near central Iceland before systematically decreasing with increasing distance away from Iceland along the Kolbeinsey Ridge. In addition to mantle source variations, there is evidence for crustal modification and several oxygen isotope studies of Icelandic basalts suggest near surface crustal assimilation and/or recycled oceanic crust in the enriched mantle source (Muhlenbachs et al., 1974; Burnard and Harrison, 2005; Thirwall et al., 2006).

Carbon dioxide (CO_2) abundance and isotope studies in Iceland are limited; however, studies from the HT axial rift zones suggest a mantle source characterized by higher than MORB-like $\delta^{13}C$ values (~-3.8 ± 0.7 ‰) with $CO_2/^3He$ ratios of ~6 × 10^9 (Poreda et al., 1992). In contrast, previous studies from off-axis regions (e.g., Vestfirðir; Hilton et al., 1998) reveal a lower range in $\delta^{13}C$ from -6 to -16 ‰ and $CO_2/^3He$ values that are generally lower than HT samples, varying over 4 orders of magnitude from 4 × 10^6 to 3 × 10^{10}. In addition, CO_2 abundance and isotope systematics of basalts from the adjacent Reykjanes and Kolbeinsey ridge segments suggest enrichments relative to the depleted MORB-mantle (73-194 ppm; Marty, 2012), with source estimates of CO_2 = 396 ppm and $\delta^{13}C$ = -3.9 ‰ for the a Reykjanes Ridge (de Leeuw, 2007) and CO_2 = 400 ± 100 ppm and $\delta^{13}C$ = -6 ± 1 ‰ for the Kolbeinsey Ridge (Macpherson et al., 2005b).

V.4 SAMPLING AND ANALYTICAL TECHNIQUES

V.4.1 Geothermal fluids and gases

Hydrothermal activity is pervasive throughout Iceland with high-temperature (HT) geothermal systems (>200 ºC) found in the axial rift zones and low-temperature (LT) systems (<200 ºC) in the off-axis volcanic flanks zones (Bodvarsson, 1961; Fridleifsson, 1979; Arnórsson et al., 2008). Both fluid and gas phase samples were collected from the Icelandic neovolcanic zones, including 21 samples from the Western Rift Zone (WRZ), 9 from the Eastern Rift Zone (ERZ), 14 from the Northern Rift Zone (NRZ), 2 from the South Iceland Volcanic Zone (SIVZ) and 2 from the Snæfellsnes Volcanic Zone (SNVZ). In addition, 9 samples were collected in the South Iceland Seismic Zone (SISZ) and 14 from the Vestfirðir region of the NW Peninsula (Figure V.1 – closed symbols). All samples were collected during

three sampling campaigns (summer 2006, 2007, and 2008) from a variety of sites, including:

(a) 10 fumaroles, (b) 15 bubbling hot pools, (c) 4 water springs, (d) 4 mud pots, and (e) 15

geothermal borehole wells. Forty-eight individual localities were sampled, along with 23

duplicate samples (e.g., same localities), making a total of 71 geothermal samples (Table V.1).

Fluids and gases were collected in evacuated low-He diffusivity 1720-glass flasks following

procedures to minimize atmospheric contamination (see Hilton et al., 2002 for sampling

details).

In the laboratory, an ultra high vacuum (UHV) extraction line was used to separate

light noble gases (He and Ne) from the condensable gas (mainly CO_2) fraction (see

Kulongoski and Hilton, 2002 for a description of the extraction line). Following sample inlet,

all fluid samples were acidified with phosphorus pentoxide to ensure complete release of CO_2

and, as a result, measured CO_2 abundances correspond to the total dissolved inorganic carbon

(DIC) content. A glass trap held at acetone-dry ice temperature was used to isolate water

vapor and a stainless-steel U-tube, held at liquid nitrogen temperature, was used to separate

CO_2 from non-condensable volatiles. The remaining light noble gases (He and Ne) were then

isolated using a hot (700 ºC) Ti-getter and charcoal finger held at liquid nitrogen temperature,

which effectively removed active gases (N_2, CO, CH_4) and heavy noble gases (Ar, Kr and Xe),

respectively. A calibrated fraction of the He and Ne gas was captured in an AR-glass

breakseal for transfer to a MAP-215 noble gas mass spectrometer for He isotope analysis (see

Füri et al., 2010 for measurement details and He results). Finally, the CO_2 fraction was

transferred to a Pyrex breakseal for transfer to a dedicated CO_2 cleanup line.

Table V.1: Carbon characteristics of Icelandic geothermal fluids and gases.

Location	Latitude (N)	Longitude (W)	Sample ID[a]	Sample[b] Type	Temp. (°C)	CO$_2$/^{3}He[c] (x10^9)	δ^{13}C ‰ vs. PDB	[CO$_2$] mmole/kg
Western Rift Zone (WRZ)								
Nesjavellir (Borehole)	64°05'45.6"	021°16'48.0"	ICE-1	B	240	-	0.40	-
			ICE-3	B	240	1.46	0.50	-
Nesjavellir (Bubbling pool)	64°05'36.6"	021°16'28.3"	ICE08-11	G	89.0	8.62	-4.69	-
			ICE08-12	G	89.0	5.59	-2.59	-
Svartsengi (Borehole HSH11)	63°52'32.8"	022°26'06.6"	ICE-5	B	240	1.54	-4.23	-
			ICE-6	B	240	1.61	-3.28	-
Reykjanes (Fumarole)	63°49'06.7"	022°41'04.7"	PBICE-1	G	100	1.67	-3.40	-
			PBICE-2	G	100	1.31	-2.99	-
Krísuvík (Fumarole)	63°53'43.1"	022°03'19.2"	PBICE-3	G	99.6	4.25	-3.43	-
			PBICE-4*	G	99.6	1.32	-3.93	-
Krísuvík (Bubbling pool)	63°53'43.1"	022°03'19.3"	ICE08-14	G	77.5	10.70	-4.23	-
			ICE08-15	G	77.5	4.79	-3.59	-
Hengill (Bubbling pool)	64°01'12.1"	021°23'41.6"	PBICE-9	G	72.8	4.17	-3.96	-
			PBICE-12	G	72.8	8.24	-4.45	-
Hengill (Fumarole)	64°00'25.0"	021°20'30.4"	ICE08-22	G	77.5	6.27	-3.10	-
Little Geysir (Bubbling pool)	64°18'38.4"	020°18'08.8"	PBICE-13	G	82.6	0.63	-2.73	-

Table V.1 continued

Location	Latitude (N)	Longitude (W)	Sample ID[a]	Sample[b] Type	Temp. (°C)	CO₂/³He[c] (x10⁹)	δ¹³C ‰ vs. PDB	[CO₂] mmole/kg
Little Geysir (Bubbling pool)	64°18'38.4"	020°18'08.8"	PBICE-14	G	82.6	0.60	-2.66	-
Kerlingafjöll (Bubbling pool)	64°38'37.0"	019°17'17.1"	PBICE-10	G	94.7	3.72	-4.06	-
Hveravellir (Bubbling pool)	64°51'55.6"	019°33'29.7"	PBICE-11	G	89.6	0.84	-5.05	-
Hveragerði (Fumarole)	64°01'20.1"	021°11'38.5"	PBICE-16	G	100.7	1.00	-2.36	-
			PBICE-8	G	100.7	1.97	-2.32	-
Eastern Rift Zone (ERZ)								
Landmannalaugar (Fumarole)	63°58'52.2"	019°05'21.3"	PBICE-5*	G	98.6	2.91	-3.04	-
Landmannalaugar (Spring)	63°59'32.7"	019°06'01.7"	ICE08-26*	W	99.5	1328	-2.21	1.95
Landmannalaugar (Fumarole)	63°59'21.2"	019°06'42.1"	ICE08-29*	G	99.1	28.7	-	-
Landmannalaugar (Pool)	63°59'26.8"	019°03'46.4"	ICE08-30*	W	64.9	165	-	0.19
Köldukvislabotnar (Borehole)	64°34'15.2"	018°06'39.9"	ICE08-17*	B	-	1760	-3.74	2.81
			ICE08-18*	B	-	1684	-2.54	2.87
Vonarskarð (Fumarole)	64°41'32.3"	017°53'47.5"	ICE08-16	G	97.7	14.1	1.62	-
			ICE08-21	G	97.7	7.81	1.42	-
Vonarskarð (Spring)	64°41'26.8"	017°52'53.9"	ICE08-13	W	64.5	27.5	-2.48	5.52

Table V.1 continued

Location	Latitude (N)	Longitude (W)	Sample ID[a]	Sample[b] Type	Temp. (°C)	CO₂/³He[c] (x10⁹)	δ¹³C ‰ vs. PDB	[CO₂] mmole/kg
Northern Rift Zone (NRZ)								
Krafla (Borehole 20)	65°42′16.3″	016°44′42.4″	ICE-11	B	-	4.92	-4.31	-
			ICE-12	B	-	3.98	-5.26	-
Krafla (Borehole 13)	65°42′31.4″	016°45′38.7″	ICE-10	B	-	3.8	-1.7	-
			ICE-17	B	-	6.11	-1.39	-
Krafla (Fumarole)	65°43′18.2″	016°47′15.5″	PBICE-20	G	76.5	2.93	-4.37	-
Krafla (Mud pot)	65°43′18.0″	016°47′15.5″	ICE08-06	G	96.7	4.58	-4.78	-
Krafla (Fumarole)	65°43′09.9″	016°47′17.4″	ICE08-10	G	96.7	18.4	-2.44	-
Námafjall (Mud pot)	65°38′26.9″	016°48′34.7″	ICE08-03	G	-	15.6	-5.29	-
Námafjall (Fumarole)	65°38′26.8″	016°48′30.4″	ICE08-02	G	-	8.78	-5.09	-
Þeystareykir (Mud pot)	65°52′23.0″	016°58′12.7″	ICE08-09	G	89.9	0.04	2.86	-
Askja, Víti crater (Bubbling pool)	65°02′40.4″	016°43′31.4″	PBICE-18	G	26.8	9.12	-3.58	-
Askja, Víti crater (Bubbling pool)	65°02′48.0″	016°43′29.2″	ICE08-05	G	30.5	9.43	-4.19	-
Kverkfjöll (Mud pot)	64°40′30.1″	016°41′33.6″	ICE08-19	G	-	7.75	-2.43	-
	64°40′30.1″	016°41′33.6″	ICE08-20	G	-	34.21	-1.98	-

Table V.1 continued

Location	Latitude (N)	Longitude (W)	Sample ID[a]	Sample[b] Type	Temp. (°C)	CO₂/³He[c] (x10⁹)	δ¹³C ‰ vs. PDB	[CO₂] mmole/kg
South Iceland Volcanic Zone (SIVZ)								
Seljavellir (Borehole)	63°33'56.1"	019°36'31.1"	ICE-8	B	50.0	0.491	-3.37	3.53
			ICE-9	B	50.0	0.648	-3.44	3.45
Snæfellsnes Volcanic Zone (SNVZ)								
Lýsuhóll (Borehole)	64°50'40.7"	023°13'10.6"	ICE-18	B	-	2.42	-6.61	-
Lýsuhóll (Borehole)	64°50'40.7"	023°13'10.6"	ICE-7	B	-	2.41	-6.07	-
South Iceland Seismic Zone (SISZ)								
Hæðaren.d.i (Borehole)	64°04'31.8"	020°51'36.3"	ICE-21	B	-	-	-3.47	-
			ICE-22	B	-	0.974	-4.52	-
Selfoss (Borehole)	63°56'46.3"	020°57'38.3"	PBICE-17	B	70.0	0.025	-18.8	-
			PBICE-19	B	70.0	0.021	-17.9	-
Þjórsárdalslaug (Bubbling pool)	64°09'41.7"	019°48'41.4"	ICE08-27	G	70.0	0.00001	-10.5	-
			ICE08-28	G	70.0	0.00002	-11	-
Flúðir (Borehole)	64°07'45.3"	020°19'25.0"	ICE08-23	B	-	1.17	-6.13	1.02
Ormsstaðir (Borehole)	64°02'29.9"	020°39'46.3"	ICE08-25	B	86.9	0.08	-5.89	0.35
Eyvik (Borehole)	64°02'48.4"	020°41'59.4"	ICE08-24	B	73.5	0.025	-2.88	3.02
Vestfirðir (NW Peninsula)								
Hveravik (Spring)	65°41'54.1"	021°33'35.2"	ICE-23	W	76.7	0.405	-3.79	0.81

Table V.1 continued

Location	Latitude (N)	Longitude (W)	Sample ID[a]	Sample[b] Type	Temp. (°C)	CO₂/He[c] (x10⁹)	δ¹³C ‰ vs. PDB	[CO₂] mmole/kg
Hveravik (Spring)	65°41′54.1″	021°33′35.2″	ICE-24	W	76.7	0.226	-	0.53
Laugarhóll (Bubbling pool)	65°46′51.5″	021°31′13.2″	ICE-25	G	40.2	0.001	-	-
			ICE-26	G	40.2	0.002	-	-
Goðdalur (Spring)	65°49′39.8″	021°35′30.2″	ICE-28	W	55.9	1.84	-	0.38
Gjögur (Bubbling pool)	66°00′01.7″	021°19′12.5″	ICE-29	G	28.6	0.0002	-	-
Gjögur (Bubbling pool)	66°00′01.7″	021°19′12.5″	ICE-30	W	71.6	0.59	4.57	0.28
Krossnes (Bubbling pool)	66°03′01.7″	021°30′22.5″	ICE-31	G	60.0	0.00008	-	-
			ICE-33	G	60.0	0.00002	-	-
Laugaland (Bubbling pool)	66°01′11.7″	022°23′43.8″	ICE-34	G	48.8	0.0007	-	-
Heyardalur (Bubbling pool)	65°50′23.0″	022° 40′39.9″	ICE-36	W	44.4	0.981	-8.81	0.35
Laugar, Orkubú Vestfjarðá (Borehole)	66°06′40.6″	023°27′17.4″	ICE-37	B	66.0	0.041	-3.84	0.29
Laugardalsá (Borehole)	65°39′23.0″	023°54′36.7″	ICE-38	W	-	0.157	-5.11	0.33
Reykhólar (Borehole)	65°27′15.8″	022°11′52.7″	ICE-39	B	95.0	2.78	-5.49	0.42

[a]Samples labeled ICE-X, PBICE-X, and ICE08-X were collected in 2006, 2007, or 2008, respectively.

[b]Samples are designated: G = gas, W = water, and B = collected from a borehole.

[c]Calculated using the total CO_2, He and $^3He/^4He$ (From Füri et al., 2010).

The condensable carbon dioxide (CO_2) sample fraction was further purified on a separate cleanup and quantification line, constructed from Pyrex glass, whereby CO_2 was separated from any sulfur-bearing species using a variable temperature trap. Following cleanup, the total amount of CO_2 was measured using a capacitance manometer in a calibrated volume thus enabling the CO_2 abundance to be combined with He content and $^3He/^4He$ values (Füri et al., 2010) to calculate the $CO_2/^3He$ ratio. Finally, CO_2 was re-frozen into a Pyrex tube for transfer to either a VG Prism mass spectrometer (2006, 2007) or a Thermo Finnigan Delta XP$_{plus}$ isotope ratio mass spectrometer (2008) for carbon isotopic ($\delta^{13}C$) analysis. Carbon isotope $\delta^{13}C$ (CO_2) values are reported relative to the international reference standard Vienna Pee Dee Belemnite (VPDB). Precision of individual analyses of standards and samples is less than 0.1 ‰; however, we estimate the accuracy of our $\delta^{13}C$ determinations (± 0.5 ‰) by repeat analyses of a working laboratory standard, itself calibrated relative to VPDB.

V.4.2 Subglacial basaltic glasses

For this study, we analyzed subglacial basaltic glasses collected from a total of 47 locations, divided between the WRZ (n = 17), ERZ (n = 10), NRZ (n = 16), SIVZ (n = 3), and SNVZ (n = 1) (Table V.2; Figure V.1). Basalts were analyzed for total CO_2 abundance and carbon isotope $\delta^{13}C$ values. Glasses were first ultrasonically cleaned in dichloromethane to remove any organic contaminants from the glass surface. Subsequently, approximately 300 mg of dried fresh glass, free of surficial alteration, phenocrysts, or large vesicles was handpicked using a binocular microscope. The selected glass was then ultrasonically cleaned in a 1:1 acetone-methanol mixture, dried, and transferred to a quartz-glass sample finger, evacuated to UHV and held at 150 ºC overnight.

Table V.2: Carbon characteristics of Icelandic subglacial basaltic glasses.

Location	Latitude (N)	Longitude (W)	Sample ID	Vesicle CO$_2$ (ppm)^a	Vesicle CO$_2$ δ^{13}C	Dissolved CO$_2$ (ppm)^b	Dissolved CO$_2$ δ^{13}C	Total CO$_2$ (ppm)^c	Total CO$_2$ δ^{13}C	CO$_2$/^{3}He (x 10^9)	CO$_2$/^{3}He^d corrected (x 10^9)	CO$_2$/Ar* (x 10^5)
Western Rift Zone (WRZ)			**WRZ**									
Skarðsmýrarfjall	64°02'37.6"	021°21'29.9"	SKARD-1	7	-26.5	12.1	-17.2	19.1	-20.6	21.7	-	-
Vifilsfell	64°02'55.4"	021°32'24.8"	VIF-1	1.1	n.d.	18.6	-8.6	19.6	-8.6	0.7	0.6	0.1
Miðfell	64°10'28.9"	021°02'50.9"	MID-1	242.1	-3.3	31.2	-6.3	273.3	-3.6	1.5	1.6	1.1
Arnarfell	64°13'02.3"	021°04'12.1"	MID-2	16.8	-21	18.1	-22.2	34.8	-21.6	11.1	-	-
Kálfstindar	64°13'06.2"	020°53'08.9"	MID-3*	48.8	-11.6	105.2	-7.9	154	-9.1	1.4	1.5	0.6
Nesjavellir	64°06'01.1"	021°14'50.4"	NES-1	32.8	-13.5	32.3	-3.3	65.1	-8.4	5.4	-	-
Ölfusvatnsfjöll	64°06'57.0"	021°08'26.4"	OLF-1	24.4	-11.2	13.5	-8.7	37.8	-10.3	2.4	2.9	2.5
Þrengsli	64°00'04.8"	021°27'45.4"	THREN-1*	23.4	-17.2	8.1	-13.4	31.5	-16.2	12.8	15.1	10.5
Reykjanesviti	63°48'44.6"	022°42'49.2"	REY-1*	50.7	-18.2	19.4	-20.8	70.1	-18.9	2.1	-	-
Hraunsvik	63°51'06.9"	022°22'07.2"	HRA-1*	16.2	-22	13.6	-14.2	29.9	-18.4	15.3	-	-
Mælifell	64°06'42.4"	021°10'51.5"	MAE-1*	17.9	-15.2	13.3	-7.5	31.2	-11.9	1.3	1.5	0.8
Lönguhlíðar	63°58'18.2"	021°56'42.2"	LON-1	17.5	-9.1	40	-7.8	57.4	-8.2	16.6	-	-
Ármannsfell	64°19'13.5"	020°59'43.9"	A1	23.4	-10	20.9	-8.6	44.3	-9.3	3.3	6.0	22.3
Þorólfsfell	64°26'55.6"	020°31'02.1"	A2	21.3	-16.3	22.3	-8.5	43.6	-12.3	3.6	4.2	3.0
Bláfell	64°30'56.3"	019°53'16.2"	A6	59.6	-26.7	98.1	-27.5	157.6	-27.2	28.0	29.9	16.3
Þverbrekknamúli-2	64°43'23.6"	019°36'52.7"	A8	13.4	-12.5	31	-9.1	44.4	-10.1	15.2	-	-
Arnarbæli	65°00'50.9"	019°35'20.7"	A9	14.6	-9.6	42.1	-6.9	56.7	-7.6	0.3	0.4	0.4
Eastern Rift Zone (ERZ)			**ERZ**									
Skerðingar-1	64°34'17.8"	018°04'14.3"	A13/ICE08R-09	16.7	-11.9	27.8	-7.5	44.5	-9.2	5.5	6.5	6.6
Kambsfell	64°49'38.5"	017°45'19.8"	A20/ICE08R-15	30.9	-13.3	48	-6.6	78.8	-9.3	0.9	1.0	0.7
Gnjótsá near Kambsfell	64°49'36.7"	017°42'08.2"	A21/ICE08R-16	7.2	-16.1	27.8	-8.4	35	-10	0.1	0.2	1.9
North of Valafell	64°43'49.9"	017°42'30.7"	A22/ICE08R-17	34.9	-6.7	64	-7.1	99	-7	0.6	1.0	2.8

Table V.2 continued

Location	Latitude (N)	Longitude (W)	Sample ID	Vesicle CO₂ (ppm)ᵃ	Vesicle CO₂ δ¹³C	Dissolved CO₂ (ppm)ᵇ	Dissolved CO₂ δ¹³C	Total CO₂ (ppm)ᶜ	Total CO₂ δ¹³C	CO₂/³He (x 10⁹)	CO₂/³Heᵈ corrected (x 10⁹)	CO₂/Ar* (x 10⁵)
Mið-Bálkafell	64°40'22.8"	017°45'58.0"	A24	58.1	-25.1	52.4	-19.2	110.5	-22.3	14.5	19.1	37.4
Kirkjuellsvatn	63°58'44.5"	018°53'46.6"	A27	28.2	-6.5	20.1	-11.8	48.4	-8.7	4.5	8.7	51.0
NW of Grænifjallgarður	64°06'20.8"	018°30'55.5"	A32	31.4	-19.3	16.5	-16	47.9	-18.2	4.8	8.7	28.9
Sigalda	64°10'19.8"	019°08'18.7"	A35	10	-17	53.3	-7.9	63.3	-9.4	0.9	2.1	23.3
Heljargjá	64°19'19.8"	018°27'37.8"	A36/ICE08R-23	11.6	-17.2	7.5	-12.3	19.1	-15.3	35.4	-	-
Bláfjall	64°23'22.4"	018°13'45.2"	ICE08R-13	26.6	-20.4	23.3	-8.5	50	-14.8	1.0	1.0	0.8
Northern Rift Zone (NRZ)			**NRZ**									
Hvammsfjöll	65°21'38.7"	016°41'11.4"	NAL-216	210.5	-7.2	34.8	-9.6	245.3	-7.6	10.3	17.8	45.8
Herðubreiðarfjöll	65°22'10.7"	016°22'29.5"	NAL-281	55.2	-16	44	-13.3	99.1	-14.8	1.5	-	-
Gæsahnjúkar	64°46'50.2"	017°30'40.7"	NAL-500	82.7	-12.5	43.6	-11.4	126.3	-12.1	8.3	-	-
Dyngjufjöll	65°09'42.1"	016°55'27.5"	NAL-584	49.5	-17.3	31.8	-26.4	81.2	-20.9	17.2	25.3	56.9
Upptyppingar	65°01'40.7"	016°13'44.4"	NAL-585	16.3	-17.1	20.4	-16.8	36.7	-16.9	11.6	14.2	7.2
Kistufell	64°47'23.8"	017°10'56.3"	NAL-595	54.4	-14.6	42.4	-12.3	96.9	-13.6	1.4	1.9	3.0
Kistufell	64°47'54.4"	017°12'01.2"	NAL-611	50.2	-6.9	15.2	-11.0	65.4	-7.9	0.8	-	-
Bláfjall	65°25'35.9"	016°48'56.2"	HS92-15	48.9	-8	67.3	-6.5	116.2	-7.1	1.0	1.2	0.6
Kvíhólafjöll	65°50'24.6"	016°59'10.4"	KVIH-1*	7	-14.1	24.3	-10.2	31.3	-11.1	20.7	51.4	369.2
Kvíhólafjöll	65°50'24.6"	016°59'10.4"	NAL-837*	8	-10	26.7	-5.6	34.6	-6.6	11.8	18.0	22.1
Hrúthálsar	65°19'25.7"	016°30'10.0"	NAL-828	13.4	-13.9	30.3	-5.1	43.7	-7.8	1.0	1.2	0.7
Kverkfjöll	64°49'00.0"	016°29'00.0"	KVK77	41.5	-25	41.9	-26.4	83.3	-25.7	40.4	-	-
Gæsahnjúkar	64°46'	017°29'	NAL-496*	79.3	-26.4	69.7	-24.9	149	-25.7	655	784	742.8
Eggert	65°15'	016°29'	NAL-688	15.2	-9.4	15.3	-10	30.5	-9.7	4.9	5.0	1.4
Upptyppingar	65°02'	016°14'	NAL-355*	23.5	-19.9	12.3	-13.3	35.8	-17.6	31.3	31.7	8.1
Upptyppingar	65°02'	016°14'	NAL-356*	25.1	-18.6	17	-16	42.1	-17.6	18.5	-	-

Table V.2 continued

Location	Latitude (N)	Longitude (W)	Sample ID	Vesicle CO$_2$ (ppm)^a	Vesicle CO$_2$ δ^{13}C	Dissolved CO$_2$ (ppm)^b	Dissolved CO$_2$ δ^{13}C	Total CO$_2$ (ppm)^c	Total CO$_2$ δ^{13}C	CO$_2$/^{3}He (x 10^9)	CO$_2$/^{3}He^d corrected (x 10^5)	CO$_2$/Ar* (x 10^5)
South Iceland Volcanic Zone (SIVZ)			**SIVZ**									
Réttarfell (Þórsmörk)	63°40'19.5"	019°29'32.4"	RÉT-1	44.5	-8.5	13.7	-10.3	58.2	-8.9	9.4	-	-
Þríhyrningur	63°47'33.0	019°55'27.3	TRÍ-3	18.04	-16.5	22.9	-17.0	40.9	-16.8	1.3	-	-
Hekla Area	64°02'15	019°46'14	BHE-43	40.56	-18.6	26	-22.0	66.6	-20	2.2	-	-
Snæfellsnes Volcanic Zone (SNVZ)			**SNVZ**									
Ólafsvíkurenni	64°53'39	023°47'48	OLAF-1	11.6	-11.3	5	-12.7	16.5	-11.7	1330	-	-

a = 700-900 °C temperature steps

b = 1000-1200 °C temperature steps

c = 700-1200 °C temperature steps

d = Degassing-solubility corrected using ^{4}He/^{40}Ar* ratio (See section 5.3)

Samples marked with an asterisk (*) are characterized by a late release of CO$_2$ during the extraction process and thus vesicle CO$_2$ = 700-1000 °C temperature steps and dissolved CO$_2$ = 1100-1200 °C temperature steps.

Carbon was extracted from basaltic glass chips using a stepped heating method (after Macpherson et al., 1999) on a dedicated all-glass extraction line. For each extraction, the temperature was incrementally raised in 100 ºC steps from 400 ºC to 1200 ºC (excluding the 500 ºC step), each lasting 30 minutes. During the first two heating steps (400 ºC and 600 ºC), samples were combusted in pure oxygen, generated using a CuO furnace, to remove possible C contaminants, whereas the 700 ºC to 1200 ºC pyrolysis steps (i.e., without oxygen) released magmatic carbon (Figure V.2). After each heating step, the CO_2 was separated from other non-condensable gases (i.e., H_2O, SO_2) using a liquid nitrogen cooled variable temperature trap. Following purification, total CO_2 abundances were measured in a calibrated volume using a Baratron capacitance manometer. CO_2 released during the (first two) combustion steps was not collected, as this gas is expected to be dominated by secondary surface contamination acquired by the glass post-eruption (Des Marais and Moore, 1984; Exley et al., 1986; Mattey et al., 1984, 1989). However, for the 700 ºC to 1200 ºC steps, CO_2 was collected in Pyrex® glass tubes at each successive temperature step for subsequent isotopic $\delta^{13}C$ analysis. Low temperature (700-900 ºC) CO_2 releases are taken to represent the vesicle carbon component whereas higher temperature (1000-1200 ºC) releases are combined and represent the "dissolved" carbon component (Figure V.2). Whenever the CO_2 yield from a single temperature step was deemed too small (< 3 ppm) for isotopic analysis, the CO_2 was combined with CO_2 released during the following step. All aliquots of CO_2 (corresponding to each temperature step) were analyzed for carbon isotopes ($\delta^{13}C$) using a VG Prism mass spectrometer (2006, 2007) or a Thermo Finnigan Delta XP_{plus} isotope ratio mass spectrometer (2008). Carbon isotope $\delta^{13}C$ (CO_2) values are reported relative to VPDB, with a precision of less than 0.1 ‰ and an accuracy of (± 0.5 ‰) based on reproducibility of laboratory standards relative to VPDB.

Magmatic (Total) Carbon = **Vesicle Component** + **Dissolved Component**
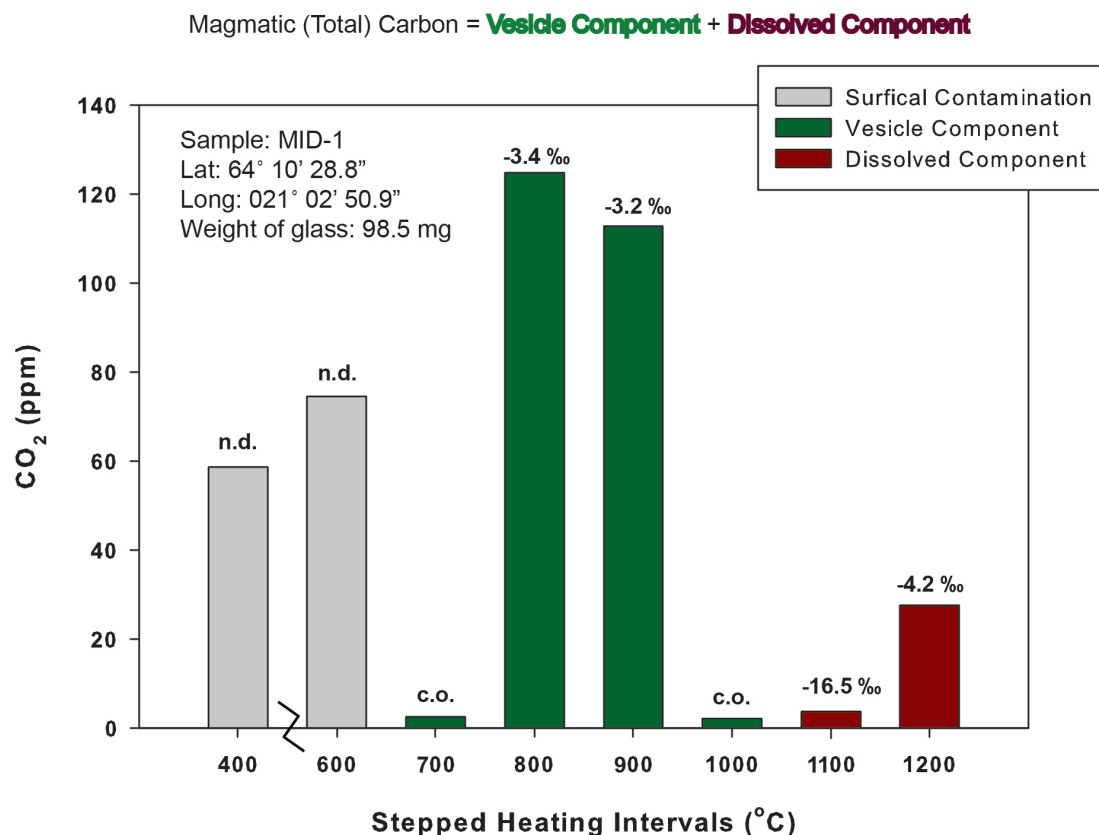
Figure V.2: Carbon content (ppm) release pattern as a function of incremental temperature step for a basalt sample (MID-1). CO_2 released between 400 – 600 ºC is derived from surficial contamination on the glass, CO_2 released from 700 – 900 ºC is derived from large vesicle-cited CO_2 within the glass and CO_2 released between 1000 – 1200 ºC represents CO_2 dissolved in the melt immediately prior to glass quenching. Carbon isotope values are also shown for individual temperature steps with ample CO_2 for a measurement. If the CO_2 yield from an individual step was too low, the CO_2 was carried over (c.o.) to the next temperature step. Carbon isotopes were not determined (n.d.) between 400 – 600 ºC, as this CO_2 is considered to be derived from surficial contamination.

V.5 RESULTS

V.5.1 Geothermal fluids

We report $\delta^{13}C$ values (vs. VPDB), CO_2 abundances (for fluid samples) and $CO_2/^3He$

ratios for a suite of 48 geothermal samples (Table V.1). Sample locations are given in Figure

V.1 (closed symbols). $CO_2/^3He$ and $\delta^{13}C$ variations as a function of latitude are plotted

(together with glass data) in Figures V.3a and V.3b, respectively.
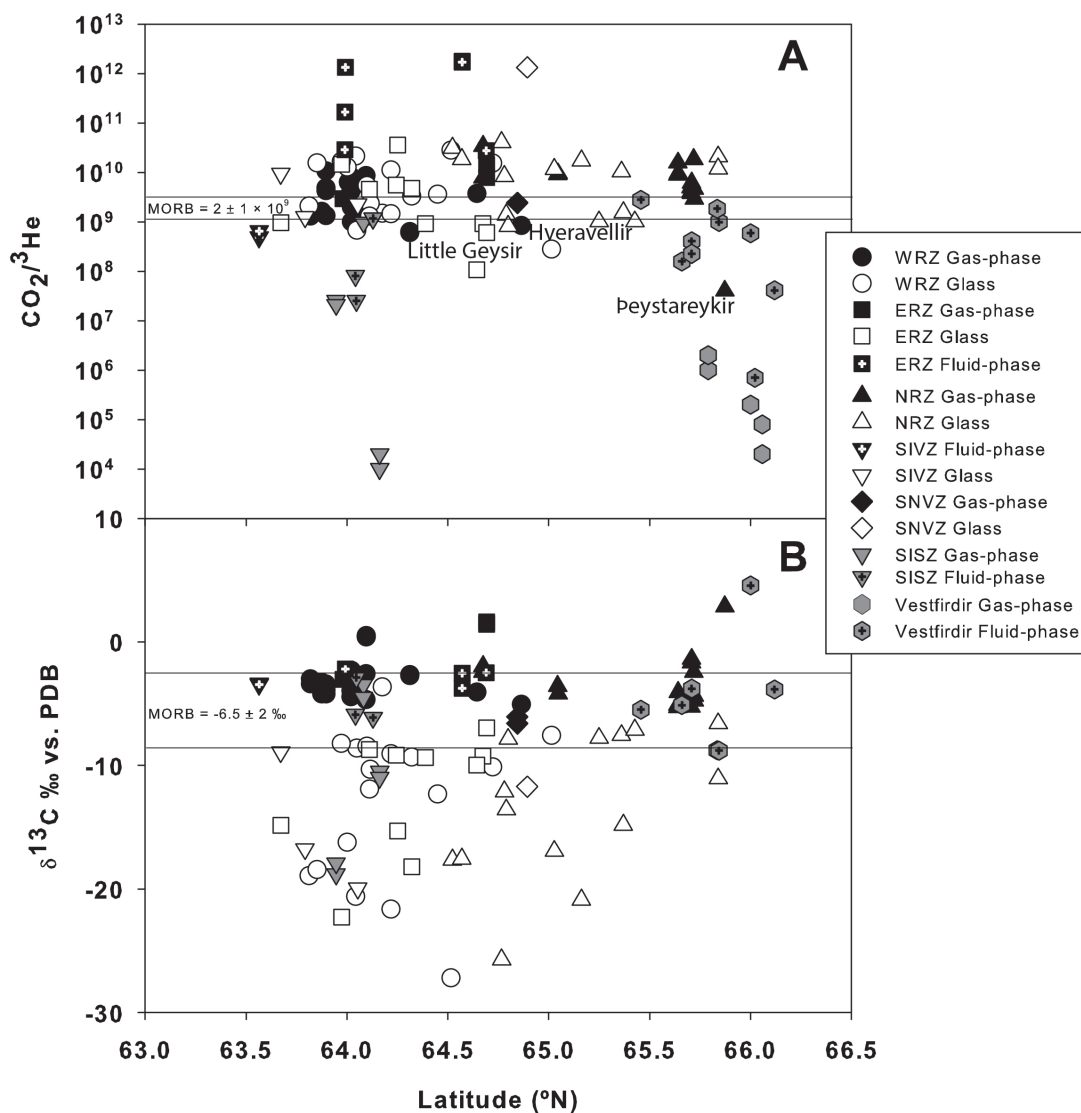
Figure V.3: $CO_2/^3He$ values (3a) and C-isotopes $\delta^{13}C$ (3b) as a function of latitude for geothermal fluids/gases and subglacial basalts of Iceland. Neovolcanic zone gas samples are show as black symbols and off-axis gas samples are represented by grey shaded symbols. Fluid samples are denoted with crosses. Subglacial basalt samples are represented with open symbols.

V.5.1.1 Geothermal carbon isotopes ($\delta^{13}C$)

Geothermal fluids and gases display carbon isotope values ranging from -18.8 to

+4.57 ‰ (Figure V.3b). Axial rift zone samples display a narrow range of $\delta^{13}C$ values

compared to Iceland as a whole, with WRZ values ranging from -5.1 to +0.5 ‰, ERZ from -

3.7 to +1.6 ‰ and NRZ from -5.3 to +2.9 ‰. In contrast, only two $\delta^{13}C$ values were obtained

in SIVZ geothermal samples, both ~ -3.4 ‰. Off-axis samples spanned a much greater range,

with SISZ values varying from -18.8 to -2.9 ‰, and Vestfirðir values ranging from -8.81 to

+4.57 ‰ (Figure V.3b). Notably, the lowest $\delta^{13}C$ (vs. VPDB) values are measured in the

Selfoss region of the SISZ and the highest value is from a bubbling pool in Gjögur, Vestfirðir

(Figure V.3b). The fact that off-axis samples have a much greater range in carbon isotope $\delta^{13}C$

values suggests that off-axis samples are more susceptible to modification than axial rift zone

samples (see Section 5.1). The mean carbon isotope value for all geothermal samples is -4.0 ±

3.7 ‰. However, as will be discussed in section 5.1.3, some LT off-axis samples display

extensively modified $\delta^{13}C$ characteristics, and thus if only axial rift zone (i.e., WRZ, ERZ,

NRZ) samples are considered then the average value increases to -3.1 ± 1.9 ‰. These values

are in good agreement with previous results (Poreda et al, 1992) whereby an average $\delta^{13}C$

value of -3.8 ± 0.7 ‰ was reported for HT CO_2-rich samples (n=8) from the axial rift zones

(i.e., WRZ, ERZ, NRZ) of Iceland.

V.5.1.2 Geothermal Abundance Characteristics and $CO_2/^3He$

Abundances of CO_2 were calculated for all 18 fluid phase samples, with

concentrations ranging between 0.28 and 5.52 [CO_2] mmole/kg H_2O (Table V.1). Generally,

neovolcanic samples displayed higher CO_2 abundances, ranging from 1.95 to 5.52 [CO_2] mmole/kg H_2O compared to off-axis samples, which ranged from 0.28 to 3.02 [CO_2] mmole/kg H_2O (see Figures V.4b and V.4d). Our samples are bracketed by previous results (Poreda et al., 1992), which range from 0.06 to 2310 [CO_2] mmole/kg H_2O for water and steam samples of Iceland. Notably, Poreda et al. (1992) also estimated gas concentrations in the steam phase (mmol of gas/ kg of steam) by dividing the volume of gas by the amount of condensate collected in the flask, however similar estimates are not made here due to the large error associated with this method of estimating steam [CO_2]. Significantly, the previously reported (n=4) water phase [CO_2] ranged from 0.06 to 1.24 [CO_2] mmole/kg H_2O (Poreda et al., 1992), in agreement with the range in fluid samples reported here.

In addition, we report $CO_2/^3He$ variations for geothermal fluids and gases by combining previously measured $^3He/^4He$ values and total helium on the present sample suite (Füri et al., 2010) with carbon concentrations (this work). $CO_2/^3He$ values vary over 8 orders of magnitude, from 1×10^4 to 2×10^{12}. Geothermal samples from neovolcanic zones vary from 4×10^7 to 2×10^{12}, with WRZ values spanning the range from 6×10^8 to 1×10^{10}, ERZ from 3×10^9 to 2×10^{12}, NRZ from 4×10^7 to 3×10^{10}, SIVZ from 5-6 $\times 10^8$, and at SNVZ both values are $\sim 2 \times 10^9$ (Figure V.3a – black symbols). In contrast, samples from older LT portions of the crust (i.e., SISZ and Vestfirðir) extend to significantly lower values, ranging from 1×10^4 to 3×10^9 (Figure V.3a – grey symbols) with a range in the SISZ from 1×10^4 to 1×10^9 and in Vestfirðir from 2×10^4 to 3×10^9. The wide range in observed values indicates that geothermal fluids and gases are likely susceptible to elemental fractionation processes – particularly in off-axis regions (see section 5.1).
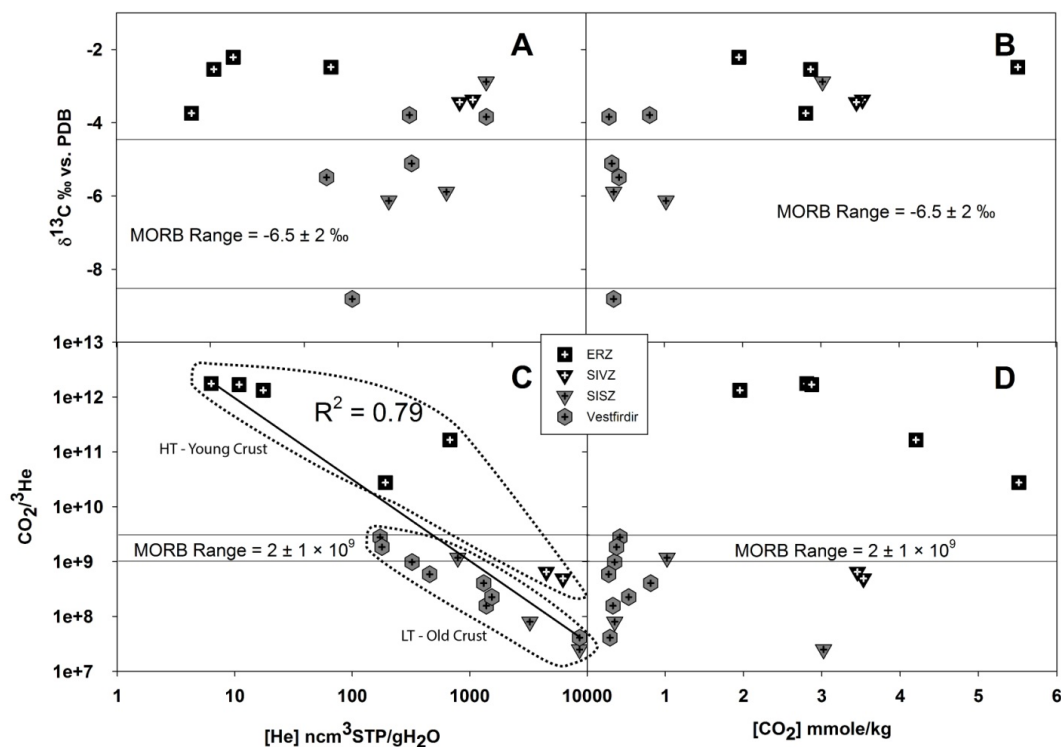
Figure V.4: $\delta^{13}C$ (a & b) and $CO_2/^3He$ (c & d) as a function of [He] and [CO_2] content for all fluid samples from younger neovolcanic zones (black symbols) and older off-axis areas of the Iceland crust (grey symbols). In Figure V.4c, we highlight two distinct fields (old vs. young crust) defined by their combined $CO_2/^3He$ and [He] characteristics and sample localities. In addition, there is a broad negative correlation ($R^2 = 0.79$) between $CO_2/^3He$ and [He] content. Figure V.4d - Off-axis samples (grey) are marked by low CO_2 and low $CO_2/^3He$ values, suggesting CO_2 loss due to calcite precipitation in older, lower enthalpy portions of the Icelandic crust.

V.5.2 Basalts

Carbon dioxide concentrations (i.e., [CO_2]) and isotopic ratios ($\delta^{13}C$) were measured in 47 fresh subglacial basalts from Iceland which were previously characterized for He-Ne-Ar characteristics (Füri et al., 2010). Sample locations are provided in Figure V.1 (open symbols) and $CO_2/^3He$ and $\delta^{13}C$ variations are plotted as a function of latitude, along with geothermal values, in Figures V.3a and V.3b respectively.

V.5.2.1 Basalt carbon isotopes (δ^{13}C)

Carbon was extracted from basalts using the stepped heating technique (Mattey et al., 1984; Macpherson and Mattey, 1994; Macpherson et al., 1999), with the principal advantage being that vesicle-sited CO_2 (CO_2^v) can be resolved from CO_2 dissolved (CO_2^d) in the glass matrix and therefore carbon isotopic ratios from both components can be determined. In order to illustrate typical CO_2 release patterns, we plot carbon content (ppm) as a function of incremental temperature step for a basalt sample (MID-1). CO_2 releases are marked by three distinct phases: 1) CO_2 released between 400 - 600 ºC, derived from surficial contamination, 2) vesicle-sited CO_2 released at intermediate temperatures (700 - 1000 ºC), and 3) matrix-dissolved CO_2 released at higher temperatures (1100 - 1200 ºC).

Vesicle CO_2^v releases ranged from -26.7 to -3.3 ‰ with an average value of -14.9 ± 5.9 ‰ whereas dissolved $\delta^{13}C^d$ values ranged from -27.5 to -3.3 ‰ and had an average value of -12.4 ± 6.4 ‰. Total magmatic carbon (weighted average of the two components) ranged from -27.2 to -3.6 ‰ with an average value of -13.3 ± 5.8. Carbon isotopic data from the stepped heating technique are given in Table V.3 and summarized in Table V.2.

WRZ samples have an average $\delta^{13}C^d$ of -11.7 ± 6.6 ‰ and range from -27.5 ‰ to -3.3‰. WRZ vesicle samples display an average $\delta^{13}C^v$ of -15.2 ± 6.5 ‰ and range from -26.7 ‰ to -3.3‰. NRZ samples display $\delta^{13}C^d$ values between -26.4‰ and -5.1‰, with an average $\delta^{13}C^d$ value of -11.7 ± 7.6 ‰. NRZ $\delta^{13}C^v$ values range from -26.4 ‰ to -6.9‰, with an average of -14.5 ± 6.1 ‰. ERZ samples display a slightly higher average $\delta^{13}C^d$ of -10.5 ± 4.

Table V.3: Stepped heating carbon concentration and isotope ratio results of Icelandic glasses.

Location	Sample ID	Weight (mg)	400°C ppm CO₂	600°C ppm CO₂	700°C ppm CO₂	700°C δ¹³C	800°C ppm CO₂	800°C δ¹³C	900°C ppm CO₂	900°C δ¹³C	1000°C ppm CO₂	1000°C δ¹³C	1100°C ppm CO₂	1100°C δ¹³C	1200°C ppm CO₂	1200°C δ¹³C
Western Rift Zone (WRZ)	**WRZ**															
Skarðsmýrarfjall	SKARD-1	199.4	99.2	63.3	2.2	c.o.	1.6	c.o.	3.1	-26.5	2.9	c.o.	3.0	-23.4	6.2	-11.2
Vifilsfell	VIF-1	205.8	32.4	13.2	0.5	c.o.	0.1	c.o.	0.0	c.o.	0.5	-8.6	2.3	n.d.	16.2	n.d.
Miðfell	MID-1	98.5	58.6	74.3	2.5	c.o.	124.7	-3.4	112.8	-3.2	2.1	c.o.	3.7	-16.5	27.5	-4.2
Arnarfell	MID-2	210.0	169.7	107.1	3.6	c.o.	5.2	-21.0	2.4	c.o.	5.6	-22.2	12.2	n.d.	5.8	n.d.
Kálfstin.dar	MID-3*	107.3	173.4	63.4	9.1	c.o.	25.1	-8.9	8.2	c.o.	6.4	-18.1	46.3	-9.4	58.9	-6.7
Nesjavellir	NES-1	180.6	132.4	95.5	17.1	n.d.	2.6	c.o.	13.1	-13.5	9.9	-3.5	8.9	n.d.	13.5	-3.1
Ölfusvatnsfjöll	OLF-1	190.6	194.5	136.5	5.4	c.o.	11.5	-6.9	2.2	c.o.	5.3	-20.8	2.4	c.o.	11.1	-8.7
Þrengsli	THREN-1*	275.7	120.5	362.6	3.8	c.o.	10.5	-12.6	4.1	c.o.	5.0	-24.4	2.8	c.o.	5.3	-13.4
Reykjanesviti	REY-1*	97.5	255.5	170.3	15.4	-20.2	17.2	-19.6	10.9	c.o.	7.2	-15.2	12.9	c.o.	6.5	-20.8
Hraunsvík	HRA-1*	206.1	58.9	53.9	4.1	c.o.	4.5	-21.9	2.5	c.o.	5.1	-22.1	3.7	c.o.	10.0	-14.2
Mælifell	MAE-1*	296.5	315.5	94.8	1.8	c.o.	9.7	-12.7	4.5	c.o.	1.9	-19.6	2.6	c.o.	10.7	-7.5
Lönguhlíðar	LON-1	314.9	74.0	14.4	3.7	c.o.	6.6	-8.9	7.2	-9.3	4.9	-10.2	30.2	-7.2	4.9	-9.5
Ármannsfell	A1	274.1	40.9	14.1	3.4	c.o.	14.1	-8.5	3.2	c.o.	2.7	-14.2	5.8	-10.3	15.1	-8.3
Þórólfsfell	A2	276.3	356.0	353.0	6.7	c.o.	5.1	-16.8	4.1	c.o.	5.5	-15.8	6.5	c.o.	15.8	-8.5
Bláfell	A6	317.6	132.1	258.2	12.6	-28	25	-25.9	22	-26.7	26.1	-28.3	35.6	-27.5	36.4	-26.9
Þverbrekknamúli-2	A8	298.8	39.1	17.5	2.5	c.o.	1.7	c.o.	9.2	-12.5	8.2	-11.7	18.1	-7.8	4.7	-9.4
Arnarbæli	A9	279.9	129.9	19.4	3.6	c.o.	8.9	-8.7	0.5	c.o.	1.6	-14.4	35	-7.8	7.1	-2.6
Eastern Rift Zone (ERZ)	**ERZ**															
Skerðingar-1	A13/ICE08 R-09	287.9	104.5	33.5	1.1	c.o.	3.7	c.o.	1.0	-15.2	10.9	-10.2	3.4	c.o.	24.4	-7.5
Kambsfell	A20/ICE08 R-15	338.9	157.9	459.8	12.4	-11.4	10.0	-13.7	8.4	-15.8	37.0	-6.9	11.1	-5.6	0.0	n.d.
Gnjótsá near Kambsfell	A21/ICE08 R-16	287.7	275.2	33.5	2.9	c.o.	1.1	c.o.	3.3	-16.1	6.9	-10.3	18.8	-6.8	2.1	-15.6
North of Valafell	A22/ICE08 R-17	268.6	4.7	195.1	4.5	c.o.	25.4	-6.2	5.1	-9.2	24.0	-7.2	8.6	-8.9	31.5	-6.6
Mið-Bálkafell	A24	348.5	153.0	39.5	24.3	-26.5	21.6	-24.2	12.2	-24.1	12.2	-24.3	15.2	-18.4	24.9	-17.1
Kirkjuellsvatn	A27	327.6	60.8	103.8	18.0	-4.2	6.8	-9.1	3.4	-13.8	11.1	-9.8	6.0	-13.5	3.1	-15.8

Table V.3 continued

86

Location	Sample ID	Weight mg	400°C ppm CO₂	600°C ppm CO₂	700°C ppm CO₂	700°C δ¹³C	800°C ppm CO₂	800°C δ¹³C	900°C ppm CO₂	900°C δ¹³C	1000°C ppm CO₂	1000°C δ¹³C	1100°C ppm CO₂	1100°C δ¹³C	1200°C ppm CO₂	1200°C δ¹³C
NW of Grænifjallgarður																
	A32	316.2	45.9	54.4	11.3	-19.5	10.1	-19.6	9.9	-18.8	6.0	-16.7	8.0	-17.9	2.4	-8.4
Sigalda	A35	333.2	64.5	35.1	2.7	c.o.	1.9	c.o.	4.4	-17.0	16.7	-7.8	9.8	-9.6	26.8	-7.4
Heljargjá	A36/ICE08R-23	290.5	164.4	12.9	1.4	c.o.	1.7	c.o.	3.8	-19.2	4.7	-14.4	4.1	c.o.	3.4	-12.3
Bláfjall	ICE08R-13	287.9	128.3	80.6	11.6	-22.1	3.7	c.o.	11.4	-19.0	2.9	-12.6	19.8	-7.8	0.6	-13.4
Northern Rift Zone (NRZ)	NRZ															
Hvammsfjöll	NAL-216	287.1	16.6	40.1	165	-5.7	28.3	-12.4	17.2	-13.5	11.7	-12.2	5.9	-11.7	17.2	-7.1
Herðubreiðarfjöll	NAL-281	291.5	328.5	110	30.6	-14.5	13.4	-18.7	11.2	-17.1	9.4	-15.3	20.9	-13.4	13.7	-11.6
Gæsahnjúkar	NAL-500	163.4	63.1	48.9	22.3	n.d.	26.9	-8.18	33.5	-15.88	8	c.o.	16.8	-13.69	18.8	-8.48
Dyngjufjöll	NAL-584	288.2	227.5	23.4	5.2	c.o.	2.6	-22.3	8.7	-22.2	32.9	-14.8	15.7	-25.2	16.1	-27.7
Upptyppingar	NAL-585	249.7	107	70.8	3.1	c.o.	4.7	-20.46	8.5	-13.93	6	c.o.	3.9	-19.04	10.5	-14.62
Kistufell	NAL-595	287.7	55.2	49.5	7	-20.3	36.8	n.d.	10.6	-9.7	4.9	-16	10.1	-20.1	27.5	-8.7
Kistufell	NAL-611	241.1	86.8	6.6	5.7	c.o.	42.7	-6.6	1.8	-15.3	1.7	-13.4	2.5	c.o.	11.1	-10.7
Bláfjall	HS92-15	301.2	56.9	38.2	3.9	c.o.	35.3	-7.2	9.6	-11.3	4.2	c.o.	6.2	-14.1	56.9	-5.1
Kvíhólafjöll	KVIH-1*	109.3	20.2	10.5	0	n.d.	0	n.d.	0	n.d.	7	-14.07	12.9	-11.55	11.4	-8.74
Kvíhólafjöll	NAL-837*	211.4	18.3	9.6	0.1	c.o.	0.1	c.o.	0.9	c.o.	6.9	-10.01	10.3	-6.05	16.3	-5.27
Hrúthálsar	NAL-828	319	43.9	20.8	1.6	c.o.	1.7	c.o.	1.3	-16.4	8.7	-12.5	18.8	-5.1	11.5	-5.1
Kverkfjöll	KVK77	294.7	128.5	47.7	19.9	-26	10.2	-23.3	11.4	-24.7	17.7	-27	15.3	-25.3	8.9	-27.3
Gæsahnjúkar	NAL-496*	288	425.6	183.7	22.1	n.d.	22.5	-26.29	34.7	-26.42	27.3	-26.43	23.8	-24.24	18.6	-23.51
Eggert	NAL-688	388.6	21.6	40.1	2.3	c.o.	1.3	c.o.	11.6	-9.42	1.5	c.o.	3.9	-15.16	9.9	-7.17
Upptyppingar	NAL-355*	251.1	86.2	59.9	3.2	c.o.	2.7	c.o.	7.1	-20.04	10.5	-19.74	4.3	c.o.	8	-13.29
Upptyppingar	NAL-356*	245.9	43.3	71.3	3.8	c.o.	3.7	c.o.	11.2	-18.41	6.4	-19.03	8.1	-17.56	8.9	-14.49

Table V.3 continued

Location	Sample ID	Weight	400°C	600°C	700°C	700°C	800°C	800°C	900°C	900°C	1000°C	1000°C	1100°C	1100°C	1200°C	1200°C
		mg	ppm CO$_2$	ppm CO$_2$	ppm CO$_2$	δ^{13}C	ppm CO$_2$	δ^{13}C	ppm CO$_2$	δ^{13}C	ppm CO$_2$	δ^{13}C	ppm CO$_2$	δ^{13}C	ppm CO$_2$	δ^{13}C
South Iceland Volcanic Zone (SIVZ)	**SIVZ**															
Réttarfell (Þórsmörk)	RET-1	271.5	572.9	139.6	9	-9.5	20.5	-7.9	15	-8.7	7.6	-8.9	4.9	c.o.	1.1	-12.1
Þríhyrningur	TRI-3	358.1	116.3	56.1	4.2	c.o.	7.1	-17.1	6.7	-15.3	7	-14.6	11.7	-19.2	4.1	-14.7
Hekla Area	BHE-43	322.6	482.1	32.1	16.5	-14	12.3	-24.5	11.8	-19.1	9.1	-23.8	13.3	-21.3	3.7	-20.1
Snæfellsnes Volcanic Zone (SNVZ)	**SNVZ**															
Ólafsvíkurenni	OLAF-1	301.2	28.6	10.6	1.6	c.o.	2.2	c.o.	2.4	-12.8	5.5	-9.5	3.8	c.o.	1.2	-12.7

c.o. = carried over to the next temperature step, when the yield from an individual temperature step was deemed too small (i.e., < 3 ppm).

n.d. = not determined

‰ and range from -19.2 ‰ to -6.6‰. ERZ vesicle samples display an average $\delta^{13}C^v$ of -15.4 ±

5.9 ‰ and range from -25.1 ‰ to -6.5‰. SIVZ samples display $\delta^{13}C^d$ values between -22.0 ‰

and -10.3 ‰, with an average $\delta^{13}C^d$ value of -16.4 ± 5.9 ‰. SIVZ $\delta^{13}C^v$ values range from -

18.6 ‰ to -8.5‰, with an average of -14.5 ± 5.3 ‰. Just one sample was collected in the

SNVZ, yielding a $\delta^{13}C^d$ value of -12.7 ‰ and $\delta^{13}C^v$ of -11.3 ‰ (Figure V.3b). Notably,

several samples from the axial rift zones display $\delta^{13}C^d$ below −25‰, suggesting degassing

fractionation (Macpherson and Mattey, 1994) and/or assimilation of an organic carbon

component (Shaw et al., 2004). In section 5.2, we consider various degassing and assimilation

scenarios and model these data.

V.5.2.2 Basalt CO_2 abundance characteristics and $CO_2/^3He$

Carbon dioxide (CO_2) contents in hyaloclastite glasses of Iceland are low (typically <

100 ppm; this work) compared to typical ocean basalts (73-194 ppm; Marty, 2012). The

average vesicle CO_2^v content is 39 ± 46 ppm vs. an average dissolved CO_2^d content of 33 ± 22

ppm, indicating that carbon contents are dominated by residual CO_2 following extensive

degassing. The average magmatic carbon ($CO_2^m = CO_2^v + CO_2^d$) content of subglacial basalts

is 70 ± 54 ppm. All carbon concentration and isotope data from the stepped heating extraction

technique are summarized in Table V.2.

Carbon dioxide (CO_2) contents of Iceland basalts are shown in Figure V.5, which

plots CO_2^v vs. CO_2^d. Approximately half of samples fall below/above the 1:1 line, indicating

that the total CO_2^m is distributed evenly. Two samples, one from the NRZ (NAL-216) and one

from the WRZ (MID-1), display significantly higher CO_2^v vs. CO_2^d, reflecting greater

retention of vesicles in these samples as they possess CO_2^d values (30-35 ppm) similar to other

NRZ and WRZ samples (Figure V.5). This concentration contrast may represent similar amounts of degassing but different confining pressures due to different glacial cover thicknesses and thus less loss of vesicles. Notably, these are the two highest concentration samples (CO_2^m = 245 and 273 ppm, respectively; Table V.2). In contrast, sample MID-3 displays the highest CO_2^d of all samples while maintaining relatively typical CO_2^v contents. The gas rich nature of Miðfell has previously been observed and subsequently exploited in a number of studies (Trieloff et al., 2000; Füri et al., 2010; Mukhopadhyay, 2012). Notably, these three samples are the only samples that have CO_2^v and CO_2^d both greater than 100 ppm (Table V.2). Indeed there are a total of 6 samples only that have a (combined) magmatic CO_2 (CO_2^m) greater than 100 ppm, illustrating the fact that most Icelandic glasses are depleted in CO_2 relative to submarine erupted MORB

By combining previously published helium isotope (^{3}He/^{4}He) and He abundance data (Füri et al., 2010) with measured CO_2 contents, we calculate CO_2/^{3}He values for the present sample suite. The total range of CO_2/^{3}He values extends from 1×10^8 to 1×10^{12}, with an average value of $28 \pm 120 \times 10^9$. WRZ samples vary from 3×10^8 to 3×10^{10}, ERZ range from 1×10^8 to 4×10^{10}, NRZ from 8×10^8 to 7×10^{11}, SIVZ from 1-9 $\times 10^9$ and at SNVZ the only value measured was 1×10^{12} (Figure V.3a – open symbols). Notably, no basalt CO_2 was measured in the older portions of the crust (i.e., SISZ and Vestfirðir) due to the lack of fresh glasses. These results, together with geothermal data, expand the CO_2 database for Iceland and demonstrate that the range in CO_2 characteristics is much broader than was previously reported (Poreda et al., 1992).
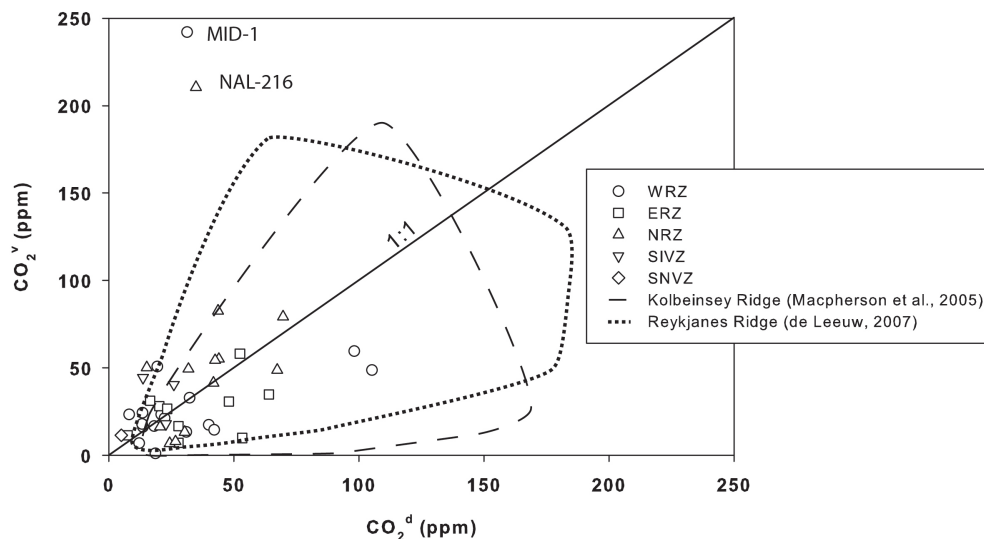
Figure V.5: Plot of CO_2 contained in vesicles (CO_2^v) vs. CO_2 in dissolved (CO_2^d) matrix measured by stepped heating methods. Magmatic CO_2 (CO_2^m) is uniformly divided between CO_2^v and CO_2^d in Iceland. Also shown are CO_2^v vs. CO_2^d values for the adjacent ridge segments: Kolbeinsey (Macpherson et al., 2005) and Reykjanes (de Leeuw, 2007).

V.6 DISCUSSION

In this section we identify geothermal and subglacial basalt samples that display carbon isotope and abundance characteristics that are likely representative of the Icelandic mantle source vs. samples whose carbon characteristics have been compromised by secondary processes. In this regard, geothermal and basalt samples are dealt with separately as they are subject to different modification processes. By identifying unmodified samples, we demonstrate how mantle source carbon characteristics can be determined and used to estimate carbon fluxes.

V.6.1 Geothermal sample integrity and modification

By making the assumption that hydrothermal systems in Iceland act to transfer magmatic volatiles from source to surface we can identify processes that act to modify magmatic volatile signatures during transport. However, intrinsic carbon characteristics can also be modified prior to interaction with the hydrothermal system – due to degassing from the magma chamber. In this respect, magma degassing can modify the $CO_2/^3He$ and $\delta^{13}C$ characteristics of both glasses and fluids, due to solubility differences between CO_2 and He in basaltic parental melts (Hilton et al., 1998a). Following the transfer of volatiles from magma chamber to hydrothermal system there are a number of remaining processes which can modify carbon characteristics within the shallow crust: (1) phase-separation and hydrothermal degassing (e.g., vapor/steam separation and/or gas exsolution) can significantly alter $CO_2/^3He$ and $\delta^{13}C$ due to solubility differences between CO_2 and He in water (Ray et al., 2009), and (2) CO_2 sequestration resulting from calcite precipitation, can modify $CO_2/^3He$ values while fractionating $\delta^{13}C$ (Ray et al., 2009). To assess the effects of magma degassing, phase separation and/or calcite precipitation, we first investigate latitudinal variations in $\delta^{13}C$ and $CO_2/^3He$ (Figure V.3) and the relationship between fluid volatile contents (i.e., [He] and [CO_2]), $\delta^{13}C$ and $CO_2/^3He$ (Figure V.4) in order to identify the origins of extreme values.

V.6.1.1 Pre-eruptive magma degassing

The He–CO_2 systematics of gases and fluids can potentially be modified by pre-eruptive magma degassing, prior to interaction with the hydrothermal system. If we assume that hydrothermal gases are derived from a tholeiitic melt and that solubility differences (i.e., $S_{He} = 6.4 \times 10^{-4}$ cm^3 STP/g; $S_{CO2} = 2.7 \times 10^{-4}$ cm^3 STP/g) between individual species (i.e., He and CO_2) will induce elemental fractionation upon degassing, then lower $CO_2/^3He$ (Hilton et al., 1998a) will be produced in residual gases remaining in the melt phase. The fractionation

factor (α) between He and CO_2 is expressed as the inverse ratio of their solubilities and is (α =) ~ 2.35. Similarly, $\delta^{13}C$ (CO_2) values are expected to decrease ($\Delta_{vapor-melt}$ = ~-2 to -4) in the residual melt phase upon degassing (Javoy et al., 1978). Variations in the type (open vs. closed system) and extent of degassing will affect the degree of fractionation (see Section 5.2.1 for further details).

Elemental $CO_2/^3He$ ratios were determined for a total of 43 axial rift zone gas and fluid samples. If we assume upper mantle starting $CO_2/^3He$ compositions, we note that only 3 samples displayed $CO_2/^3He$ values below the canonical MORB range ($2 \pm 1 \times 10^9$): Little Geysir = ~ 6×10^8, Hveravellir = 8×10^8 and Þeystareykir = 4×10^7 (Figures V.3 and V.6), indicating that pre-eruptive degassing and/or calcite precipitation affects very few axial rift zone gas and fluid samples. In contrast, the majority of off-axis samples display $CO_2/^3He$ below the MORB threshold, suggesting either a much different degassing history or, more likely, a pervasive secondary modification process (e.g., calcite precipitation) which ubiquitously modifies all off-axis hydrothermal samples. Assuming that fluid and gas samples have both MORB-like $CO_2/^3He$ and $\delta^{13}C$ starting compositions of $2 \pm 1 \times 10^9$ and of -6.5 ± 2 ‰ respectively (Sano and Marty, 1995; Hilton et al., 1998a), including Little Geysir, Hveravellir and Þeystareykir, the minimum possible $CO_2/^3He$ value achievable by closed system degassing is 5.5×10^8 (i.e., $2 \times 10^9/\alpha$), with a corresponding $\delta^{13}C$ value of -10.5 ‰ (Δ = -4‰; Javoy et al., 1978). Therefore the $CO_2/^3He$ values observed at Little Geysir and Hveravellir could potentially be explained by closed system degassing; however, an unlikely positive isotope fractionation factor of ~1.7 ‰ would be necessary in order to explain the observed $\delta^{13}C$ values. Alternatively, lower than MORB $CO_2/^3He$ values may result from magmatic degassing processes prior to interaction with the hydrothermal system whereas positive $\delta^{13}C$ values may be the result of mixing with ^{13}C enriched crustal carbon within the shallow crust. In contrast, the $CO_2/^3He$ ratio of Þeystareykir is not consistent with closed

system degassing and is better explained by calcite precipitation in a HT environment (Figure

V.6b).
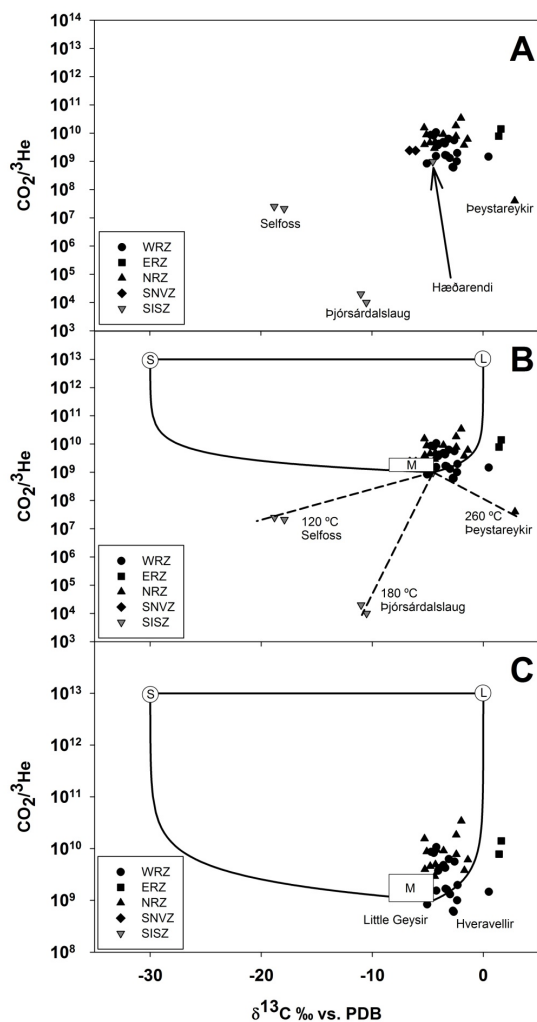
Figure V.6: (a) $CO_2/^3He$ vs. $\delta^{13}C$ for Icelandic gas-phase samples. Fluid phase samples are not considered due to the fact that they have been extensively modified. (b) $CO_2/^3He$ vs. $\delta^{13}C$ with superimposed endmember compositions. Note: sedimentary organic carbon (S), mantle carbon (M), and limestone (L) $\delta^{13}C$ = -30, -6.5 ± 2 and 0 ‰; and $CO_2/^3He$ = 1×10^{13}, $2 \pm 1 \times 10^9$ and 1×10^{13}, respectively (Sano and Marty, 1995) and mixing trajectories between components. Note: mixing trajectories from the (M)-component emanate from the upper limit of the $\delta^{13}C$ range and the lower limit of the $CO_2/^3He$ range. Dashed lines show expected calcite precipitation CO_2 loss curves at various temperatures (Bottinga, 1969). (c) $CO_2/^3He$ vs. $\delta^{13}C$ with contracted y-axis, showing only samples that are not fractionated by calcite precipitation. Approximately ~76% (NRZ, ERZ, and WRZ) of gas data can be explained by a 3-component mixing model between M-L-S.

V.6.1.2 Phase partitioning and hydrothermal degassing

Elemental fractionation will occur between CO_2 and He due to solubility (S) differences in water (e.g., $S_{CO2} >> S_{He}$) (Ellis and Golding, 1963). As a result, He will preferentially partition into the vapor phase relative to CO_2, leaving residual fluid-phase $CO_2/^3He$ values elevated relative to starting values (Figure V.7). Vapor partitioning can be caused by either boiling (> 100 ºC) and/or hydrothermal degassing due to supersaturation of a particular gas species. Loss of CO_2 from geothermal fluids will also cause isotopic fractionation between $^{13}CO_2$ and $^{12}CO_2$ (Vogel, 1970; Mook, 1974; Drever, 1982). This process is temperature dependent: dissolved carbon species will subsequently be enriched in $\delta^{13}C$, leaving $\delta^{13}C$ relatively depleted in the residual gas phase at temperatures <110 ºC. At higher temperatures (>110 ºC), the isotopic fractionation is in the opposite sense and residual gases will consequently be enriched in $\delta^{13}C$ (Szaran, 1997).
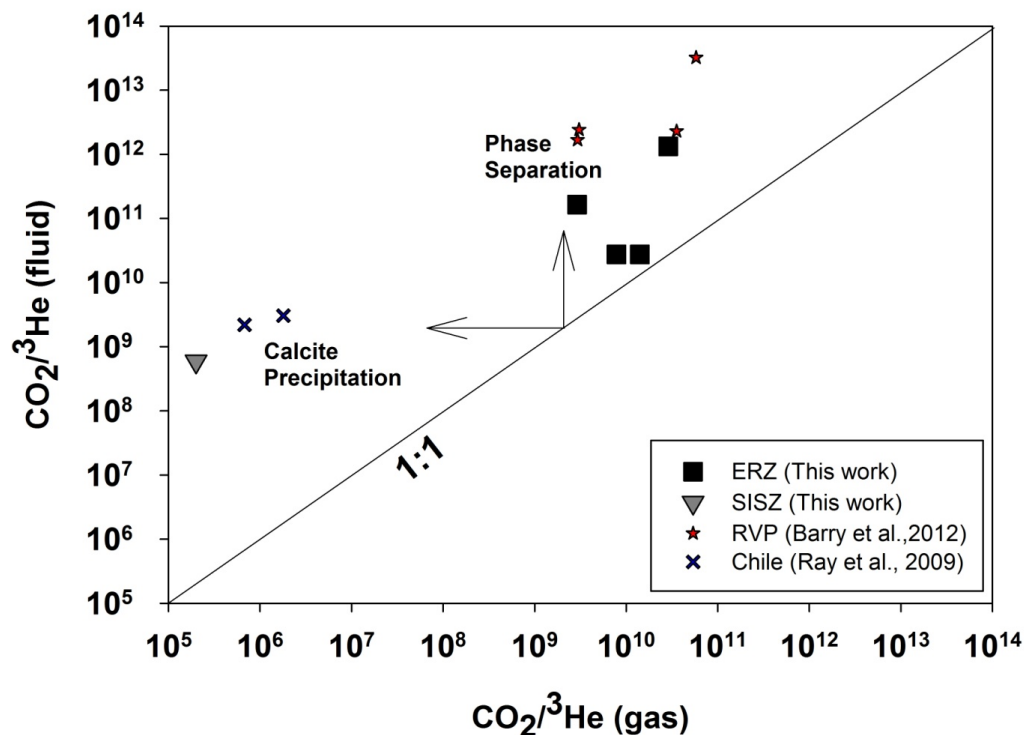
Figure V.7: $CO_2/^3He$ values measured in the fluid vs. gas phases for ERZ and SISZ samples collected from the same locality. For comparison, we show results for fluids and gases in samples of the Rungwe Volcanic Province in Tanzania (Barry et al., 2012b) and the southern volcanic zone in Chile (Ray et al., 2009) where similar fractionation features were previously observed.

In figure V.3a we plot $CO_2/^3He$ as a function of latitude for geothermal fluids/gases and note significantly higher fluid (cross symbol) vs. and gas (solid symbol) phase $CO_2/^3He$ values. The disparity is most evident in ERZ samples where the combination of (1) greater than mantle-like $CO_2/^3He$ values (3×10^{10} to 2×10^{12}), and (2) consistently higher $CO_2/^3He$ values in the fluid phase together strongly suggests hydrothermal phase separation. Notably, the ERZ is the only axial rift zone where fluid samples were collected and both phases (i.e., fluids and gases) were collected at just two of those ERZ localities (i.e., Landmannalaugar and Vonarskarð). In both cases, fluid samples display higher $CO_2/^3He$ values compared with gas phase samples at the same locality (see Figures V.3 and V.6). For example, Landmannalaugar

fluid phase $CO_2/^3He$ values are 6 – 450 times higher than corresponding gas phase samples

and Vonarskarð fluid phase $CO_2/^3He$ values are 2 – 4 times higher than gas phase values from

the same locality (Figure V.7). For comparison, we plot results from similar He-CO_2 gas-fluid

studies which identified the fractionating effects of hydrothermal phase separation (Barry et

al., 2012b) and calcite precipitation (Ray et al., 2009). In addition, Figure V.3b shows carbon

isotope ($\delta^{13}C$) variations as a function of latitude and we note that carbon isotopes are in

relatively good agreement between the fluid (-2.2 ‰) and gas (-3.0 ‰) phase at

Landmannalaugar, indicating that phase-separation must have occurred close to or slightly

below the 110 ºC temperature threshold. In contrast, gas samples at Vonarskarð are marked by

distinctly positive $\delta^{13}C$ values (1.4 – 1.6 ‰) compared with a negative $\delta^{13}C$ fluid phase value

(-2.5 ± 1.1 ‰), consistent with expected carbon isotope fractionation associated with

hydrothermal degassing and phase separation at temperatures above 110 ºC where the

fractionation factor ($\alpha^{13}CO_{2\ vapor\text{-}liquid}$) is negative.

In order to further investigate the relationship between phase separation and He-CO_2

characteristics, we plot $CO_2/^3He$ and $\delta^{13}C$ as a function of volatile (e.g., He; CO_2) content

(Figure V.4). In Figure V.4c we plot $CO_2/^3He$ vs. helium concentration $[He]_C$ (ncm^3 STP/g

H_2O) for all fluid samples and note a broad inverse correlation ($R^2 = 0.79$) for all HT and LT

samples. Furthermore, samples cluster into two distinct groups (Figure V.4c – circled): older

LT samples and younger HT axial rift zone samples. LT samples are relatively He-rich and

display $CO_2/^3He$ values which extend from the MORB range ($2 \pm 1 \times 10^9$) to $\sim10^7$. In contrast,

HT neovolcanic zone samples have significantly lower He contents and much higher $CO_2/^3He$,

extending from below MORB to values $>10^{12}$. For example, the most He depleted ($<20\ [He]_C$

ncm^3 STP/g H_2O) samples are from the ERZ and display the highest measured $CO_2/^3He$

values. Importantly, only ERZ fluid samples display $CO_2/^3He$ values above the canonical

MORB range ($2 \pm 1 \times 10^9$), suggesting hydrothermal phase separation is the principal

modification mechanism in the ERZ, but a relatively minor factor in LT regions such as the

SISZ and Vestfirðir. These results are consistent with high $CO_2/^3He$ values ($\sim 6 \times 10^9$)

previously measured in the axial rift zones (Poreda et al., 1992). In contrast, LT off-axis

$CO_2/^3He$ values predominantly fall below the MORB range (Figure V.4c) – particularly gas

samples which are relatively CO_2 depleted compared to fluid phase samples (Figure V.5).

Together, these results suggest a process which acts to lower $CO_2/^3He$ values is controlling

He-CO_2 systematics in these regions. The possible role of calcite precipitation is assessed in

the next section.

V.6.1.3 Calcite Precipitation

The loss of CO_2 due to calcite precipitation has the potential to fractionate both

$CO_2/^3He$ and carbon isotope values. Basalts are rich in magnesium and calcium silicate

minerals (e.g., olivine; plagioclase) and therefore deep circulating fluids within the

hydrothermal system are abundant in Na^+, Ca^{2+}, Mg^{2+} ions (Spane and Webber, 1995; McLing

et al., 2001). Magmatic degassing creates low-pH, CO_2-rich fluids and gases which react with

these ions to precipitate carbonate minerals according to the following reaction:

$$(Ca^{2+}, Mg^{2+}) + CO_2 + H_2O = (Ca, Mg)CO_3 + 2H^+ \tag{1}$$
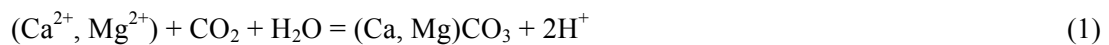
During this reaction, CO_2 fixed as calcite, forms within the basaltic crust, which leads to lower

$CO_2/^3He$ values in residual fluids.

Off-axis LT samples (grey symbols) generally display $CO_2/^3He$ values below the plume and/or MORB-mantle range ($2 - 6 \times 10^9$; Marty and Jambon, 1987; Poreda et al., 1992; Hilton et al., 1998), extending as low as 1×10^4, while most axial rift zone samples (black symbols) fall within or slightly above the MORB range (Figure V.3a). The $CO_2/^3He$ disparity between on-axis and off-axis samples is consistent with preferential CO_2 loss due to calcite precipitation in older, LT off-axis portions of the crust. These findings agree with those of Hilton et al. (1998b) who determined that the CO_2 inventory in Vestfirðir is primarily controlled by reactions that form calcite. Experimental results show calcite mineralization reactions are optimized in basaltic rocks at ~75 °C and pH of ~5.5 (Gysi and Stefansson, 2012). Notably, the average on-axis rift sample discharge temperature is 103 ºC compared to 62 ºC in off-axis samples (Table V.1).

Carbon isotope fractionation associated with calcite precipitation is highly temperature-dependent: at relatively low temperatures (<192 °C), calcite is enriched in ^{13}C relative to residual dissolved CO_2 in geothermal fluids, whereas at higher temperatures (>192 °C) calcite becomes depleted in ^{13}C relative to residual CO_2 (Bottinga, 1969). Figure V.3b shows that off-axis gas samples from SIVZ display the lowest $\delta^{13}C$ values (-18.8 ‰), consistent with low-temperature calcite precipitation. We also note that fluid samples generally display higher carbon isotopes ($\delta^{13}C$) relative to corresponding (same locality/region) gas-phase samples, suggesting that the effects of phase separation are still evident following calcite fractionation. In Figure V.4 we further investigate the fractionation effects of CO_2 loss by plotting $\delta^{13}C$ (Figure V.4b) and $CO_2/^3He$ (Figure V.4d) vs. [CO_2] content of fluid samples. We note that the most CO_2 depleted samples occur in off-axis regions of the Icelandic crust (e.g., SISZ and Vestfirðir) and display the lowest $CO_2/^3He$ and $\delta^{13}C$ values in Iceland. Thus, we conclude that calcite precipitation is the dominant process in older, LT off-axis portions of the crust.

The average geothermal carbon isotope composition for all fluid/gas samples (-4.0 ±
3.7 ‰) falls slightly above the upper limit of the MORB range (-6.5 ± 2 ‰) and is in good
agreement with previously reported estimates of -3.8 ± 0.7 ‰ (Poreda et al., 1992) for CO_2-
rich HT fluids of the Icelandic axial rift zones. If extreme values, such as those measured in
LT off-axis samples affected by calcite precipitation, are removed and only HT axial rift zone
gas samples are considered, then the average $\delta^{13}C$ value increases to -3.1 ± 1.9 ‰.
Significantly, this value overlaps with isotopically high carbon isotope values (~ -3 ‰)
previously observed at Loihi Seamount (Exley et al., 1986), an analogous plume-related
magmatic system, adjacent to Hawaii – indicating a common and isotopically-high carbon
isotope fingerprint may exist in the plume mantle source.

V.6.1.4 Crustal contamination – ($CO_2/^3$He- $\delta^{13}C$) model

In order to determine CO_2 provenance and estimate relative CO_2 contributions from
potential endmembers, $CO_2/^3$He values are plotted as a function of $\delta^{13}C$ for all Icelandic gas
samples (Figure V.6a). Of the 71 geothermal samples, only gas samples (n = 42) are
considered due to the fact that fluid samples have been extensively modified by hydrothermal
fractionation processes. The most salient feature of Figure V.6 is that nearly all Icelandic gas
phase samples require a crustal contribution in order to explain their combined $CO_2/^3$He-$\delta^{13}C$
characteristics.

In Figure V.6a, we show representative compositions of three potential endmembers
(Figures V.6b-c): mantle (M), limestone (L) and sediment (S). Their assumed endmember C-
isotope compositions are: $\delta^{13}C$ = -6.5 ± 2 ‰ for (M), 0‰ for (L), -30‰ for (S) (relative to
VPDB), and $CO_2/^3$He = 2 ± 1 × 10^9 for (M), 10^{13} for (L) and (S) (Sano and Marty, 1995). In

addition, binary mixing trajectories between the respective components (1) M and L, (2) M and S, and (3) L and S are superimposed (solid lines) on the diagram. This model assumes that the thick Icelandic crust is stratified with respect to carbon speciation and that carbon M, L, and S components can be resolved using combined $CO_2/^3He$ - $\delta^{13}C$ characteristics. These assumptions are supported by IRDP drill cores which show that the crust beneath Icelandic is composed of partially to completely altered lava flows, dikes and minor clastic material with secondary mineralization consisting of clay minerals, calcite and quartz (Mehegan et al., 1982). Low $\delta^{13}C$ signatures in crustal wall rocks may result from either deep hydrothermal circulation of organic material (Lang et al., 2006) and/or biological activity during mineralization (Thorseth et al., 1992; Fisk et al., 2003).

In Figure V.6b, we plot expected CO_2 loss-fractionation curves (dashed lines) from a mantle (M) starting composition in order to illustrate the effects of calcite precipitation at various temperatures. The modification of SIVZ (off-axis) $CO_2/^3He$- $\delta^{13}C$ compositions can be explained by calcite precipitation at temperatures between 120 ºC (Selfoss) and 180 ºC (Þjórsárdalslaug), and the composition of Þeystareykir (NRZ) can be explained by calcite precipitation at 260 ºC (see Section 5.1.2). Notably, Selfoss and Þjórsárdalslaug samples were collected at temperatures of ~70 ºC, whereas Þeystareykir was sampled at ~90 ºC. However, reported discharge temperatures represent minimum estimates only of reservoir temperatures. For example, borehole values of 120 ºC were measured at a depth of ~1400m in Selfoss (Arnórsson, 1995) and geothermometers suggest an average reservoir temperature of 240-300 ºC in the Þeystareykir area (Armannsson et al., 1986) – both estimates are in agreement with predicted reservoir temperatures based on temperature dependent calcite precipitation (this study).

In Figure V.6c, the five samples affected by calcite precipitation are removed and only the most pristine gas samples are considered (n = 37). Significantly, the average $CO_2/^3He$ value of these remaining gas samples is $5.9 \pm 6.3 \times 10^9$ compared to an unfiltered geothermal average (n=71) $CO_2/^3He$ of $76 \pm 328 \times 10^9$. Notably, the filtered gas estimate is in excellent agreement with the average $\delta^{13}C$ geothermal value of 6×10^9 previously reported by Poreda (1992) for HT CO_2-rich axial rift zone samples. Importantly, nearly all gas samples require a crustal contribution and 28 of 37 samples plot within the area bounded by the 3-component mixing trajectories in Figure V.6c, indicating that ~76% of gas samples require a contribution from all three end-members to explain their combined $CO_2/^3He$–$\delta^{13}C$ characteristics. The remaining 9 samples can only be explained if a $CO_2/^3He$ starting composition slightly below the MORB range is adopted for the mantle (M) and/or if mixing occurs with a positive $\delta^{13}C$ (L) component. Lower $CO_2/^3He$ values can be explained by either degassing (see section 5.1.3) or a lower initial $CO_2/^3He$ ratio (< MORB) in the plume source. The latter explanation can be reconciled with model estimates of CO_2 and ^3He contents in the lower mantle (Javoy, 1997; Porelli and Wasserburg, 1995) which suggest a plume $CO_2/^3He$ ratio of ~1.7×10^8, but would be in direct contrast to previous estimates for Iceland (6×10^9; Poreda et al., 1992). While there is ongoing debate as to the original $CO_2/^3He$ value in the mantle plume source (Trull et al., 1993; Marty and Tolstikhin, 1998; Garcia et al., 1998; Shaw et al., 2004), the majority of data suggest slightly higher than MORB values, indicating that all Icelandic gas samples require a crustal contribution to explain their combined $CO_2/^3He$-$\delta^{13}C$ characteristics. This observation is consistent with both IRDP drill core findings (Mehegan et al., 1982; Flower et al., 1982) and the findings of several O-isotope studies (Muhlenbachs et al., 1974; Burnard and Harrison, 2005; Thirwall et al., 2006) of Icelandic basalts, which attribute $\delta^{18}O$ heterogeneities throughout Iceland to crustal assimilation processes.

In Table V.4, we provide a quantitative estimate of contributions from the three endmembers to the total carbon inventory for the 28 Iceland gas samples which can be resolved using a 3-component mixing model. In the WRZ, 14 of 20 gas samples can be explained in this way, with mantle and limestone-derived carbon serving as the principal contributors to the carbon budget in all cases, typically representing (> 90% of the total). The highest mantle CO_2 contributions (~64 %) were measured in borehole samples of Svartsengi, a locality marked by moderately high $^3He/^4He$ value (~14.5 R_A; Füri et al., 2010). Neither of the two ERZ samples can be explained by 3-component mixing. In contrast, all 13 NRZ gas samples (Þeystareykir is not considered due to calcite precipitation) can be explained by 3-component mixing. Limestone-derived carbon is the principal contributor to the carbon budget, typically representing ~ 75% of the total. The highest mantle CO_2 contribution (~ 34 %) found in the NRZ was measured in a fumarole at Krafla. Notably, Krafla has a $^3He/^4He$ value of ~8.4 R_A (Füri et al., 2010), which is consistent will lower $^3He/^4He$ values typically found in the NRZ

Table V.4: Proportions of mantle (M) vs. sedimentary (S) vs. limestone (L) carbon contribution to each sample.

Sample Locality	%M	%L	%S
WRZ (n=14)			
Nesjavellir (Bubbling pool)	11.6	74.5	13.9
Nesjavellir (Bubbling pool)	17.9	76.2	6.0
Svartsengi (Borehole HSH11)	64.9	30.7	4.4
Svartsengi (Borehole HSH11)	62.1	36.3	1.6
Reykjanes (Fumarole)	59.9	37.8	2.4
Krísuvík (Fumarole)	23.5	68.6	7.9
Krísuvík (Fumarole)*	75.8	22.5	1.7
Krísuvík (Bubbling pool)	9.4	78.0	12.7
Krísuvík (Bubbling pool)	20.9	70.3	8.8
Hengill (Bubbling pool)	24.0	66.4	9.6
Hengill (Bubbling pool)	12.1	74.9	13.0
Hengill (Fumarole)	16.0	76.1	7.9
Kerlingafjöll (Bubbling pool)	26.9	63.6	9.5
Hveragerði (Fumarole)	50.8	49.1	0.1
ERZ (n=1)			
Landmannalaugar (Fumarole)*	34.4	60.7	5.0
NRZ (n=13)			
Krafla (Borehole 20)	20.3	68.4	11.3
Krafla (Borehole 20)	25.1	61.1	13.8
Krafla (Borehole 13)	26.3	72.0	1.7
Krafla (Borehole 13)	16.4	81.5	2.2
Krafla (Fumarole)	34.1	56.4	9.5
Krafla (Mud pot)	21.8	65.5	12.7
Krafla (Fumarole)	5.4	87.3	7.3
Námafjall (Mud pot)	6.4	76.9	16.7
Námafjall (Fumarole)	11.4	73.4	15.3
Askja, Viti crater (Bubbling pool)	11.0	78.8	10.3
Askja, Viti crater (Bubbling pool)	10.6	77.0	12.4
Kverkfjöll (Mud pot)	12.9	80.9	6.2
Kverkfjöll (Mud pot)	2.9	90.9	6.2
SNVZ (n=2)			
Lýsuhóll (Borehole)	41.3	42.8	15.8
Lýsuhóll (Borehole)	41.5	44.5	14.0

[a] Sample Phase: G = Gas.

[b] Assuming $\delta^{13}C$ values of -4.5‰, 0‰ and -30‰ (relative to VPDB) with corresponding $CO_2/^3He$ ratios of 1×10^9, 1×10^{13} and. 1×10^{13} for mantle, limestone and sediments.

* Samples are considered to be contaminated by air-derived helium (i.e., X< 5) or addition of radiogenic helium (see Füri et al., 2010).

(Poreda et al., 1992; Macpherson et al., 2005a). Both SNVZ gas samples can be explained by 3-component mixing, with mantle plus limestone-derived carbon contributions of ~ 85% of the total. The single SISZ sample considered (Hæðarendi) falls just outside of the 3-component ternary plot. Together, these results suggest that mantle $\delta^{13}C$ and He-CO_2 values are modified by various physiochemical fractionation processes but also strongly influenced by crustal assimilation within the Icelandic crust.

In conclusion, we have identified a number of secondary processes – occurring at various levels in the Icelandic crust – which can act to modify intrinsic carbon characteristics. Magma degassing prior to volatile interaction with the hydrothermal system appears to be a minor factor. Within the hydrothermal system, several HT axial rift zone samples (e.g., ERZ) appear to be modified by hydrothermal phase separation. In contrast, off-axis LT samples appear to be most significantly affected by calcite precipitation. In general, gas phase samples retain their source signatures more effectively than fluid phase samples and thus can be used to calculate relative mantle and crustal inputs. Using this quantitative approach we estimate that ~85 % of CO_2 is mantle and/or limestone derived, and show that almost all Icelandic gases require a crustal carbon contribution.

V.6.2 CO_2 Evolution of Basaltic Magmas

Magma hosts CO_2 in two forms: (1) CO_2 dissolved in the melt and/or (2) CO_2 exsolved into the vapor phase. By investigating both the dissolved (glass-matrix) and vapor (vesicle) phases, it is possible to constrain the degassing history of individual Icelandic magma batches, identify crustal assimilation processes and ultimately estimate intrinsic carbon characteristics (isotope and abundance) of the underlying mantle source. Measured carbon

signatures result from primary mantle source features, which could have been modified by secondary processes such as degassing and crustal assimilation. The degassing or loss of CO_2 from a basaltic magma can potentially lower both $CO_2/^3He$ (Hilton et al., 1998a) and $\delta^{13}C$ values (Javoy et al., 1978) in the residual dissolved phase. In addition, crustal assimilation and/or contamination can further modify source features due to mixing with isotopically distinct crustal components. Thus, before primary basalt carbon characteristics can be identified, the effects of the aforementioned modification processes need to be evaluated.

V.6.2.1 Dissolved volatiles: isotopic evolution of dissolved CO_2

The solubility of CO_2 in basaltic melts is pressure-dependent and, as a result, samples erupted under greater confining pressures (e.g., thick glacial cover) retain higher proportions of their primary CO_2 inventory. During magma ascent, CO_2 is degassed from the melt (Bottinga and Javoy, 1989) and due to the lower solubility of CO_2 compared to other major volatiles (e.g. H_2O), it forms the principal constituent of the vapor-phase in basaltic melts (Delaney et al. 1978; Moore et al. 1977; Mysen et al. 1975; Stolper and Holloway 1988) and serves as a carrier gas for other volatile species (e.g., the noble gases). Such gas loss will lead to isotopic exchange between CO_2 partitioned between the vapor phase (e.g., vesicles $= CO_2^v$) and residual CO_2 (e.g., dissolved $= CO_2^d$) in the magma (Pineau et al., 1976; Javoy et al., 1978). As a result, variations in CO_2 content and $\delta^{13}C$ values can be used to constrain the extent of degassing within a given magmatic system.

Degassing of CO_2 can occur in either an open or closed system mode (Dixon and Stolper, 1995; Gerlach and Taylor, 1990) or as a combination (two-stage) of both processes (Gerlach and Taylor, 1990; Macpherson and Mattey, 1994; Shaw et al., 2004; Macpherson et

al., 2005b). In a closed system, batch equilibrium degassing (BED) occurs, whereby vesicles form in a rising melt and subsequently stay in contact with the melt, thereby facilitating continuous isotopic exchange (Macpherson and Mattey, 1994). In contrast, Rayleigh (open system) distillation or fractional equilibrium degassing (FED) takes place when vesicles form in equilibrium with the surrounding melt, but as degassing progresses, they are removed due to the open nature of the system. The extent to which ^{13}C fractionates from ^{12}C is dependent on the fractionation factor (i.e., Δ-values) between CO_2 dissolved as carbonate ions in basaltic melt (Fine and Stopler, 1986) and free CO_2 in the vapor phase. Experimentally determined Δ-values (= $\delta^{13}C^v$ - $\delta^{13}C^d$) range from +2.3 to +4.6 ‰ (Javoy et al. 1978; Mattey 1991) and predict lower $\delta^{13}C$ values in dissolved CO_2 relative to the exsolved (vesicle) phase.

In this study approximately half of $\delta^{13}C^d > \delta^{13}C^v$ and, as a result, half of Δ-values (= $\delta^{13}C^v$ - $\delta^{13}C^d$) are negative, indicating that CO_2^v is not in equilibrium with CO_2^d, and therefore equilibrium degassing conditions may not adequately describe all gas loss from the system. Alternatively, it is possible that gases are derived from magma degassing from elsewhere within the magmatic system (Shaw et al., 2004; Hahm et al., 2012) and/or that $\delta^{13}C$ values are modified by assimilation with an isotopically distinct crustal component. If we assume equilibrium degassing can most accurately describe gas loss, then the minimum $\delta^{13}C$ value attainable in a BED system is equal to the $\delta^{13}C_{initial}$ – the fractionation factor ($\Delta_{vapor-melt}$), whereas in a FED system any $\delta^{13}C$ value is possible. Consequently, dissolved $\delta^{13}C$ values in magmas that experienced FED degassing are typically more fractionated (i.e., isotopically lower) for a given degree of gas loss compared to those constrained by BED degassing (Macpherson and Mattey, 1994). By considering the residual carbon contents and carbon isotope signatures of basalts, we can model the degassing evolution of basalts and estimate initial mantle starting compositions.

V.6.2.2 Equilibrium Degassing Modeling

Using an equilibrium degassing model (after Macpherson and Mattey, 1994), the initial mantle carbon characteristics (e.g., CO_2 contents and $\delta^{13}C$ values) of Iceland subglacial basalts are estimated. Importantly, this type of model assumes: 1) samples are derived from a distinct parental melt composition, 2) a common fractionation factor ($\Delta_{vapor-melt}$) of ~ 4.2 (defined by FED trajectory) is appropriate for all samples, 3) degassing (FED and/or BED) is solely responsible for all $\delta^{13}C$ variability unless otherwise indicated, and 4) samples which fall on or within the envelope defined by the FED and BED trajectories result from BED, FED or a combination (two stage degassing) of the two processes.

Due to the complicated effects of melt generation and source heterogeneities in the Icelandic mantle (Slater et al., 1998; Thirwall et al., 2004; Füri et al., 2010), basalt CO_2 may not be characterized by a single source composition, as was assumed for previous studies, which employed this type of degassing model (Macpherson and Mattey, 1994; Shaw et al., 2004; Macpherson et al., 2005b). In order to circumvent this potential problem, CO_2 estimates are made for individual rift zone segments (i.e., WRZ, ERZ, NRZ; Figures V.8a-c) as well as for Iceland as a whole (Figures V.8d-e). In this way, we evaluate if the CO_2 (isotope and concentration) characteristics of Iceland basalts can be best explained by degassing of a homogenous pre-eruptive melt.

Initial CO_2 contents and $\delta^{13}C$ values of the magma source prior to degassing are estimated using the following equations (after Macpherson and Mattey, 1994):

$$\delta_r BED = \delta_p - \Delta(1 - (C_r BED/C_p)) \qquad\qquad (2)$$

$$\delta_r\text{FED} = \delta_p + \Delta(\ln(C_r\text{FED}/C_p)) \qquad (3)$$

where $\delta_r\text{BED}$ and $\delta_r\text{FED}$ represent the isotopic composition ($\delta^{13}C$) of CO_2 remaining dissolved in the melt following BED and FED, $C_r\text{BED}$ and $C_r\text{FED}$ are the residual concentrations of CO_2 for BED and FED, C_p and δ_p represent the primary (initial) concentration and isotopic composition of CO_2 dissolved in the melt prior to BED and FED, and $\Delta = \delta^{13}C\text{vapor} - \delta^{13}C\text{melt}$, which is calculated for each individual rift zone. Due to the fact that one δ_r corresponds to two residual CO_2 concentrations (CrBED and CrFED) for the two types of degassing (BED and FED), the two above equations can be combined:

$$\ln C_p + (\text{CrBED}/C_p) = 1 + \ln \text{CrFED} \qquad (4)$$

and C_p can then be calculated using CrBED and CrFED values corresponding to two different residual isotopic compositions (δ_r1 and δ_r2), using:

$$C_p = (C_r\text{BED}^1 - C_r\text{BED}^2)/\ln(C_r\text{FED}^1/ C_r\text{FED}^2) \qquad (5)$$

Using this approach, we address whether there is evidence of CO_2 heterogeneity in primary melts (prior to degassing) between the various neovolcanic rift zones of Iceland.

We begin by considering WRZ samples only, where CO_2 characteristics were determined in 17 basaltic glasses and display a wide range in $\delta^{13}C^d$ and $CO_2{}^d$ content (Table V.2). A fractionation factor of ($\Delta=$) ~4.3 was determined for the WRZ by calculating the slope of a best fit regression line through samples SKARD-1 and MID-3, which are considered to represent a FED trajectory (see Figure V.8a). We then selected samples A-9 ($C_{rBED}{}^1$ = 42.1 ppm, $\delta_r{}^1$ = −6.9 ‰) and MAE-1 ($C_{rBED}{}^2$ = 13.3 ppm, $\delta_r{}^2$ = −7.5‰), which follow a BED trajectory and calculated C_rFED^1 and C_rFED^2 using the FED regression line (δ_r = 4.30 $\ln(C_{rFED})$ − 27.92), that defines the Δ-value for both the BED and FED trajectories. With C_rBED^1 & C_rFED^1 and C_rBED^2 & C_rFED^2, we are able to estimate C_p using Equation (5) and δ_pBED^1, δ_pBED^2, δ_pFED^1, and δ_pFED^2 using Equations (2) and (3), respectively. The estimated CO_2 composition of pre-eruptive melt is (C_p) = 206 ± 24 ppm, with a corresponding average δ_p = -4.2 ± 0.9 ‰ (i.e., average and standard deviation of δ_pBED^1, δ_pBED^2, δ_pFED^1, and δ_pFED^2). The degree of uncertainty associated with the C_p estimate is approximated by considering that the overall precision associated with $\delta^{13}C$ isotopic measurements of individual samples is ± 0.5‰, based on repeat analyses of internal standards. By assuming that the same uncertainty would apply to the empirically derived FED relationship of δ_r = 4.30 $\ln(C_{rFED})$ -27.92 and thus the Δ-value, then the lower extreme of Δ = 4.3-0.5 = 3.8 ‰ and produces a Cp value of 182 ppm whereas the higher estimate of Δ = 4.3+0.5 = 4.8 ‰ yields a C_p estimate of 230 ppm. Therefore, we estimate the uncertainty on Cp for the WRZ at ± 24 ppm (i.e., ~12%). The fact that all empirically derived FED trajectories have a slope of ~3.9-4.3 ‰ results in ~12-13 % uncertainties on all Cp estimates for the individual rift segments.
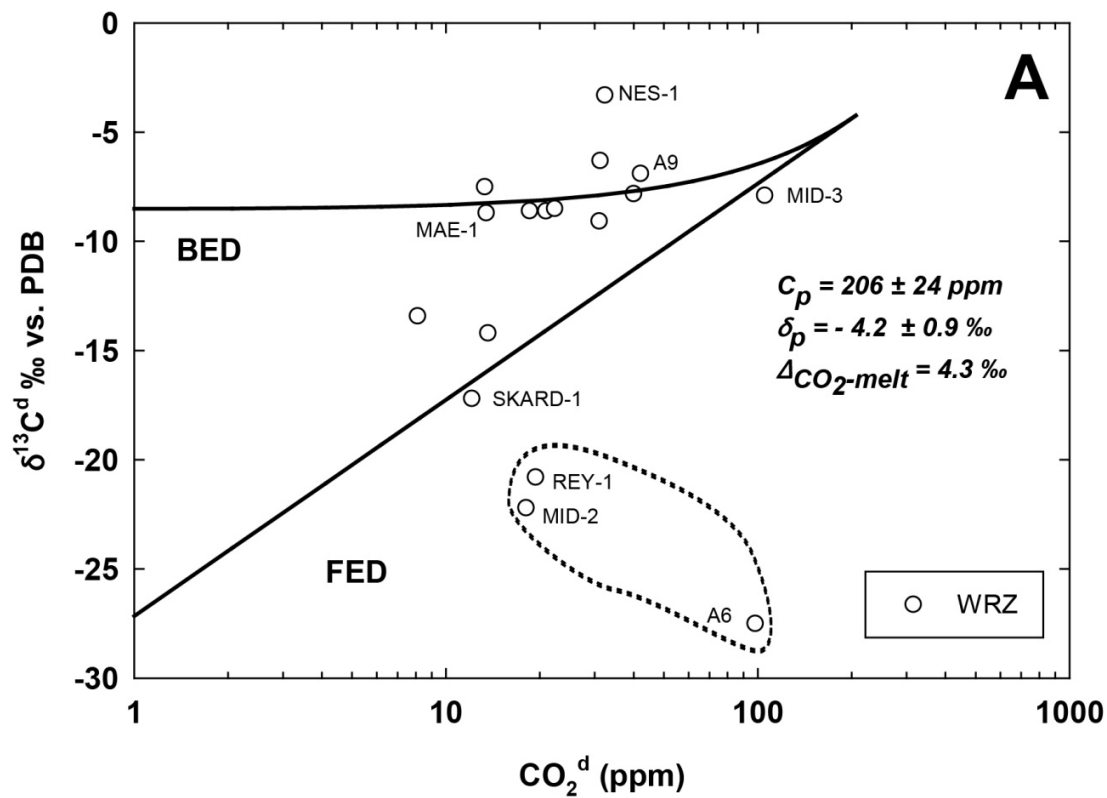
Figure V.8: Carbon-isotopes ($\delta^{13}C$) as a function of dissolved CO_2 content (ppm) in basalts of the various volcanic zones of Iceland: 8a = WRZ; 8b = NRZ; 8c = ERZ; 8d and 8e = All Iceland data. Calculated BED and FED mixing trajectories (solid line) are superimposed over CO_2 data. Figure V.8e also contains a CAFED (dashed line) which considers assimilation of isotopically light carbon in concert with FED.

Figure V.8 continued
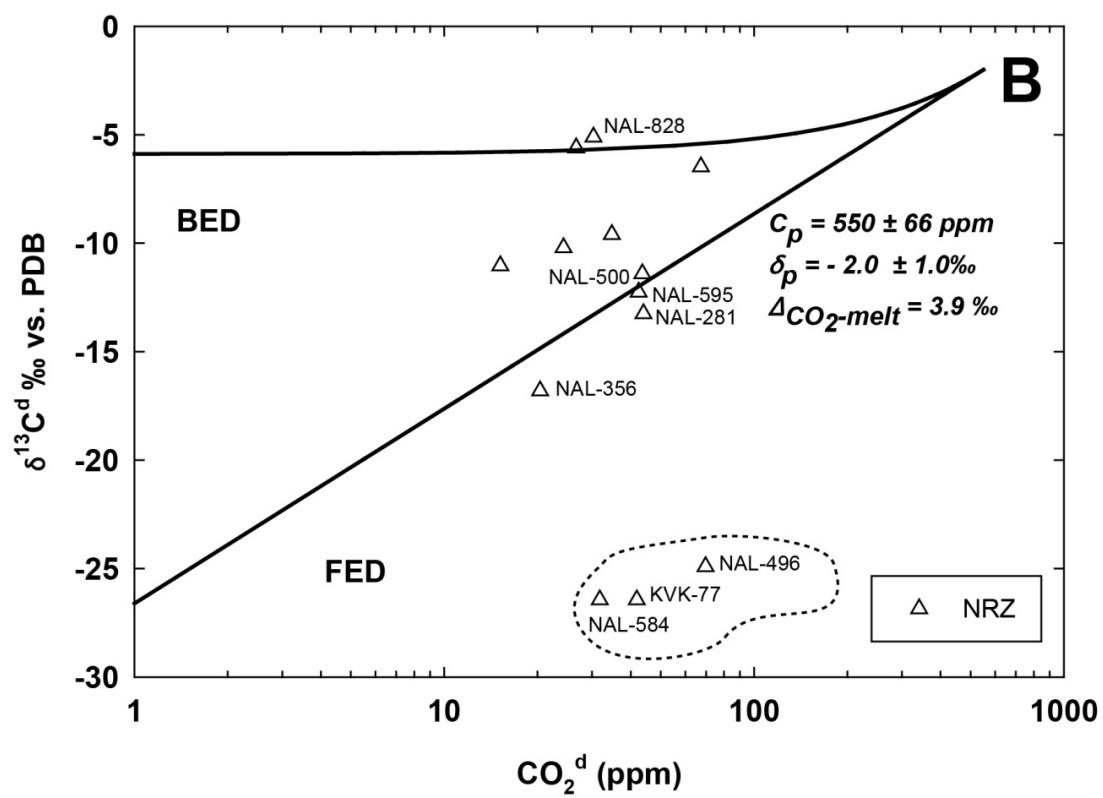
Figure V.8 continued
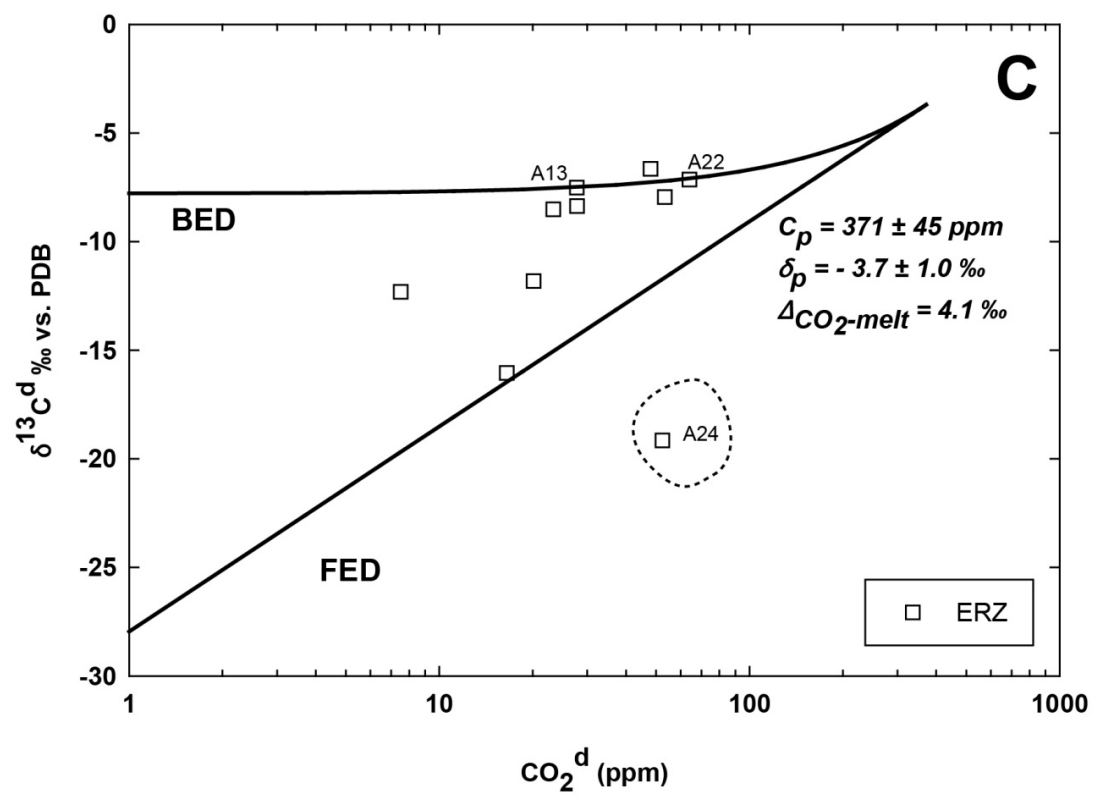
Figure V.8 continued
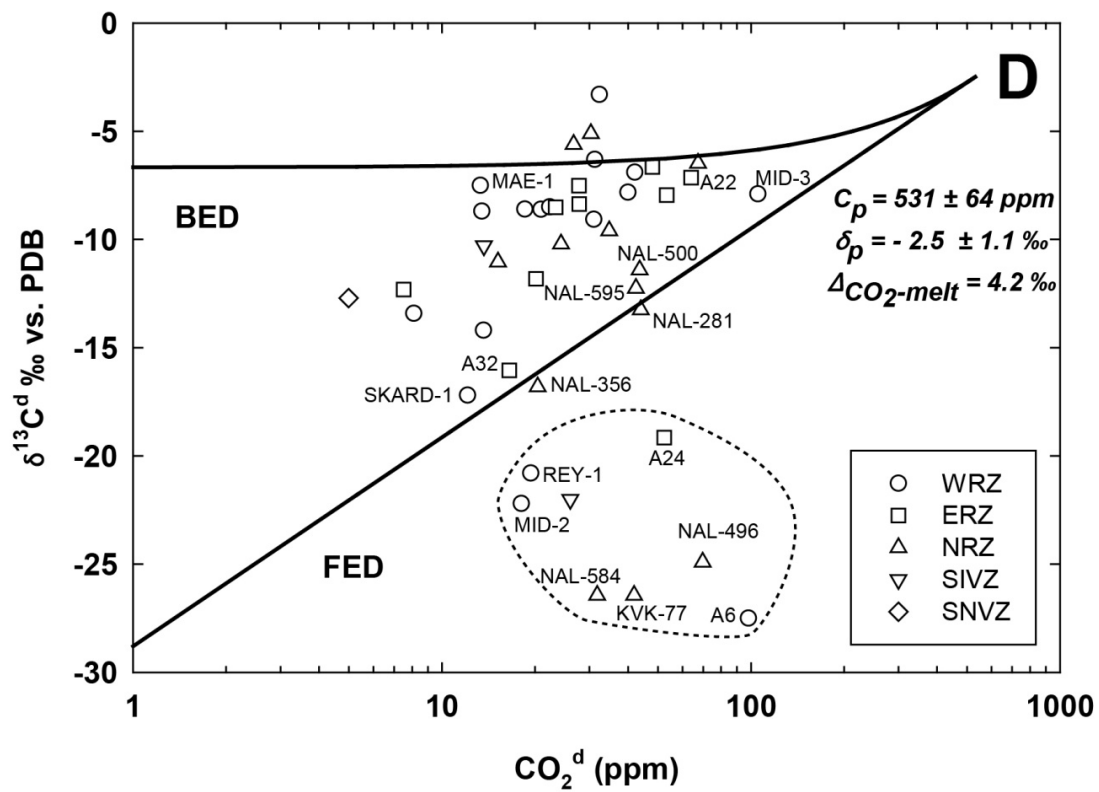
Figure V.8 continued
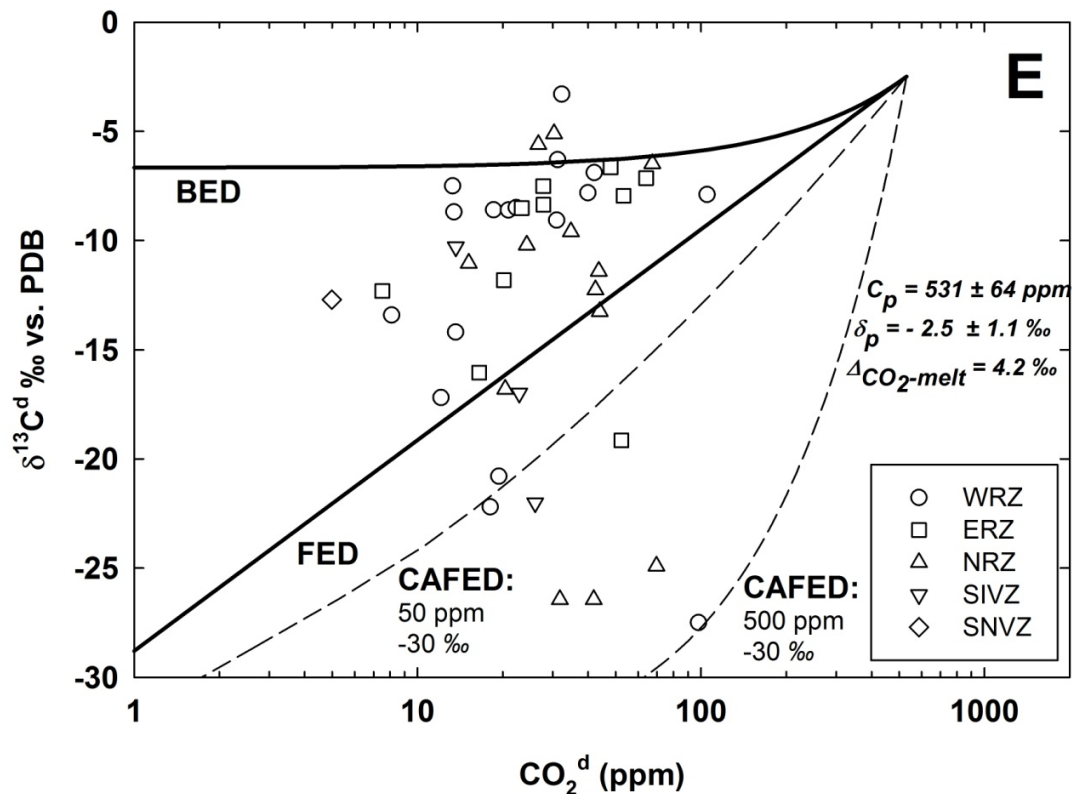
In addition, we identify three samples (MID-2, REY-1, A6; circled in Figure V.8a) that fall well below the FED trajectory and therefore cannot be explained by degassing fractionation alone (Figure V.8a). Notably, all three of these samples display $\delta^{13}C$ values lower than -20 ‰ and have higher than expected CO_2 contents considering their extreme $\delta^{13}C$ values, suggesting assimilation of an isotopically low $\delta^{13}C$ component and possibly crustal emplacement. Similar observations are made in the NRZ and ERZ (circled values – Figures V.8b and V.8c) and possible assimilation processes are addressed in section 5.3.3. In contrast to isotopically low samples, one sample (NES-1) stands alone with high $\delta^{13}C$ plotting above the BED line (Figure V.8a). As a result, C_p cannot be determined analytically as described

above for this particular sample, but could be approximated using a graphical approach.

However, if we assume that degassing is sufficiently advanced (>80%) so that the change in

$\delta^{13}C$ from the initial value is approximately equal to Δ (+4.3 ‰) then NES-1 (-3.3 ‰) would

require a positive mantle starting carbon isotope composition, which is highly unlikely in the

context of anticipated mantle values and the other values in this study. Alternatively, high $\delta^{13}C$

values result from crustal assimilation of a ^{13}C enriched endmember in the magma chamber.

Notably, most basalts that fall outside of the mixing envelope defined by BED and FED

trajectories are affected by an isotopically light (organic/sedimentary), and presumably deep

carbon component, whereas geothermal fluids and gases are mostly modified by a relatively

^{13}C enriched (limestone) component, presumably in shallower regions of the crust (see Section

5.1.4).

Estimating pre-eruptive CO_2 source compositions from the two remaining neovolcanic

rift zones is more complicated due to the lack of a clearly defined BED trajectory in the case

of the NRZ (Figure V.8b) and a FED trajectory in the case of the ERZ (Figure V.8c). As a

result, C_p cannot be determined analytically as described above (e.g., WRZ), but can only be

approximated using a graphical approach. In the NRZ, the FED trend can be defined by the

slope of a best fit regression through samples NAL-356, NAL-281, NAL-500 and NAL-595,

resulting in a slope of ($\Delta =$) ~3.9 ‰. However, no clear BED trend exists and therefore we

estimate starting values using just one sample NAL-828 (C_{rBED} = 30.3 ppm, δ_r = −5.1 ‰).

Again, if we assume that degassing is sufficiently advanced (>80%), as it is in the majority of

Iceland basalts, the change in $\delta^{13}C$ from the initial value is ~3 ‰ and therefore NRZ samples

would require starting compositions of C_p = 550 ± 66 ppm and δ_p = -2.0 ± 1.0 ‰ respectively

(Figure V.8b). As in the WRZ, three samples plot well below the FED trajectory and require

crustal assimilation to explain their extreme values.

In the ERZ there is no clearly defined FED trajectory, so we use an average Δ-value (from WRZ and NRZ) of +4.1 ‰. We then select ERZ samples A22 (C_rBED^1 = 64.0 ppm, δ_r^1 = −7.1 ‰) and A13 (C_rBED^2 = 27.8 ppm, δ_r^2 = −7.5‰) which follow a BED trajectory and calculate C_rFED^1 and C_rFED^2. With C_rBED^1 & C_rFED^1 and C_rBED^2 & C_rFED^2, we are able to estimate C_p using Equation (5) and δ_pBED^1, δ_pBED^2, δ_pFED^1, and δ_pFED^2 using Equations (2) and (3), respectively. The estimated CO_2 composition of pre-eruptive melt is (C_p) = 371 ± 45 ppm, with a corresponding average δ_p = -3.7 ± 1.0 ‰ (Figure V.8c). Notably, one ERZ sample falls well below the FED trajectory. We caution that source estimates for NRZ and ERZ samples are obtained using a graphical approach and are therefore highly model dependent.

By combining carbon data (n=47) from all three neovolcanic rift zones as well as from the SNVZ and SIVZ, we can analytically estimate pre-eruptive CO_2 source estimates for Iceland as a whole (Figure V.8d). Seven samples were selected to define the FED trajectory: SKARD-1 and MID-3 from the WRZ, NAL-356, NAL-281, NAL-500 and NAL-595 from the NRZ and A32 from the ERZ. A fractionation factor of (Δ =) ~4.2 ‰ was determined by calculating the slope of a best fit regression line (δ_r = 4.19 ln(C_rFED) – 27.87) (see Figure V.8d) through these (n=7) samples. We then selected ERZ sample A-22 (C_rBED^1 = 64.0 ppm, δ_r^1 = −7.1 ‰) and WRZ sample MAE-1 (C_rBED^2 = 13.3 ppm, δ_r^2 = −7.5‰) which follow a BED trajectory and calculated C_rFED^1 and C_rFED^2 using the FED regression line. With C_rBED^1 & C_rFED^1 and C_rBED^2 & C_rFED^2, we are able to estimate C_p using Equation (5) and δ_pBED^1, δ_pBED^2, δ_pFED^1, and δ_pFED^2 using Equations (2) and (3), respectively. The estimated CO_2 composition of pre-eruptive melt is (C_p) = 531 ± 64 ppm, with a corresponding average δ_p = -2.5 ± 1.1 ‰ (i.e., average of δ_pBED^1, δ_pBED^2, δ_pFED^1, and δ_pFED^2) (Table V.5). Notably, this estimate (~531 ± 64 ppm) is in excellent agreement with CO_2 concentration estimates for the E-MORB source (519 ppm; Marty, 2012) and slightly higher than estimates

from the adjacent Reykjanes and Kolbeinsey ridges where de Leeuw (2007) reported Cp and δ_p values of 396 ppm and -3.9 ‰ for the a Reykjanes Ridge and Macpherson et al. (2005b) reported Cp and δ_p values of 400 ± 100 ppm and -6 ± 1 ‰ for the Kolbeinsey Ridge.

Pre-eruptive carbon estimates of Icelandic basalts reveal several interesting features: 1) CO_2 source estimates increase from the WRZ (206 ± 24 ppm) to the ERZ (371 ± 45 ppm) and reach a maximum in the NRZ (550 ± 66 ppm), which is consistent with the transition from primitive 'solar-like' He-Ne characteristics in central and southern Iceland (Füri et al., 2010) to more MORB like characteristics in the north. 2) Source estimates (Cp $=531 \pm 64$ ppm) are in good agreement with previous estimates for E-MORB (519 ppm; Marty, 2012) and slightly higher than estimates of ~400 ppm from the adjacent Reykjanes and Kolbeinsey ridges. 3) the δ_p (= -2.5 ± 1.1 ‰) estimate for all of the neovolcanic zone samples is similar to the average geothermal value of -3.1 ± 1.9 ‰ reported in section 4.1.1 – suggesting that geothermal carbon isotopes closely resemble the primary mantle composition of Iceland.

Table V.5: Calculations of CO_2 in pre-eruptive melts.

	C_rBED^1 (MAE-1)	C_rBED^2 (A-22)	C_P	δ_P
δ_r (‰)	-7.5	-7.1	531[c]	-3.4[d]
C_rBED (ppm)	13.3	64.0		-3.4[e]
C_rFED (ppm)	128.9[a]	141.8[b]		-1.6[f]
				-1.6[g]

[a]Calculated from δ_r^1 and the regression line (FED trajectory).

[b]Calculated from δ_r^2 and the regression line (FED trajectory).

[c]Calculated from Eq. (5).

[d]Calculated from Eq. (2) using δ_r^1 and C_rBED^1.

[e]Calculated from Eq. (2) using δ_r^2 and C_rBED^2.

[f]Calculated from Eq. (3) using δ_r^1 and C_rFED^1.

[g]Calculated from Eq. (3) using δ_r^2 and C_rFED.

V.6.3.3 Coupled assimilation and fractional equilibrium degassing

Figures V.8 (a-d) demonstrate that most samples can be bracketed between BED and FED degassing trajectories and, as a result, the majority of Iceland CO_2 data are adequately described by the above two-stage degassing model. However, several (n=8) clear outliers plot below the well-defined FED trajectory and are marked by substantially lower $\delta^{13}C$ values compared to samples with similar CO_2 contents. While it is possible that the low $\delta^{13}C$ represents post-eruptive contamination on glass surfaces, every precaution was taken in cleaning these glasses prior to stepped-heating analysis. Also, this contaminant is observed in the dissolved phase and therefore, we consider this an unlikely possibility. Alternatively, these glasses may be derived from magma with a distinctively lower initial $\delta^{13}C$ value than the remainder of the Icelandic suite. However, no other geochemical feature of these samples suggests that they were derived from a source different from the rest of the Icelandic basalts (Füri et al., 2010) and, furthermore, low $\delta^{13}C$ values are observed in all three axial rift zones. Therefore, the most likely explanation for these data is that they were derived from similar pre-eruptive magma as other Icelandic melts but acquired low $\delta^{13}C$ during interaction with the crust. Similar assimilation processes have been observed in the adjacent Kolbeinsey Ridge (Macpherson et al., 2005b). The lack of more samples with extremely low $\delta^{13}C$ suggests that most magma escaped interaction with isotopically low $\delta^{13}C$ (organic/sedimentary-derived) crust. Alternatively, the isotopic composition of the wall rock may have been magma-like with respect to $\delta^{13}C$ and thus any modification to the isotopic composition of the magma was negligible.

In order to simulate the concurrent processes of degassing and wall rock assimilation we adopt the methods of Macpherson et al. (2010) and construct a coupled assimilation and fractional equilibrium degassing (CAFED) model in which FED occurs in increments of 1%,

followed by assimilation with a contaminant CO_2 = 50-500 ppm and $\delta^{13}C$ = -30 ‰. FED was

selected due to the longer storage and eruption times associated with open system degassing

which should promote interaction between melts and contaminants. Similarly to the 3-

component mixing model (Sano and Marty, 1995) employed in section 5.1.4 to explain crustal

contamination in gas samples, this model also assumes that the thick Icelandic crust is

heterogeneous and likely stratified with respect to carbon speciation and carbon isotopes. In

addition, average CO_2 contents of ~500 ppm were measured in altered basalts from these drill

cores (Flower et al., 1982). We postulate that low $\delta^{13}C$ organic signatures in crustal wall rocks

result from either deep hydrothermal circulation of organic material (Lang et al., 2006) and/or

biological activity during mineralization (Thorseth et al., 1992; Fisk et al., 2003). Figure V.8e

illustrates that all of the (n=8) extremely low $\delta^{13}C$ samples could be explained by CAFED

(dashed lines) with CO_2 = 50-500 ppm and $\delta^{13}C$ = -30. This type of model illustrates that

crustal interaction with melt can generate extremely low $\delta^{13}C$ values.

V.6.3.4 Vesicle CO_2 and the elemental fractionation

In addition to the new CO_2 concentration and isotope data presented here, a subset

(n=30) of Icelandic glasses were previously characterized for vesicle-sited He, Ne, and Ar

concentrations and isotopes (Füri et al., 2010). By combining these two data sets, we calculate

volatile ratios (i.e., $CO_2/^3He$ and CO_2/Ar^*), which when combined with previously reported

$^4He/^{40}Ar^*$ ratios (Füri et al., 2010) may potentially reveal further useful information about the

degassing histories of the magmas.

The extent of degassing can be approximated by the $^4He/^{40}Ar^*$ ratio (Marty and

Tolstikhin, 1998); where ^4He is produced by the radioactive decay of U and Th, and $^{40}Ar^*$ is

produced by the decay of ^{40}K. Based on known upper mantle K/U (Jochum et al., 1983) and Th/U (Allègre et al. 1986; O'Nions and McKenzie, 1993) ratios, a ^{4}He/^{40}Ar* production ratio of ~2 (Jambon et al., 1986) is assumed. In basaltic magmas, helium is more soluble than Ar (S_{He}/S_{Ar} = 9.5; Jambon et al., 1986), therefore residual ^{4}He/^{40}Ar* values should increase with increased degassing. For the present sampling suite, Füri et al (2010) showed that low ^{3}He/^{4}He ratios are not coupled with low helium concentrations, suggesting that crustal contamination has a negligible effect on He-isotopes (Hilton et al., 1993; Hilton et al., 1995; Macpherson et al., 1998, 2005a; Füri et al., 2010) and that ^{4}He/^{40}Ar* should reflect only the effects of degassing. Measured ^{4}He/^{40}Ar* ratios in several Icelandic basalts are typically higher than the mantle production ratio as a result of preferential loss of Ar.

Having identified samples that have been modified by both degassing and crustal assimilation processes in the previous section, we now plot (Figure V.9a-c) elemental ratios of vesicle-sited volatiles (^{4}He, ^{40}Ar* and CO_2) in order to highlight elemental fractionation that occurs during vesicle formation due to relative solubility differences (i.e., S_{He} = 6.4 × 10^{-4} cm^{3} STP/g, S_{CO2} = 2.7 × 10^{-4} cm^{3} STP/g, and S_{Ar} = 6.8 × 10^{-5} cm^{3} STP/g at 1 bar atm; Jambon et al., 1986; Lux, 1987; Pan et al., 1991; Dixon and Stolper, 1995; Jendrzejewski et al., 1997; Hilton et al., 1998a; Cartigny et al., 2001a) between species. We begin by assuming that WRZ sample MID-3 (^{4}He/^{40}Ar* = 2.1; CO_2/^{40}Ar = 6.0 × 10^{4}; CO_2/^{3}He = 1.4 × 10^{9}) can be used to approximate the least degassed sample, and thus provides a useful starting point to consider degassing and coupled assimilation in Icelandic basalts. This assumption is consistent with the dissolved carbon isotope and abundance systematics of MID-3 (Section 5.3.3) which indicates that it has undergone little modification. Füri et al. (2010) also used samples from the Miðfell region to approximate the undegassed mantle source using He-Ne-Ar isotope characteristics. Both BED and FED trajectories are then plotted from this presumed starting composition. Relative solubility differences between elements leads to increases in ^{4}He/^{40}Ar* and

$CO_2/^{40}Ar^*$ and a decrease in $CO_2/^3He$ in the residual phase as degassing progresses. As seen in all three sub-plots of Figure V.9, BED and FED degassing trajectories provide a reasonable fit to just a small proportion of samples and thus an additional process must be considered. For example, we identify several samples with distinctly high $CO_2/^3He$ values, accompanied by relatively low $^4He/^{40}Ar^*$ values (Figure V.9a). Such high $CO_2/^3He$ values cannot be produced by degassing alone; as such a process would require unrealistically high starting $CO_2/^3He$ values or volatile solubilities that are drastically different than experimentally-derived values. Alternatively, assimilation of crustal material ($CO_2/^3He = 1 \times 10^{11} - 1 \times 10^{13}$, $^4He/^{40}Ar^* = 2$) could provide a mechanism to produce the observed variations. An addition such as this would be consistent with assimilation of ^{13}C-depleted wall rock CO_2 into the melt during transfer to the surface and would likely occur concurrently with degassing. The methods of Macpherson et al (2010) can be used to construct a CAFED type model.
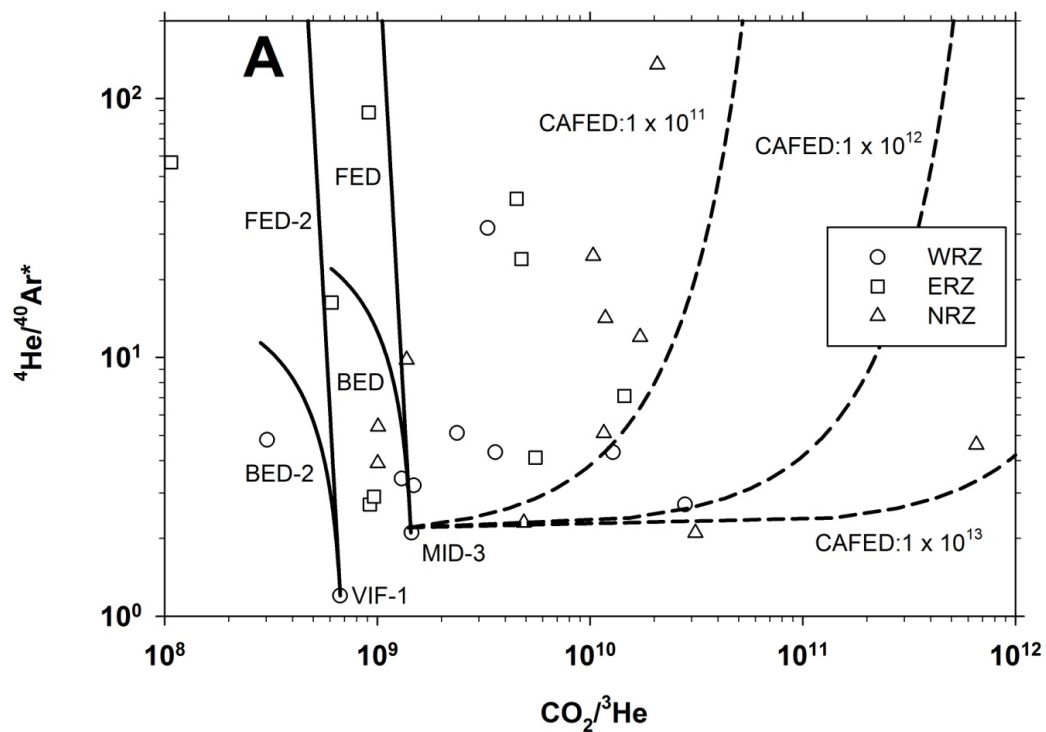
Figure V.9: Elemental ratios for vesicle derived gases from Iceland's neovolcanic axial rift zones. 9a = $CO_2/^3He$ vs. $^4He/^{40}Ar^*$; 9b – CO_2/Ar^* vs. $CO_2/^3He$; 9c – $^4He/^{40}Ar^*$ vs. CO_2/Ar^*. Superimposed on each subplot are two equilibrium degassing scenarios (FED-BED & FED-2-BED-2; solid lines) and coupled assimilation fractional equilibrium degassing (CAFED) scenarios. The CAFED assumes 1% degassing increments from a given starting composition (e.g., MID-3), followed by addition of contaminant. $CO_2/^3He$ and CO_2/Ar^* values of the crustal contaminant are assumed to be enriched by a factor of ~100-10,000 and the ratio of assimilated CO_2 to degassed CO_2 is assumed to be the same as the enrichment factor. Following the assimilation step, the degassing step is repeated from the new starting composition.

Figure V.9 continued
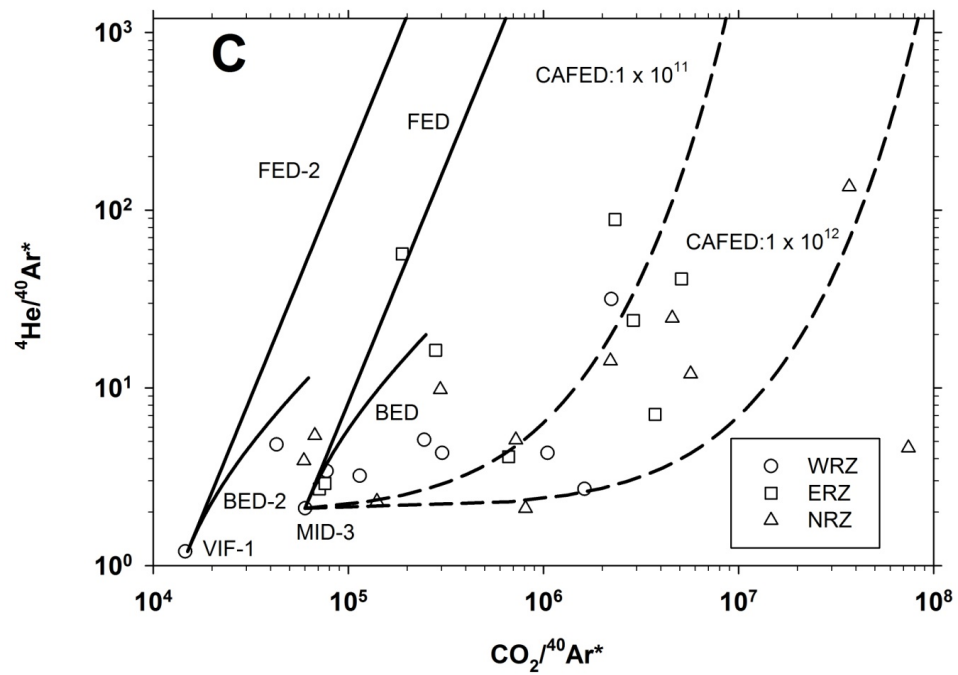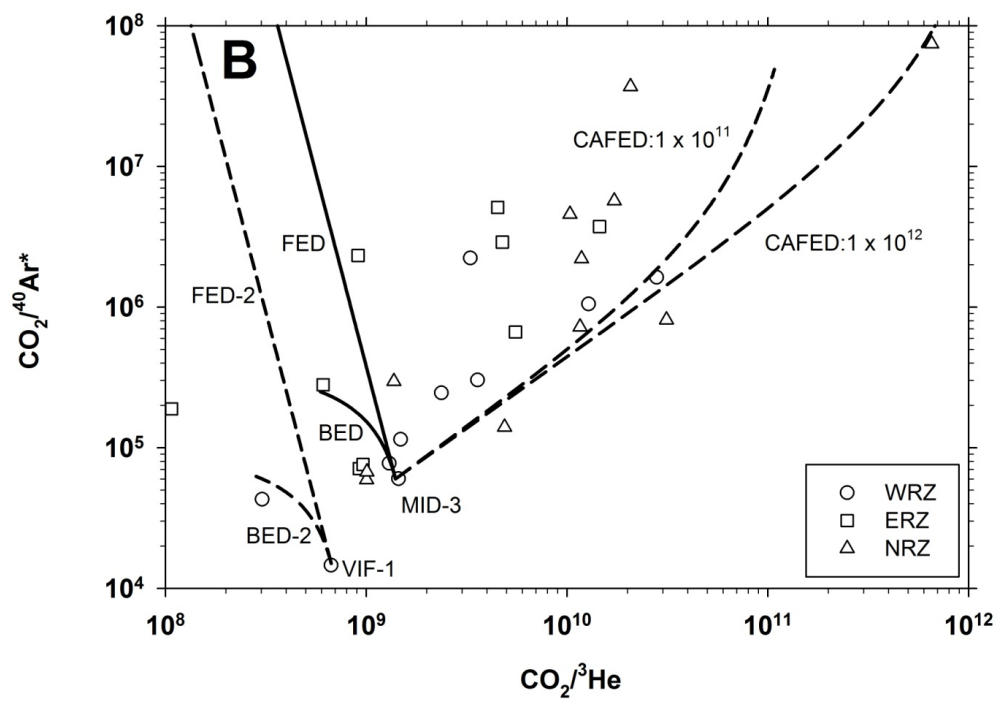
As in section V.6.3.3, the CAFED model assumes FED of CO_2 in 1% increments from a given starting composition (e.g., MID-3), followed by addition of contaminant. $CO_2/^3He$ and CO_2/Ar^* values of the crustal contaminant are assumed to be enriched by a factor of $\sim10^2$-10^4, which is consistent with their crustal provenance (e.g., $CO_2/^3He = 1 \times 10^{11} - 1 \times 10^{13}$; O'Nions and Oxburgh, 1988). The ratio of assimilated CO_2 to degassed CO_2 is assumed to be the same as the enrichment factor. Following assimilation, the degassing step is repeated from the new starting composition.

The results of this model are plotted as dashed lines in Figures V.9a-c. We conclude that CAFED is necessary to explain the majority of Iceland samples and suggest that wall rock assimilation is an important control on the volatile systematics of Iceland. However, this approach does not account for several low (vesicle) $CO_2/^3He$ samples which cannot result from degassing (assuming MID-3) and/or through CAFED. Therefore, we suggest heterogeneities in elemental source characteristics as a potential explanation. For example, if the source melt were characterized by WRZ sample VIF-1 ($^4He/^{40}Ar^* = 1.2$, $CO_2/^{40}Ar^* = 1.5 \times 10^4$, $CO_2/^3He = 6.7 \times 10^8$) then the majority of remaining samples could be explained by FED-BED (solid lines labeled FED-2 & BED-2) and CAFED processes. The overwhelming empirical evidence suggests that $CO_2/^3He$ values are greater than typical MORB-like values ($2 \pm 1 \times 10^9$) in plume derived samples (Trull et al., 1993, Marty and Tolstikhin, 1998, Shaw et al., 2004) and thus we find this scenario unlikely.

Alternatively, Hahm et al. (2012) suggested that selective assimilation of pure CO_2 by the largest vesicles in the magma could provide the mechanism to produce lower $CO_2/^3He$ (and $CO_2/^{40}Ar^*$) values with minimal modification to $^4He/^{40}Ar$ ratios. Furthermore, these same authors suggested that the origin(s) of vesicle-sited volatiles are complicated by open system conditions, which could result in different populations of vesicles becoming trapped together within a given basaltic sample (Hahm et al., 2012).

In summary, the elemental characteristics of vesicle-sited CO_2 and other volatiles are compatible with degassing and assimilation of crustal material (in most cases). We postulate that parent magma is stored in crustal magma chambers where addition of CO_2 can occur, most likely due to wall rock interaction.

V.6.4 CO_2 Flux Estimates

Having identified intrinsic CO_2 characteristics of Icelandic fluids/gases (Section 5.2) and subglacial basalts (Section 5.3), we are now able to estimate the total CO_2 output from Icelandic magmatic systems. CO_2 fluxes are estimated using three different approaches: (1) combining ^{3}He flux estimates from Iceland (Hilton et al., 1998b) with measured $CO_2/^3$He values (this study); (2) estimating initial CO_2 contents of basalts (this study) and combining these data with magma production rates for Iceland (Schilling, 1978, Crisp, 1984; White et al., 1993; Armannsson et al., 2005), and (3) by combining fluid flow rates with measured CO_2 contents in fluids (this study). These estimates are then compared to previous estimates of CO_2 output from Iceland, determined by integrating steam flow rates with CO_2 concentrations in high temperature steam fields (Armannsson et al., 2005; Fridricksson et al., 2006) and fluid flow rates at individual volcanic centers (Gislason, 1992; Agustsdottir and Brantley, 1994; Gislason, 2000). All CO_2 flux estimates are tabulated and compared to other volcanic/geothermal areas, and global rift zones (Table V.6).

The ^{3}He flux at mid ocean ridges (MOR) was first estimated by Craig et al. (1975), who measured relative ^{3}He enrichments in seawater around MOR-crests and estimated a ^{3}He flux ($\sim$1000 mol a^{-1}) from the Earth's mantle. By combining ^{3}He flux estimates with measured

Table V.6: CO$_2$ flux estimates.

Area	CO$_2$ Flux (mol/yr) x10^{10}	% of Global Ridge Flux	Method	References
Iceland				
Iceland	7-23	3-10	He flux & CO$_2$/^{3}He	This work[1]
Iceland	2-7	1-3	Source CO$_2$ = 531 ppm CO$_2$	This work[1]
Iceland	7	3	TDIC & flow rate extrapolated	Gislason, 1992, Agustsdotir and Brantley, 1994; Gislason, 2000
Iceland	2-5	1-2	Heat Flux & Steam vent and diffuse soil emissions	Arnorsson, 1991; Arnorsson and Gislason, 1994
Global Ridge	220	-	He flux & CO$_2$/^{3}He	Marty and Tolstikhin, 1998
Other Subaerial Volcanic Regions				
Solfatara, Italy	0.1			Chiodini et al., 1998
Etna, Sicily	100			Allard et al., 1991; Brantley and Koepenick, 1996
Central American Arc	6-7			Hilton et al., 2002; Shaw et al., 2004
Kilauea	3			Greenland et al., 1985; Gerlach and Graeber, 1985
Yellowstone	23-50			Werner and Brantley, 2003
Oldoinyo Lengai, Tanzania	0.06			Brantley and Koepenick, 1996
Mt. Erebus, Antarctica	1.5			Wardell and Kyle, 1998
White Island, NZ	2.2			Wardell and Kyle, 1998
Aggregate fluxes:				
Subaerial (Arc + Plume)	148-550			Varekamp et al., 1992; Williams et al., 1992; Marty and Tolstikhin, 1998
Global Ridge (MOR)	68-2300			Varekamp et al., 1992; Morner and Etiope, 2002; Kerrick 2001; Marty and Tolstikhin, 1998
Global Total	295-2300			Gerlach, 1991; Le Cloarec and Marty, 1991; Varekamp et al., 1992; Sano and Williams, 1996, Morner and Etiope, 2002; Kerrick, 2001; Delgado et al., 1998; Marty and Tolstikhin, 1998

[1] ^{3}He flux of ~10-36 mol a^{-1} using crustal production rate of 0.064-0.22 km^3 a^{-1} (Hilton et al., 1990; Hilton et al., 1998b; White et al., 1993; Armannsson, 2005).

$CO_2/^3He$ values from individual rift segments, CO_2 fluxes have been quantified in various global rift segments (Marty et al., 1987; Marty and Tolstikhin, 1998). However, more recent estimates (Farley et al., 1995; Saal et al., 2002; Bianchi et al., 2010) suggest that ^3He fluxes may be overestimated by a factor of ~2 and, as a result, previous global ridge CO_2 flux estimates (Marty and Tolstikhin, 1998) are considered upper estimates. In this contribution, we report $CO_2/^3He$ values from both geothermal manifestations and subglacial basalts of Iceland, both of which can be combined with ^3He fluxes from Iceland to estimate CO_2 fluxes.

In section 5.1 we showed that $CO_2/^3He$ values measured in fluids and off-axis gas samples were extensively modified and therefore only (n=37) on-axis gas samples (mean $CO_2/^3He = 5.9 \pm 6.3 \times 10^9$) are considered appropriate for estimating CO_2 fluxes. In contrast, all on-axis basalt (n=43) $CO_2/^3He$ values (mean $CO_2/^3He = 24 \pm 99 \times 10^9$) are considered appropriate to approximate the source. However, $CO_2/^3He$ variability in basalts is attributed to degassing and/or CAFED, and thus a similar filter must be applied to the data. In order to circumvent the effects of degassing on basalt samples, a simple degassing correction (after Marty and Tolstikhin, 1998) can be applied to the raw data by assuming that Ar loss follows a Raleigh distillation (Marty, 1995). In this way any degassing fractionation effect between two volatiles can be scaled to the $^4He/^{40}Ar^*$ ratio. Using this approach, we calculate the initial $CO_2/^3He$ ratio according to:

$$(CO_2/^3He)_{initial} = (CO_2/^3He)_{obs} \times [(^4He/^{40}Ar^*)_{obs} / (^4He/^{40}Ar^*)_{initial}]^{\wedge} [1-(S_{He}/S_{CO2})/ 1-(S_{He}/S_{Ar})]$$

$$(5)$$

As degassing increases, residual $^4He/^{40}Ar^*$ and $CO_2/^3He$ values decrease (Marty and

Tolstikhin, 1998; Hilton et al., 1998a). Consequently, the average measured $CO_2/^3He$ value of

Icelandic basalts of $24 \pm 99 \times 10^9$ can be corrected to a mean starting value of $\sim 35 \pm 140 \times$

10^9 (Table V.2). More importantly however, we only consider samples that have not been

extensively modified by crustal assimilation. In the previous section we identified several

(n=7) on-axis basalt samples suspected to be modified by assimilation (CAFED) with an

isotopically low $\delta^{13}C$ crustal component – marked by relatively high $CO_2/^3He$ values (1-100 $\times$

10^{11}). Mixing with such a high $CO_2/^3He$ contaminant will drastically counteract the effects of

degassing and increase measured $CO_2/^3He$ values markedly. By using extreme carbon isotope

values as a metric for extent of crustal modification (Figure V.8e; circled samples), we can

identify and selectively remove (n=7) samples which have been largely affected by crustal

assimilation and thus only consider the remaining on-axis samples to be representative of the

source composition. Using this approach, an average $CO_2/^3He$ value of $7.9 \pm 12 \times 10^9$ can be

calculated for the remaining basalts, which is in good agreement the average value $5.9 \pm 6.3 \times$

10^9 reported here for selected (n=37) gas phase samples, as well as previous $CO_2/^3He$

estimates (Poreda et al., 1992) from CO_2-rich, HT, fluids from the axial rift zones of Iceland.

Average filtered gas and basalt $CO_2/^3He$ values can then be combined with an

estimated ^3He flux of ~ 11 mol a^{-1} from Iceland (Hilton et al., 1998b) to estimate a CO_2 flux of

$\sim 7-9 \times 10^{10}$ mol a^{-1}. Notably, this ^3He flux estimate assumes a crustal production estimate of

0.064 km^3 a^{-1} (Schilling, 1978; Crisp, 1984; Hilton et al., 1990; Hilton et al., 1998b;

Thordarson and Höskuldsson, 2008). However, estimates of crustal production in Iceland vary

widely. For example, if we assume basaltic magma is emplaced into the Icelandic crust along

the ~ 550 km axial rift zone, with a spreading rate of 2 cm a^{-1} (Bjornsson, 1985) and an

average crustal thickness of ~ 20 km (Bjarnason et al., 1993), then we calculate a crustal

production rate of ~0.22 km^3 a^{-1} which is in agreement with other estimates (White et al., 1993; Armannsson et al., 2005). By adopting higher crustal production rates, we then estimate a significantly larger CO_2 flux of ~23 × 10^{10} mol a^{-1}. This latter value represents ~ 10 % of the global ridge flux (Marty and Tolstikhin, 1998). For perspective, Iceland comprises just less than 1 % of the length of the global ridge system. Together, these results suggest that higher crustal production rates in Iceland coupled with elevated CO_2 contents in the Icelandic mantle source can potentially result in large CO_2 fluxes relative to global ridge averages.

The second approach to estimating the mantle CO_2 flux involves combining the mantle CO_2 source estimate for all of Iceland (531 ± 64 ppm), calculated in section 5.2, with magma production rate between 0.064 and 0.22 km^3 a^{-1} (Hilton et al., 1990; White et al., 1993; Armannsson et al., 2005) and ~12% partial melting, which is considered a good approximation for olivine-tholeiites (i.e., the most common magma type generated in rift zones of Iceland) (Slater et al., 1998; Momme et al., 2003; Marty, 2012). This approach assumes that carbon is incompatible (Bottinga and Javoy, 1990) and thus passes into the melt phase, and is quantitatively degassed from basaltic melt during magma ascent. Using this approach, we calculate a CO_2 flux between 2-7 (× 10^{10} mol a^{-1}), which represents 1-3 % of the global ridge flux (Marty and Tolstikhin, 1998). In addition, by combining CO_2 source estimates (section 5.2.2) for the individual rift segments (WRZ = 206 ± 24 ppm; ERZ = 371 ± 45 ppm; NRZ = 550 ± 66 ppm) with crustal production rates (scaled to rift segment length; WRZ = ~210 km, ERZ = ~140 km, NRZ = ~200 km), we can estimate CO_2 output from the individual rift zones. In this way a range of values from 0.8 to 2.6 × 10^{10} mol a^{-1} are calculated for the WRZ, 0.5 to 1.8 × 10^{10} mol a^{-1} for the ERZ and 0.7 to 2.5 × 10^{10} mol a^{-1} for the NRZ.

Finally, measured geothermal fluid CO_2 contents (TDIC) can be combined with estimated regional fluid discharge rates (Heng, 2004) to make a first order estimate of CO_2 fluxes from Iceland via geothermal discharges. Notably, the ERZ is the only axial rift segment where fluid phase samples were collected and thus the only region where we are able to estimate CO_2 fluxes. In addition, several fluid samples were collected in LT off-axis portions of the crust (i.e., SISZ and Vestfirðir), however these samples are substantially modified by calcite precipitation (section 5.1.3) and, as a result, have almost certainly lost much of their primary CO_2, as is evident by their low CO_2 contents (typically < 1 mmole/kg H_2O). Using an average CO_2 content of ~2.84 mmole/kg H_2O measured at Köldukvíslabotnar (ERZ), and previously published fluid flow estimates of ~1000-2000 l/s (Heng, 2004) for the Köldukvíslabotnar region, we calculate a CO_2 flux of $0.9\text{-}1.8 \times 10^8$ mol a^{-1} for this segment of the ERZ. Unfortunately, published fluid flow estimates are not available for the remainder of the ERZ and thus CO_2 flux estimates cannot be directly determined for the individual localities. However, if we assume that fluid discharge rates are relatively constant throughout the ERZ, we can calculate CO_2 outputs between $0.6\text{-}1.2 \times 10^8$ mol a^{-1} for Landmannalaugar and $1.7\text{-}3.5 \times 10^8$ mol a^{-1} for the Vonarskarð region. Significantly, estimates of CO_2 provenance (section 5.1.4) indicate that ~ 34% of CO_2 in Landmannalaugar (ERZ) is mantle derived and thus these estimates may overestimate the mantle contribution.

We compare our three estimates with available CO_2 flux estimates for Iceland – calculated previously by integrating fluid and steam fluxes with measured CO_2 contents. In total, CO_2 flux estimates have been calculated for 4 of ~40 volcanic and geothermal systems of Iceland (Armannsson et al., 2005): Hekla (Gislason et al., 1992), Grímsvötn (Agustsdottir and Brantley, 1994), Eyjafjallajökull (Gislason, 2000), and Reykjanes (Kristjansson et al., 2004; Fridriksson et al., 2006). At Grímsvötn and Eyjafjallajökull, [CO_2] was measured in subglacial calderas where magmatic CO_2 is dissolved in glacial melt-water. During subsequent

catastrophic flooding events (i.e., jökulhlaups) flowrates were measured and combined with [CO_2] in order to estimate CO_2 fluxes. Notably, Grímsvötn is one of the largest and the most active volcanic system in Iceland, and thus the CO_2 flux (~44 × 10^8 mol a^{-1}; Agustsdottir and Brantley, 1994) is approximately an order of magnitude larger than other less active regions like Eyjafjallajökull (0.6-6 × 10^8 mol a^{-1}; Gislason, 2000), whereas the later estimates from Eyjafjallajökull are more consistent with our estimates from the ERZ. Using a similar approach, Gislason et al., (1992) estimated CO_2 discharge into the local groundwater system from the Hekla magma chamber to be ~16 × 10^8 mol a^{-1}. In addition, Kristjansson et al. (2004) and later Fridriksson et al. (2006) reported a CO_2 flux through soils in the Reykjanes geothermal area to be ~6 × 10^8 mol a^{-1}. Notably, the combined CO_2 flux for these four volcanic centers is ~0.7 × 10^{10} mol a^{-1}, however if this value is extrapolated to the remaining ~35-40 geothermal/volcanic systems of Iceland, the resultant flux is ~7 × 10^{10} mol a^{-1} (Gislason et al., 1992; Agustsdottir and Brantley, 1994; Gislason, 2000), which compares favorably with estimates from this study.

Using a different approach, Armannsson (1991) estimated the total steam vent CO_2 flux of Icelandic geothermal systems to be ~3 × 10^9 mol a^{-1}, by extrapolating measured steam emissions rates in the Krafla geothermal region to other geothermal areas throughout Iceland. Later, Arnórsson (1991) and Arnórsson and Gislason (1994) used heat flux estimates from Icelandic geothermal areas (Palmason et al., 1985) to estimate steam emissions – assuming that convective flow of steam is the dominant heat transport process in these areas. As with the previous approach, steam estimates were then combined with measured CO_2 steam contents to estimate a total CO_2 flux (2-5 × 10^{10} mol a^{-1}) for Iceland.

These various CO_2 flux estimates for Iceland – calculated using different methodologies – are summarized in Table V.6 and, for comparison, we show CO_2 output

estimates from other subaerial volcanic regions. We note that CO_2 output estimates from this study overlap with previous estimates for Iceland and are bracketed by estimates from other volcanically active regions. For example, CO_2 emissions from individual Italian volcanoes bracket Icelandic CO_2 output estimates, spanning ~3 orders of magnitude from $~0.1 \times 10^{10}$ mol a^{-1} at Solfatara, Italy (Chiodini et al., 1998) to $~100 \times 10^{10}$ mol a^{-1} at Mt. Etna, Sicily - the largest single volcanic CO_2 emitter on Earth (Allard et al., 1991; Brantley and Koepenick, 1996). Furthermore, the CO_2 flux from all of Iceland is comparable to previous estimates of $~6$-7×10^{10} mol a^{-1} for the entire Central American Arc (Hilton et al., 2002; Shaw et al., 2003). CO_2 output estimates from this study also overlap with estimates made for other hotspot influenced islands such as Kilauea which have a CO_2 flux of $~ 3 \times 10^{10}$ mol a^{-1} (Greenland et al., 1985; Gerlach and Graeber, 1985). In contrast, continental hotspot regions (e.g., Yellowstone) typically emit more CO_2, with estimates by Werner and Brantley (2003) representing 2-25 times the total estimated for Iceland. In the context of other well characterized volcanically-active regions on Earth, this study clearly shows that Icelandic volcanism acts to transfer a significant amount of CO_2 from the mantle to Earth's surface.

V.7 Concluding Remarks

      In conclusion, we highlight the following points:

(1) LT geothermal samples from off-axis regions of the Icelandic crust are more significantly fractionated (i.e., lower $\delta^{13}C$ and $CO_2/^3He$) vs. HT axial rift zone samples, indicating that calcite precipitation is a dominant process in the older and colder portions of the Icelandic crust.

(2) HT fluid samples of the ERZ display the highest geothermal $CO_2/^3He$ values measured. At localities where both fluid and gas phases were collected, fluid samples displayed 6 to 450 times higher $CO_2/^3He$ values vs. gas phases, suggesting that ERZ fluid samples have been affected by hydrothermal phase separation processes.

(3) Crustal assimilation is ubiquitous in all geothermal fluid and gas samples. Using a 3-component mixing model (after Sano and Marty, 1995) we estimate that 76% of hydrothermal $CO_2/^3He$ - $\delta^{13}C$ data can be explained by mixing between mantle (M), limestone (L) and sedimentary (S) components. The remaining ~24% of samples require either a lower starting $CO_2/^3He$ value and/or mixing with an isotopically high (> 0 ‰) limestone (L) component. Low $CO_2/^3He$ starting values are attributed to elemental fractionation caused by degassing.

(4) Using subglacial basalt data we are able to calculate pre-eruptive CO_2 source estimates for individual rift segments of Iceland, which show a general increase from the WRZ (206 ± 24 ppm) to the ERZ (371 ± 45 ppm) and reach a maximum in the NRZ (550 ± 66 ppm). When all data for Iceland are compiled, an average estimated pre-eruptive CO_2 source concentration of $\sim531 \pm 64$ ppm is calculated, which is in excellent agreement with previous estimates of E-MORB (519 ppm; Marty, 2012) and overlaps with the adjacently located Reykjanes (396 ppm; de Leeuw, 2007) and Kolbeinsey (400 ± 100 ppm; Macpherson et al., 2005b) ridges.

(5) Pre-eruptive $\delta^{13}C$ (δ_p) is estimated to be -2.5 ± 1.1 ‰ for all of the neovolcanic zone samples, which is in good agreement with the average geothermal value of -3.1 ± 1.9 ‰,

suggesting that geothermal carbon isotopes closely resemble the primary mantle composition of Iceland.

(6) The vast majority of vesicle-sited elemental ratio variations (i.e., $CO_2/^3He$; $^4He/^{40}Ar*$; $CO_2/^{40}Ar*$) can be explained by degassing and assimilation of crustal material. We postulate that parent magma is stored in crustal magma chambers where addition of ^{13}C depleted CO_2 can occur, most likely due to wall rock interaction.

(7) Crustal assimilation is evident in all geothermal fluid/gas samples and in some basalt samples. Significantly, basalts are modified by a ^{13}C depleted (organic/sedimentary) component – presumably at depth, whereas geothermal fluids and gases are primarily affected by a limestone-like contaminant with $\delta^{13}C$ close to ~ 0 ‰.

(8) Flux estimates of CO_2 from Iceland were made using three independent approaches. The first two approaches produce an estimate between $2 – 23 \times 10^{10}$ mol a^{-1} for the whole of Iceland. Notably, the various approaches are dependent on assumptions related to magma production rates. These estimates represent 1 to 10 % of the estimated global ridge flux (2.2×10^{12} mol CO_2 a^{-1}). The third approach is used to approximate the CO_2 output from the Köldukvíslabotnar region (ERZ), producing a CO_2 flux of ~ of 0.9-1.8×10^8 mol a^{-1} – consistent with estimates from other geothermal/volcanic regions.

CHAPTER VI: Stable isotope (C-N), noble gas (Ne-Ar) and volatile evidence for solar and recycled mantle components along the Central Indian Ridge (CIR)

VI.1 ABSTRACT

We present CO_2 ($\delta^{13}C$), N_2 ($\delta^{15}N$) and Ne-Ar abundance and isotope results of basaltic glasses collected along the Central Indian Ridge (CIR) (~17 – 21º S), as well as Ne-Ar isotope systematics of Réunion xenoliths. In addition, we report major volatile abundances (CO_2, H_2O, F, P, S, Cl) on all CIR glasses. A Réunion plume component was previously identified in He-isotopes ($^3He/^4He$) and trace elements in the same sample suite. Here, we aim to determine if the Réunion plume component is also present in C-N-Ne-Ar isotope systematics. Furthermore, we assess if CIR samples reveal evidence for solar and/or recycled contributions in their mantle sources, using a coupled Ne-He and Ne-N approach. Neon isotopes ($^{20}Ne/^{22}Ne$) range from atmospheric values of 9.84 to 11.32 and ($^{21}Ne/^{22}Ne$) from 0.0290 to 0.0401. When an air-correction is applied and $^{20}Ne/^{22}Ne$ values are extrapolated to solar (Ne-B) values, ($^{21}Ne/^{22}Ne$)$_{EX}$ ratios extend up to 0.0582. Argon isotopes ($^{40}Ar/^{36}Ar$) range from 298 (air) up to 8487 with the highest $^{40}Ar/^{36}Ar$ values occurring in samples with the highest Ne-isotope values. Nitrogen isotopes ($\delta^{15}N$) vary from -2.91 to +1.80‰ (n=16), with the majority of on-axis samples overlapping the upper end of the MORB range, and all off-axis samples displaying positive $\delta^{15}N$ anomalies. N-isotope results are in agreement with positive $\delta^{15}N$ anomalies previously observed in a single Réunion xenolith sample, and suggest a ^{15}N enriched recycled contribution to the mantle source of CIR basalts. Carbon isotopes (n=30) range from -4.2 to -29.5 ‰ versus PDB, with the majority of samples falling in the MORB range. Equilibrium degassing model results suggest primary CO_2 source concentrations of ~1300 ppm and $\delta^{13}C$ (CO_2) of -4.2 ± 0.2 ‰. Taken together, the Ne-N_2-Ar-CO_2 results suggest multiple mantle components in the source of CIR basalts, including solar and recycled contributions, both of which are possibly integrated into the Réunion plume. Conversely, CO_2 results retain close to canonical MORB-like signatures, suggesting that either the source CO_2 is masked by external processes (e.g. - degassing and/or crustal contamination) and/or that

CO_2 in the (upper and lower) mantle is homogenized to the extent that we cannot differentiate between the various reservoirs.

VI.2 Introduction

Geophysical and geochemical observations have revealed that global mid-ocean ridge (MOR) systems located in close proximity (< 1500 km) to hot spots are influenced by plume-ridge interaction (Schilling, 1991; Mittelstaedt and Ito, 2005). Systems such as these are estimated to occur between ~20 hot spots and nearby ridges, resulting in detectable geophysical and geochemical anomalies along 15–20% of the global MOR network (Ito et al., 2003). Geophysical observations include elevated topography, negative gravity anomalies (Nadin et al., 1995; Richards et al., 1988), and increased crustal melt production (Ito et al., 2003; White et al., 1992). Geochemical anomalies have previously been identified using trace elements, radiogenic isotopes and noble gases. (Schilling, 1973; Hanan et al., 1986, Hanan et al., 2000; Ito et al., 2003; Füri et al., 2011). Together, these observations highlight the significance of plume-ridge interaction on both the structure and composition of the oceanic lithosphere.

The Central Indian Ridge (CIR)-Réunion plume system is a classic example of modern plume-ridge interaction, marked by lateral flow of upwelling mantle along the base of the lithosphere towards the ridge system (Mahoney et al., 1989, Dyment et al., 2007; Füri et al., 2011). The lateral flow of material is believed to be responsible for the formation of volcanic lineaments between off-axis hot spot centers and nearby ridges, resulting in new islands and seamounts (Harpp et al., 2003). Geochemically, mixing between mid-ocean ridge basalt (MORB)-like mantle and plume-derived (i.e., Réunion) mantle has resulted in enriched trace element ratios and radiogenic isotope values (Mahoney et al., 1989; Murton et al., 2005; Nauret et al. 2006) along the axial CIR and off-axis lineaments, extending between Réunion

and the CIR. Recently, Füri et al. (2011) measured high ^{3}He/^{4}He ratios in off-axis portions of the CIR and along the rift between 19° and 20° S, and suggested that high ^{3}He/^{4}He values are evidence of mantle Réunion material in the CIR mantle source.

In this study, we present new Ne-N$_2$-Ar-CO$_2$ isotope and abundance data as well as major volatile (e.g., H$_2$O-F-P-S-Cl) abundances of glasses collected along the CIR axis between 16.7° S and 20.6° S, and the adjacent Gasitao Ridge, Three Magi Ridges, and Rodrigues Ridge. In addition, we determine the Ne-Ar isotope and abundance characteristics of olivine separates of a suite of cumulate xenoliths from Réunion Island. These new data are combined with previously published He-isotope and abundance results on the same sample suite (Füri et al., 2011) to discern underlying processes controlling elemental abundance, isotope variations, and CO$_2$-noble gas relationships. These new data reveal important information about mantle source characteristics and enable estimates of volatile (CO$_2$) source compositions. In addition, these observations allow us to evaluate the mixing dynamics of mantle components (i.e., solar, recycled) in the CIR-Réunion region, together with the effects of shallow level magmatic processes (i.e., degassing and crustal assimilation processes) that also play a role in establishing the volatile characteristics of the erupted lavas.

VI.3 Geologic background

The CIR separates the African and Indo-Australian plates and extends over ~3000 km from the Carlsberg Ridge (3.0° N, 66.0° E) southwards towards the Rodrigues Triple Junction (20.5° S, 70.0° E), where it bifurcates into the Southeast and the Southwest Indian ridges. Basalt samples of this study were collected along a segment of the CIR between 16.7° S and 20.6°S, located to the north and south of the Marie Celeste Fracture Zone (FZ), and northwest

of the Egeria FZ (Figure VI.1). The CIR axis shoals from N to S along this segment. In

addition, several off-axis samples were collected along a perpendicularly offset lineament

which extends westward from 66° E to 64° E toward the Mascarene Islands (e.g., Réunion,

Mauritius, Rodrigues islands) (Parson et al., 1993).
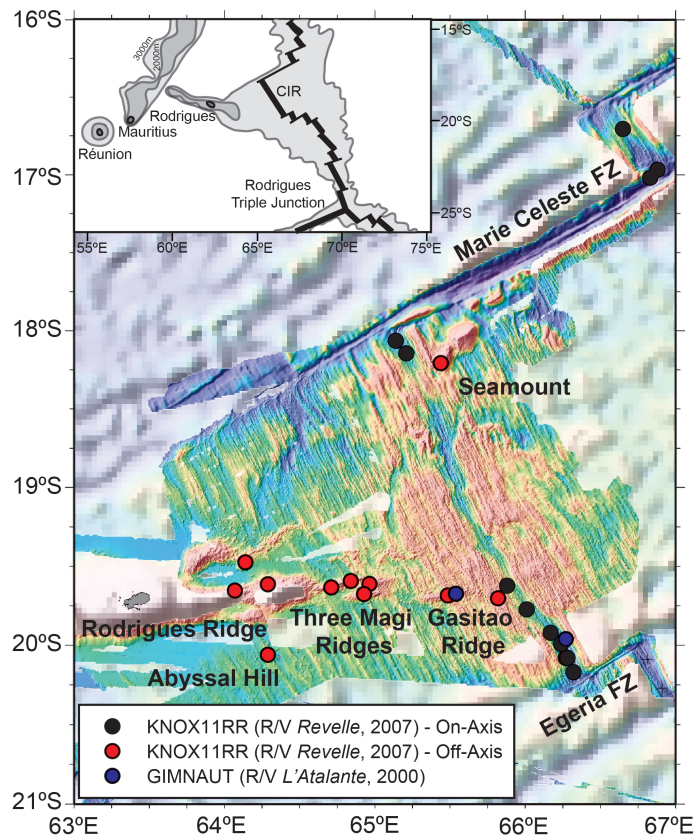
Figure VI.1: Bathymetric map of the (on-axis) CIR and the adjacent (off-axis) Gasitao Ridge, Three Magi Ridges, Rodrigues Ridge and Abyssal Hill. Three shades of colors represent bathymetry data: (1) pale colors are bathymetry "predicted" from satellite altimetry (Smith and Sandwell, 1997); (2) intermediate colors represent previous multi-beam bathymetric data from R/V Marion Dufresne (Dyment et al., 1999), R/V L'Atalante (Dyment et al., 2000), and R/V Hakuho-Maru (Okino et al., 2008); (3) bright colors are multibeam bathymetric data collected by R/V Revelle in 2007 (Füri et al., 2008; Füri et al., 2011). The circles indicate the location of samples collected during the KNOX11RR (black = CIR on-axis; red = off-axis) and GIMNAUT (blue) cruises. The inset shows the Mascarene Islands (i.e., Réunion, Mauritius, and Rodrigues islands) to the west and the Rodrigues Triple Junction.

During the past ~ 70 Ma the Réunion hot spot formed the Deccan Trap flood basalts, the Chagos-Maldive-Laccadive Ridge, the Mascarene Plateau and the Mascarene Islands (Duncan et al., 1989, Duncan et al., 1990). At ~34 Ma, the northeastward migrating CIR moved over the Réunion hot spot (Duncan et al., 1990) and embedded a "fossil" Réunion hot spot mantle component into the sub-ridge mantle. Currently, the center of the plume is located beneath the island of Réunion, located ~1100 km west of the CIR axis (Mahoney et al., 1989; Murton et al., 2005). Réunion Island is composed of two volcanoes: Piton des Neiges, which was active between ~2 Ma and 43 ka, and the currently active Piton de la Fournaise, where volcanic activity began ~530 ka ago (Gillot and Nativel, 1989). The island of Mauritius is located 250 km east of Réunion Island and 850 km west of the CIR, at the previous site of the Réunion hot spot (~8 Ma) (Morgan, 1981; Paul et al., 2005). Rodrigues Island is located ~600 km east of Mauritius and formed at 1.5 Ma (McDougall et al., 1965); it marks the eastern extent of the Rodrigues Ridge, an east-west trending volcanic ridge that is between 8 to 10 Ma old (Duncan et al., 1990). Smaller en-échelon volcanic ridges at 19° S (e.g., the Three Magi Ridges and the Gasitao Ridge) extend the Rodrigues Ridge close to the CIR (Figure VI.1) (Dyment et al., 1999; Dyment et al., 2000).

Various models have been proposed to explain the occurrence of volcanism between the Mascarene Islands and the CIR. First, Morgan (1978) proposed that the Rodrigues Ridge was formed by volcanism above a channel of upwelling Réunion hot spot mantle, which was deflected toward the CIR as it migrated northeastward away from the hot spot, and predicted a Réunion signature would be present at the intersection of the CIR with a line projected through Réunion and Rodrigues islands. Mahoney et al. (1989) later detected this Réunion-like isotope signature (low $^{143}Nd/^{144}Nd$, high $^{87}Sr/^{86}Sr$, high $^{207}Pb/^{204}Pb$, and high $^{206}Pb/^{204}Pb$) in basalts from the Marie Celeste FZ portion of the CIR. As a result, several detailed geochemical studies have focused on plume-ridge interaction in the region between the

Rodrigues Triple Junction and the Marie Celeste fracture zone. Murton et al. (2005) conducted a detailed study in this area and reported enrichments in incompatible elements that increased northward, which they interpreted to reflect the presence of an enriched mantle originating at the Réunion hot spot, which had subsequently migrating eastward toward the CIR against the direction of motion of the lithosphere. Nauret et al. (2006) also targeted a suite of basalts collected both on and off the CIR axis between 18° and 20° S for Sr-Nd-Pb isotopes and showed that the most trace element enriched samples display the most radiogenic Pb isotopic compositions. Furthermore, they compared basalt samples with submarine Réunion lavas (Fretzdorff and Haase, 2002) and concluded that radiogenic isotope characteristics of the majority of on-axis samples cannot be explained with a Réunion -like endmember. Recently, however, Ulrich et al. (2012) showed that trace element and isotopic enrichments in the 18° to 20° S region of the CIR are consistent with a binary mixture between the regional depleted MORB mantle source and a recycled Ocean Iceland Basalt (OIB)/seamount. In contrast, off-axis basalts from the Gasitao Ridge, as well as a single on-ridge sample collected at ~19.9° S, appeared to record a Réunion source signature. As a result, these authors proposed that Réunion hot spot material flows eastward toward the CIR on a trajectory that impinges the ridge at ~19.9° S, in agreement with the initial hypothesis put forth by Morgan (1978). Furthermore, they concluded that mantle source enrichment in the vicinity of the Marie Celeste FZ, ~100 km to the north, cannot be related to influx of mantle material from Réunion. Füri et al. (2011), however, suggested that these enrichments, along with slightly radiogenic He-isotope values could result from a "fossil" Réunion plume component in the region. In addition, they showed that the highest ^{3}He/^{4}He values (~ 12.2 R_A) were measured in glasses from off-axis portions of the CIR, and are consistent with flow of hot spot mantle material from Réunion (~1100 km to the west) toward the CIR.

In this contribution we report stable isotope (C-N) and noble gas (Ne-Ar) characteristics of the same sample suite that was previously characterized for He isotopes (Füri et al., 2011). To date, few volatile data exist on CIR basalts, with a single study only (Cartigny et al., 2001a) reporting $\delta^{15}N$ values (n=3) between –0.8 ‰ and -4.0 ‰ and $\delta^{13}C$ values (n=2) of -6.6 and -4.4 ‰. Cartigny et al. (2001a) also report C-N-Ar characteristics of (n=33) fresh basaltic glasses from the Southwest Indian, Southeast Indian, and Central Indian ridges as well as from the Rodriguez Triple Junction. These authors reported $\delta^{15}N$ values between −5.9 ‰ and +2.1 ‰ and $\delta^{13}C$ values between −11.4 and −4.3‰. In addition, Nishio et al. (1999) also reported volatile data (C–N–He–Ar) from the Rodriguez Triple Junction, located ~ 800 km south of the CIR. In contrast, lavas and xenoliths of Réunion have been well characterized for He-isotopes (Kaneoka et al., 1986; Staudacher et al., 1986; Graham et al., 1990; Staudacher et al., 1990; Hanyu et al., 2001; Trieloff et al., 2002; Hopp and Trieloff, 2005), neon isotopes (Hanyu et al., 2001; Trieloff et al., 2002; Hopp and Trieloff 2005) and volatiles (Bureau et al., 1999). However, only a single xenolith sample has been characterized for nitrogen isotopes (Fischer et al., 2005).

VI.4 Sampling and analytical techniques

Submarine pillow basalts were collected during the KNOX11RR cruise in November, 2007 aboard the R/V Revelle. Basalts were dredged from the ocean floor along the CIR axis (16.7° S to 20.1° S), and the adjacent Gasitao, Three Magi, and Rodrigues ridges (Füri et al., 2008; Füri et al., 2011). Fresh basaltic glass was recovered from 24 dredges sites and these samples were supplemented by glasses from 2 sites collected during the GIMNAUT cruise (Figure VI.1) (Nauret et al., 2006). In addition, cumulate dunite xenoliths (n=4) were collected from Piton Chisny on Réunion Island during a field campaign following the cruise.

Fresh glasses were removed from the outer rinds of pillow basalts and ultrasonically cleaned in a 1:1 acetone-methanol mixture. The cleaned glasses were then examined using a binocular microscope, and fresh glasses – free of any surficial alteration – were hand-picked. Selected glasses were then analyzed for light noble gas (Ne and Ar) isotopes and abundances, stable (carbon and nitrogen) isotopes, CO_2 and N_2 abundances and major volatile abundances (H_2O, CO_2, F, P, S, Cl). The analytical techniques employed and facilities used are described below.

Neon and argon gases were released from basalts using a custom-built piston-activated in vacuo rock-crusher (see Hahm et al., 2012 for details). The released gas was then purified using a dedicated cryogenic separation line whereby Ne and Ar were separated and analyzed independently. Neon and argon abundances and isotope ratios (as well as He abundances) were measured using a modified VG5440 mass spectrometer equipped with five Faraday cups and Daly photo-multiplier detector (Craig et al., 1993; Hahm et al., 2012), operated in peak jumping mode.

Neon results were corrected for procedural blanks and contributions of doubly-charged ^{40}Ar and CO_2 to ^{20}Ne and ^{22}Ne, respectively, following Niedermann et al. (1993). Procedural crusher blanks were $(15 \pm 8) \times 10^{-12}$ cm^3STP for ^{20}Ne; and $(6 \pm 2) \times 10^{-9}$ cm^3STP for ^{40}Ar, typically representing less than 10% of sample yields.

Nitrogen gases were released using the same rock crushing mechanism described above, however gases were purified on a separate vacuum clean-up line (see Barry et al., 2012a for details) prior to inlet into the mass spectrometer. Nitrogen isotope and abundance measurements were made on the same VG5440 mass spectrometer – operated in static triple

collection mode. Interfering CO species were monitored and CO corrections were applied to all samples. Procedural crusher blanks (average = $\sim4.2 \pm 0.5 \times 10^{-6}$ cm^{3}STP for N_2) were run prior to each sample analysis and blank subtractions were subsequently applied, representing less than 20% of the sample size on average. In addition, N_2/Ar ratios were measured separately using a quadrupole mass spectrometer (QMS).

Carbon was extracted from selected basaltic glass chips using a stepped heating procedure (after Macpherson and Mattey, 1994; Macpherson et al., 1999), on a dedicated all-glass extraction line. During each individual extraction procedure, the temperature was incrementally raised in 100 ºC steps from 400 ºC to 1200 ºC (excluding the 500 ºC step), each lasting 30 minutes. During the first two heating steps (400 ºC and 600 ºC), samples were combusted in pure oxygen, generated using a CuO furnace, to remove any surface contamination, whereas the 700 ºC to 1200 ºC pyrolysis heating steps (i.e., conducted without oxygen) released magmatic carbon. Following individual heating steps, the CO_2 was separated from other non-condensable gases (e.g., H_2O, SO_2) using a liquid nitrogen cooled variable temperature trap (Des Marais, 1978). After purification and separation were completed, total CO_2 abundances were measured in a calibrated volume using a Baratron capacitance manometer.

Carbon dioxide (CO_2) released during the first two combustion steps was not collected, as this gas is considered to be dominated by post-eruption surface contamination (Des Marais and Moore 1984; Exley et al. 1986; Mattey et al. 1984, Mattey et al., 1989). In contrast, CO_2 released during each of the 700 ºC to 1200 ºC steps, CO_2 was collected in Pyrex® glass tubes at each successive temperature step for later isotopic $\delta^{13}C$ analysis. Low temperature (700-900 ºC) CO_2 releases are taken to represent the "vesicular" carbon component whereas higher temperature (1000-1200 ºC) releases are considered derived from

the "dissolved" carbon component. Whenever the CO_2 yield from a single temperature step was deemed too small (< 3 ppm) for isotopic analysis, it was combined with CO_2 released during the following step. Aliquots of CO_2 gas (corresponding to each temperature step) were then analyzed for carbon isotopes ($\delta^{13}C$) using a Thermo Finnigan Delta XP_{plus} isotope ratio mass spectrometer. Carbon isotope $\delta^{13}C$ (CO_2) values are reported relative to PDB, with a precision of less than 0.1 ‰ and an accuracy of (± 0.5 ‰) based on the reproducibility of laboratory standards relative to PDB.

The abundances of H_2O, CO_2, F, P, S and Cl were determined using secondary ion mass spectrometry (SIMS) at the Department of Terrestrial Magnetism, Carnegie Institution of Washington (Hauri, 2002). All measurements were made on a Cameca IMS 6f ion microprobe which measures volatile components sputtered from the glass matrix by a Cs^+ primary beam. Reported volatile content results represent the dissolved component in the glass matrix.

VI.5 RESULTS

We report CO_2 ($\delta^{13}C$), N_2 ($\delta^{15}N$) and Ne-Ar isotope and abundance results for basaltic glasses of the CIR (16.7° - 20.6° S) and Ne-Ar isotope and abundance characteristics of (n=4) Réunion xenoliths. In addition, we report major volatile abundances (CO_2, H_2O, F, P, S, Cl) on all glasses. All basalt and Réunion xenolith samples were previously characterized for $^3He/^4He$ ratios (Füri et al., 2011), with basalts extending as high as ~9.7 R_A, and xenoliths up to ~14 R_A.

VI.5.1 Neon

Neon concentrations of basaltic glasses (n=16) and Réunion xenoliths (n=4) vary from 0.10 to ~2.28 × 10^{-9} cm^{3}STP ^{20}Ne/g (Table VI.1). In Figure VI.2, the (%) deviation of the Ne-isotope compositions from air (= 0%; dashed line) is demonstrated using δ^{20}Ne and δ^{21}Ne notation (after Poreda and di Brozolo, 1984). Ne-isotope anomalies (i.e., δ^{21}Ne) are shown as a function of latitude (on-axis samples) and longitude (off-axis samples) in Figure VI.3. On-axis samples exhibit a negative correlation between concentration and Ne-isotopes (δ^{20}Ne and δ^{21}Ne values), suggesting that low concentration samples are the least contaminated by air – an observation consistent with previous Ne-isotope studies of ocean basalts (e.g., Shaw et al., 2001 and Macpherson et al., 2005). Off-axis basalts and Réunion xenoliths generally display smaller offset from air with lower concentration samples again displaying the largest offsets.

In Figure VI.4, we plot ^{20}Ne/^{22}Ne versus ^{21}Ne/^{22}Ne for all CIR glasses and Réunion xenoliths in a three-isotope neon space. The ^{20}Ne/^{22}Ne ratios range from air-like values (9.84) up to 11.32, whereas the ^{21}Ne/^{22}Ne ratios plot between the atmospheric ratio (0.0290) and 0.401. All but two off-axis samples (D20-5 and duplicate) are air-like. Additionally, on-axis samples D3-1 and D2-1 also plot within error of the air value.

Table VI.1: Neon systematics of submarine basaltic glasses from the CIR (on-axis) and adjacent (off-axis) Gasitao Ridge, Three Magi Ridges and Abyssal Hill and olivine separates from dunite xenoliths of Piton Chisny (Réunion).

Sample	Phase	Latitude (°S)	Longitude (°E)	Depth (m)	Amount Processed (g)	$^{20}Ne/^{22}Ne$	$^{21}Ne/^{22}Ne$	$(^{21}Ne/^{22}Ne)_{EX}$	$\delta^{20}Ne$ (%)	$\delta^{21}Ne$ (%)	^{20}Ne (10^{-9} cm³ STP/g)
On-Axis											
D1-1	G	16.70	66.65	3146	1.4245	10.10 ± 0.11	0.0316 ± 0.0003	0.0524 ± 0.0011	3.1 ± 1.1	9.1 ± 1.2	0.67 ± 0.012
D3-1	G	16.96	66.88	4272	1.9100	9.90 ± 0.10	0.0291 ± 0.0001	-	1.0 ± 1.1	0.3 ± 0.5	2.28 ± 0.025
D2-1	G	17.01	66.83	4038	1.5678	9.85 ± 0.10	0.0295 ± 0.0003	0.0560 ± 0.0011	0.5 ± 1.1	1.6 ± 1.0	2.21 ± 0.030
D8-2	G	18.05	65.14	3202	1.5042	9.93 ± 0.10	0.0302 ± 0.0002	0.0539 ± 0.0010	1.3 ± 1.1	4.2 ± 0.8	0.76 ± 0.017
D15-1	G	19.76	66.01	2794	1.3267	10.34 ± 0.11	0.0327 ± 0.0004	0.0475 ± 0.0010	5.6 ± 1.1	12.6 ± 1.3	0.55 ± 0.008
D14-1	G	19.91	66.17	3267	0.7299	10.34 ± 0.12	0.0324 ± 0.0008	0.0460 ± 0.0014	5.5 ± 1.2	11.6 ± 2.8	0.25 ± 0.019
D14-1 (Dup)	G	19.91	66.17	3267	1.7487	10.43 ± 0.11	0.0331 ± 0.0004	0.0466 ± 0.0010	6.5 ± 1.2	14.1 ± 1.5	0.25 ± 0.012
D13-1	G	19.98	66.24	3511	1.5137	10.72 ± 0.12	0.0340 ± 0.0006	0.0437 ± 0.0011	9.4 ± 1.2	17.1 ± 2.0	0.20 ± 0.023
D13-1 (Dup)	G	19.98	66.24	3511	2.0531	11.32 ± 0.13	0.0401 ± 0.0007	0.0487 ± 0.0012	15.5 ± 1.3	38.2 ± 2.4	0.10 ± 0.004
Off-Axis											
Three Magi Ridges											
D22-1	G	19.62	64.97	1687	0.7313	9.89 ± 0.10	0.0296 ± 0.0002	0.0470 ± 0.0009	0.9 ± 1.1	2.2 ± 0.6	1.89 ± 0.011
D26-2	G	19.62	64.71	1785	1.1605	9.87 ± 0.10	0.0296 ± 0.0002	0.0521 ± 0.0010	0.8 ± 1.1	2.1 ± 0.7	1.15 ± 0.025
Gasitao Ridge											
D20-5	G	19.70	65.49	2002	0.7328	9.84 ± 0.23	0.0294 ± 0.0013	0.0560 ± 0.0023	0.5 ± 2.3	1.4 ± 4.4	0.17 ± 0.020
D20-5 (Dup #1)	G	19.70	65.49	2002	1.5228	10.05 ± 0.13	0.0304 ± 0.0009	0.0441 ± 0.0017	2.6 ± 1.3	4.7 ± 3.0	0.12 ± 0.007
D20-5 (Dup #2)	G	19.70	65.49	2002	0.9100	10.05 ± 0.12	0.0317 ± 0.0010	0.0582 ± 0.0013	2.5 ± 1.2	9.3 ± 3.4	0.14 ± 0.013
D18-1	G	19.72	65.86	2216	2.0652	9.89 ± 0.11	0.0290 ± 0.0004	-	1.0 ± 1.1	0.2 ± 1.5	0.14 ± 0.006
Abyssal Hill											
D37-2	G	20.05	64.29	2833	1.2237	9.86 ± 0.10	0.0294 ± 0.0001	0.0470 ± 0.0008	0.6 ± 1.1	1.3 ± 0.5	1.19 ± 0.022
Reunion – Piton de la Fournaise											
CH07-01	Ol	21.23	55.66	-	1.1449	10.49 ± 0.11	0.0306 ± 0.0005	0.0353 ± 0.0009	7.1 ± 1.2	5.5 ± 1.9	0.30 ± 0.006
CH07-02	Ol	21.23	55.67	-	1.3267	10.00 ± 0.11	0.0296 ± 0.0004	0.0371 ± 0.0008	2.1 ± 1.1	2.2 ± 1.5	0.33 ± 0.007
CH07-04	Ol	21.23	55.67	-	1.2240	10.09 ± 0.12	0.0314 ± 0.0014	0.0513 ± 0.0025	3.0 ± 1.2	8.1 ± 4.8	0.06 ± 0.007
CH07-07	Ol	21.23	55.67	-	1.1263	10.26 ± 0.11	0.0296 ± 0.0008	0.0325 ± 0.0011	4.7 ± 1.1	1.9 ± 2.6	0.20 ± 0.006

Ol = Olivine; G = Basaltic Glass.
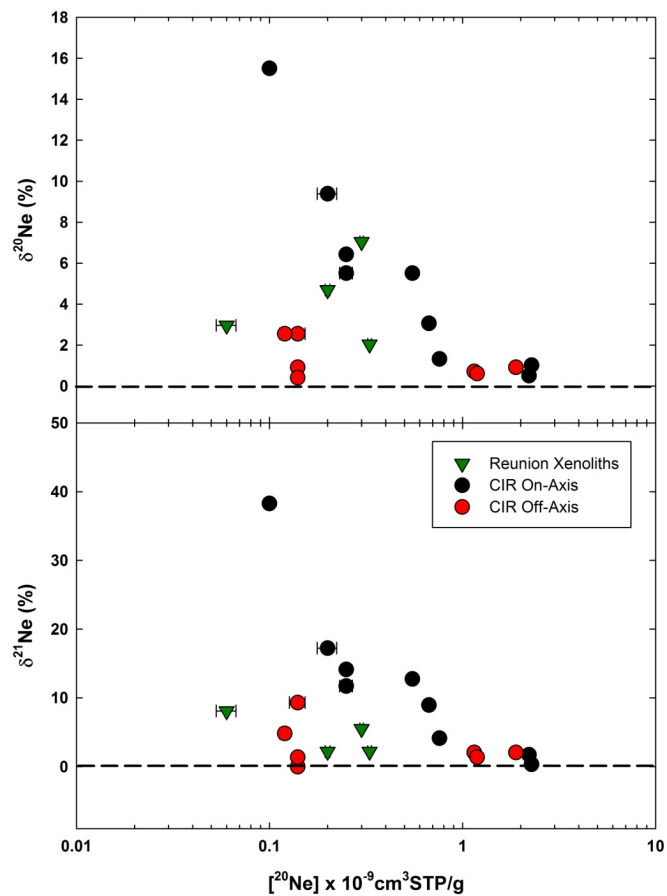
Figure VI.2: Neon isotope (δ^{20}Ne and δ^{21}Ne) enrichment (%) of CIR glasses (black and red circles) and Réunion xenoliths (green inverted triangles) relative to air as a function of ^{20}Ne concentration. Neon isotope enrichments are shown in the delta notation where δiNe = $[(iNe/^{22}Ne_{sample} \; / \; iNe/^{22}Ne_{air}) - 1] \times 100$ (iNe = ^{20}Ne or ^{21}Ne).
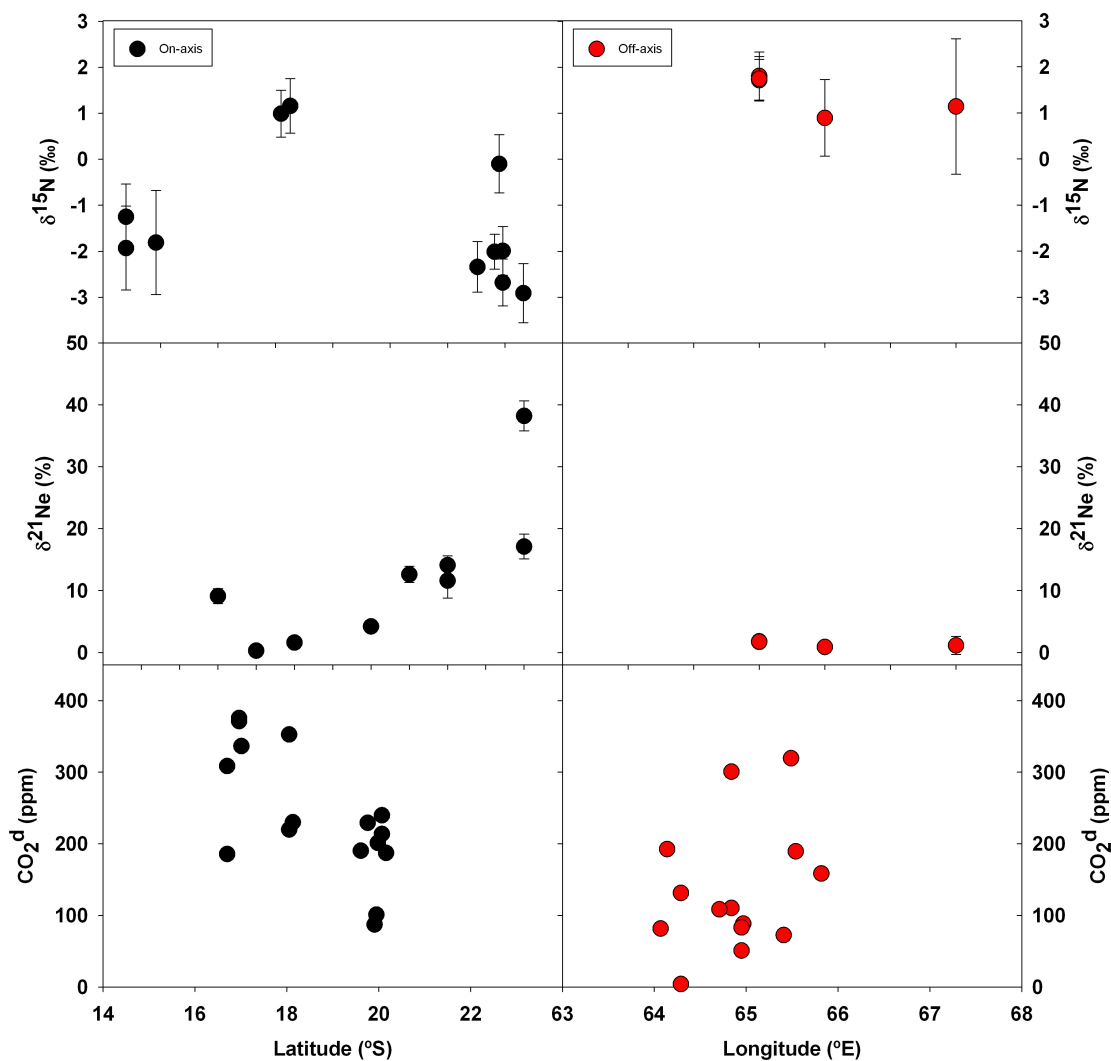
Figure VI.3: Nitrogen (δ^{15}N) and Ne-isotope (δ^{21}Ne) variations as a function of latitude (on-axis samples) and longitude (off-axis samples). Dissolved CO_2 (ppm) variations are also shown versus latitude and longitude.

The remaining samples show non-atmospheric neon isotope ratios, and plot between the MORB trajectory, defined by mid-ocean ridge popping rock 2∏D43 (Moreira and Allegre, 1998), and the air-solar wind mixing trajectory (Benkert et al., 1993) (Figure VI.4), suggesting that neon in CIR basalts and Réunion xenoliths is derived from a mixture of MORB-like mantle and a more primordial or "solar" mantle component. Notably, the highest ^{20}Ne/^{22}Ne

ratio (11.32 ± 0.13; on-axis sample D13-1) is still significantly lower than proposed primordial

mantle values (i.e., Ne-B ^{20}Ne/^{22}Ne = 12.5; Black, 1972; solar wind ^{20}Ne/^{22}Ne = 13.8; Benkert

et al., 1993; Kallenbach et al., 1997). In contrast, Hopp and Trieloff (2005) reported ^{20}Ne/^{22}Ne

values in Réunion xenoliths up to 11.70 ± 0.05, and these results are used to define an

additional (Réunion) trajectory in Figure VI.4. In addition, two of the four Réunion xenolith

samples reported here fall below the Réunion (Hopp and Trieloff, 2005) line and two fall

above it. All CIR basalts fall between the Réunion and MORB trajectories, consistent with

mixing between these two distinct mantle components.
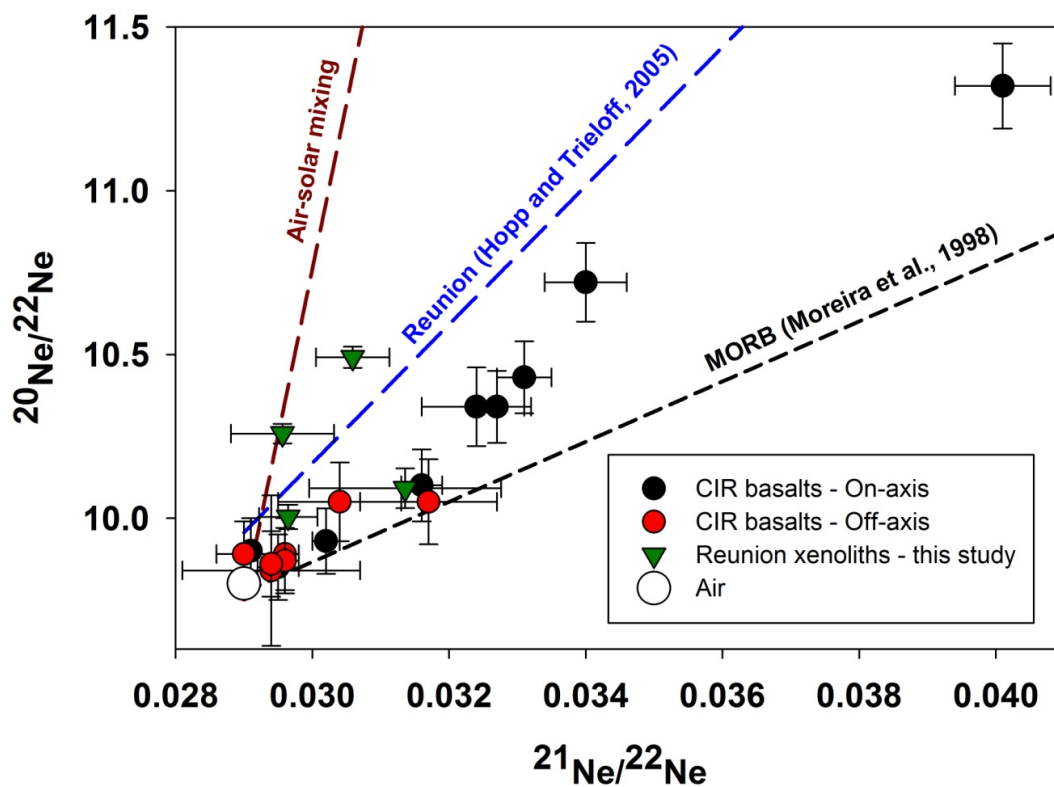
Figure VI.4: Neon three-isotope plot (^{20}Ne/^{22}Ne versus ^{21}Ne/^{22}Ne) of CIR basaltic glasses and
Réunion xenoliths. In addition, three trend-lines are superimposed over these data: (1) the air-
solar mixing line; (2) the Réunion line (Hopp and Trieloff, 2005); (3) the MORB (2∏D43)
line (Moreira et al., 1998). Errors are shown at the 1σ level.

VI.5.2 Argon

CIR glasses and Réunion xenolith samples span a wide range in argon concentrations from ~16 to 2400 × 10^{-9} cm^{3}STP ^{40}Ar /g (Table VI.2). The highest argon contents are found in on-axis glasses (e.g., D1-1, D15-1), and in off-axis samples of the Three Magi Ridges (D22-1, D26-2). The remainder of off-axis samples are Ar poor and fall below typical MORB values (~ 1200 × 10^{-9} cm^{3}STP ^{40}Ar /g; Sarda et al., 1985; Staudacher et al., 1986; Allègre et al., 1987), suggesting that they experienced more extensive degassing.

Argon isotope compositions of basaltic glasses (^{40}Ar/^{36}Ar) range from 291 to 8487, with both high and low ratios occurring in on- and off-axis samples. Réunion xenolith samples range from 501 to 1294, and are bracketed by the basalt range. Notably, all measured (basalt and xenolith) ^{40}Ar/^{36}Ar values are significantly lower than source estimates for MORB of (~28,000-32,000; Matsuda and Marty, 1995; Burnard et al., 1997; Trieloff et al, 2003), and the majority fall well below plume-source estimates (~6,000-8,000; Valbracht et al., 1997; Marty et al., 1998; Trieloff et al., 2003) and Réunion estimates (~11,000; Hopp and Trieloff, 2005), suggesting a considerable air-derived Ar contribution is present in most samples. In addition, most samples with Ne-isotope anomalies also display elevated (i.e., non-atmospheric) ^{40}Ar/^{36}Ar values (Figure VI.5). For example, on-axis sample D13-1 has the largest neon isotope anomaly (δ^{20}Ne = 15.5 ± 1.3 %; δ^{21}Ne = 38.2 ± 2.4 %) of all CIR basalts as well as the highest measured ^{40}Ar/^{36}Ar value (= 8487). Sample D-20 is the only off-axis sample which displays significant neon isotope deviations from air (δ^{20}Ne = 9.3 ± 3.4), and significantly, this sample (and duplicates) also yields the highest ^{40}Ar/^{36}Ar (= 1786 ± 4.8) amongst off-axis samples

Table VI.2: Argon systematics of submarine basaltic glasses from the CIR (on-axis) and adjacent (off-axis) Gasitao Ridge, Three Magi Ridges and Abyssal Hill and olivine separates from dunite xenoliths of Piton Chisny (Réunion).

Sample	Phase	Latitude (°S)	Longitude (°E)	Depth (m)	Amount processed (g)	^{3}He/^{4}He (R/R$_A$)^a	[^{40}Ar] 10^{-9} cm^{3}STP/g	^{40}Ar/^{36}Ar	^{4}He/^{40}Ar*
On-Axis									
D1-1	G	16.70	66.65	3146	1.4245	8.11 ± 0.11	2416 ± 0.3	290.6 ± 0.1	-
D3-1	G	16.96	66.88	4272	1.9100	7.91 ± 0.02	765 ± 0.5	296.1 ± 0.3	-
D2-1	G	17.01	66.83	4038	1.5678	8.19 ± 0.09	1415 ± 0.9	349.4 ± 0.3	62 ± 0.2
D8-2	G	18.05	65.14	3202	1.5042	7.08 ± 0.14	724 ± 0.2	3520 ± 12	7.5 ± 0.9
D15-1	G	19.76	66.01	2794	1.3267	8.68 ± 0.01	1968 ± 2.6	2193 ± 3.3	8.4 ± 0.3
D14-1	G	19.91	66.17	3267	0.7299	8.46 ± 0.02	1326 ± 0.3	2413 ± 5.8	6.9 ± 0.4
D14-1 (Dup)	G	19.91	66.17	3267	1.7487	-	761 ± 0.7	1514 ± 3.9	10 ± 0.4
D13-1	G	19.98	66.24	3511	1.5137	8.26 ± 0.03	1192 ± 0.1	450.1 ± 0.5	3.0 ± 0.1
D13-1 (Dup)	G	19.98	66.24	3511	2.0531	-	1272 ± 0.5	8487 ± 43	6.0 ± 2.6
Off-Axis									
Three Magi Ridges									
D22-1	G	19.62	64.97	1687	0.7313	9.40 ± 0.06	1903 ± 0.8	408.5 ± 0.6	23 ± 0.1
D26-2	G	19.62	64.71	1785	1.1605	9.51 ± 0.02	1268 ± 0.9	554.6 ± 0.5	5.2 ± 0.1
Gasitao Ridge									
D20-5	G	19.70	65.49	2002	0.7328	8.28 ± 0.05	421 ± 0.1	1725 ± 12	11 ± 1.3
D20-5 (Dup #1)	G	19.70	65.49	2002	1.5228	-	383 ± 0.1	1786 ± 4.8	9.3 ± 0.4
D20-5 (Dup #2)	G	19.70	65.49	2002	0.9100	-	401 ± 0.3	1576 ± 5.2	11 ± 0.6
D18-1	G	19.72	65.86	2216	2.0652	9.09 ± 0.06	16 ± 0.1	396.1 ± 3.0	31 ± 0.9
Abyssal Hill									
D37-2	G	20.05	64.29	2833	1.2237	9.67 ± 0.17	849 ± 0.7	318.4 ± 0.4	18 ± 0.1
Reunion – Piton de la Fournaise									
CH07-01	Ol	21.23	55.66	-	1.1449	13.95 ± 0.25	776 ± 0.2	1294 ± 3.0	1.3 ± 0.1
CH07-02	Ol	21.23	55.67	-	1.3267	13.66 ± 0.22	327 ± 0.2	501.2 ± 1.0	1.5 ± 0.1
CH07-04	Ol	21.23	55.67	-	1.2240	14.09 ± 0.23	125 ± 0.1	705.1 ± 3.5	2.0 ± 0.1
CH07-07	Ol	21.23	55.67	-	1.1263	13.58 ± 0.15	308 ± 0.1	831.3 ± 2.0	1.5 ± 0.1

Ol = Olivine; G = Basaltic Glass.

^{a} = He-isotope data from Füri et al. (2011).
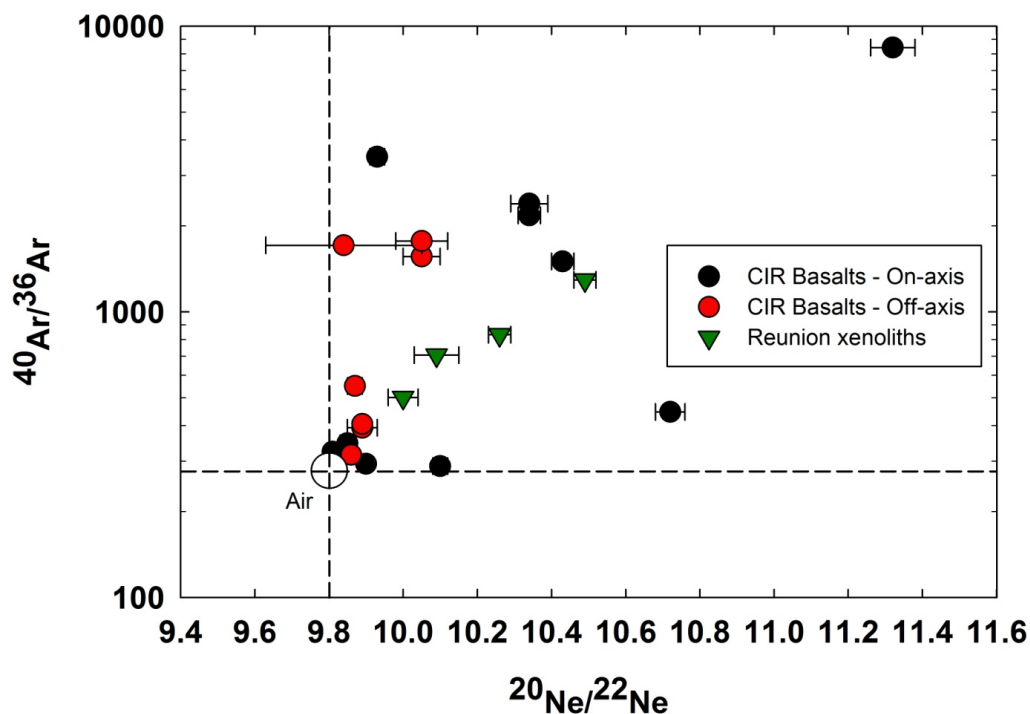
Figure VI.5: Ar-isotopes versus Ne-isotopes. Ne-Ar systematics are coupled for the majority of samples, i.e., air-contamination and isotope anomalies are evident in the same samples.

VI.5.3 N_2 and $\delta^{15}N$ Results

Nitrogen isotope and abundance characteristics were determined on a subset (n=16) of CIR samples and revealed $\delta^{15}N$ values between -2.91 to +1.80‰ versus air. All but two on-axis $\delta^{15}N$ values are ^{15}N depleted relative to air (i.e., <0 ‰), and range from -2.91 to 0.99 ‰ (Figure VI.3), falling just above the upper end of the MORB range (-5 ± 2 ‰; Marty and Dauphas, 2003). In contrast, all off-axis samples are ^{15}N enriched relative to air (i.e., >0 ‰) and range between +0.89 and +1.80 ‰ (Figure VI.3), and overlap with the postulated plume

mantle-source range of +3 ± 2 (Marty and Dauphas, 2003) but lie just below the average ocean sediment range of ~+7 ‰ (Pinti et al., 2001). N_2 concentrations range from 4.79 to 48.0 mcm^3 STP N_2/g for on-axis samples and from 2.34 to 92.6 μcm^3 STP N_2/g for off-axis samples. N_2/Ar ratios span from 47.9 to 267 (Table VI.3), and extend from below the typical MORB range (i.e., 84-164; Marty and Dauphas, 2003) up to significantly higher values.
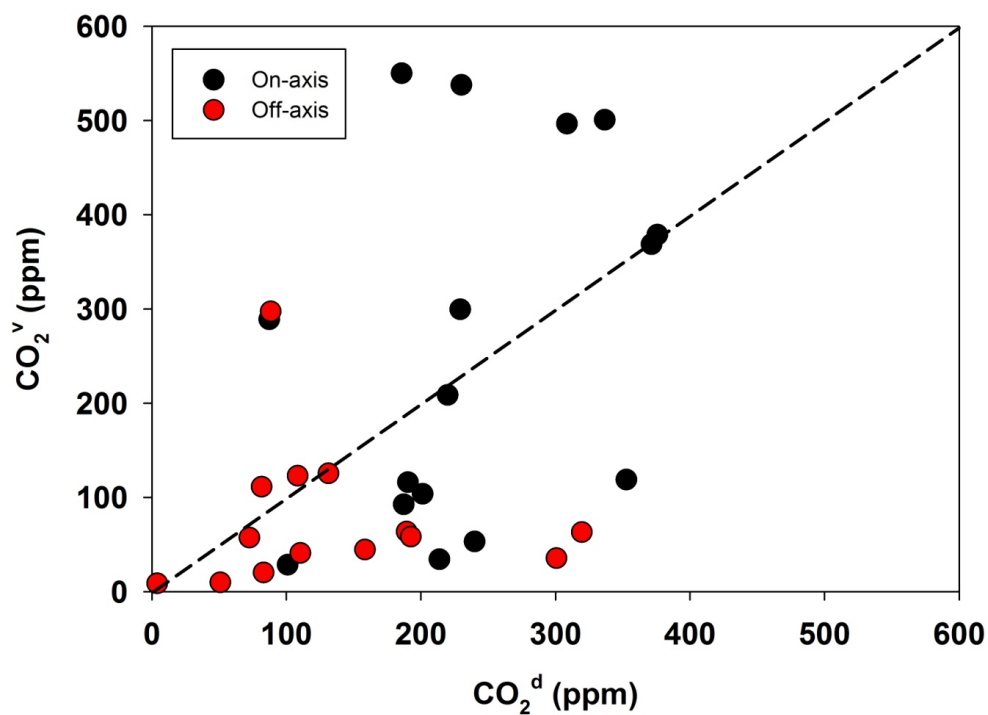
Figure VI.6: Plot of CO_2 (ppm) in vesicles (CO_2^v) versus CO_2 (ppm) dissolved in matrix (CO_2^d), measured by stepped heating method. In addition, we plot the 1:1 line and note that magmatic CO_2 (CO_2^m in Table VI.3) is dominated by CO_2^d for most samples.

Table VI.3: Nitrogen and N_2/Ar systematics of submarine basaltic glasses from the CIR (on-axis) and adjacent (off-axis) Gasitao and Three Magi ridges.

| Sample	Amount Processed (g)	$[N_2] \times 10^{-6} cm^3$ STP/g[a]	$\delta^{15}N$ (‰)[b]	N_2/Ar[c]	N_2 Blank (%)	R_C/R_A[d]	X-value[e]
On-Axis							
D1-1	2.80	5.56	-1.93 ± 0.91	132	25	8.11	1,445
D1-1 (Dup)	2.30	5.21	-1.25 ± 0.71	99.9	25	-	-
D3-12	1.75	4.97	-1.81 ± 1.13	68.5	52	7.96	9,451
D9-2	2.23	10.5	1.16 ± 0.59	267	10	7.25	25,499
D8-2	2.01	21.1	0.99 ± 0.51	156	9	7.08	696
D15-1	2.07	38.7	-2.34 ± 0.55	281	4	8.68	4,530
D14-1	2.19	16.0	-2.01 ± 0.38	238	10	8.46	14,235
DR10-1	0.75	48.0	-0.10 ± 0.63	47.9	24	10.31	157
D13-1	2.16	20.9	-1.99 ± 0.53	85.6	5	8.26	1,871
D13-1 (Dup)	1.95	14.1	-2.68 ± 0.51	131	12	-	-
D10-2	2.57	8.40	-2.91 ± 0.64	229	18	8.38	1,267
Off-Axis							
Three Magi Ridges							
D22-1*	1.90	74.2	1.71 ± 0.45	82.8	3	8.25	16,957
D22-1*	1.91	78.7	1.80 ± 0.52	127	3	-	-
D22-1*	0.50	92.6	1.74 ± 0.48	104	10	-	-
D26-2	2.56	15.2	0.89 ± 0.83	129	11	9.52	4883
Gasitao Ridge							
D18-1	2.14	2.34	1.14 ± 1.47	244	67	9.09	1,833

[a] N_2 concentration measurements are accurate within 3%, based on the reproducibility STDs.

[b] Uncertainties on $\delta^{15}N$ are 1σ. Blank subtractions have been applied to all $\delta^{15}N$ results and a comprehensive CO correction has been applied to all $\delta^{15}N$ results.

[c] All N_2/Ar uncertainties are less than 10%. Blank subtractions have been applied to all N_2/Ar results.

[d] He-isotope data from Füri et al. (2011).

[e] X-value = $(^4He/^{20}Ne)_{Sample}/(^4He/^{20}Ne)_{Air}$.

*Data published previously in Barry et al. (2012).

VI.5.4 CO_2 and $\delta^{13}C$ Results

Carbon dioxide (CO_2) concentrations and isotopic ratios were measured using a stepped heating technique (after Mattey et al., 1984; Macpherson et al., 1999). The principal advantage of this approach is that vesicle-sited CO_2 can be resolved from CO_2 dissolved in the glass and carbon isotopic ratios can be determined on both components. Relative CO_2 concentrations of CIR basalts are shown in Figure VI.6, which plots vesicle-sited CO_2 (CO_2^v) versus CO_2 dissolved in the glass matrix (CO_2^d). Most samples fall below the 1:1 line, indicating the total magmatic CO_2^m (= $CO_2^v + CO_2^d$; Table VI.4) is generally dominated by CO_2 dissolved in the glass. The highest concentrations of CO_2 are found in on-axis samples which (Figure VI.3), with the exception of D14-1, all display CO_2^d contents >100 ppm (Figure VI.6; Table VI.4). The highest CO_2 concentration samples (CO_2^m = 736-837 ppm) are from the segment of the CIR located directly north of the Marie Celeste FZ – (samples D1-1, D1-2, D3-3, D3-9, D2-1; Table VI.4) which display both high vesicle-sited and dissolved CO_2 contents. These samples were previously identified as having the highest ^{4}He contents among all CIR samples, together with MORB-like ^{3}He/^{4}He values (~8 R_A), and moderately high incompatible trace element ratios (e.g., La/Sm = 1.0-1.5). High CO_2^v contents (i.e., $CO_2^v >$ CO_2^d) likely reflects greater retention of vesicles at greater eruption depths; however CO_2^d values plot in the same range as all other CIR basalts. In contrast, off-axis samples have lower CO_2 contents – typically yielding < 200 ppm for CO_2^v and CO_2^d. Samples D24-6 and D29-1 are particularly CO_2 poor and display the lowest concentrations (i.e., CO_2^m <100 ppm; Table VI.4).

On-axis samples have $\delta^{13}C^v$ in the range of -5.1 to -13.9 ‰ and $\delta^{13}C^d$ spanning from -5.6 to -8.5 ‰. In contrast, off-axis samples show a greater range with $\delta^{13}C^v$ varying from -4.4 to -24.2 ‰ and $\delta^{13}C^d$ from -4.2 to -29.5 ‰. Extremely low $\delta^{13}C$ values can result from fractionation associated with degassing (Macpherson and Mattey, 1994) and/or addition of an organic C component (Shaw et al., 2004). Carbon isotope data from the stepped heating technique are given in Table VI.5 and summarized in Table VI.4.

Table VI.4: Carbon systematics and volatile data of submarine basaltic glasses from the CIR (on-axis) and adjacent (off-axis) Seamount, Gasitao Ridge, Three Magi Ridges, Rodrigues Ridge and Abyssal Hill.

Sample	Phase	Latitude (°S)	Longitude (°E)	Depth (m)	CO_2^v (ppm)	$\delta^{13}C^v$ (‰)	CO_2^d (ppm)	$\delta^{13}C^d$ (‰)	CO_2^m (ppm)	$\delta^{13}C^m$ (‰)	CO_2^{SIMS} (ppm)	H_2O^{SIMS} (wt%)	F (ppm)	P (ppm)	S (ppm)	Cl (ppm)
On-Axis																
D1-1	G	16.70	66.65	3146	550.0	-6.3	185.7	-6.8	735.7	-6.4	184.6	0.35	197.5	664.0	918.0	61.3
D1-2	G	16.70	66.65	3146	496.6	-6.7	308.6	-6.3	805.2	-6.5	236.2	0.35	195.7	657.9	924.1	59.4
D3-3	G	16.96	66.88	4272	378.8	-7.4	375.8	-7.0	754.6	-7.2	-	-	-	-	-	-
D3-9	G	16.96	66.88	4272	368.6	-7.0	371.4	-6.5	740.0	-6.8	275.6	0.51	260.1	857.4	995.9	93.9
D2-1	G	17.01	66.83	4038	500.7	-6.6	336.6	-5.9	837.3	-6.3	226.1	0.33	200.7	656.5	941.8	61.0
D8-2	G	18.05	65.14	3202	118.9	-7.8	352.7	-7.2	471.6	-7.4	148.4	0.60	323.1	976.4	1084	105.1
D8-3	G	18.05	65.14	3202	208.8	-7.5	219.9	-7.0	428.7	-7.2	148.6	0.53	296.0	844.3	1132	92.1
D9-1	G	18.13	65.21	3127	537.7	-6.5	230.1	-7.4	767.8	-6.7	151.9	0.69	368.9	1023.7	1133	140.1
D17-1	G	19.61	65.88	2742	116.2	-8.2	190.4	-8.5	306.6	-8.4	127.5	0.30	185.9	597.2	1036	46.1
D15-1	G	19.76	66.01	2794	299.6	-5.1	229.3	-5.6	528.9	-5.3	173.9	0.21	136.4	434.0	987.0	18.9
D14-1	G	19.91	66.17	3267	288.9	-5.9	87.3	-8.1	376.2	-6.4	132.0	0.21	146.7	491.5	977.8	28.6
DR10-1*b	G	19.95	66.27	3550	28.5	-12.3	101.0	-5.9	129.5	-7.3	-	-	-	-	-	-
D13-1*	G	19.98	66.24	3511	103.8	-6.2	201.3	-5.6	305.1	-5.8	138.0	0.18	133.0	447.2	997.6	11.6
D12-2	G	20.07	66.27	3550	53.3	-8.3	239.9	-5.8	293.2	-6.3	132.1	0.11	85.5	286.9	868.4	6.8
D11-2	G	20.07	66.28	3370	34.3	-13.9	213.8	-6.3	248.1	-7.4	133.9	0.11	84.1	283.4	862.0	7.3
D10-2*	G	20.16	66.32	3483	92.6	-12.5	187.3	-6.7	279.9	-8.6	131.2	0.14	112.2	390.2	944.3	8.6
Off-Axis																
Seamount																
D6-2	G	18.22	65.41	2048	57.4	-6.9	72.5	-7.3	129.9	-7.1	78.6	0.43	226.7	629.2	1037	165.2
Three Magi Ridges																
D25-1	G	19.58	64.84	2123	41.1	-9.0	110.4	-6.1	151.5	-6.9	101.7	0.37	179.2	480.3	1144	24.4
D25-2	G	19.58	64.84	2123	35.5	-8.5	300.8	-5.7	336.3	-6.0	103.1	0.36	173.1	473.5	1118	23.7
D22-1*	G	19.62	64.97	1687	297.4	-4.9	88.4	-10.1	385.8	-6.1	66.4	0.33	159.1	513.4	859.9	46.0
D26-2	G	19.62	64.71	1785	123.0	-4.4	108.4	-8.4	231.4	-6.3	79.5	0.25	107.9	266.3	965.8	12.1
D24-1*	G	19.67	64.95	2019	20.4	-17.0	83.1	-7.0	103.5	-9.0	108.3	0.11	60.4	144.1	680.8	3.0
D24-6	G	19.67	64.95	2019	9.9	-9.1	50.9	-6.1	60.8	-6.6	104.4	0.11	61.5	144.6	689.9	1.7
Gasitao Ridge																
DR08-1b	G	19.66	65.54	2110	63.7	-5.7	189.4	-4.2	253.1	-4.6	160.6	0.41	201.2	473.4	1452	4.8
D19-2	G	19.69	65.82	2176	44.7	-10.3	158.5	-7.0	203.2	-7.7	94.4	0.13	105.9	339.0	942.7	10.4
D20-5*	G	19.70	65.49	2002	63.2	-20.2	319.6	-10.6	382.8	-12.1	197.8	0.14	120.1	273.4	907.2	8.1
Rodrigues Ridge																
D34-1	G	19.46	64.14	2134	58.3	-24.2	192.5	-20.9	250.8	-21.6	34.1	0.22	132.3	380.2	969.1	115.1
D29-1*	G	19.60	64.29	1820	8.8	-22.6	4.0	-29.5	12.8	-24.7	2.9	0.11	196.0	580.8	320.9	29.7

Table VI.4 continued

Sample	Phase	Latitude (°S)	Longitude (°E)	Depth (m)	CO_2^v (ppm)	$\delta^{13}C^v$ (‰)	CO_2^d (ppm)	$\delta^{13}C^d$ (‰)	CO_2^m (ppm)	$\delta^{13}C^m$ (‰)	CO_2^{SIMS} (ppm)	H_2O^{SIMS} (wt%)	F (ppm)	P (ppm)	S (ppm)	Cl (ppm)
D30-3	G	19.64	64.07	2156	111.4	-4.4	81.6	-5.2	193.0	-4.7	56.7	0.37	128.3	346.3	1019	28.1
Abyssal Hill																
D37-2	G	20.05	64.29	2833	125.6	-8.1	131.3	-6.9	256.9	-7.5	109.5	0.33	188.8	576.8	1202	101.8

Ol = Olivine; G = Basaltic Glass.

[a] Nitrogen data were previously published in Barry et al., 2012.

[b] Samples collected in 2000 on the GIMNAUT cruise (Nauret et al., 2006).

Errors on the volatile data are less than 5%.

Table VI.5: Stepped heating carbon concentration and $\delta^{13}C$ isotope ratio results of CIR glasses.

Sample	Weight	400°C	600°C	700°C	700°C	800°C	800°C	900°C	900°C	1000°C	1000°C	1100°C	1100°C	1200°C	1200°C
	mg	ppm CO$_2$	ppm CO$_2$	ppm CO$_2$	$\delta^{13}C$	ppm CO$_2$	$\delta^{13}C$	ppm CO$_2$	$\delta^{13}C$	ppm CO$_2$	$\delta^{13}C$	ppm CO$_2$	$\delta^{13}C$	ppm CO$_2$	$\delta^{13}C$
On-Axis															
D1-1	123.4	32.4	11.5	164.7	-7.43	338.3	-6.03	47	-4.62	134.6	-6.7	42.2	-7.04	8.9	n.d.
D1-2	96.4	4	1.3	0.4	co	405.5	-6.21	90.7	-8.63	51.6	-6.53	154.3	-6.23	102.7	-6.22
D3-3	90.1	18.4	27.9	48.4	-7.42	173.6	-6.72	156.8	-8.1	131.1	-7.97	194.6	-6.31	50.1	-7.02
D3-9	115.5	35.9	7.7	51.3	-6.36	92.8	-6.55	224.5	-7.4	115	-7.12	198.3	-6.22	58.1	-6.05
D2-1	95.1	14.7	10.1	7.9	co	425.1	-6.37	67.7	-7.86	93.1	-6.7	124.2	-6.14	119.3	-5.05
D8-2	111.9	8.1	42.5	9	co	73.4	-8.09	36.5	-7.29	205.2	-7.22	110.9	-7.16	36.6	-7.25
D8-3	106.8	18.8	59.1	61	-7.71	80.4	-6.68	67.4	-8.18	80.9	-7.46	100.6	-6.81	38.4	-6.55
D9-1	98.5	9.9	18.8	121.6	-6.83	274	-6.02	142.1	-7.02	68.7	-7.46	124	-7.15	37.4	-8.05
D17-1	110.9	17.7	14.7	2.6	co	44.5	-8.32	69.1	-8.11	47.9	-9.33	69.3	-8.69	73.2	-7.71
D15-1	150.8	13.5	13.7	16.6	-7.4	264.7	-4.58	18.3	-10.13	39.7	-6.19	17.6	-6.31	172	-5.38
D14-1	158.9	10.5	41.7	5.5	co	241.7	-5.53	41.7	-7.89	25.4	-8.32	35.8	-7.74	26.1	-8.3
DR10-1*b	196.6	81.6	14.5	1.9	co	5.5	co	13.2	-10.22	7.9	-17.85	26.4	-7.75	74.6	-5.2
D13-1*	150.2	14.3	4.8	2.3	co	40.9	-5.14	8.6	co	52	-6.93	16.2	-6.86	185.1	-5.49
D12-2	198.2	10.9	1.8	6	co	29.5	-5.92	17.8	-13.18	38	-7.18	17.7	-10.89	184.2	-5.07
D11-2	150.2	33.6	14	4.7	co	13.9	-15.09	15.7	-12.57	35.6	-8.61	15.3	-11.35	162.9	-5.34
D10-2*	101.9	6.9	1.8	7.8	co	22.4	-14.56	8.9	co	53.5	-11.51	22	-13.29	165.3	-5.8
Off-Axis															
Seamount															
D6-2	142.7	5.3	25.8	1.9	co	24.9	-7.28	30.6	-6.59	45.1	-6.69	19.7	-6.9	7.7	-12.2
Three Magi Ridges															
D25-1	202.7	26.8	15.7	8.7	-12.59	12.1	-8.39	20.3	-7.78	15.5	-7.35	12	-9.71	82.9	-5.33
D25-2	190.1	32	22	4.4	co	10.8	-9.82	20.3	-7.49	27.6	-5.92	7.1	co	266.1	-5.68

163

Table VI.5 continued

Sample	Weight mg	400°C ppm CO$_2$	600°C ppm CO$_2$	700°C ppm CO$_2$	700°C δ^{13}C	800°C ppm CO$_2$	800°C δ^{13}C	900°C ppm CO$_2$	900°C δ^{13}C	1000°C ppm CO$_2$	1000°C δ^{13}C	1100°C ppm CO$_2$	1100°C δ^{13}C	1200°C ppm CO$_2$	1200°C δ^{13}C
D22-1*	139.9	13	34.7	75.8	-5.14	213.2	-4.52	8.4	-12.9	21.7	-8.77	31	-12.62	35.7	-8.7
D26-2	178.2	29.8	28.2	25.8	-4.24	85.8	-3.55	11.4	-11.2	13.6	-11.26	13.3	-19.57	81.5	-6.05
D24-1*	175.1	27.5	29.8	3.7	co	1.5	co	9.4	-16.25	5.8	-18.9	26.5	-10.18	56.6	-5.52
D24-6	163	20.6	39.1	3.4	co	0.4	co	6.1	-9.08	4.1	co	10.1	-7.03	36.7	-5.71
Gasitao Ridge															
DR08-1b	142.2	71.9	23.5	9.6	co	14	-6.69	40.1	-5.18	44.5	-4.61	19.1	-8.83	125.8	-3.37
D19-2	152.2	8.4	3.7	2.7	co	28.5	-8.99	13.5	-13.37	13.7	-12.01	9.5	co	135.3	-6.48
D20-5*	206.1	53.3	58.7	3.2	co	5.7	-19.65	14.6	-10.28	39.7	-23.95	67.5	-16	252.1	-9.1
Rodrigues Ridge															
D34-1	111.5	25.5	83.2	2.9	co	13.5	-24.18	11.1	co	30.8	-24.16	62.4	-27.02	130.1	-17.91
D29-1*	193.1	48.2	487.2	0.1	n.d.	3.8	co	2.2	co	2.7	-22.82	1.6	co	2.4	-29.5
D30-3	210.3	33.8	19.7	14.6	-5.44	85.9	-3.81	10.9	-7.21	35.6	-5.16	4.1	co	41.9	-5.17
Abyssal Hill															
D37-2	180	39.9	28.8	41	-8.58	67.9	-7.03	16.7	-11.02	36.1	-8.16	43.6	-6.67	51.6	-6.24

Notably, $\delta^{13}C^d > \delta^{13}C^v$, i.e., Δ-values (= $\delta^{13}C^v - \delta^{13}C^d$) are negative for the majority of samples, which is inconsistent with predicted ^{13}C enrichments in CO_2 vapor during equilibrium degassing (Javoy et al., 1978; Mattey, 1991). The predominance of negative Δ-values in CIR samples indicates that vesicle-sited CO_2 is not in equilibrium with dissolved CO_2 within a single sample, and could be derived from degassing of magma elsewhere in the system (see discussion in Shaw et al., 2004; Hahm et al., 2012).

In addition to the stepped heating results, we also measured dissolved CO_2 contents using SIMS (CO_2^{SIMS}; Table VI.4), and report relatively good agreement between the two techniques (Figure VI.7), however stepped heating results generally display slightly higher CO_2 yields versus CO_2^{SIMS} data. These CO_2^{SIMS} data were then combined with H_2O data, measured on the same glass chip, to calculate equilibrium solubility pressures for each sample. In Figure VI.8, we plot saturation vapor pressure (Dixon et al., 1995; Newman and Lowenstern, 2002) as a function of confining pressure at the depth of eruption. Most of the on-axis CIR samples plot above the 1:1 line, indicating they are oversaturated with respect to CO_2, such that degassing was likely inhibited by rapid eruption (Dixon et al., 1988). However, many samples are close to CO_2 equilibrium for their depth of eruption, implying relatively slow magma ascent and eruption rates and/or faster diffusion of CO_2 due to higher H_2O contents (Watson, 1991). In addition, several off-axis samples from the Rodrigues Ridge (i.e., D34-1, D29-1 and D30-3) fall below the 1:1 line (Figure VI.8), which suggests extreme understaturation. These samples have likely experienced much slower ascent rates which allowed large vesicles to form, and ultimately resulted in depletion of CO_2 in the accompanying melt. Alternatively, these samples may have been erupted at shallow water depths, extensively degassed and flowed down gradient before quenching (Hahm et al., 2012), resulting in overestimates of eruption pressure.
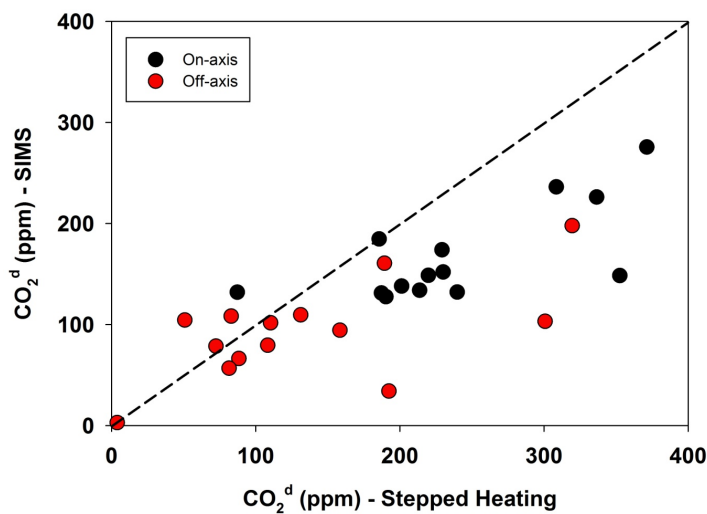
Figure VI.7: Dissolved CO_2 (ppm) measured using two different methods – CO_2^d SIMS versus CO_2^d stepped heating. In addition, we plot the 1:1 line and note that the majority of results plot slightly below this line.
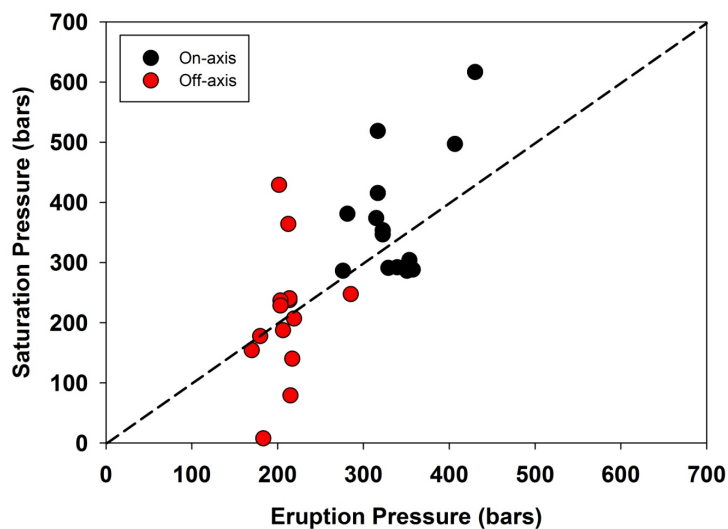

Figure VI.8: Plot between saturation (bars) and eruption pressures (bars). The saturation pressures are calculated using VolatileCalc 1.1 (Newman and Lowenstern, 2002) with H_2O and CO_2^{sims}. Most on-axis samples fall above 1:1 line, indicating over-saturation with CO_2, whereas several (n=3) off-axis samples are extremely undersaturated.

VI.5.5 H$_2$O

Dissolved H$_2$O concentrations vary from 0.11 and 0.69 wt% in on-axis CIR samples (Table VI.4) and from 0.11 to 0.43 wt% in off-axis samples. The concentrations of CO$_2$ versus H$_2$O (SIMS data) are plotted in Figure VI.9. Most on- and all off-axis samples have H$_2$O contents below 0.50 wt% in the range of average MORB values (0.17–0.60 wt%; Jambon and Zimmermann, 1990); however, a distinct group of intermediate H$_2$O (i.e., H$_2$O > 0.50 wt %) samples (e.g., D8-2, D8-3, D9-1) is located just south of the Marie Celeste FZ. In general, intermediate H$_2$O samples also display high major volatile contents (e.g., P, S, Cl; Table VI.4). In addition, sample D8-2 also has high Ne and Ar contents (Tables VI.1 and VI.2). These samples were previously identified as having enriched incompatible elements signatures (Mahoney et al., 1989; Murton et al., 2005; Nauret et al., 2006) and Füri et al. (2011) showed that they display the most radiogenic He-isotope values along the entire CIR, which they attributed to radiogenic in-growth following interaction with a "fossil" Réunion plume. Elevated H$_2$O concentrations (0.53 and 0.69 wt %) could result from remnants of the (water-rich) Réunion hotspot, which is thought to be characterized by OIB-like water contents of (0.59 to 1.10 wt %; Bureau et al., 1998). The remaining on-axis samples generally fall on the low end of the MORB H$_2$O range, along with all off-axis samples.
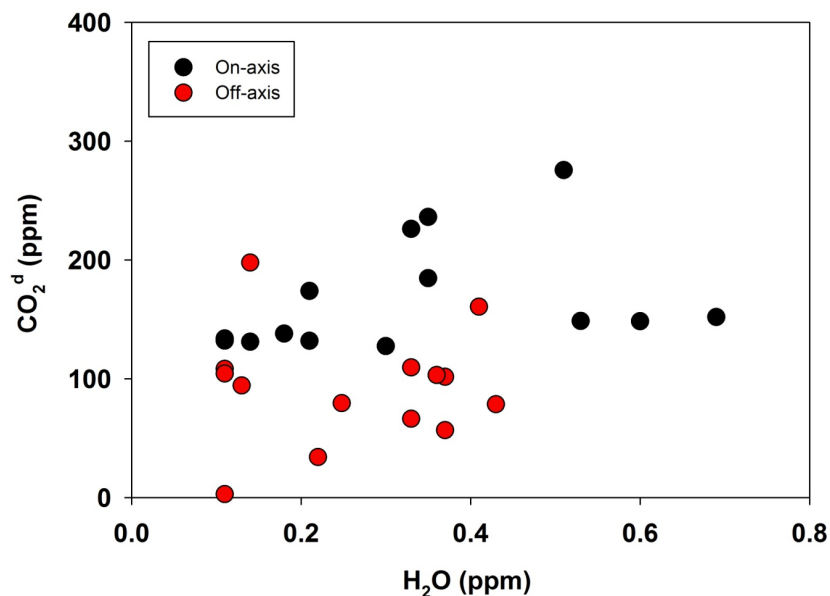
Figure VI.9: CO_2^d versus H_2O – measured using SIMS on the sample glass chip.

4.6. Additional volatiles (F, Cl, S, P)

Fluorine contents in CIR basalts vary widely from as low as 60 ppm (off-axis) to as high as 369 ppm. Low F concentrations (i.e., < 100 ppm) are observed in both on-axis and off-axis samples, whereas the highest values occur in the on-axis samples which are marked by intermediate H_2O contents, low (< MORB) He-isotopes and trace element enrichments (e.g., high La/Sm, Ba/La and Nb/Zr; Murton et al., 2005; Füri et al., 2011). Similar enrichments are observed for Cl, S and P contents throughout the CIR. The observation that volatiles and highly incompatible trace elements are enriched in the same subset of samples is consistent with their low partition coefficient in basaltic melts. In Figure VI.10 we plot H_2O (wt %) as a function of F (ppm), and note a strong 1:1 correlation between the two species, characterized by a relatively constant H_2O/F ratio of ~17.1.
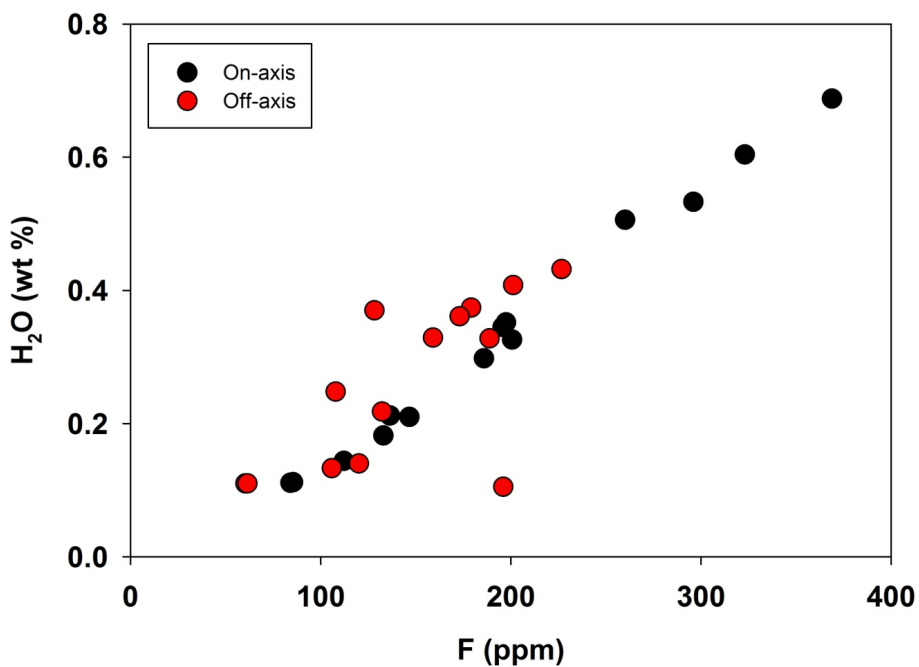
Figure VI.10: H_2O (wt %) versus F (ppm), measured using SIMS. The direct correlation between H_2O and F indicates similar geochemical behavior between the two species and a constant H_2O/F ratio of ~17.1 in the mantle.

Cl contents vary by roughly two orders of magnitude from 1.7 to 165. The lowest Cl contents occur in the most H_2O depleted (<0.15 wt %) samples, with the exception of sample DR08-1b which has a H_2O content of 0.43 wt% and a Cl content <5 ppm. Sample D6-2 and D9-1 display the two highest Cl contents (165 and 140 ppm), along with the highest H_2O contents (0.43 and 0.69 wt %), indicating possible contamination with seawater.

Sulfur contents are significantly less variable, particularly in on-axis samples, which span a limited range from 862 to 1133. Again, the highest volatile content samples are the H_2O rich, trace element enriched samples, located just to the south of the Marie Celeste FZ. In contrast off-axis samples are more variable with a range from 321 to 1118 ppm. Finally, P

contents range from 283 to 1024 in on-axis samples and from 321 to 1452 ppm in off-axis

samples. The highest P value measured (1452 ppm) is from Gasitao Ridge sample DR08-1b.

In Figure VI.11 we plot F, Cl and S (ppm) versus K_2O – which will partition strongly

into the silicate melt phase during crystallization. CIR basalts show a strong correlation

between F and K_2O (Figure VI.11a), with a relatively constant F/K_2O ratio of ~0.15,

illustrating that volatile elements also behave incompatibly. The constancy of this ratio

suggests that on- and off-axis portions of the CIR are influenced by source magmas with

similar F/K_2O ratio, and that extraneous plume and/or recycled contributions in the source do

not significantly alter this ratio. Similar patterns are observed in Cl (Figure VI.11b) contents

versus K_2O throughout the CIR, with a relatively constant Cl/K_2O ratio of ~0.03. The co-

variance of these two species suggests that crystallization exerts the primary control on the Cl

content in CIR basalts; however off-axis sample D34-1 has a clear Cl anomaly, suggesting

possible post-eruptive seawater assimilation (Kent et al., 1999). Finally, we note a broad

correlation between sulfur content and K_2O of CIR basalts (Figure VI.11c), indicating that

crystallization is also the primary control on S content, however small offsets may result due

to solubility differences in source magmas. A more detailed discussion of volatile variations is

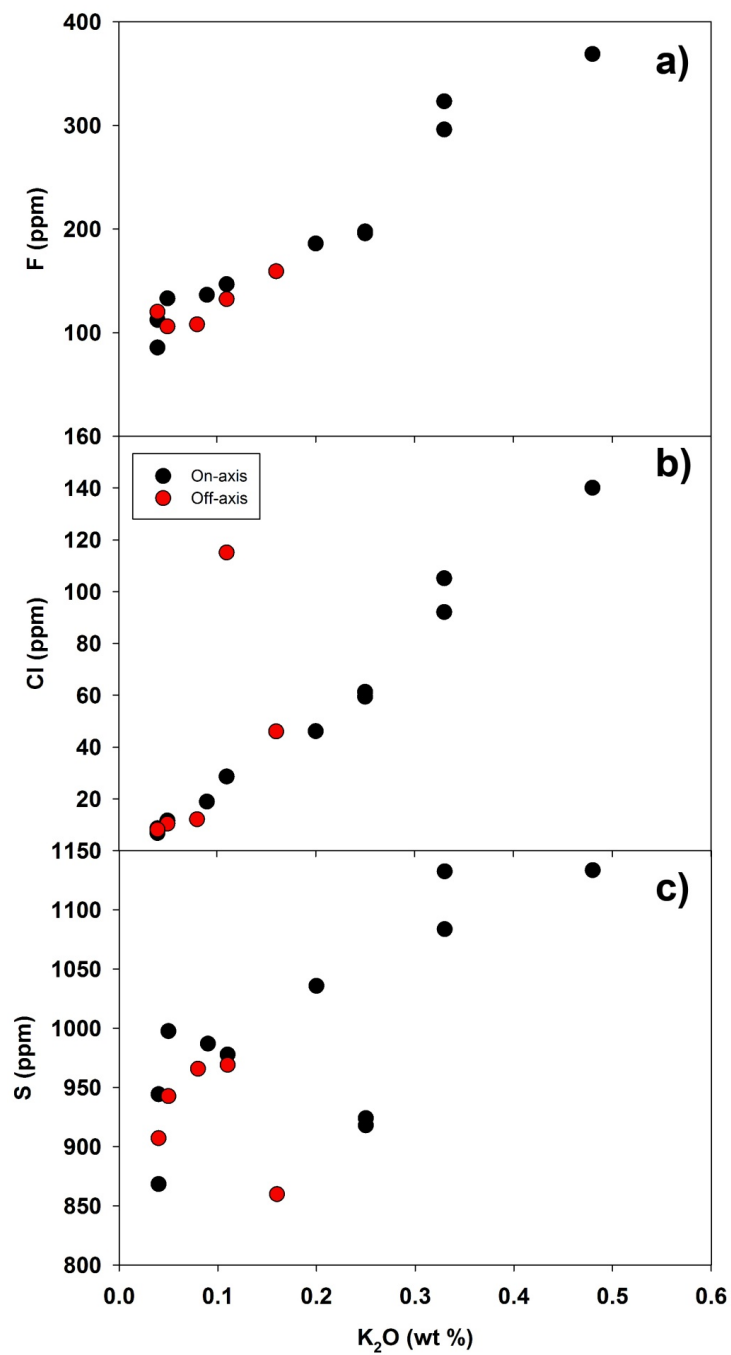beyond the scope of this contribution.

Figure VI.11: F, Cl, and S (ppm) versus K_2O (wt %) in CIR samples. (a) The F/K_2O ratio of most CIR samples is constant at ~0.15. (b) The Cl/K_2O for most CIR samples is ~0.03, however, off-axis sample D34-1 Cl shows a distinct Cl anomaly, suggesting possible post-eruptive assimilation of seawater. (c) S versus K_2O.

VI.6 Discussion

The principal goal of this study is to identify intrinsic mantle C-N-Ne-Ar characteristics in order to understand the petrogenic evolution of CIR basalts and the dynamics of mantle mixing in the CIR mantle source region. We aim to differentiate between intrinsic source features and altered components by investigating processes such as air-contamination, degassing, and crustal assimilation, which can act to modify primary mantle characteristics. If appropriate, corrections are applied to account for the effects of these modification processes. In the following discussion, we evaluate different mantle-mixing, contamination, and degassing models to assess their validity in explaining the volatile systematics of the CIR. Only after the effects of degassing and contamination are assessed can the volatile characteristics of CIR basalts be used to explore the evolution of mantle sources in the region and details of plume-ridge interaction.

VI.6.1 Sample integrity

In order to determine the integrity of the volatile record, we attempt to identify individual samples and sub-regions where contamination and/or modification occur so that magma source characteristics can be assessed accordingly. If contaminated samples – affected by the complicating effects of degassing and/or air-addition – can be identified and removed from further consideration, then pristine samples can be used to assess the initial mantle source characteristics of CIR basalts.

VI.6.1.1 Ne and Ar air-contamination

Different volatile species are variably affected by air-contamination – depending, in part, on their relative abundances in the mantle versus the Earth's surface. For example, Ne ($\sim$2 × 10^{-5} cm^3 STP) and Ar ($\sim$9 × 10^{-3} cm^3 STP) are enriched in the Earth's atmosphere relative to basaltic abundances (Tables VI.1 and VI.2), and therefore basalts are highly susceptible to air-contamination processes. Air-like Ne-isotope contributions are ubiquitous in natural samples (Graham et al., 2002) with atmospheric infiltration into basalts occurring through small micro-fractures, which can develop in glasses during seafloor sampling and/or handling in the laboratory (Ballentine and Barfod, 2000), and/or by assimilation of seawater-derived components (Farley and Craig, 1994). The apparent effects of atmospheric contamination are illustrated in Figure VI.2 by plotting δ^{21}Ne and δ^{20}Ne as a function of Ne concentration. Samples with high ^{20}Ne contents (e.g., D3-1, D2-1, D22-1, D26-2 and D37-2; i.e., where [^{20}Ne] >1 × 10^{-9} cm^3 STP/g) display δ-values close to atmosphere (= 0 %). These particular (air-contaminated) samples also have relatively high ^{40}Ar abundances and low ^{40}Ar/^{36}Ar values < 600, suggesting considerable air-derived ^{36}Ar is also present (Figure VI.5; Table VI.2).

VI.6.1.2 Ne-isotope Air-correction

Although Ne-isotopes in basalts are highly susceptibility to air-contamination, air-derived Ne contributions can be corrected by assuming that measured neon isotope values represent a binary mixture of atmospheric and mantle-derived neon. Following the methods of Honda et al. (1991), we extrapolate measured ^{20}Ne/^{22}Ne values to "solar" (i.e., Ne-B = 12.5) values in order to estimate air-corrected (i.e., ^{21}Ne/^{22}Ne$_{EX}$) values. The following equations are used:

$$^{21}\text{Ne}/^{22}\text{Ne}_{EX} = (^{21}\text{Ne}/^{22}\text{Ne}_M - {}^{21}\text{Ne}/^{22}\text{Ne}_A) \, / \, f_{22} + {}^{21}\text{Ne}/^{22}\text{Ne}_A$$

(1)

where f_{22} is the proportion of mantle-derived Ne in a sample:

$$f_{22} = (^{20}\text{Ne}/^{22}\text{Ne}_M - {}^{20}\text{Ne}/^{22}\text{Ne}_A) \, / \, (^{20}\text{Ne}/^{22}\text{Ne}_S - {}^{20}\text{Ne}/^{22}\text{Ne}_A)$$

(2)

and $^{20}\text{Ne}/^{22}\text{Ne}_A$ and $^{21}\text{Ne}/^{22}\text{Ne}_A$ are the isotopic ratios of air, assumed to be 9.8 and 0.029,

respectively, whereas $^{21}\text{Ne}/^{22}\text{Ne}_M$ is the measured sample $^{21}\text{Ne}/^{22}\text{Ne}$ value and $^{20}\text{Ne}/^{22}\text{Ne}_S$ is

the assumed $^{21}\text{Ne}/^{22}\text{Ne}$ "solar" (i.e., Ne-B) neon component (=12.5; Trieloff et al., 2000).

Notably, the most air-like sample (e.g., D3-1; highest ^{20}Ne content) cannot be corrected due to

a $^{21}\text{Ne}/^{22}\text{Ne}_M$ value that is indistinguishable from air. The Ne–B endmember is obtained from

gas-rich meteorites and lunar soils: their $^{20}\text{Ne}/^{22}\text{Ne}$ ratio of 12.52 ± 0.18 is considered to

represent implanted solar neon within Earth's mantle (Black, 1972; Trieloff et al., 2000;

Trieloff et al., 2002; Ballentine et al., 2005). The primordial, "solar" neon component in

Earth's mantle has also been assumed to be best represented by present-day solar wind

(i.e., $^{20}\text{Ne}/^{22}\text{Ne} = 13.8$; Benkert et al., 1993; Kallenbach et al., 1997); note however, that

selection of this endmember as opposed to Ne-B will not significantly affect the conclusions

in the following discussion. Basalt CIR $^{21}\text{Ne}/^{22}\text{Ne}_{ex}$ values vary between 0.0437 ± 0.0009 and

0.0582 ± 0.0013 and fall in the range of values observed in previous studies of plume-rift

related systems (e.g., Füri et al., 2010; Hahm et al., 2012). On-axis CIR $^{21}Ne/^{22}Ne_{ex}$ values range from 0.0437 ± 0.0011 to 0.0560 ± 0.0023, whereas off-axis samples range from 0.0441 ± 0.0017 to 0.0582 ± 0.0013.

VI.6.1.3 CO_2 and N_2 air-contamination

Carbon dioxide and N_2 are also potentially susceptible to both air and seawater contamination processes. CO_2 concentrations are similar in mantle and terrestrial reservoirs with the current atmospheric CO_2 concentration of ~400 ppm being comparable to CO_2 contents in MORB (Marty, 2012). However, air-like $\delta^{13}C$ values (-8 ‰) are not pervasive in CIR basalts, which instead display a significantly wider range in $\delta^{13}C$, likely resulting from crustal contamination and/or degassing related fractionation. Notably, Ne-Ar systematics appear to be decoupled from CO_2 systematics, and as a result, samples with air-like Ne-Ar (i.e., [Ne] $> 1 \times 10^{-9}$ cm^{3}STP/g; $\delta^{20}Ne < 1$; $^{40}Ar/^{36}Ar < 300$) display a wide range of CO_2^d contents (~100 to 800 ppm) and $\delta^{13}C$ values (-5.9 to -10.1 ‰).

Nitrogen is the most abundant (~78 %) gaseous species in the atmosphere; however, it occurs only in trace amounts in CIR basalts (Table VI.3), thus the potential for atmospheric contamination is substantial. Samples identified to be air-like with respect to Ne-Ar isotope systematics (Figure VI.5) display non-air-like $\delta^{15}N$ ($\neq 0$ ‰) values. In addition, the majority of CIR samples have N_2/Ar ratios well above the air value, indicating that air contamination is minimal. In Figure VI.12, we plot $\delta^{15}N$ versus the air-normalized He/Ne values $(^4He/^{20}Ne)_{Sample}/(^4He/^{20}Ne)_{Air}$ – a useful indicator of extent of air contamination. We show that both on-axis and off-axis CIR glasses have markedly higher $^4He/^{20}Ne$ ratios than air (>100x), and thus are not considered to be significantly modified by air-contributions.
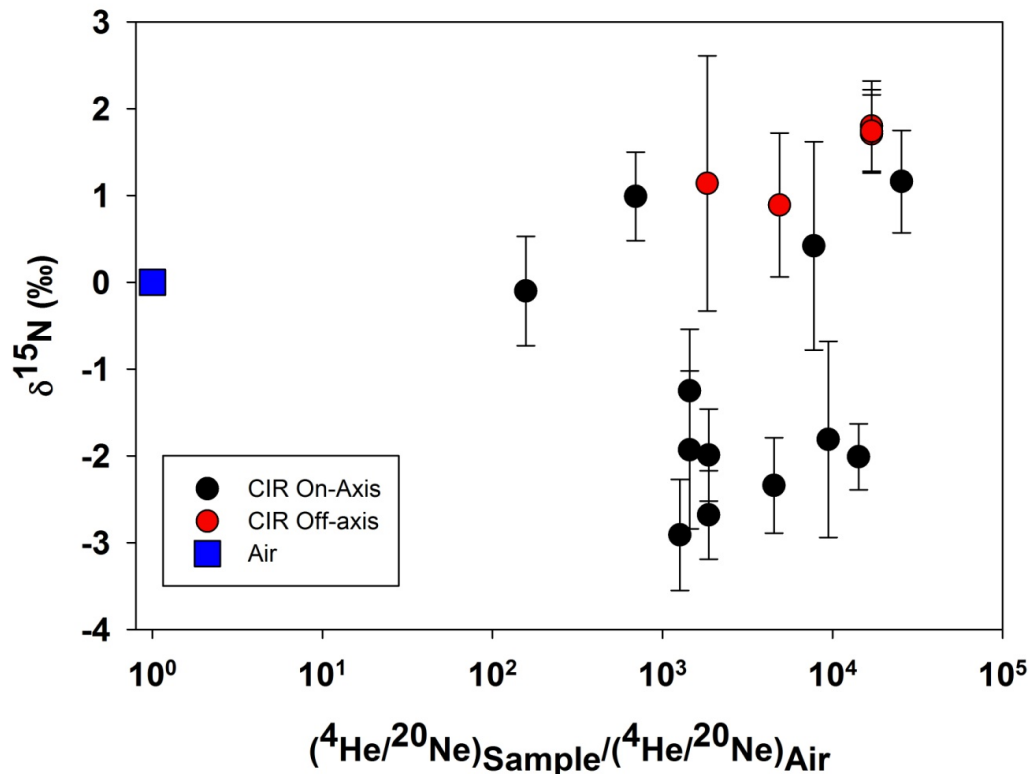
Figure VI.12: N-isotopes ($\delta^{15}N$) versus air-normalized He/Ne values ($=^{4}He/^{20}Ne_S/^{4}He/^{20}Ne_A$). High He/Ne values relative to air (>100) suggest that all CIR basalt samples have undergone minimal air-contamination.

VI.6.1.4 Sample integrity – degassing fractionation of noble gases ($^{4}He/^{40}Ar^*$)

In addition to air contamination, another process capable of modifying intrinsic

mantle volatile features is degassing. Having discussed the importance of identifying air-

contaminated samples and applying a correction when necessary, we now focus on additional

processes which can modify source features, such as degassing. Degassing can potentially

cause both isotope and relative abundance fractionation. For example, the degassing history

can be constrained using a coupled investigation of dissolved (CO_2^d) and vesicle-sited (CO_2^v)

phases, which enables reconstruction of primary volatile source characteristics in the melt

prior to gas loss (see Section 5.5 for details). Additionally, relative noble gas abundances (e.g., $^{4}He/^{40}Ar*$) can provide useful information about the mode and extent of volatile loss. Using the latter approach, an air-correction is first applied to the argon data by assuming that all ^{36}Ar is derived from the atmosphere. In this way the measured ^{40}Ar content in each sample can be corrected for the presence of atmospheric Ar to radiogenic Ar (i.e., 40Ar*):

$$^{40}Ar* = [^{36}Ar_M] \times [(^{40}Ar/^{36}Ar)_M - (^{40}Ar/^{36}Ar)_A] \qquad (3)$$

where $^{36}Ar_M$ and $(^{40}Ar/^{36}Ar)_M$ are the measured ^{36}Ar abundance and argon isotope ratio, respectively, and $(^{40}Ar/^{36}Ar)_A$ is the air ratio (= 298.56 ± 0.31; Lee et al., 2006).

The measured He contents and calculated $^{40}Ar*$, from Eq. (3), are then combined to give $^{4}He/^{40}Ar*$ ratios, which can be used to model the approximate extent of degassing (Marty and Tolstikhin, 1998), because He is more soluble than Ar ($S_{He}/S_{Ar} = 9.5$; Jambon et al., 1986) in basaltic magmas. Thus, residual (i.e., basalt) $^{4}He/^{40}Ar*$ values should increase with increased degassing. Using estimates of upper mantle K/U (Jochum et al., 1983) and Th/U (O'Nions and McKenzie, 1993), a production ratio for $^{4}He/^{40}Ar*$ of ~2 (Jambon et al., 1986; Marty and Zimmermann, 1999) is assumed as a mantle starting value. In the case of the present sample suite, $^{4}He/^{40}Ar*$ could not be calculated for two on-axis CIR basalt samples only (D1-1 and D3-1) due to measured air-like $^{40}Ar/^{36}Ar$ ratios (i.e., insignificant radiogenic ^{40}Ar contributions). Notably, all $^{4}He/^{40}Ar^*$ ratios calculated for CIR basalts are higher than the mantle production ratio of ~2 and range from 3.0 to 62, compared to Réunion xenoliths which fall between 1.3 and 2.0 (Table VI.2). In general, $^{4}He/^{40}Ar^*$ are low (< 20), suggesting only moderate amounts of degassing, however the $^{4}He/^{40}Ar^*$ ratio of individual samples are

variable, indicating that CIR basalts have experienced different amounts of degassing. Two groups are evident; on axis samples, which all have $^4He/^{40}Ar^*$ ratios $< \sim 10$, with the exception of sample D2-1 ($^4He/^{40}Ar^* = 62$) and off-axis samples, which have $^4He/^{40}Ar^*$ ratios $> \sim 10$ with the exception of D26-2 ($^4He/^{40}Ar^* = 5.2$). Higher $^4He/^{40}Ar^*$ ratios in off-axis samples (~ 5-$10x$ the production ratio) suggest more extensive degassing in off-axis portions of the crust, compared with on-axis samples. In contrast, $^4He/^{40}Ar*$ values close to the mantle production value are measured in Réunion xenoliths, indicating that gas loss was insignificant or very minor.

In Figure VI.3, we plot N-isotopes as a function of latitude (for on-axis samples) and longitude for off-axis samples and note that all but two on-axis CIR basalts exhibit negative $\delta^{15}N$ values whereas all off-axis samples display positive values. In order to test if the observed N-isotope variations result from degassing-related modification, we plot $^4He/^{40}Ar*$ versus $\delta^{15}N$ (Figure VI.13a) and note that two distinct (i.e., a positive and negative) fields are evident. Significantly, both fields have variable $^4He/^{40}Ar^*$ ratios yet exhibit overlapping $\delta^{15}N$ values. For example, positive $\delta^{15}N$ samples have $^4He/^{40}Ar^*$ values that vary by a factor of 10, but all $\delta^{15}N$ values are indistinguishable within error. The same observation can be made for the negative $\delta^{15}N$ field where $^4He/^{40}Ar^*$ values range from 2 to 5, however, all $\delta^{15}N$ values overlap. These results indicate that N-isotopes variations are independent of $^4He/^{40}Ar^*$ and thus we conclude that N-isotopes of CIR basalts have not experienced degassing fractionation. Significantly, this observation is consistent with previous compilation studies of various mid ocean ridge (MOR) and OIB settings (e.g., Marty and Humbert, 1997; Fischer et al., 2005), which also suggest that nitrogen isotope variations are independent of degassing. Therefore, nitrogen isotope variability in CIR basalts must be attributed to other processes – either mixing between isotopically distinct components in the mantle source and/or crustal

contributions. In the following section, we investigate coupled He-Ne-Ar isotope systematics

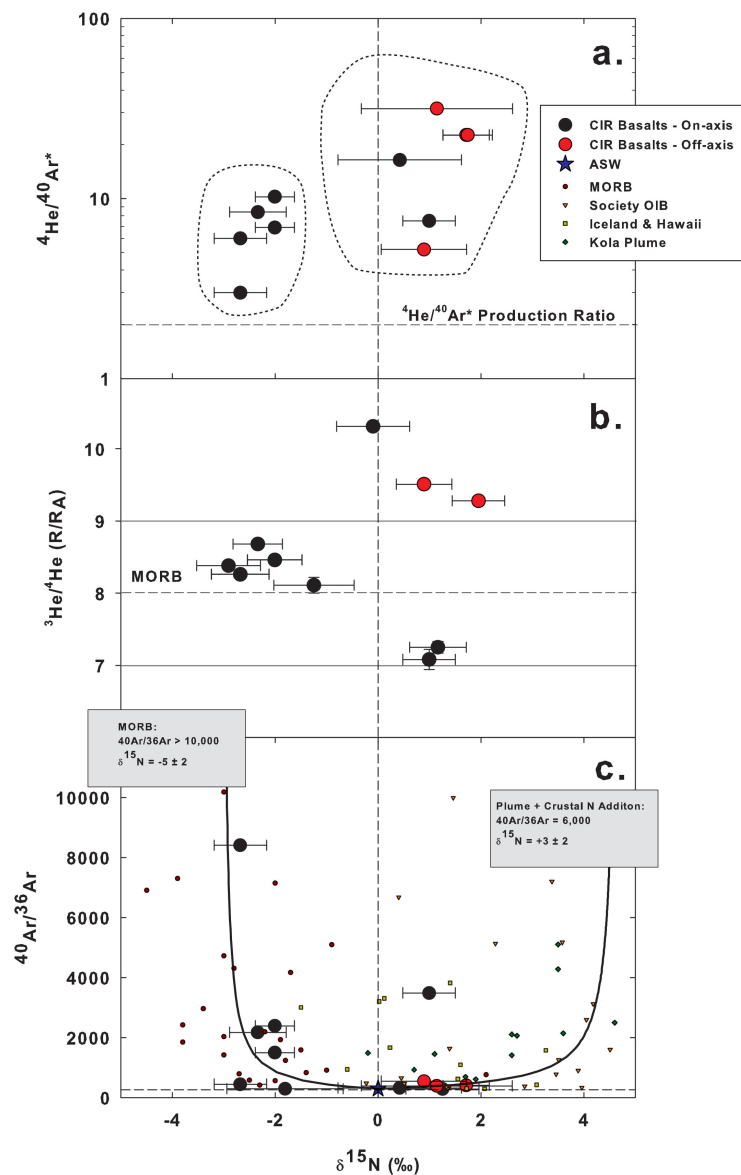in order to assess if observed co-variations can be explained by mantle-mixing processes.

Figure VI.13: (a) ^{4}He/^{40}Ar* ratio versus nitrogen isotopes (δ^{15}N), the lack of a correlation suggests that CIR basalt nitrogen isotopes are not affected by degassing. (b) He-isotopes (^{3}He/^{4}He) versus nitrogen isotopes (c) Argon isotopes (^{40}Ar/^{36}Ar) versus nitrogen isotopes together with Air and postulated MORB (δ^{15}N = -5 ± 2 ‰; ^{40}Ar/^{36}Ar = 10,000) and Plume (δ^{15}N = +3 ± 2 ‰; ^{40}Ar/^{36}Ar = 6,000) endmembers as well as mixing trajectories. Positive δ^{15}N anomalies observed in plume-derived samples (e.g., off-axis CIR basalts) likely result from crustal N additions.

VI.6.2 CIR mantle mixing – MORB versus primitive contributions

Previous He isotope studies have shown that high ^{3}He/^{4}He ratios (i.e., ^{3}He/^{4}He values > MORB-like values) between the ~19° and 20° S segment of the CIR axis, and along the adjacent off-axis Gasitao, Three Magi, and Rodrigues ridges, suggest primitive (Réunion) hot spot mantle is flowing laterally toward the CIR (Füri et al., 2011). In this section, we combine these He-isotope results with new Ne-N-Ar data to investigate if mixing between primordial and mantle components, together with variable crustal contributions, can adequately explain the coupled N-Ne-Ar evolution of the CIR mantle.

VI.6.2.1 N-He-Ar isotope relationships of CIR basalts

Positive δ^{15}N values are observed in all off-axis basalts, as well as in two on-axis CIR basalts at ~18.1º S (i.e., D9-2 and D8-2; Figure VI.3). In Figure VI.13b, we plot He-isotopes versus N-isotopes and demonstrate that two of the three highest ^{3}He/^{4}He values are from off-axis portions of the CIR and also display positive δ^{15}N values. In addition, two on-axis low ^{3}He/^{4}He samples, collected directly south of the Marie Celeste FZ (~18.1º S), exhibit positive δ^{15}N values. Using He-isotopes and incompatible trace element ratios, Füri et al. (2011) identified off-axis samples to be affected by current plume-ridge interaction (~19.5º S) and on-axis samples (with high La/Sm and low ^{3}He/^{4}He) at ~18.1º S to be interacting with the remnants of a "fossil" Réunion mantle plume component. If the Réunion-plume is indeed the source of ^{3}He enrichments in the CIR mantle, then we postulate that ^{15}N enrichments in off-axis basalts may also be derived from interaction between the CIR and the Réunion plume. Similarly, we propose that the positive δ^{15}N component observed in on-axis samples at ~18.1º

S is derived from fossil Réunion-plume material located immediately south of the Marie Celeste FZ (~18.1º S).

In Figure VI.13c, $^{40}Ar/^{36}Ar$ values are plotted as a function of $\delta^{15}N$, together with binary mixing curves between presumed mantle endmembers and the atmosphere. Unlike Ne-isotopes, Ar-isotopes are not corrected for air-contributions, due to the assumption that all ^{36}Ar is air-derived. The majority of on-axis basalts can be explained by mixing between a MORB endmember ($\delta^{15}N$ = -5 ± 2 ‰; $^{40}Ar/^{36}Ar$ > 10,000) and air ($\delta^{15}N$ = 0 ‰; $^{40}Ar/^{36}Ar$ = 298.56), whereas off-axis samples can be explained by mixing with a plume-mantle endmember ($\delta^{15}N$ = +3 ± 2 ‰; $^{40}Ar/^{36}Ar$ = 6,000) and air. For comparison, published N-Ar results from MORB and plume-mantle settings are also shown (Dauphas and Marty et al., 1999). Coupled N-Ar results suggest that distinct MORB- and plume-like mantle components are present in the CIR mantle source and that combined N-Ar isotope systematics can be explained by mixing between mantle and air components.

VI.6.2.2 N-Ne isotopes of CIR basalts

Ne-isotopes variations of CIR basalts suggest a solar component is present in the CIR mantle, with observed Ne-isotope variations best explained by mixing between MORB and primitive Réunion plume-like mantle endmembers (Figure VI.3). Assuming solar wind samples accurately approximate the proto-solar nebula (PSN; Marty et al., 2011; Marty, 2012), there may also be a small, but detectable, primitive (i.e., solar) nitrogen component in the CIR mantle. In this section, we assess if primitive contributions are detectable in the coupled N-Ne isotope systematics of CIR basalts.

Marty (2012) suggested that mantle nitrogen isotope compositions could potentially be explained by mixing between small amounts of PSN nitrogen ($\delta^{15}N$ = -383 ± 8 ‰), recycled atmospheric nitrogen (= 0 ‰) and/or crustal nitrogen (= ~ +7 ‰) components. In order to test if the solar nitrogen hypothesis is consistent with the occurrence of solar-Ne in the CIR mantle source, we plot $^{21}Ne/^{22}Ne_{EX}$ values (see Section 5.1.2) of CIR basalts against N-isotopes ($^{15}N/^{14}N$) in Figure VI.14, together with binary mixing trajectories between a postulated solar endmember and two distinct mantle endmembers with $\delta^{15}N$ values between MORB mantle (-5 ‰) and crustal nitrogen (+7 ‰) values. The solar $^{21}Ne/^{22}Ne$ is assumed to be 0.03118 (Trieloff and Kunz, 2005), whereas the $^{15}N/^{14}N$ of 2.2681 × 10^{-3} (i.e., $\delta^{15}N$ = -383 ‰) is the measured solar wind value (Marty et al., 2011). The MORB $^{21}Ne/^{22}Ne$ endmember value is estimated to be 0.0594 by extrapolating the MORB trajectory (Sarda et al., 1988) to the $^{20}Ne/^{22}Ne$ of Ne-B (=12.5). We adopt two distinct mantle $^{15}N/^{14}N$ endmembers (3.6687 × 10^{-3}; $\delta^{15}N$ = -2 ‰, 3.6815× 10^{-3}; $\delta^{15}N$ = +1.5 ‰), both of which fall between MORB (3.6576 × 10^{-3}; $\delta^{15}N$ = -5 ‰) and sediments (3.7017 × 10^{-3}; $\delta^{15}N$ = +7 ‰) (Marty and Dauphas, 2003).
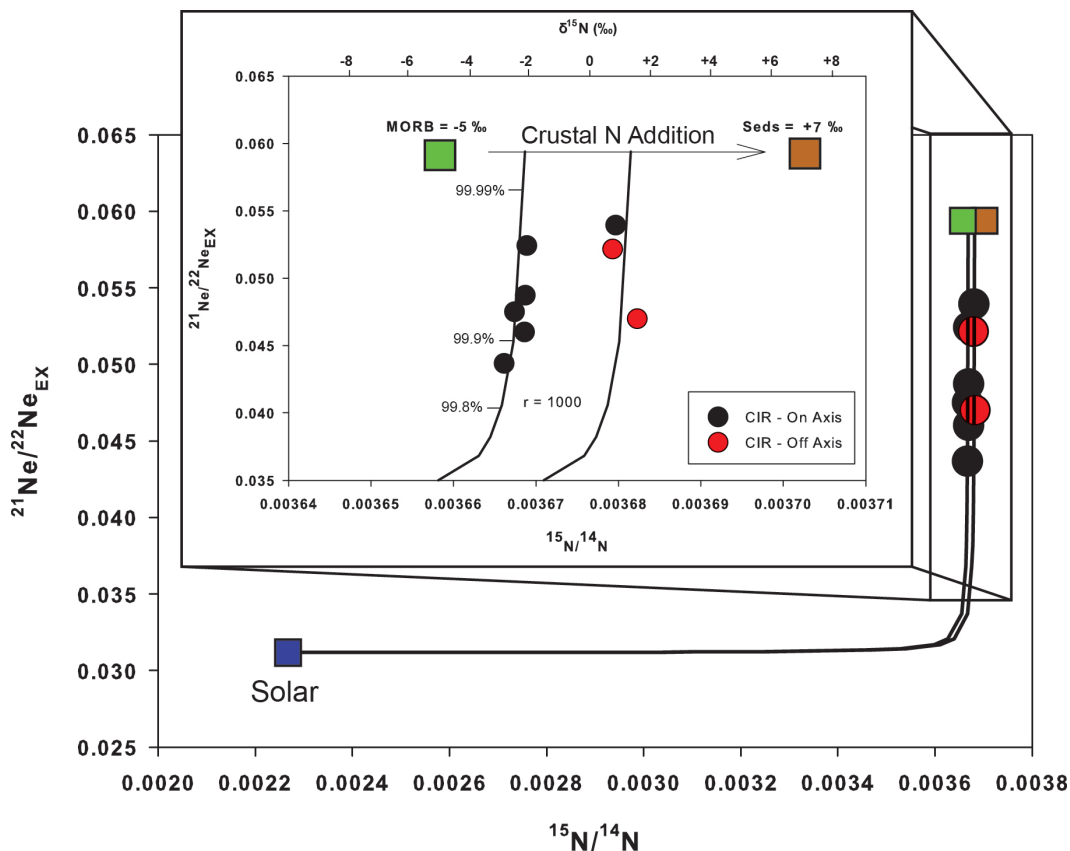
Figure VI.14: $(^{21}Ne/^{22}Ne)_{EX}$ (i.e., air-corrected $^{21}Ne/^{22}Ne$ values) versus $^{15}N/^{14}N$ values of CIR basalts, plotted together with binary mixing curves between a solar component and mantle endmember components with variable ^{15}N enriched sedimentary contributions (see Section 5.3 for details). The curvature of the hyperbolic mixing lines is described by r = $(^{14}N/^{22}Ne)_{MORB}$ / $(^{14}N/^{22}Ne)_{SOLAR}$ = ~1000.

Coupled Ne-N variations can be explained by binary mixing between a solar endmember and a MORB-like mantle endmember, modified by variable ^{15}N enriched contributions – consistent with addition of crustal material. All N-Ne data fall on one of two well-defined mixing curves, between solar and mantle/crustal $^{15}N/^{14}N$ endmember components. The curvature of the binary mixing trajectories is controlled by the r value = $(^{14}N/^{22}Ne)_{MORB}$ / $(^{14}N/^{22}Ne)_{SOLAR}$ and in both cases is equal to ~1000 (Figure VI.14), which indicates that either higher relative ^{14}N or lower ^{22}Ne contents occur in the mantle endmember

versus the solar endmember. Significantly, only very small amounts of solar contributions (< 0.2 %) are required to explain the observed Ne-N isotope systematics. All but one on-axis CIR sample plots on a solar-mantle mixing curve, where the mantle endmember δ^{15}N component is ~ -2 ‰ (^{15}N/^{14}N = 3.6687 × 10^{-3}). In contrast, both off-axis samples and on-axis sample D8-2, require mixing with a ^{15}N enriched mantle endmember component (^{15}N/^{14}N = 3.6815 × 10^{-3}; δ^{15}N = ~ +1.5 ‰). The disparity between necessary mantle endmembers δ^{15}N components suggests that off-axis samples require a larger ^{15}N-enriched component to explain their combined Ne-N systematics. By assuming a MORB starting value of -5 ‰ and a sedimentary end member of +7 ‰ we estimate that on-axis samples have ~ 20 % of sedimentary-derived N and that off axis samples have ~ 50 % sedimentary-derived N.

If we assume that off-axis samples are more heavily influenced by recent plume contributions (Füri et al., 2011), then the occurrence of positive δ^{15}N values is consistent with previous findings (Marty and Dauphas, 2003; Fischer et al., 2005), which show that OIB/plume-influenced systems have ^{15}N-enriched sources. In addition, on-axis sample D8-2 – which plots on a mixing trajectory with off-axis samples in Figure VI.14 – was previously characterized as having been influenced by a "fossil" Réunion component based on high La/Sm and radiogenic ^{3}He/^{4}He ratios (Füri et al., 2011). Trace element and radiogenic isotopic compositions of CIR samples from ~18.1° S have also been explained by binary mixing between regional depleted MORB mantle and a recycled OIB/seamount component (Ulrich et al., 2012). Thus, we conclude that the enriched on-axis sample may have acquired larger ^{15}N enriched contributions compared with other on-axis basalts, due to plume-ridge interaction and perhaps due to recycling of a ^{15}N enriched component.

VI.6.3 Source of ^{15}N enriched component?

In this section, we investigate possible sources of the ^{15}N enriched sedimentary component identified in plume-related CIR basalts. Enriched crustal δ^{15}N signatures can potentially be integrated in two distinct ways: (1) through incorporation of recycled oceanic crust and ocean sediments, into the convecting mantle by subduction (e.g., Hofmann and White, 1982; Marty and Humbert, 1997; Marty and Dauphas, 2003; Day et al., 2009), and/or (2) by shallow-assimilation within the existing crust during magma eruption (Shaw et al., 2004; Macpherson et al., 2005).

Nitrogen in the mantle is considered to be predominantly recycled (Marty and Dauphas, 2003) on the basis of N_2/K and $N_2/^{36}Ar$ ratios (Marty and Dauphas, 2003). Potassium is a strongly recycled, nonvolatile, and highly incompatible lithophile element and N_2/K ratios are nearly constant between the exosphere and the various mantle reservoirs. Conversely, the ratio between N and ^{36}Ar – an extremely volatile element – varies over three orders of magnitude in these same reservoirs (Marty, 1995; Marty and Dauphas, 2003). In contrast, Ne and He are not efficiently recycled into the mantle source (Moreira et al., 2003; Ballentine et al., 2005; Mukhopadhyay, 2012).

Due to the recycled nature of mantle nitrogen, it serves as an excellent tracer of deep crustal recycling processes (Marty and Dauphas, 2003), due in part to large isotopic and concentration contrasts between reservoirs. For example, MORB mantle is depleted in ^{15}N versus surface reservoirs (i.e., atmosphere, sediments), and δ^{15}N vales range from -5 ± 2 ‰ (Marty and Dauphas, 2003) to as low as -30 ‰ (Javoy et al., 1986; Cartigny et al., 1998a; Marty and Zimmermann, 1999; Marty, 2012). In contrast, plume-influenced regions sample an isotopically distinct ^{15}N enriched component (i.e., δ^{15}N = 3 ± 2; Marty and Dauphas, 2003). The δ^{15}N disparity between MORB and plume-derived samples indicates that two isolated reservoirs exist in the mantle – presumably the depleted upper (MORB) mantle and the less

degassed lower mantle. In contrast, nitrogen isotopes in crustal material ranges from ~ +4 to +8 ‰ in kerogens and ocean sediments (Pinti et al., 2001) due to kinetic isotope fractionation of nitrogen associated with the dissimilatory denitrification of NO_3^- in the oceans. Due to the isotopic similarity between crustal material and plume-derived material, Marty and Humbert (1997) and Marty and Dauphas (2003) suggested that the positive $\delta^{15}N$ plume component may result from preferential recycling of crustal material into the plume-mantle source.

The preponderance of isotopically high $\delta^{15}N$ values in plume related samples along the CIR indicates that ^{15}N enriched crustal material is efficiently recycled into the Réunion-CIR mantle source. All off-axis samples and one two on-axis samples from ~18.1º S display positive $\delta^{15}N$ characteristics, consistent with significant plume contributions (Füri et al., 2011). Based on trace element and radiogenic isotope compositions, Ulrich et al. (2012) suggested that samples from ~18º to 20º S can be explained by a binary mixture between depleted MORB mantle source and a recycled OIB/seamount source.

In Figure VI.14, high (~1000) r-values $[(^{14}N/^{22}Ne)_{MORB}/(^{14}N/^{22}Ne)_{SOLAR} = 1000]$ are required to explain Ne-N isotope systematics of CIR basalts, suggesting that N is recycled into the mantle ~1000 times more efficiently than Ne. This observation is consistent with previous mass balance arguments that suggest Ne is removed during the subduction process (Moreira et al., 2003; Ballentine et al., 2005; Mukhopadhyay, 2012). If air-like neon were recycled into the mantle, it would dominate the neon budget, thus significantly lowering the measured $^{14}N/^{22}Ne$ value of the mantle.

Alternatively, it is possible that positive $\delta^{15}N$ signatures are acquired during magma emplacement events. The oceanic crust is heterogeneous with respect to nitrogen speciation and isotope characteristics, and thus there is potential for assimilation of crustal material during eruption events (Pinti et al., 2001; Busigny et al., 2005b; Li et al., 2007). Magma

mixing with isotopically distinct N_2 in the shallow crust would be expected to result in variable amounts of crustal addition, likely depending on the thickness of the crust. In this way, off-axis samples may acquire an isotopically higher $\delta^{15}N$ signature due to more interaction with thicker oceanic crust during emplacement. However, if contamination during eruption were the source of the crustal ^{15}N enrichment we would expect to observe the highest $\delta^{15}N$ values in the highest N_2 concentration samples, but no clear relationship is evident between these two parameters (Table VI.3). Furthermore, the fact that all ^{15}N enriched CIR basalts show ancillary evidence (e.g., He-isotope and/or La/Sm enrichments) that they are plume-derived, suggests that the crustal component is integrated into the mantle source. Moreover, the observation that the positive $\delta^{15}N$ component is detectable in both modern and fossil plume-related settings indicates that the source of the ^{15}N enrichment is long-lived in the mantle source. The confluence of these factors leads us to favor the former (i.e., recycling) explanation for crustal enrichments.

In summary, we conclude that the coupled N-Ne isotope characteristics of CIR basalts can be explained by mixing between an extremely small (< 0.2 %) solar contribution and mantle contributions that have been variably (20-50 %) modified by crustal nitrogen additions. The occurrence of positive $\delta^{15}N$ in plume related samples, together with the overwhelming evidence for the recycled nature of mantle nitrogen leads us to conclude that crustal nitrogen is likely recycled into the Réunion-plume source and is detectable along portions of the CIR due to plume ridge interaction.

VI.6.4 Additional constraints on mantle mixing

Additional constraints on mantle mixing processes are available through coupling Ne and He isotope data, measured on the same sample suite. This approach allows us to assess if He-Ne co-variations observed in CIR basalts and Réunion xenoliths can also be explained by binary mixing between plume-type and MORB-like mantle He/Ne endmembers.

VI.6.4.1 He-Ne isotope variability

In Figure VI.15, the air-corrected $^{21}Ne/^{22}Ne_{EX}$ values of CIR basalts as well as Réunion xenolith samples are plotted against He-isotopes, together with a series of binary mixing trajectories between postulated primordial (PRIM) and MORB end-members. Notably, $^{21}Ne/^{22}Ne_{EX}$ values in Réunion xenoliths range from 0.0325 ± 0.0108 to 0.0513 ± 0.0120, and fall in the range previously measured in Réunion lavas (Hanyu et al., 2001; Trieloff et al., 2002; Hopp and Trieloff, 2005). The $^{21}Ne/^{22}Ne$ of PRIM (i.e., primitive solar component) is again assumed to be 0.03118 (Trieloff and Kunz, 2005) and the MORB $^{21}Ne/^{22}Ne$ endmember value is estimated to be 0.0594 by extrapolating the MORB trajectory (Sarda et al., 1988) to the $^{20}Ne/^{22}Ne$ of Ne-B (=12.5), in the same way as in the previous section. In the case of He-isotopes, we assume a MORB endmember $^{4}He/^{3}He$ ratio of 90,000 (=8 R_A) (Graham, 2002), and a PRIM He-isotope endmember value of 280 R_A (Black, 1972; $^{4}He/^{3}He$ = 2580) in order to be consistent with the Ne-B component (i.e., both values were measured in gas-rich meteorite samples; Black, 1972). The curvature of binary mixing trajectories are controlled by the r value = $(^{3}He/^{22}Ne)_{MORB} / (^{3}He/^{22}Ne)_{PLUME}$. For reference, we also plot $^{21}Ne/^{22}Ne_{EX}$ versus $^{4}He/^{3}He$ data fields for previous studies of Réunion lavas (Hanyu et al., 2001), and Iceland (Füri et al., 2010), which represent the Réunion-plume component as well as an archetypal plume-MOR interaction.
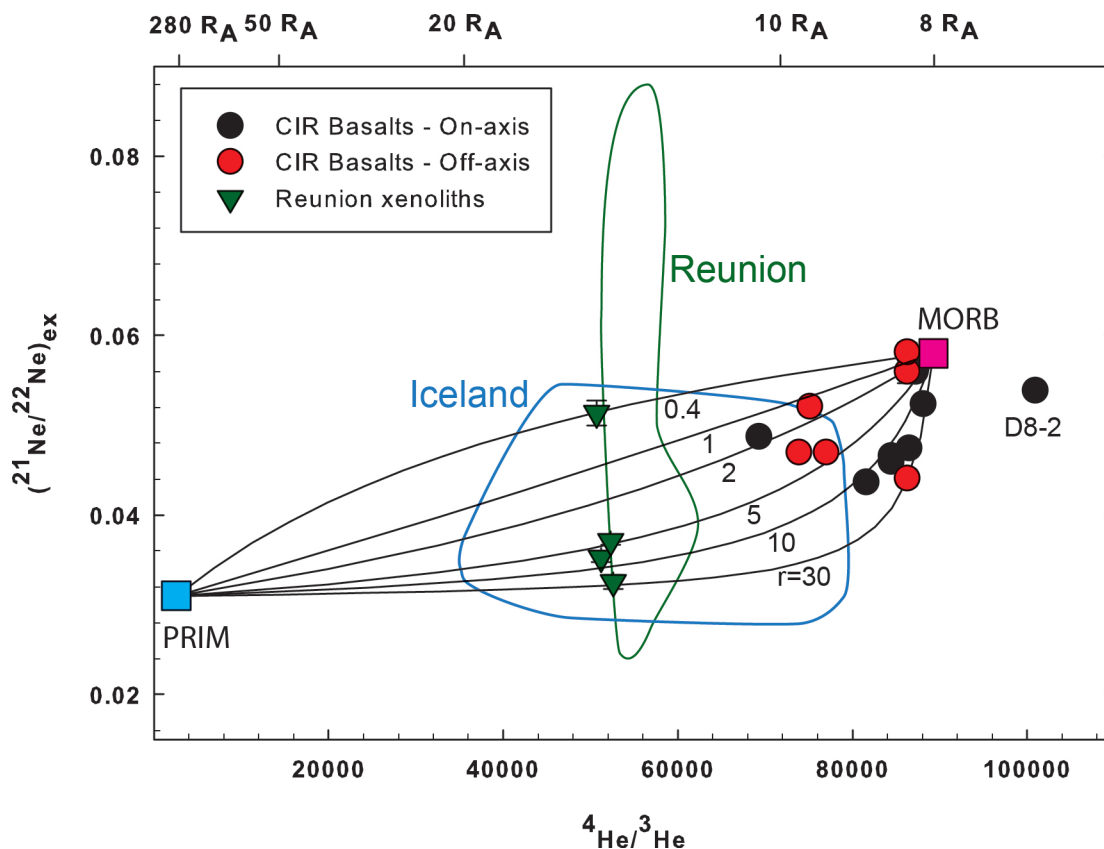
Figure VI.15: $(^{21}Ne/^{22}Ne)_{EX}$ (i.e., air-corrected $^{21}Ne/^{22}Ne$ values) versus $^{4}He/^{3}He$ values of CIR basalts and Réunion xenoliths, plotted together with binary mixing curves between a primordial mantle endmember (PRIM) and a MORB-like component (see Section 5.3 for details). The curvature of the hyperbolic mixing lines is described by r = $(^{3}He/^{22}Ne)_{MORB}/(^{3}He/^{22}Ne)_{PRIM}$. In addition, data fields are shown for Réunion lavas (Hanyu et al., 2001) and Iceland subglacial basalts (Füri et al., 2010).

The observed variations between Ne and He isotopes can be described by binary mixing between a primordial mantle endmember (PRIM) and a second endmember similar to MORB-mantle. However, unlike Ne-N relationships, CIR basalt and Réunion xenolith samples do not fall on a single Ne-He mixing curve, but rather require r-values between 0.4 and 30 to explain observed variations (Figure VI.15). Apart from an obvious outlier, on-axis CIR samples plot close to PRIM-MORB mixing curves with an r-values between 1 and 30, whereas the majority of off-axis samples fall between 1 and 5, with one outlier with an r-value

of 30. The fact that all basalt samples require r-values greater than unity, implies a

higher $^3He/^{22}Ne$ ratio of the MORB endmember compared to the $^3He/^{22}Ne$ ratio of the

primordial mantle component (i.e., $(^3He/^{22}Ne)_{MORB} > (^3He/^{22}Ne)_{PRIM}$).

If we assume that the MORB endmember $^3He/^{22}Ne$ ratio is constant throughout the

CIR, then lower r-values in off-axis samples suggest a higher relative PRIM $^3He/^{22}Ne$

endmember in the plume source. In this regard, CIR basalts resemble other plume-related

glasses (e.g., Iceland; Füri et al., 2010). Significantly, all Réunion xenolith samples plot closer

to the PRIM endmember compared with CIR basalt samples and overlap with Réunion lavas

(Hanyu et al., 2001), consistent with a higher $^3He/^{22}Ne$ plume contribution in the admixture.

Notably, mixing trajectories for xenolith samples span the entire range observed in CIR

basalts (i.e., r-values between ~ 0.4 and 30), however, this range is bracketed by Réunion lava

samples (Hanyu et al., 2001), which span an even broader range (Figure VI.15). The single

outlying on-axis basalt sample (Figure VI.15; D8-2) falls outside the mixing envelope defined

by the series of binary mixing curves between PRIM and MORB endmembers; D8-2 is

marked by lower than MORB He-isotopes and thus an additional endmember (with

low $^3He/^4He$) is required to account for the He–Ne systematics; radiogenic He (accompanied

by insignificant nucleogenic Ne) produced within the crust is a possibility. This observation in

agreement with the conclusions of Füri et al. (2011), who explained low He-isotope (i.e.,

$^3He/^4He$ < MORB) samples observed in the ~18.1 ºS portion of the CIR by closed system

radiogenic ^4He in-growth in a "fossil" Réunion mantle component. Furthermore, this finding

is consistent with larger contributions from the Réunion-like (i.e., plume) component, which

were identified in the Ne-N isotope systematics of sample D8-2.

An alternative explanation for variations in $^{21}Ne/^{22}Ne_{ex}$ values between presumed

upper and lower mantle reservoirs is elemental He/Ne heterogeneities in the mantle. For

example, Moreira et al. (2001) proposed that different mantle reservoirs (i.e., MORB versus PRIM) could have evolved from the same He and Ne isotope compositions but with distinct ^{3}He/^{22}Ne ratios and that subsequent ingrowth of nucleogenic ^{21}Ne and radiogenic ^{4}He have produced the observed range in ^{21}Ne/^{22}Ne$_{ex}$ and ^{3}He/^{4}He values. Nucleogenic ^{21}Ne is generated by the ^{18}O (α,n) ^{21}Ne and ^{24}Mg (n,α) ^{21}Ne reactions (Wetherill, 1954), resulting in an increase in the ^{21}Ne/^{22}Ne ratio and δ^{21}Ne values over time. Since the α-particles are derived from U and Th decay, the production of radiogenic ^{4}He and nucleogenic ^{21}Ne (^{21}Ne∗) should therefore be directly coupled, and high ^{4}He/^{3}He (i.e., low ^{3}He/^{4}He) ratios would therefore correlate with high ^{21}Ne/^{22}Ne$_{EX}$ values. However, in CIR basalts and Réunion xenoliths, measured ^{3}He/^{22}Ne ratios vary over 2 orders of magnitude (0.02 to 3.93). If mantle heterogeneities were the origin of these variations it would imply that the ^{3}He/^{22}Ne ratio in the mantle source varied by a factor of ~200. However, there is no mechanism know to exist that can preserve such large ^{3}He/^{22}Ne disparities within a single mantle domain for such long durations (i.e., over Earth history). Therefore, we propose that the He–Ne characteristics of CIR basalt and Réunion xenolith samples are better explained by the binary mixing scenario presented in Figure VI.15.

VI.6.4.2 Solar and nucleogenic Ne variations

The observation that endmember ^{3}He/^{22}Ne compositions used in the binary mixing model above are different ($r \neq 1$) and variable ($0.4 < r < 30$) indicates that the He/Ne ratio in either one or both mantle endmembers of the CIR (i.e., the PRIM and/or MORB mantle component) was fractionated prior to mixing (Hopp and Trieloff, 2008). We can assess this fractionation hypothesis for the CIR samples by considering the ^{4}He/^{21}Ne∗ and the ^{3}He/^{22}Ne$_S$ ratios. The ratio of primordial ^{3}He to solar ^{22}Ne$_S$ (Graham, 2002) is calculated using:

$$^{22}Ne_S = [^{22}Ne]_M \times f_{22} \tag{4}$$

$$^{3}He/^{22}Ne_S = (^{3}He/^{4}He_M \times [^{4}He]_M) / {}^{22}Ne_S \tag{5}$$

The amount of mantle-derived nucleogenic ^{21}Ne (i.e., $^{21}Ne*$) in a sample is given by:

$$^{21}Ne* = {}^{22}Ne_S ({}^{21}Ne/^{22}Ne_{EX} - {}^{21}Ne/^{22}Ne_S) \tag{6}$$

Again, we use the isotope composition of Ne-B as the value for "solar" mantle neon in order to calculate $^{3}He/^{22}Ne_S$ and $^{4}He/^{21}Ne*$.

Figure VI.16a shows the relationship between of $^{3}He/^{22}Ne_S$ and $^{4}He/^{21}Ne*$ for CIR basalt and Réunion xenolith samples of this study. Also plotted for comparison are data fields for lavas of Réunion (Hanyu et al., 2001), Iceland (Füri et al., 2010), and MORB (Sarda et al., 1988; Moreira et al., 1998). Réunion xenoliths (this study) and previously characterized plume-derived materials (e.g., Réunion and Iceland fields – Figure VI.16a) display distinctly lower He/Ne ratios versus the mean primordial $^{3}He/^{22}Ne_S$ value of 7.7 (Honda and McDougall, 1998) and the theoretical radiogenic ^{4}He to nucleogenic ^{21}Ne (i.e., $^{4}He/^{21}Ne*$) production ratio of 2.2×10^{7} (Yatsevich and Honda, 1997) proposed for Earth's mantle (= Mantle EM; Figure VI.16a), consistent with a significant contribution from a mantle component that is depleted in He relative to Ne. Hopp and Trieloff (2008) and Füri et al. (2010), suggested that

plume-derived materials may exhibit lower He/Ne ratios due to a helium deficit which they attribute to the more compatible behavior of He relative to Ne (and Ar) during partial melting. In this way, a small amount of He-deficient plume-derived melt mixes with a larger degree of MORB melt to produce the observed variability in He–Ne isotope compositions in plume related systems.
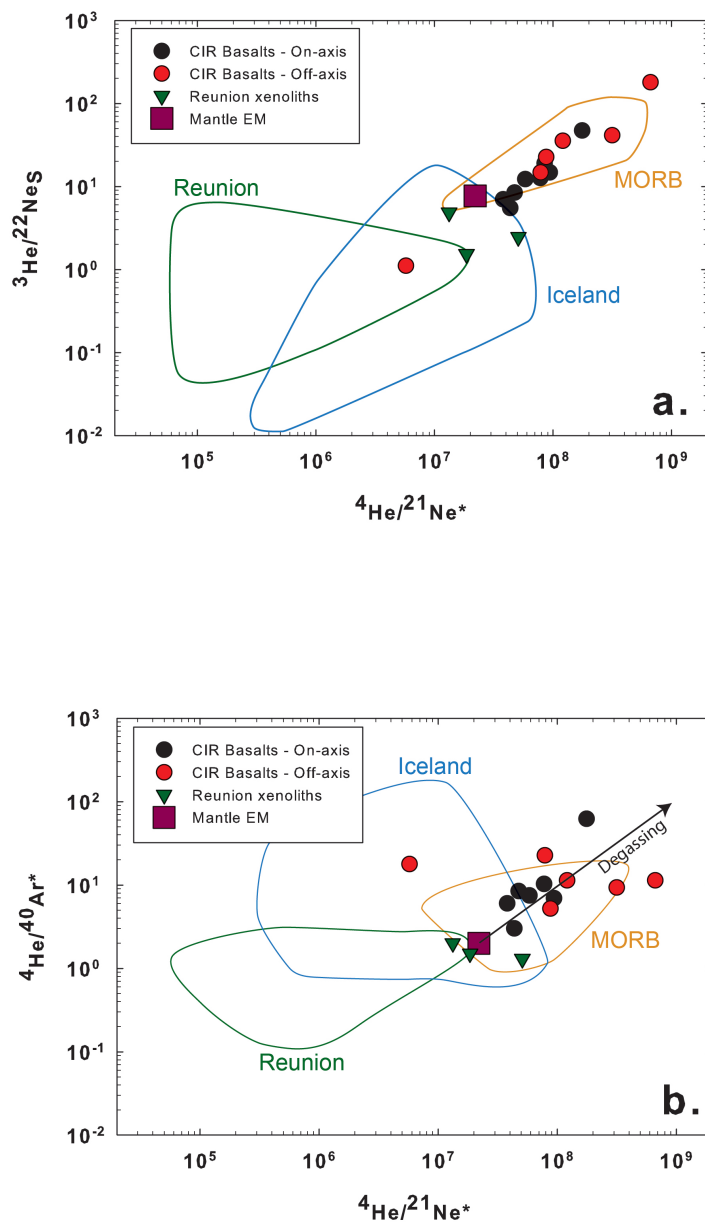
Figure VI.16: (a) $^{3}He/^{22}Ne_S$ and (b) $^{4}He/^{40}Ar*$ versus $^{4}He/^{21}Ne*$ of CIR basalt and Réunion xenoliths. In addition, we plot MORB (Sarda et al., 1988; Moreira et al., 1998), Réunion (Hanyu et al., 2001) and Iceland (Füri et al., 2010) fields. The grey square represents assumed values for Earth's mantle: $^{4}He/^{21}Ne* = 2.2 \times 10^{7}$ (Yatsevich and Honda, 1997), $^{3}He/^{22}Ne = 7.7$ (Honda and McDougall, 1998), $^{4}He/^{40}Ar* = 2$ (Jambon et al., 1986; Marty and Zimmermann, 1999). All $^{3}He/^{22}Ne_S$ and $^{4}He/^{21}Ne*$ ratios are calculated under the assumption that Ne–B is representative of the primordial, "solar" neon component.

In contrast, the majority of CIR basalts have elevated He/Ne (Figure VI.16a) ratios versus the proposed mantle endmember value and overlap with glasses previously characterized in MORB settings (Sarda et al., 1988; Moreira et al., 1998). This observation indicates significant recent elemental fractionation which has enriched CIR glasses in both primordial ^{3}He and radiogenic ^{4}He relative to mantle Ne. Honda and Patterson (1999) suggested that the systematic He enrichment observed in MORB glasses may reflect the preferential concentration of helium, liberated from the crystallizing oceanic crust, into the relatively small volume of residual magma that is erupted to form glasses. Alternatively, more extensive vesicle loss in MORB magma (versus plume-derived magma) during degassing could enable preferential loss of Ne relative to He, due to lower Ne solubilities in magma (Sarda and Moreira, 2002). In both cases, the linear correlation (slope = ~1) between ^{3}He/^{22}Ne$_S$ and ^{4}He/^{21}Ne$_*$ of all sample suites, including CIR basalts and Réunion xenoliths, suggests that any He–Ne fractionation must have occurred relatively recently in order to preserve distinct ^{4}He/^{21}Ne$_*$ values, i.e., ≠ mantle production values (i.e., Mantle EM; Honda and Patterson, 1999). In turn, the timing of He–Ne fractionation restricts the subsequent mixing event between mantle endmembers to the relatively shallow mantle and/or eruption site, suggesting that degassing fractionation during eruption may be the most viable explanation. In the following section we further investigate degassing losses using an equilibrium degassing model.

VI.6.4.3 Relative noble gas (He-Ne-Ar) variations

In Figure VI.16b, we plot ^{4}He/^{40}Ar∗ (see Section 5.1.4) values as a function

of ^{4}He/^{21}Ne∗ ratios for CIR basalts, Réunion xenoliths together with fields for Réunion lavas

(Hanyu et al., 2001), MORB (Sarda et al., 1988; Moreira et al., 1998) and Icelandic subglacial

glasses (Füri et al., 2010). Most CIR basalts plot close to a linear array with an observed slope

of ∼1, defined by MORB and plume-derived samples, which include the mantle endmember,

defined by the theoretical ^{4}He/^{40}Ar∗ and ^{4}He/^{21}Ne∗ production ratios (Jambon et al., 1986;

Marty and Zimmerman, 1999; Yatsevich and Honda, 1997). Réunion xenolith samples of this

study display ^{4}He/^{40}Ar∗ and ^{4}He/^{21}Ne∗ values close the assumed mantle production values

(i.e., Mantle EM) and overlap with Réunion (Hanyu et al., 2001) and Iceland values (Füri et

al., 2010).

However, all but one CIR basalt sample displays He/Ne ratios higher than the mantle

production value, indicating elemental fractionation associated with degassing. Furthermore,

the correlation observed in Figure VI.16b supports the conclusion from the previous section

that He/Ne variations likely result from degassing. Similar observations were previously made

in MORB samples (Honda et al., 1993b; Honda and Patterson, 1999) and recently in the Lau

Basin (Hahm et al., 2012). If the Réunion plume component were dominant in all off-axis

basalt samples, we might expect lower ^{4}He/^{40}Ar∗ and ^{4}He/^{21}Ne∗ values, overlapping with

Réunion xenoliths and other plume related localities that possess similarly high ^{3}He/^{4}He

values. Significantly, the outlying sample (D37-2) also has the most primitive ^{3}He/^{4}He ratio

(9.67 R$_A$) of all basalts reported here (Füri et al., 2011). Based on these results we conclude

that CIR basalts are primarily characterized by MORB-like He-Ne-Ar and have substantial

fractionated due to degassing processes.

In summary, we conclude that the majority of CIR basalts have been modified by

degassing processes but retain He/Ne and He/Ar characteristics of the MORB mantle (i.e., plot

within the MORB field in Figure VI.16; Sarda et al., 1988; Moreira et al., 1998). In contrast, Réunion xenoliths and several off-axis CIR basalt samples overlap with plume like values – defined by the Réunion and Iceland fields (Figure VI.16). Observed He/Ne ratios help constrain the timing and location of mantle mixing – indicating that it occurred recently in the upper-most crust, which is consistent with elemental degassing fractionation. In the following section, we investigate the effects of degassing on the CO_2 and volatile element ratios in more detail.

VI.6.5 CO_2 solubility and degassing

During magma ascent, confining pressures are reduced and CO_2 is degassed from the melt (Bottinga and Javoy, 1989; Dixon et al., 1995; Jendrzejewski et al., 1997), forming vesicles in the basalt (Delaney et al. 1978; Mysen et al. 1975; Stolper and Holloway 1988). CO_2 has the lowest solubility among major volatile species and thus vesicles are comprised mainly of CO_2. As a result, virtually all oceanic basalts become CO_2 supersaturated (Sarda and Graham, 1990). CO_2 solubility is also directly related to eruption (water) depth and basalts erupted at shallower depths will typically lose a greater proportion of their primary volatile inventory. This process is observed along the CIR, where the highest CO_2 and major volatile contents occur in basalts erupted at the greatest eruption depth (~4,000 m; Table VI.4). Water content can also potentially exert an addition control on CO_2 solubility, as the two are inversely related (Dixon et al., 1995); however, H_2O contents are relatively homogeneous in all CIR basalts, suggesting hydrostatic confining pressures (eruption depths) are the primary control on extent of degassing.

Degassing occurs in either an open or closed system (Dixon et al., 1995; Gerlach and Taylor, 1990) or as a combination (two-stage) of both processes (Gerlach and Taylor, 1990; Macpherson and Mattey 1994; Shaw et al., 2004; Macpherson et al., 2005). Batch equilibrium degassing (BED) takes place in a closed system, whereby vesicles which form in a rising melt stay in contact with the melt, facilitating constant isotopic exchange (Macpherson and Mattey, 1994). In contrast, fractional equilibrium degassing (FED) occurs in an open system, where vesicles form in equilibrium with the surrounding melt but are removed as degassing progresses. Degassing will lead to isotopic exchange between CO_2 partitioned between the vesicles (CO_2^v) and residual dissolved CO_2 (CO_2^d) in the magma (Pineau et al. 1976; Javoy et al. 1978), with the extent of isotopic exchange controlled by degassing type (i.e., FED versus BED). As a result, variations in residual CO_2 content and $\delta^{13}C$ values can be used to constrain the extent of degassing within a given magmatic system.

VI.6.5.1 Dissolved CO_2: equilibrium degassing modeling

Using a degassing model (after Macpherson and Mattey, 1994), we estimate the initial carbon isotope and abundance characteristics of the CIR mantle source, assuming that measured CO_2 values result from primary mantle source features which have been modified by secondary processes such as degassing and crustal assimilation. Additionally, this type of model assumes that all samples are derived from a distinct parental melt composition and that isotopic exchange between dissolved and vesicle sited carbon can be explained by a common fractionation factor ($\Delta_{vapor-melt}$). In this way, primary CO_2 contents and $\delta^{13}C$ values of the magma source, prior to degassing, are estimated using the following equations (after Macpherson and Mattey, 1994):

$$\delta_r BED = \delta_p - \Delta(1 - (C_r BED/C_p)) \tag{7}$$

$$\delta_r FED = \delta_p + \Delta(\ln(C_r FED/C_p)) \tag{8}$$

where $\delta_r BED$ and $\delta_r FED$ correspond to the isotopic composition ($\delta^{13}C$) of CO_2 remaining

dissolved in the melt following BED and FED, $C_r BED$ and $C_r FED$ are the residual

concentrations of CO_2 for BED and FED, C_p and δ_p represent the primary carbon

concentration and isotopic composition of CO_2 dissolved in the melt prior to BED and FED,

and $\Delta = \delta^{13}Cvapor - \delta^{13}Cmelt$. Because one δ_r corresponds to two residual CO_2 concentrations

(CrBED and CrFED) for the two types of degassing (BED and FED), the two equations can be

combined:

$$\ln Cp + (CrBED/Cp) = 1 + \ln CrFED \tag{9}$$

and Cp can then be calculated using CrBED and CrFED values corresponding to two different

residual isotopic compositions ($\delta r1$ and $\delta r2$), using:

$$Cp = (C_r BED^1 - C_r BED^2)/\ln(C_r FED^1/ C_r FED^2) \tag{10}$$

CO_2 characteristics were determined for a total of 30 CIR basaltic glasses, which display a wide range in $\delta^{13}C^d$ and $CO_2{}^d$ contents (Table VI.4). A fractionation factor of ($\Delta=$) ~2.2 was estimated by calculating the slope of a best fit regression line through on-axis samples D3-3, D8-2 and D17-1 and off-axis sample D22-1, which are assumed to represent a FED trajectory. On-axis sample D12-2 ($C_{rBED}{}^1 = 239.9$ ppm, $\delta_r{}^1 = -5.8$ ‰) and off-axis sample D25-2 ($C_{rBED}{}^2 = 300.8$ ppm, $\delta_r{}^2 = -5.7$ ‰) were selected to define a BED trajectory and subsequently used to calculate C_rFED^1 and C_rFED^2 using the FED regression line ($\delta_r = 2.12 \ln(C_{rFED}) - 19.63$; $R^2 = 0.9996$), which defines the Δ-value for both the BED and FED trajectories. Using C_rBED^1 & C_rFED^1 and C_rBED^2 & C_rFED^2, C_p can then be estimated using Equation (10) and δ_pBED^1, δ_pBED^2, δ_pFED^1, and δ_pFED^2 using Equations (7) and (8), respectively. The estimated CO_2 composition of pre-eruptive melt is (C_p) = 1293 ppm, with a corresponding average $\delta_p = -4.2 \pm 0.2$ ‰ (i.e., average of δ_pBED^1, δ_pBED^2, δ_pFED^1, and δ_pFED^2; see Table VI.6).

Notably, CO_2 source estimates for CIR basalts are higher than typical MORB estimates of ~ 400 ppm CO_2 (Macpherson and Mattey, 1994; Shaw et al., 2004) and overlap with the lower end of previous estimates for the Indian Ocean, which extend from ~1,100 ppm CO_2 to as high as ~5,000 ppm CO_2 (Cartigny et al., 2001a) in the mantle source. These same authors estimated starting $\delta^{13}C$ values of -4.5 $\pm$ 0.2 ‰ in the Indian Ocean mantle source. In contrast, more recent estimates (e.g., Hirschman et al., 2006; Dixon et al., 2008; Marty, 2012) suggest that the mantle source may be as low as 20-120 ppm CO_2. Clearly, a consensus has not been formed regarding CO_2 source estimates in the mantle, due in part to the various approaches and modeling techniques employed to make these estimates.

Table VI.6: Calculations of CO_2 in pre-eruptive melts.

	C_rBED^1 (D12-2)	C_rBED^2 (D25-2)	C_P	δ_P
δ_r (‰)	-5.8	-5.7	1293[c]	-4.1[d]
C_rBED (ppm)	239.9	300.8		-4.1[e]
C_rFED (ppm)	673.1[a]	705.6[b]		-4.4[f]
				-4.4[g]

[a]Calculated from δ_r^1 and the regression line (FED trajectory).

[b]Calculated from δ_r^2 and the regression line (FED trajectory).

[c]Calculated from Eq. (10).

[d]Calculated from Eq. (7) using δ_r^1 and C_rBED^1.

[e]Calculated from Eq. (7) using δ_r^2 and C_rBED^2.

[f]Calculated from Eq. (8) using δ_r^1 and C_rFED^1.

[g]Calculated from Eq. (8) using δ_r^2 and C_rFED^2.

VI.6.5.2 Coupled assimilation and fractional equilibrium degassing (CAFED)

Figure VI.17 demonstrates that all on-axis CO_2 data and most (i.e., 9 of 14) off-axis data can be adequately described by the above two-stage degassing model. Of the five off-axis outliers, three samples (D20-5, D29-1 and D34-1) display the lowest $\delta^{13}C$ values along the entire CIR, well below the FED trajectory, and thus cannot be explained by degassing fractionation alone. For example, sample D29-1 is characterized by an extremely low CO_2^d content (<5ppm) and $\delta^{13}C$ value (-29.5 ‰). These outlying values can potentially result from extensive degassing, however, when a significant proportion (>99 %) of primary CO_2 has been degassed the sample is also more susceptible to post- or syn-eruptive CO_2 additions. Samples D20-5 and D34-1 are distinct in that they display rather low $\delta^{13}C$ values considering their relatively high CO_2^d contents (~190-320 ppm), suggesting assimilation of

isotopically low carbon. In contrast, two other off-axis samples (DR08-1b and D30-3) display relatively high $\delta^{13}C$ values and plot above the BED line. Isotopically high values indicate that samples are either derived from a magma source with a different source composition or have been subjected to contamination. The observation that the highest and lowest $\delta^{13}C$ values are observed in the Gasitao and Rodrigues ridges effectively rules out source heterogeneity as the basis for isotopic variation. Instead, we conclude that extreme $\delta^{13}C$ values in off-axis samples are derived from similar pre-eruptive magma which has been extensively degassed and subsequently acquired low $\delta^{13}C$ during interaction with the crust. The fact that all on-axis samples can be explained by the two stage degassing model suggests that significant crustal interaction only occurs primarily in off-axis portions of the CIR crust. This observation is consistent with increased crustal thicknesses with distance from the ridge axis. Similar assimilation of shallow crust has been observed in the submarine ridges that are suspected to be interacting with a mantle plume (Macpherson et al., 2005).
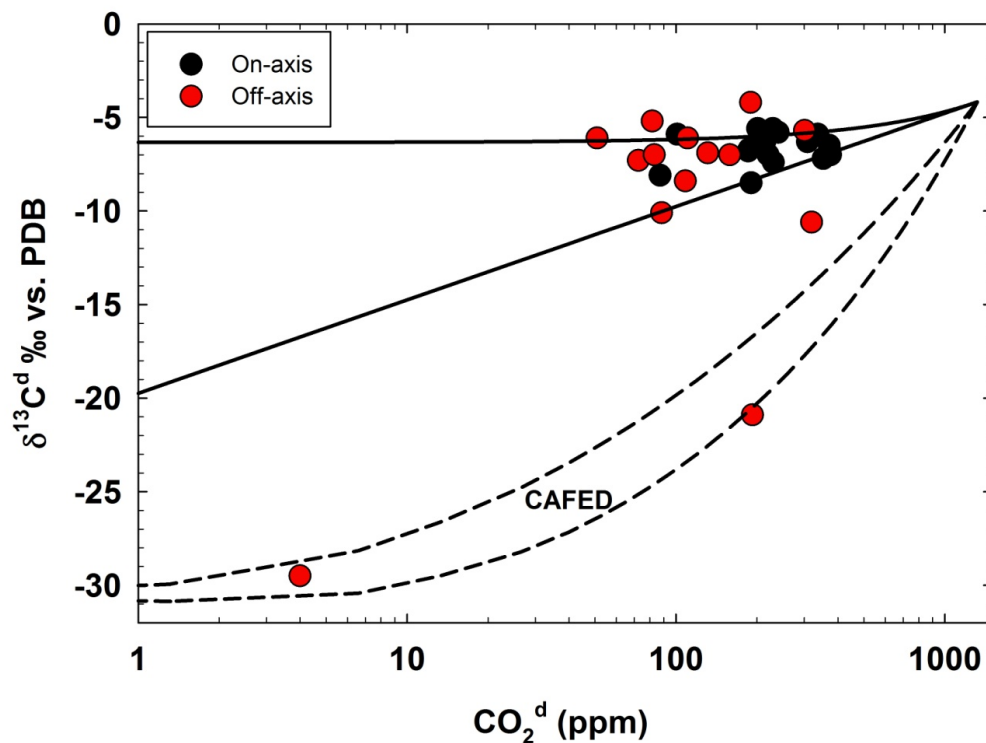
Figure VI.17: Carbon-isotopes ($\delta^{13}C$) as a function of dissolved CO_2 content (ppm) in CIR basalts. Calculated BED and FED mixing trajectories (solid line) are superimposed over CO_2 data assuming starting compositions of ~1300 ppm CO_2, with a $\delta^{13}C$ value of -4.2 ± 0.2 ‰. In addition, two CAFED trajectories are shown (dashed lines) which considers assimilation (300-500 ppm) of isotopically light carbon ($\delta^{13}C$ = -30 ‰) in concert with FED.

In order to simulate the concurrent processes of degassing and wall rock assimilation, we adopt the methods of Macpherson et al. (2010) and implement a coupled assimilation and fractional equilibrium degassing (CAFED) model in which FED occurs in increments of 1%, followed by assimilation with a contaminant CO_2 = 300-500 ppm and $\delta^{13}C$ = -30 ‰. FED was selected as the preferred mechanism of degassing due to the longer storage and eruption times in an open system, which should promote interaction between melts and contaminants. This model also assumes that the thick oceanic crust is heterogeneous with respect to carbon

speciation and isotope characteristics. This assumption is supported by oceanic drilling in the

CIR region that has identified a number of organic-carbon-rich-sediment beds, some of which

contain up to 26 % marine-derived organic carbon (Meyers and Dickens, 1992). These

sediments are expected to be characterized by isotopically low $\delta^{13}C$ values of -20 to -30 ‰

(Schubert and Calvert, 2001). In addition, drill cores from the Indian Ocean also show

abundant carbonates, clays and mixed-layer chlorite-smectites (Dick et al., 2000), which are

expected to be characterized by higher $\delta^{13}C$ values. Alternatively, we postulate that

isotopically low ($\delta^{13}C$) organic signatures in crustal wall rocks may result from deep

hydrothermal circulation of organic material (Lang et al., 2006). Figure VI.17 illustrates that

the (n=2) low $\delta^{13}C$ samples could be explained by CAFED (dashed lines) with CO_2 = 300-500

ppm and $\delta^{13}C$ = -30 ‰.

VI.6.5.3 Vesicle CO_2 elemental fractionation and assimilation

In addition to new CO_2 isotope and abundance data presented here, all samples were

previously characterized for vesicle-sited He isotopes and abundances (Füri et al., 2011) as

well as Ne-Ar isotope and abundance systematics. By combining measured abundances of

various different species, we calculate volatile ratios (i.e., $CO_2/^3He$; $CO_2/^{40}Ar^*$; $^4He/^{40}Ar^*$)

which, when evaluated together, may reveal valuable information about the degassing

histories of the magmas.

The extent of degassing is approximated using the $^4He/^{40}Ar^*$ ratio (Marty and

Tolstikhin, 1998), assuming a $^4He/^{40}Ar^*$ production ratio of ~2 (Jambon et al., 1986; Marty

and Zimmermann, 1999) (see Section 5.1.4 for details). Füri et al. (2011) demonstrated that

low helium contents are not coupled with low $^3He/^4He$ ratios in CIR basalts, which implies

that crustal contamination has a negligible effect on He, and thus ^{4}He/^{40}Ar* is only expected to increase due to degassing effects.

In the previous section, we identified samples with CO_2 abundance and isotope characteristics that had been modified by both degassing and crustal assimilation processes. Here, we further evaluate these processes by plotting elemental ratios (Figure VI.18a-c) of various vesicle-sited volatile species (^{4}He, ^{40}Ar* and CO_2). By investigating coupled elemental ratio variations we assess the extent of solubility fractionation between different chemical species during vesicle formation (i.e., degassing). Elements are predicted to fractionate based on their relative solubility differences in basaltic melts of 2.4 (S_{He}/S_{CO2}; Hilton et al., 1998) and 4 (S_{CO2}/S_{Ar}; Cartigny et al., 2001a), resulting in an increases in ^{4}He/^{40}Ar$_*$ and CO_2/^{40}Ar$_*$ and a decrease in CO_2/^{3}He in the residual phase as degassing progresses.
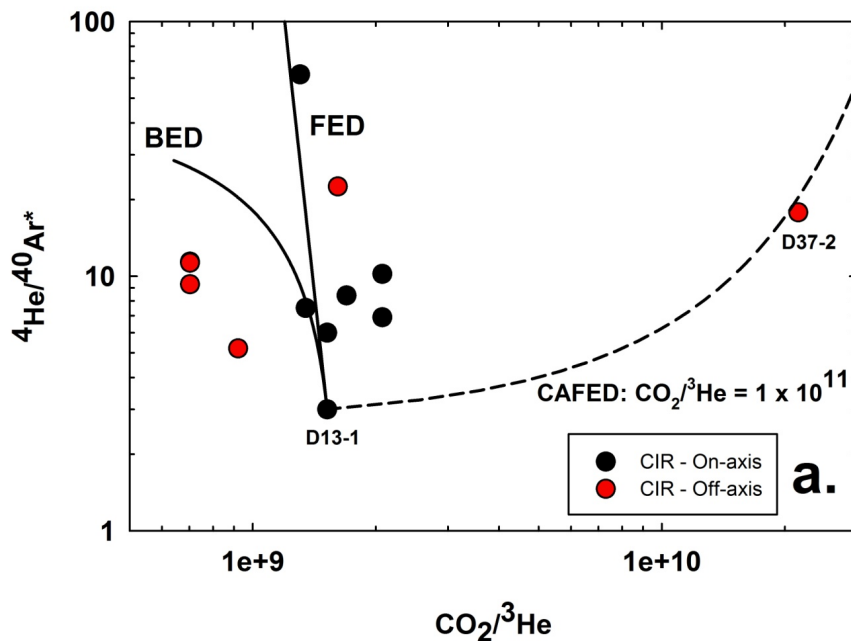
Figure VI.18: Elemental ratios for vesicle derived gases of CIR basalts. (a) – ^{4}He/^{40}Ar* versus CO_2/^{3}He (b) – CO_2/Ar* versus CO_2/^{3}He; (c) – ^{4}He/^{40}Ar* versus CO_2/Ar*. Superimposed on each subplot are equilibrium degassing trajectories (FED-BED; solid lines) and coupled assimilation fractional equilibrium degassing (CAFED; dashed lines) scenarios. The CAFED assumes 1% degassing increments from a given starting composition (e.g., D13-1), followed by addition of contaminant. CO_2/^{3}He and CO_2/Ar* values of the crustal contaminant are assumed to be enriched by a factor of ~20-350 and the ratio of assimilated CO_2 to degassed CO_2 is assumed to be the same as the enrichment factor. Following the assimilation step, the degassing step is repeated from the new starting composition.

Figure VI.18 continued
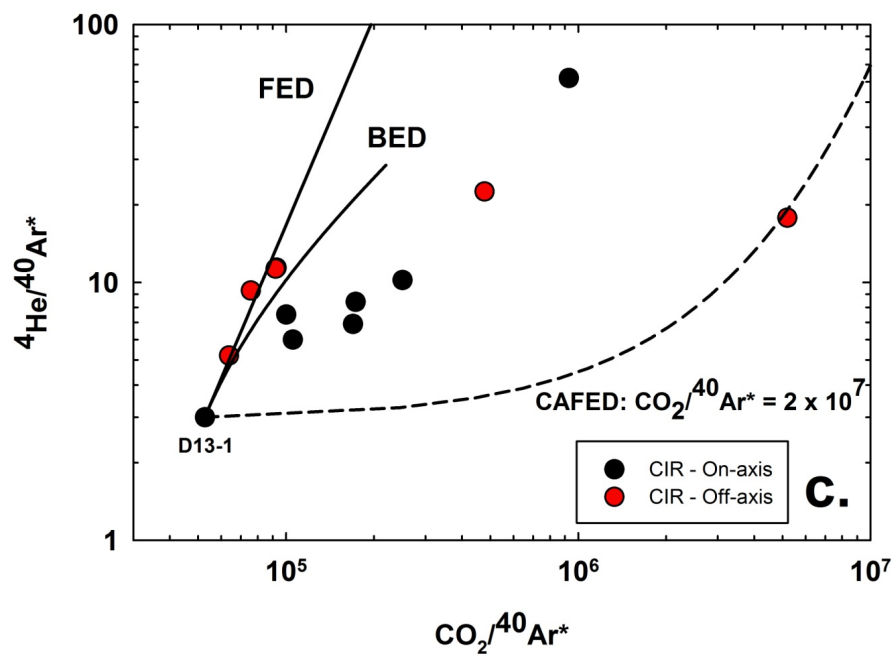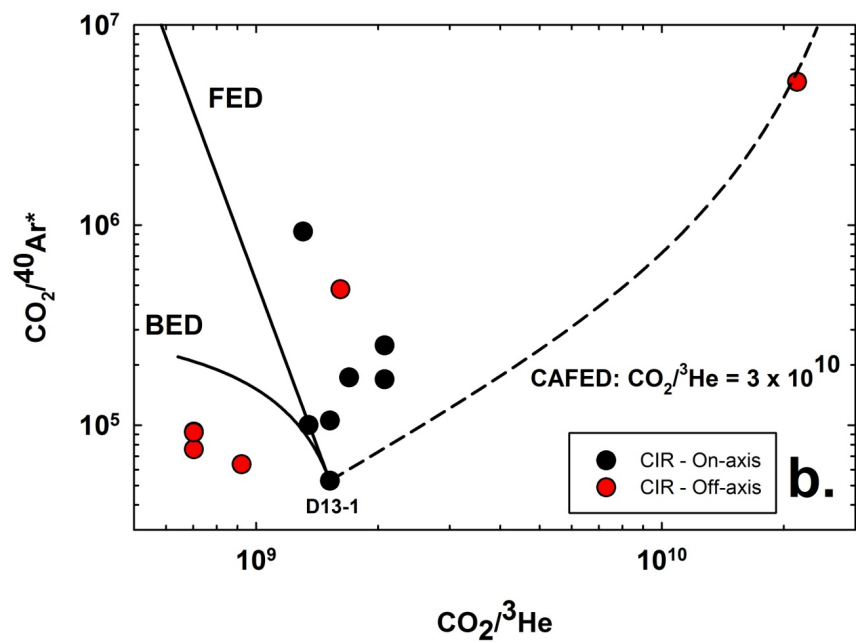
We begin by assuming that the lowest $^4He/^{40}Ar^*$ CIR sample D13-1 ($^4He/^{40}Ar^* = 3.0$;

$CO_2/^{40}Ar = 5.3 \times 10^4$; $CO_2/^3He = 1.5 \times 10^9$) can be used to approximate the least degassed

sample, and thus provide an accurate starting point to consider degassing and coupled

assimilation in CIR basalts. The observation that D13-1 is slightly higher than the mantle

production ratio of $^4He/^{40}Ar_* \sim 2$ (Jambon et al., 1986; Marty and Zimmermann, 1999),

suggests that it may have experienced some very moderate degassing, most likely during the

transfer process from the mantle source to shallower reservoirs in the crust. This assumption is

consistent with dissolved carbon isotope (-5.6 ‰) and CO_2 abundance (201.3 ppm)

systematics of D13-1 (Table VI.4), which also suggest small degrees of

degassing/modification. Using D13-1 as the starting composition, we plot BED and FED

trajectories. As degassing progresses, relative solubility differences between volatile species

causes increases in $^4He/^{40}Ar^*$ and $CO_2/^{40}Ar^*$ and a decrease in $CO_2/^3He$ in the residual phase.

As seen in Figure VI.18a-c, BED and FED degassing trajectories provide a reasonable

fit to a relatively small proportion of samples, and thus an additional process must be

considered. For example, we identify sample D37-2, which has a distinctly high $CO_2/^3He$

value of $\sim 2.2 \times 10^{10}$, accompanied by relatively low $^4He/^{40}Ar^*$ value of ~ 18 (Figure VI.18a).

Such elevated $CO_2/^3He$ values cannot be produced by degassing alone; as such a process

would require unrealistically high starting $CO_2/^3He$ values or volatile solubilities that are

considerably different than experimentally derived values. However, assimilation of crustal

material ($CO_2/^3He = 1 \times 10^{11}$, $^4He/^{40}Ar^* = 3$) could provide a mechanism to produce the values

observed in D37-2, and assimilation of a contaminant with $CO_2/^3He < 1 \times 10^{11}$ could explain

the values that plot between the FED and CAFED trajectories. Using the same approach as

was adopted in Section 5.5.2, the CAFED model assumes FED of CO_2 in 1% increments from

a given starting composition (e.g., D13-1), followed by addition of a contaminant.

Assimilation of wall-rock CO_2 into the melt during transfer to the surface would be a likely mechanism, occurring concomitantly with degassing. $CO_2/^3He$ and $CO_2/Ar*$ values of the crustal contaminant are assumed to be enriched by a factor of ~20-350, which is consistent with their crustal provenance (e.g., $CO_2/^3He = \sim 1 \times 10^{11} - 1 \times 10^{13}$; O'Nions and Oxburgh, 1988). The ratio of assimilated CO_2 to degassed CO_2 is assumed to be the same as the enrichment factor. Following assimilation, the degassing step is repeated from the new starting composition. The results of this model are plotted as dashed lines in Figures 18a-c. We conclude that CAFED is necessary to explain the majority of CIR samples and, as a result, we consider wall rock interaction as an important control on the volatile systematics of the CIR.

However, this approach does not account for low $CO_2/^3He$ values of off-axis samples (D20-5 and duplicate and D26-2), which cannot result from degassing (assuming D13-1 as the starting value) and/or through CAFED. We suggest instead that these two samples may have preferentially lost CO_2 versus He, due to formation of CO_2-rich minerals (e.g., calcite) following eruption, an observation consistent with abundant carbonate occurrence in the region (Meyers and Dickens, 1992; Dick et al., 2000). Alternatively, small heterogeneities in initial elemental ratios (i.e., a starting $CO_2/^3He$ of ~9×10^8) could explain the off-axis elemental ratio variations, however this is inconsistent with recent studies (Shaw et al., 2004) which indicate that $CO_2/^3He$ ratios of high $^3He/^4He$ mantle (i.e., $^3He/^4He$ > MORB) are equal to or greater than MORB-like values of ~2×10^9. Another possibility is that small variations in $CO_2/^3He$ (and not $^4He/^{40}Ar*$) may result from assimilation of pure CO_2 in the largest vesicles in the magma, followed by preferential selection of small vesicles in smaller pieces of glass (Hahm et al., 2012).

In summary, the elemental characteristics of vesicle-sited CO_2 and other volatiles are compatible with degassing and assimilation of crustal material in all but two off-axis samples.

We conclude that parent magma is stored in crustal magma chambers where addition of CO_2 (enriched by a factor of ~20-350) can occur, most likely due to wall rock interaction. Using this approach we are able to identify intrinsic CO_2 and relative volatile characteristics of the CIR mantle source.

VI.7 Summary and concluding remarks

In conclusion, we highlight the following points:

1) Volatiles (i.e., Ne-N-Ar-CO_2) measured in basaltic glasses of the CIR are heterogeneous with respect to both abundance and isotope characteristics, however a combined analytical approach suggests plume-ridge interaction is occurring between the Réunion hot spot and the CIR.

2) CIR samples have distinct Ne-isotope anomalies and plot intermediately between MORB and Réunion on a Ne three-isotope, suggesting a solar-derived Ne component in the CIR mantle source. Ne-He mixing relationships suggest that both a primitive/solar and MORB-like mantle components are present in the CIR mantle.

3) Nitrogen in the mantle is mostly recycled and thus N-isotopes in mantle-derived rocks are useful tracers for crustal recycling into the mantle. N-isotopes of CIR basalts range from -2.91 to +1.80 ‰ and are > MORB, suggesting that ^{15}N enriched oceanic sediments are recycled into the CIR mantle source. Ne-N mixing relationships indicate CIR basalts can be explained by mixing of a mantle component (with 20-50 % recycled sedimentary contributions) and a

relatively small (< 0.2 %) proportion of a solar component. Significantly, higher sedimentary contributions are observed in samples which show ancillary evidence (e.g., high ^{3}He/^{4}He and/or La/Sm) for plume contributions.

4) CIR basalts retain He/Ne and He/Ar characteristics of the MORB mantle. In contrast, Réunion xenoliths and one high ^{3}He/^{4}He off-axis basalt sample (D37-2) overlap with plume like values. Observed He/Ne ratios (i.e., ^{3}He/^{22}Ne$_S$ and ^{4}He/^{21}Ne$_*$) likely result from degassing processes, and elemental deviations from production ratios suggests degassing occurred recently and most likely in the upper portions of the crust.

5) The highest CO_2 concentrations (>800 ppm) were observed in on-axis CIR basalts collected just north of the Marie Celeste FZ, with lower concentrations measured along the CIR to the south and in off-axis lineaments. However, these CO_2 values represent residual traces following magmatic degassing and additions of extraneous volatiles (from air, seawater, and/or crustal contamination), which act to mask intrinsic mantle source characteristics. Using an equilibrium degassing model, we reconstruct primary CO_2 contents prior to degassing by combining constraints imposed by CO_2–δ^{13}C variations, in order to estimate primary CO_2 concentrations for the CIR mantle source (CO_2 = ~1300 ppm; δ^{13}C = -4.2 ± 0.2 ‰).

6) The observed elemental ratios (i.e., CO^2/^{3}He, CO_2/^{40}Ar* and ^{4}He/^{40}Ar*) in some CIR basalts can be explained by simple degassing from a mantle like starting composition, however a small amount of shallow level crustal contamination is required to explain several outliers. Using this approach we are able to evaluate mixing dynamics of mantle components

in the CIR-Réunion region, together with the effects of shallow level magmatic processes such as degassing and crustal assimilation.

CHAPTER VII: Concluding Remarks

This dissertation has discussed laboratory and field-based instrumentation advances as well as the origin, transport and behavior of volatiles (noble gases, CO_2 and N_2) at three different geologic settings: a) the Rungwe Volcanic Province (RVP), southern Tanzania, an area of active continental rifting, b) Iceland, a ridge-centered hotspot, and c) the Central Indian Ridge, a mid-ocean ridge segment near an off-axis hotspot.

In Chapter II, we discussed the development and initial test deployment of a syringe pump apparatus for the retrieval and temporal analysis of helium (SPARTAH). We demonstrated that the use of SPARTAH can produce time-series records of geochemical perturbations in groundwater systems and that SPARTAH provides several advantages over conventional sampling strategies, including long-term deployment and monitoring ability. The instrument requires little-to-no maintenance, and changing of Cu-coils in the field can prolong the monitoring period indefinitely. Sample resolution can be controlled by two independent parameters: (1) the withdrawal rate and/or (2) the length of Cu-tubing sectioned, and thus both short- (days to weeks) and long-term (up to 6 months) deployments can be achieved. Sampling with SPARTAH is continuous and no hiatus exists in the time record. Irrespective of the duration of a geochemical anomaly, SPARAH will capture any event, transient or long-term. For example, in the case of a seismic event occurring sometime during a SPARTAH deployment, the tubing can be subsequently collected and sectioned to reveal He isotope variations prior to, during and/or after the event. Additionally, SPARTAH reduces analytical efforts considerably in that samples of interest can be preferentially targeted for analysis. Finally, we emphasize that use of SPARTAH is not restricted to He or any other dissolved gas and can be used to investigate trace elements, stable isotopes or any other intrinsic water property of interest.

Chapter III described a newly constructed nitrogen extraction and purification system, interfaced to a noble gas VG-5440 mass spectrometer designed for simultaneous triple collection of nitrogen isotopes. We demonstrated the advantages provided by our new extraction system when used in conjunction with a static triple collection technique. Triple collection improved overall precision by enabling shorter analytical times, thus allowing standards and samples to be better characterized prior to sample measurement. Moreover, shorter analytical times helped minimize sample depletion and memory effects in the mass spectrometer. We also carried out an individual CO and blank correction on all runs, improving both precision on individual measurements and accuracy of results. The new system was tested with a series of oceanic basalts, which were analyzed for $\delta^{15}N$, N_2 concentration and N_2/Ar ratios. Based on these results, we concluded that static triple collection, utilizing simultaneous-collection on two Faraday and one Daly collector, provides clear advantages over peak jumping methods as is demonstrated by the highly reproducible nature of both internal and external standards as well as unknowns (i.e., samples).

Our study of He-CO_2 isotope and abundance characteristics at Rungwe Volcanic Province (RVP; Chapter IV) demonstrated that RVP fluids and gases are characterized by a wide range of $^3He/^4He$ and $CO_2/^3He$ ratios, and a narrow range in $\delta^{13}C$ (CO_2) values, reflecting variable mantle and crustal contributions. We showed that phase-separation within the hydrothermal system has a clear influence on fluid-phase samples and likely exerts the principal control on $CO_2/^3He$ ratios and $\delta^{13}C$ values. Fluid samples are particularly susceptible to radiogenic helium additions following gas (He) loss and subsequent ^4He addition due to prolonged interaction with the crust during fluid transport. A somewhat surprising finding of the study was that several cold CO_2 mazuku-like gas vents display He-CO_2 characteristics typical of MORB/SCLM. The low temperatures, rarity, and occurrence of mazuku at stratigraphic contacts, suggests that they may be derived from an isolated source that is

decoupled from the modern hydrothermal system. In addition, we used a $CO_2/^3He$–$\delta^{13}C$ model to quantitatively assess mantle and crustal CO_2 budgets and calculate CO_2 fluxes for fluid samples. We suggest that the extent of crustal contamination in samples is regionally controlled by proximity to volcanic edifices and extent of hydrothermal interaction; however, rift zone evolution (e.g., stage of rifting) also heavily influences observed regional trends as it acts to control the extent of ^4He addition from old, He-rich reservoir rocks. Finally, we concluded that the apparent He-isotope disparity between mafic phenocrysts and hydrothermal fluids does not exist on small spatial scales and that the absence of hydrothermal manifestations and/or mazuku-like features in close proximity to high $^3He/^4He$ phenocryst localities is a possible explanation for this apparent He-isotope disparity at RVP.

Chapter V examined the CO_2 systematics (isotope and relative abundance characteristics) of geothermal fluids and subglacial glasses from Iceland. Crustal assimilation appears to be ubiquitous in all geothermal fluid and gas samples and in some basalt samples. Significantly, basalts are modified by a ^{13}C-depleted (organic/sedimentary) component – presumably at depth, whereas geothermal fluids and gases are primarily affected by a limestone-like contaminant, with $\delta^{13}C$ close to ~ 0 ‰. Low-temperature (LT) off-axis samples are more significantly fractionated (i.e., lower $\delta^{13}C$ and $CO_2/^3He$) vs. high-temperature (HT) axial rift zone samples, which generally display the highest $CO_2/^3He$ values measured. Modified $\delta^{13}C$ and $CO_2/^3He$ characteristics in LT areas were attributed to calcite precipitation. At localities where both fluid and gas phases were collected, fluid samples displayed 6 to 450 times higher $CO_2/^3He$ values vs. gas phases, suggesting that Eastern Rift Zone (ERZ) fluid samples have been modified by hydrothermal phase separation processes. Using subglacial basalt data, we calculated pre-eruptive CO_2 source estimates of ~531 ± 64 (ppm) and pre-eruptive $\delta^{13}C$ (δ_p) estimates of -2.5 ± 1.1 ‰, both consistent with previous E-MORB/plume endmember estimates. Furthermore, elemental ratio variations (i.e., $CO_2/^3He$; $^4He/^{40}Ar*$;

$CO_2/^{40}Ar*$) can be explained by degassing and assimilation of crustal material. Finally, CO_2 flux estimates were made using three independent approaches. The first two approaches produced an estimate between $2 - 23 \times 10^{10}$ mol a^{-1} for the whole of Iceland and the third approach was used to approximate the CO_2 output from the Köldukvíslabotnar region (ERZ), producing a CO_2 flux of ~ of 0.9-1.8×10^8 mol a^{-1} – consistent with estimates from other geothermal/volcanic regions of Iceland.

Chapter VI investigated plume-ridge interaction between the Central Indian Ridge (CIR) and the Réunion hotspot. We measured stable isotope (C-N) and noble gas (Ne-Ar) characteristics in basalts collected on the CIR spreading axis between 17 ºS and 21 ºS, and along the adjacent Gasitao, Three Magi, and Rodrigues ridges to the west of the CIR. We demonstrated that CIR samples have distinct Ne-isotope anomalies and plot intermediately between MORB and Réunion on a Ne three-isotope, suggesting a solar-derived Ne component in the CIR mantle source. Ne-He mixing relationships suggest that both a primitive/solar and MORB-like mantle components occur in the CIR mantle. Coupled Ne-N mixing relationships indicate CIR basalts can be explained by mixing of a mantle component (with 20-50 % recycled sedimentary contributions) and a relatively small (< 0.2 %) proportion of a solar component. CIR basalts retain He/Ne and He/Ar elemental characteristics of the MORB mantle. In contrast, Réunion xenoliths and a single high ^{3}He/^{4}He off-axis basalt sample overlap with plume-like values. Observed He/Ne ratios likely result from degassing processes, and elemental deviations from production ratios suggests degassing occurred recently and most likely in the upper portions of the crust. Using an equilibrium degassing model, we reconstruct primary CO_2 contents prior to degassing by combining constraints imposed by CO_2–$\delta^{13}C$ variations and estimated primary CO_2 concentrations for the CIR mantle source (CO_2 = ~1300 ppm; $\delta^{13}C$ = -4.2 ± 0.2 ‰). In addition, we explained elemental ratio variations

by simple degassing from a mantle-like starting composition, together with a small amount of shallow level crustal contamination.

Finally, we briefly discuss some possible directions of future work. A considerable amount of this dissertation focused on field and laboratory instrumentation developments and, as a result, we have opened the door to numerous possibilities for future research. However, there is still a significant amount of work to be done to ensure that the capabilities of these systems are fully utilized in the future. Furthermore, as we gain a better understanding about volatile source features and geochemical behavior, we are able to identify uncertainties in many of the assumptions, which are build into our models. For example, the latter two chapters depend heavily on experimental volatile solubility coefficients and isotopic fractionation factors as well as assumptions about endmember compositions in the mantle. Better constraints on these parameters will enable more robust geochemical studies in the future and help geochemists more accurately interpret isotope and relative abundance results.

In Chapter II (reprint of Barry et al., 2009), we argue that SPARTAH has the potential to revolutionize the approach to time-series geochemical monitoring. In this initial study, we successfully completed two test deployments in San Bernardino, California and Selfoss, Iceland and demonstrated the capabilities of SPARTAH for capturing all geochemical perturbations, irrespective of deployment duration. Following the initial test period, SPARTAH has been deployed in two locations along the San Jacinto Fault for the past three years, both within the city of San Bernardino, California. However, in order to increase the likelihood of detecting a geochemical anomaly related to seismic activity, the distribution of SPARTAH devices must be expanded. To this end, plans are currently in place to deploy SPARTAH in two additional seismically-active regions of California as well as in the seismogenic forearc region of Costa Rica, in order to determine temporal patterns of He and

CO_2. The aims of these studies will be to ascertain if dissolved He and CO_2 respond to any crustal disturbances and/or seismic activity. Previous studies at Kobe, Japan (Sano et al., 1998), the Georgian Caucasus (Areshidze et al., 1992), the North Anatolian Fault in Turkey (de Leeuw et al., 2010), Oshima Volcano, Japan (Sano et al., 1995), and Umbria-Marche, Italy (Italiano et al., 2001) are examples where monitoring of helium trends in aqueous fluids has identified stress readjustments in aquifers, resulting in changes in fluid provenance, mixing and/or flow histories related to specific seismic events. As a result, we view these localities as potentially ideal locations for future deployments of SPARTAH.

In Chapter III (reprint of Barry et al., 2012a), we describe a newly constructed N_2 extraction and purification system as well as the simultaneous triple collection technique employed for measuring nitrogen isotopes. With the addition of this system, the Fluids and Volatiles Laboratory at SIO has become the only US-based laboratory measuring N-isotopes in such low concentration rock samples, and one of just a handful world-wide with these capabilities. Through continued use and additional refinement to the system, we intend to further improve analytical and procedural blanks associated with the line. The biggest challenge moving forward will be measuring N-isotopes in phenocrysts and xenoliths, which contain extremely small amounts of N_2 – a feat that will require extremely low background levels. To date, only a single study (Fischer et al., 2005) has reported N-isotope data from mantle-derived mineral separates, thus there is enormous potential for future studies. We will be able to better characterize distinct regions of Earth's mantle and address fundamental questions in isotope geochemistry. For example, due to the recycled nature of nitrogen in the mantle, we plan to characterize mantle-derived samples that show ancillary evidence for recycled components in their mantle source. This work will form the basis of my postdoctoral research, which is slated to occur at SIO over the next two years.

Chapters V and VI utilize coupled assimilation and fractional equilibrium degassing (CAFED) models which rely heavily on experimentally-derived solubility and isotopic fractionation coefficients. However, uncertainties associated with the determination of experimentally-derived solubility coefficients can potentially result in significant changes to model predictions. Such uncertainties could result from compositional differences between magmas, speciation differences, as well as temperature and pressure variations. As a result, more solubility coefficient data is essential if realistic models of the distribution and transport of mantle noble gases are to be constructed (Jambon et al., 1986; Lux et al., 1987; Pan et al., 1991; Dixon and Stolper, 1995; Jendrzejewski et al., 1997; Hilton et al., 1998a; Cartigny et al., 2001a). Similarly, the predicted isotopic fractionation between ^{13}C and ^{12}C during degassing and/or in the hydrothermal system will vary depending on the fractionation factor that is employed (Bottinga, 1969; Vogel, 1970; Mook, 1974; Drever, 1982; Szaran, 1997). Carbon-isotope fractionation factors are also experimentally-derived and subject to the same uncertainties as mentioned above. For example, carbon isotope fractionation in hydrothermal systems is highly temperature dependent. Continued experimental work in these fields will allow geochemists to refine their modeling techniques and better explain their data.

In addition, there is on-going debate regarding the source of solar-like components in Earth's mantle. For example, the solar Ne component could be derived from solar nebula gas (Benkert et al., 1993; Kallenbach et al., 1997) or, alternatively, implanted solar wind, (e.g., Ne- B), sampled by gas-rich meteorites and in lunar soils (Black, 1972; Trieloff et al., 2000; Trieloff et al., 2002; Ballentine et al., 2005). Similar debates are also on-going with regard to which primitive/solar He- and N-isotope endmember component is most appropriate. Model results will vary significantly if proto-solar He-isotope values of 120 R_A (Mahaffy et al., 1998) are selected as opposed to meteoritic ratios of 280 R_A (Black, 1972). With regard to nitrogen isotopes, Javoy et al. (1986) suggested that the composition of Earth's mantle can be

explained by accretion of enstatite chondrite material surrounded by a small veneer (< 1-2% of

the upper mantle's mass) of C1- or C2-type chondrite material. More recently, Marty (2012)

suggested a solar N component may be present in Earth's mantle, following measurement of

highly depleted ^{15}N values in Genesis solar wind samples (Marty et al., 2011). Significantly,

the solar N hypothesis is consistent with the occurrence of solar-Ne in the mantle, and thus, is

the preferred endmember component used in this dissertation.

REFERENCES

Agustsdottir A. M., Brantley S. L. (1994) Volatile fluxes integrated over four decades at Grímsvötn volcano, Iceland. *J. Geophys. Res.* 99 (B5), 9505–9522.

Allard P., Carbonelle J., Dajlevic D., Le Bronec J., Morel P., Robe M. C., Maurenas J. M., Faivre-Pierret R., Martin D., Sabroux J. C., Zettwoog P. (1991) Eruptive and diffuse emissions of CO_2 from Mount Etna. *Nature* 351, 387-391.

Allègre C. J., Hart S. R., Minster J. F. (1983) Chemical structure and evolution of the mantle and continents determined by inversion of Nd and the Sr isotope data, I. Theoretical methods. *Earth. Planet. Sci. Lett.,* 66, 177–190.

Allègre C. J., Dupré B., Lewin E. (1986) Thorium/uranium ratio of the Earth *Chem Geol* 56:219-227.

Areshidze G., Bella F., Biagi P. F., Caputo M., Della Monica G., Ermini A., Manjgaladze P., Melikadze G., Sgrigna V., Zilpimiani D. (1992) Anomalies in geophysical and geochemical parameters revealed on the occasion of the Paravani (M = 5.6) and Spitak (M = 6.9) earthquakes (Caucasus), *Tectonophysics*, 202, 23 – 41, doi:10.1016/ 0040-1951(92)90453-D.

Armannsson H., Gislason G., Torfason H. (1986) Surface exploration of the Theistareykir high-temperature geothermal area, Iceland, with special reference to the application of geochemical methods. *Appl. Geochem.* 1, 47-64.

Armannsson H. (1991) Geothermal energy and the environment. In: Geoscience Society of Iceland. *Conference on Geology and Environmental Matters. Programme and Abstracts*, pp. 16–17.

Armannsson H. (1998) Oxarfjordur. Studies of Gas. *Orkustofnun* OS-98051, p. 14.

Armannsson H., Fridriksson T., Kristjansson B. R. (2005) CO_2 emissions from geothermal power plants and natural geothermal activity in Iceland. *Geothermics*, 34, 286–96.

Arnórsson S., Gıslason S. R. (1994) CO_2 from magmatic sources in Iceland. *Mineralogical Magazine* 58A, 27–28.

Arnórsson S. (1995) Geothermal systems in Iceland: Structure and conceptual models-II: Low temperature areas. *Geothermics* 24, 603–629.

Arnórsson S., Axelsson G., Sæmundsson K. (2008) Geothermal systems in Iceland. *Jökull*, 58, 269-302.

Ballentine C. J., Barfod D. N. (2000) The origin of air-like noble gases in MORB and OIB. *Earth Planet. Sci. Lett.* 180, 39–48.

Ballentine C. J., Marty B., Lollar B. S., Cassidy M. (2005) Neon isotopes constrain convection and volatile origin in the Earth's mantle. *Nature* 433, 33–38.

Barry P. H., Hilton D. R., Tryon M. D., Brown K. M., Kulongoski J. T. (2009) A new syringe pump apparatus for the retrieval and temporal analysis of helium in groundwaters and geothermal fluids. *Geochem. Geophys. Geosys: Technical Brief, 10,* Q05004, doi:10.1029/2009GC002422.

Barry P. H., Hilton D. R., Halldórsson S. A., Hahm D., Marti K. (2012a) High precision nitrogen isotope measurements in oceanic basalts using a static triple collection noble gas mass spectrometer. *Geochem. Geophys. Geosyst*: *Technical Brief,* 13, Q01019.

Barry, P. H., Hilton, D. R., Fischer, T. P., de Moor, J. M., Mangasini, F., Ramirez, C. (2012b) Helium and carbon isotope systematics of cold "mazuku" CO_2 vents and hydrothermal gases and fluids from Rungwe Volcanic Province, southern Tanzania. *Chemical Geology.* doi: http://dx.doi.org/10.1016/j.chemgeo.2012.07.003.

Benkert J. P., Baur H., Signer P., Wieler R. (1993) He, Ne, and Ar from the solar-wind and solar energetic particles in lunar ilmenites and pyroxenes. *J. Geophys. Res. – Planets* 98, 13147–13162.

Bianchi D., Sarmiento J. L., Gnanadesikan A., Key R. M., Schlosser P., Newton R. (2010) Low helium flux from the mantle inferred from simulations of oceanic helium isotope data, *Earth Planet. Sci. Lett.*, 297, 379-386.

Bijwaard H., Spakman W. (1999) Tomographic evidence for a narrow whole mantle plume below Iceland, *Earth Planet. Sci. Lett.,* 166 121-126.

Bjarnason I. T., Menke W., Flovenz O. G., Caress D. (1993) Tomographic image of the Mid-Atlantic plate boundary in southwestern Iceland. *J. Geophys. Res.* 98 (B4), 6607–6622.

Bjarnason I. T., Wolfe C. J., Solomon S. C. (1996) Initial results from the ICEMELT experiment: Body-wave delay times and shear-wave splitting across Iceland, *Geophys. Res. Lett.* 23, 459-462, 1996.

Bjornsson A. (1985) Dynamics of crustal rifting in Iceland. *J. Geophys. Res.* 90, 151–162.

Black D. C. (1972) On the origins of trapped helium, neon and argon isotopic variations in meteorites – I. Gas-rich meteorites, lunar soil and breccia. *Geochim. Cosmochim. Acta* 36, 347–375.

Bodvarsson G. (1961) Physical characteristics of natural heat resources in Iceland. *Jökull.* 11, 29-38.

Bottinga Y. (1969) Calculated fractionation factors for carbon and hydrogen isotope exchange in the system calcite–CO_2 –graphite–methane–hydrogen and water vapour. *Geochim. Cosmochim. Acta* 33, 49–64.

Bottinga Y., Javoy M. (1989) MORB degassing: evolution of CO_2. *Earth Planet. Sci. Lett.* 95, 215–225.

Boyd S. R., Mattey D. P., Pillinger C. T., Milledge H. J., Mendelssohn M., Seal M. (1987) Multiple growth events during diamond genesis: an integrated study of carbon and nitrogen isotopes and nitrogen aggregation state in coated stones *Earth Planet. Sci. Lett.*, 86, 341‑353.

Boyd S. R., Wright I. P., Franchi I. A., Pillinger C. T. (1988) Preparation of sub-nanomole quantities of nitrogen gas for stable isotopic analysis, *J. Phys. E Sci. Instrum.,* 21, 876–885, doi:10.1088/0022-3735/21/9/012.

Boyd S. R., Wright I. P., Pillinger C. T. (1993) Accurate determination of nitrogen concentrations by static vacuum mass spectrometry, *Meas. Sci. Technol.,* 4, 1000–1005, doi:10.1088/0957-0233/4/9/014.

Boyd S. R., Philippot P. (1998) Precambrian ammonium biogeochemistry: A study of the Moine metasediments, Scotland, *Chem. Geol.,* 144, 257–268, doi:10.1016/S0009-2541(97)00135-6.

Brantley S. L., Koepenick K. W. (1995) Measured carbon dioxide emissions from Oldoinyo Lengai and the skewed distribution of passive volcanic fluxes, *Geology* 23, 933–936.

Breddam K., Kurz M. D., Storey M. (2000) Mapping out the conduit of the Iceland mantle plume with helium isotopes. *Earth Planet. Sci. Lett.* 176(1), 45–55.

Burbidge E. M., Burbidge G. R., Fowler W. A., Hoyle F. (1957) Synthesis of the elements in stars. *Revs. Mod. Phys.* 29, 547-650.

Bureau H., Pineau F., Métrich N., Semet M. P., Javoy M. (1998) A melt and fluid inclusion study of the gas phase at Piton de la Fournaise volcano (Réunion Island). *Chem Geol.* 147, 115-130.

Bureau H., Métrich N., Semet M. P., Staudacher T. (1999) Fluid-magma decoupling in a hot-spot volcano. *Geoph. Res. Lett.* 26, 3501-3504.

Burnard P., Graham D., Turner G. (1997) Vesicle-specific noble gas analyses of "popping rock": implications for primordial noble gases in Earth. *Science* 276, 568–571.

Burnard P., Harrison D. (2005) Argon isotope constraints on modification of oxygen isotopes in Iceland Basalts by surficial processes. *Chem. Geol.* 216, 143–156.

Busigny V., Ader M., Cartigny P. (2005a) Quantification and isotopic analysis of nitrogen in rocks at the ppm level using tube combustion technique: A prelude to the study of altered oceanic crust. *Chem. Geol.*, 223, 249–258, doi:10.1016/j.chemgeo.2005.08.002.

Busigny V., Laverne C., Bonifacie M. (2005b) Nitrogen content and isotopic composition of oceanic crust at a superfast spreading ridge: a profile in altered basalts from ODP Site 1256, Leg 206. *Geochem. Geophys. Geosyst.* 6, Q12O01. doi:10.1029/2005GC001020.

Cartigny P., Boyd S. R., Harris J. W., Javoy M. (1997) Nitrogen isotopes in peridotitic diamonds from Fuxian, China: The mantle signature, *Terra Nova*, 9, 175–179, doi:10.1046/j.1365-3121.1997.d01-26.x.

Cartigny P., Harris J. W., Phillips D., Girard M., Javoy M. (1998a) Subduction-related diamonds? The evidence for a mantle-derived origin from coupled $\delta^{13}C$ - $\delta^{15}N$ determinations. *Chem. Geol.* 147, 147-159.

Cartigny P., Harris J. W., Javoy M. (1998b) Eclogitic diamond formation at Jwaneng: no room for a recycled component, *Science* 280, 1421-1424, 1998b.

Cartigny P., Jendrzejewski N., Pineau F., Petit E., Javoy M. (2001a) Volatile (C, N, Ar) variability in MORB and the respective roles of mantle source heterogeneity and degassing: the case of the Southwest Indian Ridge. *Earth Planet. Sci. Lett.* 194, 241–257.

Cartigny P., Harris J. W., Javoy M. (2001b) Diamond genesis, mantle fractionations and mantle nitrogen content: A study of $\delta^{13}C$-N concentrations in diamonds, *Earth Planet. Sci. Lett.*, 185, 85–98, doi:10.1016/S0012-821X(00)00357-5.

Chang S., Lawless J., Romiez M., Kaplan I. R., Petrowski C., Sakai H., Smith J. W. (1974) Carbon, nitrogen and sulfur in lunar fines 15012 and 15013: Abundances, distributions and isotopic composition, *Geochim. Cosmochim. Acta*, 38, 853–872, doi:10.1016/0016-7037(74)90060-X.

Chauvel C., Hemond C. (2000) Melting of a complete section of recycled oceanic crust: trace element and Pb isotopic evidence from Iceland. *Geochem. Geophys. Geosyst.* 1(2), 1001, doi:10.1029/1999GC000002.

Chiodini G., Cioni R., Guidi M., Raco B., Marini L. (1998) Soil CO_2 flux measurements in volcanic and geothermal areas. *Appl. Geochem.* 13, 543–552.

Condomines M., Grönvold K., Hooker P. J., Muehlenbachs K., O'Nions R. K., Oskarsson N., Oxburgh E. R. (1983) Helium, oxygen and strontium isotopic relationships in Icelandic volcanics. *Earth Planet. Sci. Lett.* 66, 125–136.

Craig H., Clarke W. B., Beg M. A. (1975) Excess ^{3}He in deep water on the East Pacific Rise. *Earth Planet. Sci. Lett.* 26, 125–132.

Craig H., Marti K., Wiens R. (1993) A Static Mass Spectrometer With Triple Collection for Nitrogen and Neon Isotopes, *SIO Reference Ser.*, vol. 93-11, pp. 1–20A, Scripps Inst. of Oceanogr., La Jolla, Calif.

Crisp J. A. (1984) Rates of magma emplacement and volcanic output. *J. Volcanol. Geotherm. Res.*, 20: 177-212.

Darbyshire F. A., White R. S., Priestley K. F. (2000) Structure of the crust and uppermost mantle of Iceland from a combined seismic and gravity study, *Earth Planet. Sci. Lett.* 181 409–428.

Dasgupta R., Hirschmann, M. M. (2010) The deep carbon cycle and melting in Earth's interior. *Earth Planet. Sci. Lett.* 298 (1–2), 1–13.

Dauphas N., Marty B. (1999) Heavy nitrogen in carbonatites of the Kola Peninsula: A possible signature of the deep mantle. *Science* 286, 2488–2490.

Day J. M. D., Pearson D. G., Macpherson C. G., Lowry D., Carracedo J. C. (2009) Pyroxenite-rich mantle formed by recycled oceanic lithosphere: Oxygen-osmium isotope evidence from Canary Island lavas. *Geology* 37, 555-558.

de Leeuw G. A. M. (2007) The noble gas and carbon systematics of divergent, convergent and strike-slip plate boundaries: examples from the Reykjanes Ridge, Central American Arc and North Anatolian Fault Zone. Ph.D. thesis, University of California, San Diego.

de Leeuw G. A. M., Hilton D. R., Gulec N. Mutlu H. (2010) Regional and temporal variations in $CO_2/^3He$, $^3He/^4He$ and $\delta^{13}C$ along the North Anatolian Fault Zone, Turkey. *Appl Geochem* 25: 524–539.

Delaney J. R., Muenow D. W., Graham D. G. (1978) Abundance and distribution of water, carbon and sulfur in the glassy rims of submarine pillow basalts. *Geochim. Cosmochim. Acta.* 42, 581–594.

Delgado H., Piedad-Sanchez N., Galvian L., Julio P., Alvarez J. M., Cardenas L. (1998) CO_2 flux measurements at Popocatepetl volcano: II. Magnitude of emissions and significance *(AGU abstract). EOS Trans.* 79 (45), 926.

Des Marais D. J. (1978) Variable-temperature cryogenic trap for the separation of gas mixtures. *Anal. Che.* 50, 1405–1406.

Des Marais D. J., Moore G. (1984) Carbon and its isotopes in mid-oceanic basaltic glasses. *Earth Planet. Sci. Lett*. 69, 43-57.

Dick H. J. B., Natland J. H., Alt J. C., Bach W., Bideau D., Gee J. S., Haggas S., Hertogen J. G. H., Hirth G., Holm P. M., Ildefonse B., Iturrino G. J., John B. E., Kelley D. S., Kikawa E., Kingdon A., LeRoux P. J., Maeda J., Meyer P. S., Miller D. J., Naslund H. R., Niu Y.-L., Robinson P. T., Snow J., Stephen R. A., Trimby P. W., Worm H.-U., Yoshinobu A. (2000) A long in situ section of the lower ocean crust: results of ODP Leg 176 drilling at the Southwest Indian Ridge. *Earth Planet. Sci. Lett.* 179, 31-51.

Dickin A. P. 2005 Neon. *Radiogenic isotope geology*. p. 303. ISBN 978-0-521-82316-6.

Dixon E. T., Honda M., McDougall I., Campbell I. H. and Sigurdsson I. (2000) Preservation of near-solar neon isotopic ratios in Icelandic basalts. *Earth Planet. Sci. Lett.* 180(3–4), 309–324.

Dixon E. T. (2003) Interpretation of helium and neon isotopic heterogeneity in Icelandic basalts. *Earth Planet. Sci. Lett.* 206 (1–2), 83–99.

Dixon J. E., Stolper E. M., Delaney, J. R. (1988) Infrared spectroscopic measurements of CO_2 and H_2O in Juan de Fuca Ridge basaltic glasses. *Earth Planet. Sci. Lett.* 90, 87–104.

Dixon J. E., Stolper E. M., Holloway J. R. (1995) An experimental study of water and carbon dioxide solubilities in mid-ocean ridge basaltic liquids: Part I. Calibration and solubility models. *J. Petrol.* 36, 1607–1631.

Dixon J. E., Clague D. A., Cousens B., Monsalve M. L., Uhl J. (2008) Carbonatite and silicate melt metasomatism of the mantle surrounding the Hawaiian plume: Evidence from volatiles, trace elements, and radiogenic isotopes in rejuvenated-stage lavas from Niihau, Hawaii. *Geochem. Geophys. Geosyst*. 9, Q09005.

Drever, J. I. (1982) *The Geochemistry of Natural Waters.* Prentice-Hall, Inc., Englewood Cliffs, NJ.

Duncan R. A., Backman J., Peterson L., and The Shipboard Scientific Party (1989) Réunion hotspot activitity through tertiary time: Initial results from the ocean drilling program, leg 115. *J. Volcanol. Geotherm. Res* 36, 193-198.

Duncan R. A., Backman J., and Peterson L. (1990) The volcanic record of the Réunion hot spot, Proc. *Ocean Drill. Program Sci. Results* 115, 3–10.

Dyment, J., Gallet Y., and the Magofond 2 Scientific Party (1999) The Magofond 2 cruise: A surface and deep tow survey on the past and present Central Indian Ridge. *InterRidge News* 8, 25–31.

Dyment J., Hémond C., and the Gimnaut Scientific Party (2000) Deep-sea exploration of the Central Indian Ridge at 19°S. *InterRidge News* 9, 29–32.

Dyment J., Lin J., Baker E. T. (2007) Ridge-hotspot interactions: what mid-ocean ridges tell us about deep Earth processes. *Oceanography* 20, 102-115.

Einarsson T., Albertsson K. J. (1988) The glacial history of Iceland during the past three milion years, *Philosophical Transactions of the Royal Society of London*, 318, 637-644.

Einarsson P. (2008) Plate boundaries, rifts and transform zones in Iceland. *Jökull* 58, 35–58.

Exley R. A., Mattey D. P., Clague D. A., Pillinger C. T. (1986) Carbon isotope systematic of a mantle hotspot: A comparison of Loihi seamount and MORB glasses. *Earth Planet. Sci. Lett.* 78, 189–199.

Farley K. A., Craig H. (1994) Atmospheric argon contamination of ocean island basalt olivine phenocrysts. *Geochim. Cosmochim. Acta*. 58, 2509–2517.

Farley K. A., Maier-Reimer E., Schlosser P., Broecker W. S. (1995) Constraints on mantle ^{3}He fluxes and deep-sea circulation from an oceanic general circulation model, *J. Geophys. res.*, 100, 3829-3839.

Fine G., Stolper E. (1986) Dissolved carbon dioxide in basaltic glasses: Concentration and speciation, *Earth Planet. Sci. Lett.*, 76 (3‑4), 263‑278, doi:10.1016/0012-821X(86) 90078-6.

Fischer T. P., Takahata N., Sano Y., Sumino H., Hilton D. R. (2005) Nitrogen isotopes of the mantle: Insights from mineral separates. *Geophys. Res. Lett*. 32, L11305.

Fisk M. R., Storrie-Lombardi M. C., Douglas S., Popa R., McDonald G., Di Meo-Savoie C. (2003) Evidence of biological activity in Hawaiian subsurface basalts, *Geochem. Geophys. Geosyst.* 4 2003GC000387.

Fitton J. G., Saunders A. D., Kempton P. D., Hardarson B. S. (2003) Does depleted mantle form an intrinsic part of the Iceland plume? *Geochem. Geophys. Geosyst*. 4, 1032. doi:10.1029/2002GC000424.

Flower M. F. J., Pritchard R. G., Brem G., Cann J. R., Delaney J., Emmermann R., Gibson I. L., Oakley P. J., Robinson P. T., Schmincke H. U. (1982) Chemical stratigraphy, Iceland

Research Drilling Project Reydarfjordur, eastern Iceland. *Journal of Geophysical Research*, 87 B, 6489– 6510.

Foulger G. R., Pritchard M. J., Julian B. R., Evans J. R., Allen R. M., Nolet G., Morgan W. J., Bergsson B. H., Erlendsson P., Jakobsdottir S., Ragnarsson S., Stefansson R. and Vogfjord K. (2000) The seismic anomaly beneath Iceland extends down to the mantle transition zone and no deeper. *Geophys. J. Int.* 142(3), F1–F5.

Foulger G. R., Pritchard M. J., Julian B. R., Evans J. R., Allen R. M., Nolet G., Morgan W. J., Bergsson B. H., Erlendsson P., Jakobsdottir S., Ragnarsson S., Stefansson R., and Vogfjord K. (2001) Seismic tomography shows that upwelling beneath Iceland is confined to the upper mantle. *Geophys. J. Int*. 146, 504–530.

Fretzdorff S., Haase K. M. (2002) Geochemistry and petrology of lavas from the submarine flanks of Réunion Island (western Indian Ocean): implications for magma genesis and the mantle source. *Min. and Petr*. 75, 153-184.

Frick U., Pepin R. O. (1981) Microanalysis of nitrogen isotope abundances: Association of nitrogen with noble gas carriers in Allende, *Earth Planet. Sci. Lett.,* 56, 64–81, doi:10.1016/0012-821X(81)90117-5.

Fridleifsson I. B. (1979) Geothermal activity in Iceland. *Jökull* 29, 47-56.

Friedlingstein P., Houghton R. A., Marland G., Hackler J., Boden T. A., Conway T. J. (2010) Update on CO_2 emissions. *Nature Geoscience* 3 (12), 811-812.

Fridriksson T., Kristjansson B. R., Armannsson H., Margretardottir E. O., Lafsdottir S., Chiodini G. (2006) CO_2 emissions and heat flow through soil, fumaroles, and steam heated mud pools at the Reykjanes geothermal area, SW Iceland. *Appl. Geochem.* 21, 1551–1569.

Füri E., Hilton D. R., and the KNOX11RR Scientific Party (2008) Sampling and surveying ridge-hot spot interaction on the Central Indian Ridge, 19°S: Cruise KNOX11RR. *InterRidge News* 17, 28–29.

Füri E., Hilton D. R., Halldórsson S. A., Barry P. H., Hahm D., Fischer T. P., and Grönvold K. (2010) Apparent decoupling of the He and Ne isotope systematics of the Icelandic mantle: the role of He depletion, melt mixing, degassing fractionation and air interaction. *Geochim. Cosmochim. Acta* 74, 3307–3332.

Füri E., Hilton D. R., Murton B. J., Hemond C., Dyment J., Day J. M. D. (2011) Helium isotope variations between Réunion Island and the Central Indian Ridge (17˚-21˚S): new evidence for ridge-hotspot interaction. *Journal of Geophysical Research – Solid Earth* 116, B02207.

Garcia M. O., Rubin K. H., Norman M. D., Rhodes J. M., Graham D. W., Muenow D. W., Spencer K. (1998) Petrology and geochronology of basalt breccia from the 1996 earthquake swarm of Loihi seamount, Hawaii: magmatic history of its 1996 eruption. *Bull Volcanol.* 59, 577–592.

Geirsdottir A., Eiriksson J. (1994) Growth of an intermittent ice sheet in Iceland during the Late Pliocene and Early Pleistocene, *Quaternary Research*, 42, 115-130.

Gerlach T. M., Graeber E. J. (1985) Volatile budget of Kilauea volcano, *Nature*, 313, 273.

Gerlach T. M. and Taylor B. E. (1990) Carbon isotope constraints on degassing of carbon dioxide from Kilauea volcano. *Geochim. Cosmochim. Acta* 54, 2051–2058.

Gerlach T. M. (1991) Etna's greenhouse pump. *Nature* 315, 352–353.

Gerlach T. (2011) Volcanic versus anthropogenic carbon dioxide. *EOS.* 92, 201–202.

Gillot P. Y., Nativel P. (1989) Eruptive history of the Piton de la Fournaise volcano, Réunion, Indian Ocean. *J. Volcanol. Geotherm. Res.* 36, 53–65.

Gislason S. R. (2000) Carbon dioxide from Eyjafjallajökull and Chemical Composition of Spring Water and River Water in the Eyjafjallajökull –Myrdalsjökull region. *Science Institute, University of Iceland, Report* RH-06- 2000, p. 40.

Gislason S. R., Andresdottir A., Sveinbjornsdottir, A. E., Oskarsson N., Thordarson Th., Torssander, Novak M., Zak K. (1992) Local effects of volcanoes on the hydrosphere: example from Hekla, southern Iceland. In: Kharaka, Y.K., Maest, A.S. (Eds.), *Water–Rock Interaction.* Balkema, Rotterdam, pp. 477–481.

Gonnermann H. M., Mukhopadhyay S. (2007) Non-equilibrium degassing and a primordial source for helium in ocean-island volcanism. *Nature* 449, 1037–1040.

Graham D. W., Lupton J., Albarède F., Condomines M. (1990) Extreme temporal homogeneity of helium isotopes at Piton de la Fournaise, Réunion Island. *Nature* 347, 545–548.

Graham D. W. (2002) Noble gas isotope geochemistry of mid-ocean ridge and ocean island basalts: Characterization of mantle source reservoirs. In Noble Gases in Geochemistry and Cosmochemistry, Rev. Mineral. Geochem, vol. 47, edited by D. Porcelli et al., pp. 247–317. *Rev. Mineral. Geochem..* Mineral. Soc. Am., Washington, DC.

Greenland L. P., Rose W. I., Stokes J. B. (1985) An estimate of gas emissions and magmatic gas content from Kilauea volcano, *Geochim. Cosmochim. Acta*., 49, 125.

Hahm D., Hilton D. R., Castillo P. R., Hawkins J. W., Hanan B. B., Hauri E. H. (2012) An overview of the volatile systematics of the Lau Basin – Resolving the effects of source variation, magmatic degassing and crustal contamination. *Geochim. Cosmochim. Acta* 85, 88-113.

Hanan B. B., Kingsley R. H., Schilling J.G. (1986) Pb isotope evidence in the South Atlantic for migrating ridge hotspot interactions. *Nature* 322, 137–144.

Hanan B. B., Blichert-Toft J., Kingsley R., Schilling J. (2000) Depleted Iceland mantle plume geochemical signature: Artifact of multicomponent mixing? *Geochem. Geophys. Geosyst*. 1, 1003.

Hanyu T., Dunai T. J., Davies G. R., Kaneoka I., Nohda S., Uto K. (2001) Noble gas study of the Reunion hot spot: evidence for distinct less-degassed mantle sources. *Earth Planet. Sci. Lett.* 193, 83–98.

Hardarson B. S., Fitton J. G., Ellam R. M., Pringle M. S. (1997) Rift relocation – a geochemical and geochronological investigation of a palaeo-rift in NW Iceland. *Earth Planet. Sci. Lett.*, 153, pp. 181‑195.

Hardarson B. S., Fitton J. G., Hjartarson A. (2008) Tertiary volcanism in Iceland. *Jökull* 58, 161–178.

Harpp K. S., Fornari D. J., Geist D. J., Kurz M. D. (2003) Genovesa Submarine Ridge: A manifestation of plume-ridge interaction in the northern Gala´pagos Islands. *Geochem. Geophys. Geosyst.* 4, 8511.

Hart S. R., Schilling J. G., Powell J. L. (1973) Basalts from Iceland and along the Reykjanes Ridge: Sr isotope geochemistry. *Nat. Phys. Sci.* 246 (155), 104–107.

Hart S. R., Dymond J., Hogan L., Schilling J. G. (1983) Mantle plume noble gas component in glassy basalts. *Nature,* 305, 403-407.

Hashizume K., Marty B. (2004) Nitrogen isotopic analyses at the sub-picomole level using an ultra-low blank laser extraction technique, *in Handbook of Stable Isotope Analytical Techniques*, edited by P. D. Groot, pp. 361–375, Elsevier, Amsterdam.

Hashizume K., Sugiura N. (1990) Precise measurement of nitrogen isotopic composition using a quadrupole mass spectrometer, *Mass Spectrosc.,* 38, 269–286.

Hauri E. (2002) SIMS analysis of volatiles in silicate glasses: 2. Isotopes and abundances in Hawaiian melt inclusions. *Chem. Geol*. 183, 115–141.

Helmberger D., Wen L., Ding, X. (1998) Seismic evidence that the source of the Iceland hotspot lies at the core–mantle boundary. *Nature* 396, 251–258.

Heng L. (2004) Preliminary environmental impact assessment for the Hagongur high-temperature area, central Iceland. *The United Nations University: Geothermal Training Programme*, report number 10.

Hilton D. R., Grönvold K., O'Nions R. K., Oxburgh E.R. (1990) Regional distribution of [3]He anomalies in the Icelandic crust. *Chem. Geol.* 88(1–2), 53–67.

Hilton D. R., Hammerschmidt K., Loock G., Friedrichsen H. (1993) Helium and argon isotope systematics of the central Lau Basin and Valu Fa Ridge: Evidence of crust/mantle interactions in a backarc basin. *Geochim. Cosmochim. Acta,* 57, 2819–2841.

Hilton D. R., McMurtry G. M., Goff F. (1998a) Large variations in vent fluid $CO_2/^3He$ ratios signal rapid changes in magma chemistry at Loihi seamount, Hawaii. *Nature* 396, 359–362.

Hilton D. R., Grönvold K., Sveinbjornsdottir A. E., Hammerschmidt K. (1998b) Helium isotope evidence for off-axis degassing of the Icelandic hotspot. *Chem. Geol.* 149 (3–4), 173–187.

Hilton D. R., Macpherson C. G., Elliott T. R. (2000) Helium isotope ratios in mafic phenocrysts and geothermal fluids from La Palma, the Canary Islands (Spain): Implications for HIMU mantle sources. *Geochim. Cosmochim. Acta* 64 (12), 2119–2132.

Hilton D. R., Fischer T. P., Marty B. (2002) Noble gases and volatile recycling at subduction zones, in: D. Porcelli, C.J. Ballentine, R. Wieler (Eds.), Noble Gases in Cosmochemistry and Geochemistry, *Mineral. Soc. Am*. 47 319-370.

Hilton D. R., Porcelli D. (2003) Noble gases as mantle tracers, *in*, Carlson, R.W., ed., The mantle and core, Volume 2, *in* Holland, H.D., and Turekian, K.K., eds., *Treatise on geochemistry*: Oxford, UK, Elsevier-Per-gamon, p. 277–318.

Hilton D. R., Halldórsson S.A., Barry P. H., Fischer T. P., de Moor J. M., Ramirez C. J., Mangasini F., Scarsi P., (2011) Helium isotopes at Rungwe Volcanic Province, Tanzania, and the origin of East African Plateaux. *Geophysical Research Letters,* 38, L21304. http://dx.doi.org/10.1029/2011GL049589.

Hirschmann M. M. (2006) Water, Melting, and the Deep Earth H_2O Cycle. *Annu. Rev. Earth Planet. Sci.* 34, 629–653.

Hofmann A. W., White W. M. (1982) Mantle plumes from ancient oceanic crust. *Earth Planet. Sci. Lett*. 57, 421-436.

Honda M., McDougall I. M., Patterson D. B. Doulgeris A., Clague D. A. (1991) Possible solar noble-gas component in Hawaiian basalts, *Nature* 349, 149-151.

Honda M., Patterson D. B., McDougall I. Falloon T. J. (1993) Noble gases in submarine pillow basalt glasses from the Lau Basin: detection of a solar component in backarc basin basalts. *Earth Planet. Sci. Lett.* 120, 135–148.

Honda M., McDougall I. M. (1998) Primordial helium and neon in the earth – a speculation on early degassing. *Geophys. Res. Lett.* 25, 1951–1954.

Honda M., Patterson D. B. (1999) Systematic elemental fractionation of mantle-derived helium, neon, and argon in mid-oceanic ridge glasses. *Geochim. Cosmochim. Acta* 63, 2863–2874.

Hopp J., Trieloff M. (2005) Refining the noble gas record of the Réunion mantle plume source: Implications on mantle geochemistry. *Earth Planet. Sci. Lett.* 240, 573–588.

Hopp J., Trieloff M. (2008) Helium deficit in high-^{3}He/^{4}He parent magmas: predegassing fractionation, not a "helium paradox". *Geochem. Geophys. Geosyst.* 9, Q03009.

Höskuldsson A., Sparks R. S. J., Carroll M. R. (2006) Constraints on the dynamics of subglacial basalt eruptions from geological and geochemical observations at Kverkfjöll, NE-Iceland. *Bull. Volcanol.* 68, 689–701.

Ingolfsson O., (1991) A review of the Late Weichselien and early Holocene glacial and environmental history of Iceland, in Maizels, J. L. and Caseldine C. J. (Eds), *Environmental Changes in Iceland: Past and Present,* Kluwer Academic Publishers, Dordrecht, 13-29.

Italiano F., Martinelli G., Nuccio P. M. (2001) Anomalies of mantle-derived helium during the 1997-1998 seismic swarm of Umbria-Marche, Italy, *Geophys. Res. Lett.,* 28(5), 839-842, doi:10.1029/2000GL012059.

Ito G., Lin J., Graham D. (2003) Observational and theoretical studies of the dynamics of mantle plume-mid-ocean ridge interaction. *Rev. Geophys.* 41, 1017.

Jakobsson S. P., (1979) Petrology of recent basalts of the Eastern Volcanic Zone, Iceland. *Acta Nat. Isl.* 26, 1–103.

Jambon A., Weber H. W., Braun O. (1986) Solubility of He, Ne, Ar, Kr and Xe in a basalt melt in the range 1250–1600°C - Geochemical implications. *Geochim. Cosmochim. Acta* 50, 401–408, doi:10.1016/0016-7037(86)90193-6.

Jambon A., Zimmermann J. L. (1990) Water in oceanic basalts: evidence for dehydration of recycled crust. *Earth Planet. Sci. Lett.* 101, 323–331.

Javoy M., Pineau F., Iiyama I. (1978) Experimental-determination of isotopic fractionation between gaseous CO_2 and carbon dissolved in tholeiitic magma; a preliminary study. *Contrib. Mineral. Petrol.* 67, 35–39.

Javoy M., Pineau F., Demaiffe D. (1984) Nitrogen and carbon isotopic composition in the diamonds of Mbuji Mayi (Zaire) *Earth Planet. Sci. Lett.*, 107, 598‑611.

Javoy M., Pineau F., Delorme H. (1986) Carbon and nitrogen isotopes in the mantle. *Chem. Geol.* 57, 41–62.

Javoy M., Pineau F. (1991) The volatile record of a popping rock from the Mid-Atlantic Ridge at 14°N: Chemical and isotopic composition of gases trapped in the vesicles, *Earth Planet. Sci. Lett.,* 107, 598–611, doi:10.1016/0012- 821X(91)90104-P.

Jendrzejewski N., Trull T. W., Pineau F., Javoy M. (1997) Carbon solubility in mid-ocean ridge basaltic melt at low pressures (250-1950 bar). *Chem. Geol.* 138, 81-92.

Jochum K. P., Hofmann A. W., Ito E., Seufert H. M., White W. M. (1983) K, U and Th in mid-ocean ridge basalt glasses and heat production, K/U and K/Rb in the mantle. *Nature*, 306, 431-436.

Kallenbach R., Ipavich F. M., Bochsler P., Hefti S., Hovestadt D., Grünwaldt H., Hilchenbach M., Axford W. I., Balsiger H., Bürgi A., Coplan M. A., Galvin A. B., Geiss J., Gliem F., Gloeckler G., Hsieh K. C., Klecker B., Lee M. A., Livi S., Managadze G. G., Marsch E., Möbius E., Neugebauer M., Reiche K.-U., Scholer M., Verigin M. I., Wilken B., Wurz P. (1997) Isotopic composition of solar wind neon measured by CELIAS/MTOF on board SOHO. *J. Geophys. Res. – Space* 102 (A12), 26895–26904.

Kaneoka I., Takaoka N., Upton B. G. J. (1986) Noble gas systematics in basalts and a dunite nodule from Réunion and Grand Comore Islands, Indian Ocean, *Chem. Geol.* 59, 35–42.

Kempton P. D., Fitton J. G., Saunders A. D., Nowell G. M., Taylor R. N., Hardarson B. S., Pearson G. (2000) The Iceland plume in space and time: a Sr‑Nd‑Pb‑Hf study of the North Atlantic rifted margin. *Earth Planet. Sci. Lett.* 177(3–4), 255–271.

Kerrick D. M., (2001) Present and past non-anthropogenic CO_2 degassing from the solid *Earth. Rev. Geophys.* 39 (4), 564–585.

Kienast M. (2000) Unchanged nitrogen isotopic composition of organic matter in the South China Sea during the last climatic cycle: global implications, *Paleoceanography* 15, 244-253.

Kristjansson B. R., Fridriksson Th., Armannsson H., (2004) CO_2 emissions from Icelandic geothermal systems: geological constraints and preliminary results. *GFF* 126 (1), 153–154.

Kurz M. D., Meyer P. S., Sigurdsson H. (1985) Helium isotopic systematics within the neovolcanic zones of Iceland. *Earth Planet. Sci. Lett.* 74(4), 291–305.

Lang S. Q., Butterfield D. A., Lilley M. D., Johnson H. P., Hedges J. I. (2006) Dissolved organic carbon in ridge-axis and ridge-flank hydrothermal systems. *Geochim. Cosmochim. Acta* 70, 3830–3842.

Le Cloarec M. F., Marty B. (1991) Volatile fluxes from volcanoes. *Terra Nova* 3, 17– 27.

Lee J. Y., Marti K., Severinghaus J. P., Kawamura K., Yoo H. S., Lee J. B., Kim J. S. (2006) A redetermination of the isotopic abundances of atmospheric Ar. *Geochim. Cosmochim. Acta* 70, 4507–4512.

Li L., Bebout G. E. (2005) Carbon and nitrogen geochemistry of sediments in the Central American convergent margin: insights regarding subduction input fluxes, diagenesis and paleoproductivity. *J. Geophys. Res.* 110, B11202. doi:10.1029/2004JB003276.

Lux G. (1987) The behavior of noble gases in silicate liquids: solution, diffusion, bubbles and surface effects, with applications to natural samples. *Geochim. Cosmochim. Acta* 51(6),

1549–1560.

Macpherson C. G., Mattey D. P. (1994) Carbon isotope variations of CO_2 in Lau Basin basalts and ferrobasalts. *Earth Planet. Sci. Lett.* 121, 263–276.

Macpherson C. G., Hilton D. R., Sinton J. M., Poreda R. J., Craig H. (1998) High $^3He/^4He$ ratios in the Manus backarc basin: Implications for mantle mixing and the origin of plumes in the western Pacific Ocean. *Geology* 26, 1007–1010.

Macpherson C. G., Hilton D. R., Newman S., Mattey D. P. (1999) CO_2, $^{13}C/^{12}C$ and H_2O variability in natural basaltic glasses: A study comparing stepped heating and FTIR spectroscopic techniques. *Geochim. Cosmochim. Acta* 63, 1805–1813.

Macpherson C. G., Hilton D. R., Day J. M. D., Lowry D., Grönvold K. (2005a) High-$^3He/^4He$, depleted mantle and low-$\delta^{18}O$, recycled oceanic lithosphere in the source of central Iceland magmatism. Earth Planet. Sci. Lett. 233, 411–427.

Macpherson C. G., Hilton D. R., Mertz D. F., Dunai T. J. (2005b) Sources, degassing, and contamination of CO_2, H_2O, He, Ne, and Ar in basaltic glasses from Kolbeinsey Ridge, North Atlantic. Geochim. Cosmochim. Acta 69(24), 5729–5746.

Macpherson C. G., Hilton D. R., Hammerschmidt K. (2010) No slab-derived CO_2 in Mariana Trough back-arc basalts: implications for carbon subduction and for temporary storage of CO_2 beneath slow spreading ridges. *Geochim. Cosmochim. Acta* 11.

Mahaffy P. R., Donahue T. M., Atreya S. K., Owen T. C., Niemann H. B. (1998) Galileo probe measurements of D/H and $^3He/^4He$ in Jupiter's atmosphere. *Space Sci. Rev.* 84(1–2), 251– 263.

Mahoney J. J., Natland J. H., White W. M., Poreda R., Bloomer S. H., Baxter A. N. (1989) Isotopic and geochemical provinces of the Western Indian Ocean spreading centers. *J. Geophys. Res.* 94, 4033–4052.

Marty B. Jambon A. (1987) C/^{3}He in volatile fluxes from the solid Earth: Implications for carbon geodynamics. *Earth Planet. Sci. Lett.* 83, 16–26.

Marty B., Jambon A., Sano Y. (1989) Helium isotopes and CO_2 in volcanic gases of Japan. *Chem. Geol.,* 76, 25–40.

Marty, B. (1995) Nitrogen content of the mantle inferred from N_2 –Ar correlation in oceanic basalts. *Nature* 377, 326–329.

Marty B., Lenoble M., Vassard N. (1995) Nitrogen, helium and argon in basalt: A static mass spectrometer study, *Chem. Geol.*, 120, 183–195, doi:10.1016/0009-2541(94) 00120-W.

Marty B., Humbert F. (1997) Nitrogen and argon isotopes in oceanic basalts. *Earth Planet. Sci. Lett.* 152, 101-112.

Marty B., Tolstikhin I., Kamensky I. L., Nivin V., Balaganskaya E., Zimmermann J. L. (1998). Plume-derived rare gases in 380 Ma carbonatites from the Kola region (Russia) and the argon isotopic composition in the deep mantle. *Earth Planet. Sci. Lett*. 164, 179–192.

Marty B., Tolstikhin I. N. (1998) CO_2 fluxes from mid-ocean ridges, arc and plumes. *Chem. Geol.* 145, 233–248.

Marty B., Zimmermann L. (1999) Volatiles (He, C, N, Ar) in mid-ocean ridge basalts: assessment of shallow-level fractionation and characterization of source composition. *Geochim. Cosmochim. Acta* 63, 3619–3633.

Marty B., Dauphas N. (2003) The nitrogen record of crust-mantle interaction and mantle convection from Archean to present. *Earth Planet. Sci. Lett*. 206, 397– 410.

Marty B., Chaussidon M., Jurewicz A.,Wiens R., and Burnett D. S. (2011) A ^{15}N-poor isotopic composition for the solar system as shown by Genesis solar wind samples. *Science* 332, 1533–1536.

Marty B. (2012) The origins and concentrations of water, carbon, nitrogen and noble gases on Earth. *Earth Planet. Sci. Lett.* 313-314, 56-66.

Matsuda J. I., Marty B. (1995) The $^{40}Ar/^{36}Ar$ ratio of the undepleted mantle; A reevaluation. *Geophys. Res. Lett*. 22, 1937–1940.

Matter J. M., Takahashi T., Goldberg D., (2007) Experimental evaluation of in situ CO_2-water-rock reactions during CO_2 injection in basaltic rocks. Implications for geological CO_2 sequestration. *Geochemistry, Geophysics, Geosystems* 8, doi 10.1029/2006GC001427.

Mattey D. P., Carr R. H., Wright I. P., Pillinger C. T. (1984) Carbon isotopes in submarine basalts. *Earth Planet. Sci. Lett.* 70, 196–206.

Mattey D. P., Exley R. A., Pillinger C. T. (1989) Isotopic composition of CO_2 and dissolved carbon species in basalt glass. *Geochim. Cosmochim. Acta 53,* 2377–2386.

Mattey D. P. (1991) Carbon-dioxide solubility and carbon isotope fractionation in basaltic melt. *Geochim. Cosmochim. Acta* 55, 3467–3473.

McDougall I., Upton B. G. J., and Wadsworth W. J. (1965) A geological reconnaissance of Rodriguez Island Indian Ocean. *Nature* 206, 26–27.

McDougall I., Kristjansson L., Saemundsson K. (1984) Magnetostratigraphy and geochronology of northwest Iceland *J. Geophys. Res.,* 89, pp. 7029‑7060.

McLing T. L., Smith R. W., Johnson T. M. (2001) Chemical characteristics of thermal water beneath the eastern Snake River Plain, *Spec. Pap. Geol. Soc. Am.,* 353, 205–211.

Mehegan J., Robinson J., Delaney J. (1982) Secondary mineralization and hydrothermal alteration in the Reydarfjordur Drill Core, East Iceland, *J. Geophys. Res.,* 87, 6511 – 6524.

Mertz D. F., Devey C. W., Todt W., Stoffers P., Hofmann A.W. (1991) Sr‑Nd‑Pb isotope evidence against plume-asthenosphere mixing north of Iceland. *Earth Planet. Sci. Lett.* 107(2), 243–255.

Meyers P. A., Dickens G. R. (1992) Accumulations of organic matter in sediments of the Indian Ocean. *American Geophysical Union Monograph* 70, 295–309.

Mittelstaedt E., Ito G. (2005) Plume-ridge interaction, lithospheric stresses, and the origin of near-ridge volcanic lineaments, *Geochem. Geophys. Geosyst.* 6, Q06002.

Mohapatra R. K., Murty S. V. S. (2004) Nitrogen isotopic composition of the MORB mantle: A reevaluation, *Geochemistry, Geophysics, Geosystems - G^3* 5, 9 pp.

Momme P., Oskarsson N., Keays R. R. (2003) Platinum-group elements in the Icelandic rift system: melting processes and mantle sources beneath Iceland. *Chem. Geol.* 196, 209–234.

Montaggioni L., Nativel P. (1988) La Réunion, Ile Maurice : Géologie et Aperçus Biologiques, Plantes et Animaux, *Guides Géol.* Regionaux, Masson, Paris.

Montelli R., Nolet G., Dahlen F. A., Masters G. (2006) A catalogue of deep mantle plumes: new results from finite frequency tomography. *Geochem. Geophys. Geosyst*. 7, Q11007. doi:10.1029/2006GC001248.

Mook W. G., Bommerson J. C., Stavermann W. H. (1974) Carbon isotope fractionation between dissolved bicarbonate and gaseous carbon dioxide. *Earth and Planetary Science Letters* 22, 169. http://dx.doi.org/10.1016/0012-821X(74)90078-8.

Moore J. G., Batchelder J. N., Cunningham C. G. (1977) CO_2 filled vesicles in mid ocean basalt. *J. Volcanol. Geotherm. Res.,* 2, 309–327.

Moreira M., Staudacher T., Sarda P., Schilling J. G., and Allègre C. J. (1995) A primitive plume neon component in MORB: The Shona ridge-anomaly, South-Atlantic (51- 52°S). *Earth Planet. Sci. Lett.* 133(3-4), 367-377.

Moreira M., Allègre C. J. (1998) Helium-neon systematics and the structure of the mantle. *Chem. Geol.* 147, 53–59.

Moreira M., Breddam K., Curtice J., Kurz M. D. (2001) Solar neon in the Icelandic mantle: new evidence for an undegassed lower mantle. *Earth Planet. Sci. Lett.* 185, 15–23.

Moreira M., Blusztain J., Curtice J., Hart S., Dick H., Hurz M. D. (2003) He and Ne isotopes in oceanic crust: implications for noble gas recycling in the mantle. *Earth Planet. Sci. Lett.* 216, 635-643.

Morgan W. J. (1978) Rodriguez, Darwin, Amsterdam, a second type of hot spot island. *J. Geophys. Res.* 83, 5355–5360.

Morgan W. J. (1981) Hot spot tracks and the opening of the Atlantic and Indian oceans. *In The Sea,* vol. 7, edited by C. Emiliani, pp. 443–487, Wiley, New York.

Morner N. A., Etiope G. (2002) Carbon degassing from the lithosphere. *Global Planet. Change* 33, 185–203.

Muhlenbachs K., Anderson A.T. Jr., Sigvaldason G.E. (1974) Low ^{18}O basalts from Iceland. *Geochim. Cosmochim. Acta,* 38: 577-588.

Mukhopadhyay S. (2012) Early differentiation and volatile accretion recorded in deep-mantle neon and xenon, *Nature* 486, 101–104.

Murton B. J., Tindle A. G., Milton J. A., Sauter D. (2005) Heterogeneity in southern Central Indian Ridge MORB: implications for ridge– hot spot interaction. *Geochem. Geophys. Geosyst*. 6, Q03E20.

Murty S. V. S., Marti K. (1994) Nitrogen isotopic signatures in Cape York: Implications for formation of Group III A irons, *Geochim. Cosmochim. Acta,* 58, 1841–1848, doi:10.1016/0016-7037(94)90540-1.

Mysen B. O., Arculus R. J., Eggler D. H. (1975) Solubility of carbon dioxide in melts of andesite, tholeiite, and olivine nephelinite composition to 30 Kbar pressure. *Contrib. Mineral. Petrol.* 53, 227–239.

Nadin P. A., Kusznir N. J., Toth J. (1995) Transient regional uplift in the Early Tertiary of the northern North Sea and the development of the Iceland Plume. *J. Geol. Soc. London* 152, 953–958.

Nauret F., Abouchami W., Galer S. J. G., Hofmann A. W., Hémond C., Chauvel C., Dyment J. (2006) Correlated trace element - Pb isotope enrichments in Indian MORB along 18–20°S, Central Indian Ridge. *Earth Planet. Sci. Lett.* 245, 137–152.

Newman S., Lowenstern J. B. (2002) VolatileCalc: a silicate melt–H_2O–CO_2 solution model written in Visual Basic for Excel. *Comput. Geosci.* 28, 597–604.

Niedermann S., Graf T., Marti K. (1993) Mass spectrometric identification of cosmic-ray-produced neon in terrestrial rocks with multiple neon components. *Earth Planet. Sci. Lett.* 118, 65–73.

Nishio Y., Ishii T., Gamo T., Sano Y. (1999) Volatile element isotopic systematics of the Rodrigues Triple Junction Indian Ocean MORB: implications for mantle heterogeneity. *Earth Planet. Sci. Lett.*170, 241–253.

Norddahl H. (1990) Late Weichselian and Early Holocene deglaciation history of Iceland', *Jökull*, 40, 27-50.

Okino K., Ichikawa Y., Tamaki T. (2008) Detailed morphology of the Central Indian Ridge between 20º 15S and 15deg30S: Implication for hot spot‐ridge interaction, in Proceedings of the *Japan Geoscience Union (JPGU)*, Chiba, Japan, Abstract J164‐002.

O'Nions R. K., Oxburgh E. R. (1988) Helium, volatile fluxes and the development of the continental crust. *Earth Planet. Sci. Lett.* 90, 331-347.

O'Nions R. K., McKenzie D. (1993) Estimates of mantle thorium/uranium ratios from Th, U and Pb isotope abundances in basaltic melts. *Philos. Trans. R. Soc. London* 342, 65–77.

Oelkers E. H., Cole D. R. (2008) Carbon dioxide sequestration. A solution to a global problem. *Elements* 4, 305–310.

Oskarsson N., Sigvaldason G. E., Steinthorsson S. (1982) A dynamic model of rift zone petrogenesis and the regional petrology of Iceland. J. Petrol. 23, 28–74.

Ozima M., Podosek F. A. (2002) Noble Gas Geochemistry. *Cambridge University Press*, Cambridge. 286 pp.

Pan V., Holloway J. R., Hervig, R. L. (1991) The pressure and temperature dependence of carbon dioxide solubility in tholeiitic basalt melts. *Geochimica et Cosmochimica Acta* 56, 1875–1883.

Paul D., White W. M., Blichert-Toft J. (2005) Geochemistry of Mauritius and the origin of rejuvenescent volcanism on oceanic island volcanoes. *Geochem. Geophys. Geosyst,* 6, Q06007.

Peters K. E., Sweeny R. E., Kaplan I. R. (1978) Correlation of carbon and nitrogen stable isotope ratios in sedimentary organic matter, *Limnol. Ocean,* 23, 598-604, 1978.

Pik R., Marty B., Hilton D. R. (2006) How many mantle plumes in Africa? The geochem- ical point of view. *Chemical Geology* 226, 100–114. http://dx.doi.org/10.1016/j.chemgeo.2005.09.016.

Pineau F., Javoy M., Bottinga Y. (1976) $^{13}C/^{12}C$ ratios of rocks and inclusions in popping-rocks of the mid-Atlantic ridge and their bearing on the problem of isotopic composition of deep-seated carbon. *Earth Planet. Sci. Lett.,* 29, 413-421.

Pinti D. L., Hashizume K., Matsuda J. I. (2001) Nitrogen and argon signatures in 3.8 to 2.8 Ga metasediments: Clues on the chemical state of the Archean ocean and the deep biosphere. *Geochim. Cosmochim. Acta* 65, 2301-2316.

Poreda R., di Brozolo F. R. (1984) Neon isotope variations in Mid-Atlantic Ridge basalts. *Earth Planet. Sci. Lett.* 69, 277–289.

Poreda R., Shilling J. G., Craig H. (1986) Helium and hydrogen isotopes in ocean-ridge basalts north and south of Iceland, *Earth Planet. Sci. Lett.,* 78, 1-17.

Poreda R. J., Craig H., Arnorsson S., Welhan J. A. (1992) Helium isotopes in Icelandic geothermal systems: I. ^{3}He, gas chemistry, and 13C relations. *Geochim. Cosmochim. Acta* 56(12), 4221–4228.

Ray M. C., Hilton D. R., Muñoz J., Fischer T. P., Shaw, A. M. (2009) The effects of volatile recycling, degassing and crustal contamination on the helium and carbon geochemistry of hydrothermal fluids from the Southern Volcanic Zone of Chile. *Chem. Geol.* 266, 38–49.

Ritsema J., van Heijst H. J., Woodhouse J. H. (1999) Complex shear wave velocity structure imaged beneath Africa and Iceland, *Science* 286 1925-1928.

Saemundsson K. (1978) Fissure swarms and central volcanoes of the neovolcanic zones of Iceland. *Geol. J. Spec*. Issue 10, 415-32.

Saal A. L., Hauri E. H., Langmuir C. H., Perfit M. R. (2002) Vapour undersaturation in primitive mid-ocean-ridge basalt and the volatile content of Earth's upper mantle. *Nature* 419, 451–455.

Sano Y., Urabe A., Wakita H., Chiba H., Sakai H. (1985) Chemical and isotopic compositions of gases in geothermal fluids in Iceland. *Geochem. J.* 19, 135-148.

Sano Y., Gamo T., Notsu K., Wakita, H. (1995) Secular variations of carbon and helium isotopes at Izu-Oshima volcano, Japan: *J. Volcanol. Geotherm. Res.,* v. 64, p. 83-94.

Sano Y., Marty B. (1995) Origin of carbon in fumarolic gas from island arcs. *Chemical Geology* 119, 265–274.

Sano Y., Williams S. N. (1996) Fluxes of mantle and subducted carbon along convergent plate boundaries. *Geophys. Res. Lett.* 23 (20), 2749–2752.

Sano Y., Takahata N., Nishio Y., Marty B. (1998) Nitrogen recycling in subduction zones, Geophys. Res. Lett., 25, 2289–2292, doi:10.1029/98GL01687.

Sarda P., Staudacher T., Allègre C. J. (1985) ^{40}Ar/^{36}Ar in MORB glasses: constraints on atmosphere and mantle evolution. *Earth Planet. Sci. Lett*. 72, 357–375.

Sarda P., Staudacher T., Allègre C. J. (1988) Neon isotopes in submarine basalts. *Earth Planet. Sci. Lett*. 91, 73–88.

Sarda P., Graham D., (1990) Mid-ocean ridge popping rocks: Implications for degassing at ridge crests, *Earth Planet. Sci. Lett.,* 97, 268–289.

Scheele N., Hoefs J. (1992) Carbon isotope fractionation between calcite, graphite and CO_2: An experimental study. *Contrib. Mineral. Petrol.* 112, 35–45.

Schilling J. G. (1973) Iceland mantle plume: geochemical study of Reykjanes Ridge. *Nature* 242(5400), 565–571.

Schilling J. G. (1991) Fluxes and excess temperatures of mantle plumes inferred from their interaction with migrating mid-ocean ridges. *Nature* 352, 397–403.

Schubert C. J., Calvert S. E. (2001) Nitrogen and carbon isotopic composition of marine and terrestrial organic matter in Arctic Ocean sediments:: implications for nutrient utilization and organic matter composition. *Deep Sea Research Part I: Oceanographic Research Papers* 48, 789-810.

Shaw A. M., Hilton D. R., Macpherson C. G., Sinton J. M. (2001) Nucleogenic neon in high ^{3}He/^{4}He lavas from the Manus back-arc basin: a new perspective on He–Ne decoupling. *Earth Planet. Sci. Lett*. 194, 53–66.

Shaw A. M., Hilton D. R., Fischer T. P., Walker J. A., Alvarado G. (2003) Contrasting He–C relationships in Nicaragua and Costa Rica: insights into C cycling through subduction zones. *Earth Planet. Sci. Lett.* 214, 499–513.

Shaw A. M., Hilton D. R., Macpherson C. G., Sinton J. M. (2004) The CO_2-He-Ar-H_2O systematics of the Manus back-arc basin: Resolving source composition from degassing and contamination effects. *Geochim. Cosmochim. Acta* 68, 1837–1855, doi:10.1016/j.gca.2003.10.015.

Sigvaldason G. E. (1968) Structure and products of subaquatic volcanoes in Iceland. *Contrib Mineral Petrol* 18:1–16.

Slater L., Jull M., McKenzie D., Grönvold K. (1998) Deglaciation effects on mantle melting under Iceland: results from the northern zone, *Earth Planet. Sci. Lett.* 164 (1998) 151-164.

Smith W. H. F., Sandwell D. T. (1997) Global sea floor topography from satellite altimetry and ship depth soundings, *Science*, 277(5334), 1956‑1962, doi:10.1126/science.277.5334.1956.

Spane F. A., Webber W. D. (1995) Hydrochemistry and hydrogeologic conditions within the Hanford Site upper basalt confined aquifer system, *PNL*-10817, Pac. Northw. Natl. Lab., Richland, Wash.

Staudacher T., Kurz M. D., Allègre C. J. (1986) New noble-gas data on glass samples from Loihi Seamount and Hualalai and on dunite samples from Loihi and Reunion Island. *Chem. Geol*. 56, 193-205.

Stolper E., Holloway J. R. (1988) Experimental determination of the solubility of carbon dioxide in molten basalt at low pressure. *Earth Planet. Sci. Lett.* 87:397–408.

Stuart F. M., Lass-Evans S., Fitton J. G., Ellam R. M. (2003) High ^{3}He/^{4}He ratios in pictritic basalts from Baffin Island and the role of a mixed reservoir in mantle plumes. *Nature* 424, 57–59.

Sun S. S., Tatsumoto M., Schilling J. G. (1975) Mantle plume mixing along the Reykjanes Ridge axis: lead isotopic evidence. *Science* 190(4210), 143–147.

Sveinbjörnsdóttir Á. E., Heinemeier J., Arnórsson S. (1995) Origin of ^{14}C in Icelandic groundwater. *Radiocarbon* 37(2): 551–65.

Szaran J., 1997. Achievement of carbon isotope equilibrium in the system HCO_3^- (solution) – CO_2 (gas). *Chemical Geology* 142, 79–86. http://dx.doi.org/10.1016/ S0009-2541(97)00077-6.

Takahata N., Nishio Y., Yoshida N., Sano Y. (1998) Precise isotopic measurements of nitrogen at the sub-nanomole level, *Anal. Sci.,* 14, 485–491, doi:10.2116/analsci.14.485.

Tedesco D., Nagao K., Scarsi P. (1998) Noble gas isotopic ratios from historical lavas and fumaroles at Mount Vesuvius (southern Italy): constraints for current and future volcanic activity, *Earth Planet. Sci. Lett*., 164(1-2), 61-78, doi:10.1016/S0012- 821X(98)00167-8.

Thirlwall M. F., Gee M. A. M., Taylor R. N., Murton B. J. (2004) Mantle components in Iceland and adjacent ridges investigated using double-spike Pb isotope ratios. *Geochim. Cosmochim. Acta* 68(2), 361–386.

Thirlwall M. F., Gee M. A. M., Lowry D., Mattey D. P., Murton B. J., Taylor R. N. (2006) Low δ^{18}O in the Icelandic mantle and its origins: evidence from Reykjanes Ridge and Icelandic lavas. *Geochim. Cosmochim. Acta* 70, 993–1019.

Thordarson T., Höskuldsson Á. (2008) Postglacial volcanism in Iceland. *Jökull* 58: 197–228.

Thorseth, I. H., Furnes H., Heldal M. (1992) The importance of microbiological activity in the alteration of natural basaltic glass, *Geochim. Cosmochim. Acta,* 56, 845–850.

Thiemens M. H., Clayton R. N. (1983) Nitrogen contents and isotopic ratios of clasts from enstatite chondrite Abee, Earth Planet. Sci. Lett., 62(1), 165–168, doi:10.1016/0012-821X(83)90080-8.

Trieloff M., Kunz J., Clague D. A., Harrison D., Allègre C. J. (2000) The nature of pristine noble gases in mantle plumes. *Science* 288, 1036–1038.

Trieloff M., Kunz J., Allègre C. J. (2002) Noble gas systematics of the Réunion mantle plume source and the origin of primordial noble gases in Earth's mantle. *Earth Planet. Sci. Lett*. 200, 297–313.

Trieloff M., Falter M., Jessberger E. K. (2003) The distribution of mantle and atmospheric argon in oceanic basalt glasses. *Geochim. Cosmochim. Acta* 67, 1229–1245.

Trieloff M., Kunz J. (2005). Isotope systematics of noble gases in the Earth's mantle: possible sources of primordial isotopes and implications for mantle structure. *Phys. Earth Planet. Inter*. 148, 13–38.

Trull T. W., Kurz M. D. (1993) Experimental measurements of ^{3}He and ^{4}He mobility in olivine and clinopyroxene at magmatic temperatures. *Geochim. Cosmochim. Acta* 57, 1313–1324.

Tryggvason K., Husebye E. S., Stefansson R. (1983) Seismic image of the hypothesized Icelandic hot spot. *Tectonophysics* 100(1–3), 97–118.

Tuffen H, Owen J, Denton J. (2010) Magma degassing during subglacial eruptions and its use to reconstruct palaeo-ice thicknesses. *Earth-Sci Rev*. 99(1–2):1–18. doi:10.1016/j.earscirev.2010.01.001.

Ulrich M., Hemond C., Nonnotte P., Jochum K. P. (2012) OIB/seamount recycling as a possible process for E-MORB genesis. *Geochem. Geophys. Geosyst*: Vol. 13, Q0AC19, 24 PP., doi:10.1029/2012GC004078.

Varekamp J. C., Kreulen R., Poorter R. P. E., Van Bergen, M. J. (1992) Carbon sources in arc volcanism, with implications for the carbon cycle. *Terra Nova* 4, 363–373.

Valbracht P. J., Staudacher T., Malahoff A., Allegre C. J. (1997) Noble gas systematics of deep rift zone glasses from Loihi Seamount, Hawaii. *Earth Planet. Sci. Lett*. 150, 399–411.

Vogel J. C., Grootes P. M., Mook W. G. (1970) Isotope fractionation between gaseous and dissolved carbon dioxide. *Zeitschrift für Physik* 230, 255–258. http://dx.doi.org/10.1007/BF01394688.

Wardell L. J., Kyle, P. R. (1998) Volcanic carbon dioxide emission rates: White Island, New Zealand and Mt. Erebus, Antarctica *(AGU abstract). EOS Trans., (Fall Meeting Suppl.)* 79 (45), 927.

Watson E. B. (1991) Diffusion of dissolved CO_2 and Cl in hydrous silicic to intermediate magmas. *Geochim. Cosmochim. Acta* 55, 1897–1902.

Werner C., Brantley S. (2003) CO_2 emissions from the Yellowstone volcanic system. *Geochem. Geophys. Geosyst.* 4 (article 1061), 27.

Wetherill G. W. (1954) Variations in the isotopic abundances of neon and argon extracted from radioactive minerals. *Phys. Rev.* 96, 679–683.

White R., McKenzie D., O'Nions K. (1992) Oceanic crustal thickness from seismic measurements and rare earth element inversions. *J. Geophys. Res.* 97, 683–715.

White R. S. (1993) Melt production rates in mantle plumes. *Philos. Trans. R. Soc. London* A342, 137–153.

White R. S., Bown J. W., Smallwood J. R. (1995) The temperature of the Iceland plume and origin of outward-propagating V-shaped ridges. *J. Geol. Soc.* London 152, 1039–1045.

Williams S. N., Schaefer S. J., Calvache M. L., Lopez, D. (1992) Global carbon dioxide emission to the atmosphere by volcanoes. *Geochim. Cosmochim. Acta* 56, 1765– 1770.

Wolfe C., Bjarnason I., VanDecar J., Soloman S. (1997) Seismic structure of the Iceland mantle plume. *Nature* 385, 245–247.

Wright I. P., Boyd S. R., Franchi I. A., Pillinger C. T. (1988) Determination of high precision nitrogen stable isotope ratios at the sub-nanomole level, *J. Phys. E Sci. Instrum.,* 21, 865–875, doi:10.1088/0022-3735/21/9/011.

Yatsevich I., Honda M. (1997) Production of nucleogenic neon in the Earth from natural radioactive decay. *J. Geophys. Res. – Sol. Earth* 102, 10291–10298.

Zhao D. P. (2004) Global tomographic images of mantle plumes and subducting slabs: insight into deep Earth dynamics. *Phys. Earth Planet. Inter.* 146(1–2), 3–34.